NASA-CR-200094

FY1995 Report Enclosure
NASA Grant S-09936-F
(PI: Woods)

# RESPONSE OF THE UPPER ATMOSPHERE TO VARIATIONS IN THE SOLAR SOFT X-RAY IRRADIANCE

IN-46-CR
7683
P-254

by

Scott M. Bailey

B. S., Virginia Tech, 1990

M. S., University of Colorado, 1994

(NASA-CR-200094) RESPONSE OF THE UPPER ATMOSPHERE TO VARIATIONS IN THE SOLAR SOFT X-RAY IRRADIANCE Ph.D. Thesis (Colorado Univ.) 254 p

N96-18502

Unclas

G3/46 0098926

A thesis submitted to the

Faculty of the Graduate School of the

University of Colorado in partial fulfillment

of the requirement for the degree of

Doctor of Philosophy

Department of Astrophysical, Planetary, and Atmospheric Science

1995

# RESPONSE OF THE UPPER ATMOSPHERE TO VARIATIONS IN THE SOLAR SOFT X-RAY IRRADIANCE

by

Scott M. Bailey

B. S., Virginia Tech, 1990

M. S., University of Colorado, 1994

A thesis submitted to the

Faculty of the Graduate School of the

University of Colorado in partial fulfillment

of the requirement for the degree of

Doctor of Philosophy

Department of Astrophysical, Planetary, and Atmospheric Science

1995

This dissertation for the Doctor of Philosophy degree by

Scott Martin Bailey

has been approved for the

Department of

Astrophysical, Planetary and Atmospheric Sciences

by

Charles A. Barth

Daniel N. Baker

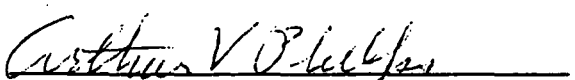

Arthur V. Phelps

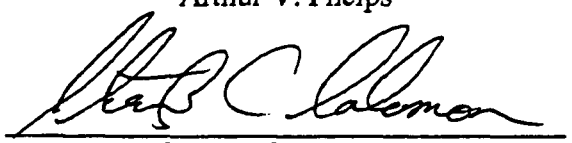

Stanley C. Solomon

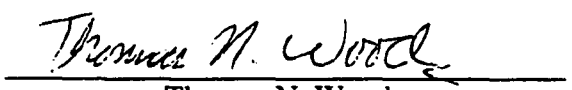

Thomas N. Woods

Date July 17, 1995

PRECEDING PAGE BLANK NOT FILMED

PAGE 1 INTENTIONALLY BLANK

Bailey, Scott M. (Ph.D., Astrophysical, Planetary, and Atmospheric Sciences)

Response of the Upper Atmosphere to Variations in the Solar Soft X-ray Irradiance

Thesis directed by Professor Charles A. Barth

Terrestrial Far Ultraviolet (FUV) airglow emissions have been suggested as a means for remote sensing the structure of the upper atmosphere. The energy which leads to the excitation of FUV airglow emissions is solar irradiance at Extreme Ultraviolet (EUV) and soft x-ray wavelengths. Solar irradiance at these wavelengths is known to be highly variable; studies of Nitric Oxide (NO) in the lower thermosphere have suggested a variability of more than an order of magnitude in the solar soft x-ray irradiance. To properly interpret the FUV airglow, the magnitude of the solar energy deposition must be known. Previous analyses have used the electron impact excited Lyman-Birge-Hopfield (LBH) bands of $N_2$ to infer the flux of photoelectrons in the atmosphere and thus to infer the magnitude of the solar irradiance. This dissertation presents the first simultaneous measurements of the FUV airglow, the major atmospheric constituent densities, and the solar EUV and soft x-ray irradiances. The measurements were made on three flights of an identical sounding rocket payload at different levels of solar activity. The linear response in brightness of the LBH bands to variations in solar irradiance is demonstrated. In addition to the $N_2$ LBH bands, atomic oxygen lines at 135.6 and 130.4 nm are also studied. Unlike the LBH bands, these emissions undergo radiative transfer effects in the atmosphere. The OI emission at 135.6 nm is found to be well modeled using a radiative transfer calculation and the known excitation processes. Unfortunately, the assumed processes leading to OI 130.4 nm excitation are found to be insufficient to reproduce the observed variability of this emission. Production of NO in the thermosphere is examined; it is shown that a lower than previously reported variability in the solar soft x-ray irradiance is required to explain the variability of NO.

PRECEDING PAGE BLANK NOT FILMED

PAGE 4 INTENTIONALLY BLANK

## Dedication

This dissertation represents the culmination of my academic education, eleven years of undergraduate and graduate work. In these years I have seen times of great success and also times when failure seemed inevitable. The one constant during all those times was a large basis of support from friends and family, without whom I could not have made it this far. The friends I have made are spread throughout the US and several other countries. I met them in past jobs, high school, Virginia Tech, University of Colorado, and on some especially memorable adventures. To point out all the people I would like to thank would take many more pages than this dissertation can hold; therefore, I would like to dedicate this work to all those people. In particular to my family: my parents Andrew and Carol, my brothers Randy and Tom, my grandparents Nick and Margaret, and Mike and Tove, my uncle and aunt.

PRECEDING PAGE BLANK NOT FILMED
PAGE 6 INTENTIONALLY BLANK

## Acknowledgments

This section of the dissertation was the hardest one to write. I have benefited from so many friendships and work relationships that I could not possibly list them all. I'm thankful to a great many people and I will list as many as I can here.

Undoubtedly the greatest measure of my gratitude goes to the three men who served as mentors in my graduate research: Charles Barth, Stan Solomon, and Tom Woods. They presented me with tremendous opportunities to do the research I loved; and together we enjoyed great adventures in rocket launches, massive deserts, and burning of midnight oil. The happiest part about graduating is knowing that I will continue to work with these three on future projects.

In addition, the two other members of my committee, Dan Baker and Art Phelps read my thesis carefully and provided many useful comments. I thank them for their effort and for several very helpful conversations.

My partners in the rocket work include Rick Kohnert, Greg Ucker, and Tom Woods. They were patient when I had to be shown everything twice and have always been there for me. We've seen a lot of long days and nights together; I wouldn't trade those times for all the ice cream and pizza in the world. Janet Tracy and Ray Wrigley are other valuable people who were part of our adventures. I thank the great many other people at LASP and HAO who helped. A few that I must mention include, Paul Bay, Don Hassler, Jim Johnson, Terry Leach, Kim Streander, Jim Westfall, and John Worden. Paul and Jim were especially helpful and made things easier.

In each rocket launch, a tremendous number of people are involved. I thank all of the people at Aerodyne, Lockheed, Physical Sciences Lab, Poker Flat Research Range, Space Environment Lab, Space Vector, SURF II at NIST, Wallops Flight

PRECEDING PAGE BLANK NOT FILMED
PAGE 8 INTENTIONALLY BLANK

Facility, and White Sands Missile Range. I especially thank Geoff Bland of Wallops Flight Facility for making rocket launches even more fun.

Randy Canfield of NIST and Raj Korde of IRD were collaborators in the development of the soft x-ray photometers. Their help is greatly appreciated.

At LASP, I have benefited from discussions with many people, especially Steve Lane, Mark Lankton, George Lawrence, Bill McClintock, Wayne Pryor, Ian Stewart, and Gary Thomas.

Many office mates have been there to help make grad school more enjoyable, they are Li Chen, Stefanie Lawson, Justin Maki, Rob McFeeters, Steve Ostermann, Jeff Perich, Bob Portmann, and Huck Wach. In my first year Frank Eparvier was there to point the way as I faced each new situation. I would also like to thank all the students in my first year class for sharing the painful parts of grad school with me, especially Andrew Fusco and Jody Wilson with whom I shared some of the best times during these five years. Other students who made life more fun were Joan Alexander, Will Colwell, Brad Sandor, and Felicity Wong.

One group of people that have made my last year as a student an especially fun one are the SNOE team members. I thank every member of the group for all the fun we've had and for all we have in front of us. In particular, I want to thank Aimee Merkel, Erica Rodgers, and Stan Straight for being patient with me as I finished this dissertation. Mark Salada and Pete Withnell have always been ready to provide a night out to help deal with the stress.

There are some people at LASP without whom the lab would have to shut down. Some of these people saved me several times, I would like to thank Nancy Byers, Melissa Crogle, John Daspit, Phil Evans, Sara Lankton, and Liz Petersen. An

especially big thanks goes to Bonnie Hotard who kept me out of trouble all this time. I owe many favors to Russ and Cindy who made night work much more fun.

I would like to thank all the many friends I made at NRL; their continued support has meant a great deal to me. I would especially like to thank Don Anderson, Dave Cleary, Ken Dymond, Bob McCoy, Bob Meier, Jeff Morrill, Larry Paxton, and Dianne Prinz for introducing me to aeronomy, and also Katherine Andersen, Sandy Daniels, Ronen Feldman, Clyde Fortna, Debbie McIntire, John Moser, Bill Sawchuck, Stefan Thonnard, and Kenny Wolfram for making NRL a fun place to work. Dave Cleary, Ken Dymond, Bob McCoy, Bob Meier, and Larry Paxton have been very supportive of me throughout my education. Their encouragement has been a big help to me. Stefan Thonnard has been a close friend and sounding board for ideas.

Jean Auleta, Stefanie Lawson, Justin Maki, and Wayne Pryor each did me a great service by reading my thesis and making many helpful suggestions. Stefanie went above and beyond the call of duty in how she carefully read each page of my thesis; her suggestions have made it a much better document.

Some friends I need to thank are Steve Henderson, Trevor Taylor, and Dat Nguyen, they also made life easier and more fun while I was in school. I want to thank all the people who came to my pizza nights, we have had and will continue to have many great times together. I met Grace Kwok and Doobie Soo during a hard time, but my continuing friendship with them certainly helped me through it. Angie Loo has been a close friend and constant companion from afar. I thank Jean Auleta for her friendship and for introducing me to a new point of view. Jody Wilson and I have had many great conversations which made life easier to understand. Uyen Tran has been a special friend of mine for many years.

Finally, I would like to thank once again all the members of my family for all of their constant support and encouragement. I could not have done this without you.

## Table of Contents


Introduction ..... 25

1.1 Overview of Dissertation Topics ..... 25

1.1.1 Solar Irradiance ..... 26

1.1.2 Photoelectron Modeling ..... 30

1.1.3 Previous Analyses of FUV Airglow Data ..... 31

1.2 Overview of Dissertation ..... 33

Spectroscopy and Excitation of Terrestrial Far Ultraviolet Dayglow Emissions ..... 35

2.1 Introduction ..... 35

2.2 Notation and Terminology of Spectroscopy ..... 35

2.2.1 Atomic Spectroscopy ..... 36

2.2.2 Diatomic Molecular Spectroscopy ..... 40

2.3 The Cross Section ..... 44

2.4 Electron Impact Excitation Cross Sections ..... 45

2.4.1 The Excitation of the LBH Bands ..... 46

2.4.2 Excitation of the OI 135.6 nm Emission ..... 51

2.4.3 Excitation of the OI 130.4 nm Emission ..... 58

2.4.3.1 Photoelectron Impact Excitation ..... 58

2.4.3.2 Fluorescent Scattering of Sunlight ..... 61

2.5 Spectroscopy of the Lyman Birge Hopfield Bands of $N_2$ ..... 62

2.5.1 The Franck-Condon Principle ..... 62

2.5.2 Calculation of Synthetic LBH Spectra ..... 64

2.5.3 Deviations from Franck-Condon Theory ..... 68

2.6 Summary ..... 71

Modeling of Photoelectron and Airglow Processes ..... 73

3.1 Introduction ..... 73



PRECEDING PAGE BLANK NOT FILMED

PAGE 12 INTENTIONALLY BLANK

3.2 The */glow* Photoelectron Model ..... 73

3.2.1 Model Formalism ..... 73

3.2.2 Photoabsorption and Photoionization Cross Sections ..... 82

3.2.3 Auger Ionization ..... 84

3.3 Radiative Transfer ..... 85

3.3.1 Optically Thin Emissions ..... 85

3.3.2 Optically Thick Emissions ..... 87

3.3.3 Cross Section for Pure Absorption by $O_2$ ..... 96

3.4 Effect of Solar Irradiance Bins on Model Calculations ..... 96

3.5 Summary ..... 106

Sounding Rocket Instrumentation and Calibration ..... 109

4.1 Introduction ..... 109

4.2 CODACON Array Detectors ..... 109

4.3 The Solar EUV Irradiance and Terrestrial Airglow Experiment ..... 110

4.3.1 EUV Grating Spectrograph (EGS) ..... 112

4.3.2 Calibration of the EGS Using a Synchrotron Light Source ..... 114

4.3.3 Solar X-ray Photometers (SXP ..... 120

4.3.4 Calibration of the Solar X-ray Photometers ..... 126

4.3.5 FUV Airglow Spectrograph ..... 127

4.3.6 Laboratory Calibration of the FUV Airglow Spectrograph ..... 135

4.4 Summary ..... 145

Reduction and Analysis of Rocket Data ..... 147

5.1 Introduction ..... 147

5.2 The Solar EUV Irradiance and Terrestrial Airglow Experiment ..... 147

5.2.1 Reduction of EUV Grating Spectrograph Data ..... 147

5.2.2 Absolute Solar EUV Irradiances ..... 149

5.2.3 Attenuation of the Solar Irradiance ..... 151

5.2.4 Analysis of Solar X-ray Photometer Data ..... 164
5.2.5 Reduction of FUV Airglow Measurements ..... 172
5.3 Summary ..... 182
Comparison of Airglow Measurements to Models ..... 183
6.1 Introduction ..... 183
6.2 Application of Numerical Models ..... 183
6.3 Comparison of Model Results to Airglow Data ..... 184
6.3.1 Analysis of 36.124 Data ..... 185
6.3.2 Analysis of 36.098 Data ..... 187
6.3.3 Analysis of 36.107 Data ..... 190
6.3.4 Discussion of Comparison Results ..... 194
6.4 Production of Airglow Emissions by Solar Irradiance ..... 195
6.5 Summary ..... 200
Effect of Solar Soft X-rays on Nitric Oxide Production ..... 203
7.1 Introduction ..... 203
7.2 NOx 1-D Photochemical Model ..... 203
7.2.1 Model Formalism ..... 203
7.2.2 The PEGFAC Photoelectron Model ..... 206
7.2.3 $N_2$ Photoelectron Dissociation Cross Section ..... 208
7.2.4 Comparison of NOx 1-D with */glow* and PEGFAC ..... 209
7.3 Summary ..... 216
Conclusions ..... 217
8.1 Summary ..... 217
8.2 Future Research ..... 220
Bibliography ..... 221
Appendix A Analytic Models of Electron Impact Cross Sections ..... 233
Appendix B Solar Irradiance and Cross Sections in */glow* Bins ..... 241

Appendix C Results of Solar Irradiance Measurements .....253

## List of Tables


Table 1-1 Analyses of LBH Emissions ..... 32

Table 2-1 Measurements of the LBH Electron Impact Cross Section ..... 47

Table 2-2 OI Electron Impact Emission Cross Sections (x $10^{-18}$ $cm^2$) for the OI 135.6 and 130.4 nm Emissions† ..... 53

Table 2-3 OI Atomic Absorption and Emission Line Parameters at 1000K ..... 54

Table 2-4 Spectroscopic Constants of the $N_2$ $a^1\Pi_g$ - $X^1\Sigma_g^+$ Transition ..... 65

Table 3-1 MSIS Model Atmosphere Parameters ..... 79

Table 3-2 Ionization and Dissociation Energies (eV) ..... 86

Table 4-1 Photodiode Coatings used in Rocket Flights ..... 124

Table 4-2 Calibration Uncertainty for the FUV Airglow Spectrograph ..... 142

Table 5-1 Conditions for Rocket Flights ..... 148

Table 5-2 MSIS Parameter Modifications Derived from EGS Data ..... 164

Table 5-3 Scale Factors and Solar Irradiances from SXP Data ..... 170

Table 5-4 Peak Brightnesses for Airglow Emissions† ..... 182

Table A-1 Ionization Cross Section Parameters ..... 236

Table A-2 Excitation Cross Section Parameters ..... 237

Table A-3 Elastic Cross Sections and Backscatter Probabilities for O ..... 238

Table A-4 Elastic Cross Sections and Backscatter Probabilities for $O_2$ ..... 239

Table A-5 Elastic Cross Sections and Backscatter Probabilities for $N_2$ ..... 240

Table B-1 Binned Solar Irradiance and Cross Sections for O ..... 242

Table B-2 Binned Solar Irradiance and Cross Sections for $O_2$ ..... 246

Table B-3 Binned Solar Irradiance and Cross Sections for $N_2$ ..... 250

Table C-1 Solar Irradiance for October 27, 1992 (Rocket Flight 36.098) ..... 254

Table C-2 Solar Irradiance for October 4, 1993 (Rocket Flight 36.107) ..... 257

Table C-3 Solar Irradiance for November 3, 1994 (Flight 36.124) ..... 260

## List of Figures

Figure 1-1 The SC#21REFW solar reference spectrum. This solar minimum reference spectrum is the basis for several models of solar variability.....28

Figure 2-1 Energy level diagram for atomic oxygen, taken from Meier (1991).....39

Figure 2-2 Energy level diagram for molecular nitrogen, taken from Meier (1991)....42

Figure 2-3 A comparison of differential cross section measurements for the LBH bands. Both measurements are made at an electron energy of 15 eV.....49

Figure 2-4 Cross section for photoelectron impact excitation of the LBH bands.....52

Figure 2-5 Photoelectron impact excitation cross sections, cascade and total, for the OI 135.6 and 130.4 nm emissions.....57

Figure 2-6 Illustration of the Franck-Condon principle. The most probable absorption is from v''=0 is to v' = 5. The most probable emissions are from v'=2 are to v''=1 and v''=6. This figure is taken from Thorne (1988).....63

Figure 2-7 Synthetic LBH spectrum for 1000 K. .....69

Figure 2-8 Synthetic LBH (2,0) bands at high resolution for temperatures of 500 and 1500K.....70

Figure 3-1 Photoelectron spectrum calculated by the */glow* model for the solar maximum conditions described in Table 3-1.....80

Figure 3-2 Photoelectron spectrum calculated by the */glow* model for the solar minimum conditions described in Table 3-1.....81

Figure 3-3 Cross sections for photoionization and pure absorption by O, $O_2$, and $N_2$.83

Figure 3-4 Initial volume excitation rate for the LBH bands and the OI 135.6 nm emission calculated by the */glow* model for the conditions described in Table 3-1.92

Figure 3-5 Initial excitation rate for the OI 130.4 nm emission calculated by the */glow* model for the conditions described in Table 3-1.....93

Figure 3-6 Final excitation rate for the OI 135.6 nm emission calculated by the Feautrier radiative transfer model for the conditions described in Table 3-1. The initial excitation rate calculated by the */glow* model is shown in Figure 3-3.....94

Figure 3-7 Final excitation rate for the OI 130.4 nm emission calculated by the Feautrier radiative transfer model for the conditions described in Table 3-1. The initial excitation rate calculated by the */glow* model is shown in Figure 3-4.....95

Figure 3-8 LBH limb brightness calculated by the optically thin radiative transfer model using initial excitation rates from */glow* (Figure 3-4). The geophysical conditions are listed in Table 3-1. .....97

PRECEDING PAGE BLANK NOT FILMED
PAGE 18 INTENTIONALLY BLANK

Figure 3-9 Limb brightness of the OI 135.6 nm emission calculated by the Feautrier radiative transfer model using initial excitation rates from */glow* (Figure 3-4). The geophysical conditions are listed in Table 3-1..... 98

Figure 3-10 Limb brightnesses of the OI 130.4 nm emission calculated by the Feautrier radiative transfer model using initial excitation rates from */glow* (Figure 3-4). The geophysical conditions are listed in Table 3-1..... 99

Figure 3-11 Cross section for pure absorption by $O_2$.....100

Figure 3-12 The */glow* calculations of LBH volume excitation rate and $N_2$ photoelectron dissociation rate using various solar irradiance binning schemes described in the text.....103

Figure 3-13 The */glow* calculations of O and $N_2$ photoionization using various solar irradiance binning schemes described in the text.....104

Figure 3-14 The */glow* calculations of $O_2$ photoionization using various solar irradiance binning schemes described in the text. .....105

Figure 4-1 Layout of the Solar EUV Irradiance and Terrestrial Airglow Experiment. The arrows point in the aft direction during launch and toward the sun for an observing period of approximately 5 minutes during flight.....111

Figure 4-2 Optical layout of the EUV Grating Spectrograph (EGS). The EGS is a Rowland circle grating spectrograph with a 1 x 1024 CODACON array detector.113

Figure 4-3 Transmission of SnGe foil filter. This filter is used to determine wavelength and second order grating contributions during the SURF calibration of the EGS.116

Figure 4-4 SURF fluxes for 180 and 284 MeV beam energies.....118

Figure 4-5 Quantum throughput of the EGS spectrograph. The scatter in the result is due to the flat field of the detector and is not due to counting statistics.....121

Figure 4-6 Schematic of the solar x-ray photometer electronics. Current from the photodiode is converted to a series of pulses such that the frequency of the pulses is proportional to the original current.....123

Figure 4-7 Sensitivity of the coated photodiodes flown on 36.107. An uncoated photodiode is shown for comparison. Error bars are discussed in the text. .....128

Figure 4-8 Sensitivity of the coated photodiodes flown on 36.124. Those photodiodes which were also flown on 36.107 are not shown. Error bars are discussed in the text.....129

Figure 4-9 Optical layout of the FUV airglow spectrograph. The spectrometer is a Wadsworth mount. .....130

Figure 4-10 Focal length of $CaF_2$ lens as a function of wavelength. The focal length is measured from the back (exit) side of the lens. The dotted line shows the 27.65 mm chosen as the focal length used in the telescope.....133

Figure 4-11 Altitude resolution of the telescope for the FUV airglow instrument shown for various wavelengths. At 138.3 nm the telescope is in near perfect focus. The observation angles, relative to the horizon, represented by the altitudes are also shown. Note that the area under each curve is the same..... 134

Figure 4-12 Layout of the Calibration - Test - Equipment (CTE) facility. Instruments can be placed in the test chamber (to the right) to view the monochromator output. A scattering screen can also be placed inside the vacuum chamber to simulate an extended source. This requires a calibration lamp to be mounted to a vacuum port at the top (coming out of the page) of the chamber..... 136

Figure 4-13 Transmission of the $CaF_2$ lens used in the airglow spectrograph telescope. Transmission of the $CaF_2$ filter is similar..... 139

Figure 4-14 Quantum throughput of the airglow spectrograph. This *QT* is at the center of the spectrograph and over a small FOV defined by the CTE monochromator. Results are not shown for the wavelength region between 142 and 147 nm where the CODACON detector has several defective pixels..... 141

Figure 4-15 Ratio of relative *QT* for Full FOV to small FOV for the airglow spectrograph. Results are not shown for the wavelength region between 142 and 147 nm where the CODACON detector has several defective pixels..... 144

Figure 4-16 Sensitivity of the airglow spectrograph. The sensitivity, as calculated by Equation 4-11, is the product of the results presented in the last three figures. Results are not shown for the wavelength region between 142 and 147 nm where the CODACON detector has several defective pixels..... 146

Figure 5-1 Spectrum from the EGS, taken at apogee..... 150

Figure 5-2 Attenuation of the 55.4 nm solar emission. Crosses are measurements, solid line is MSIS prediction. Data and MSIS prediction are shown in units of transmission of the atmosphere..... 153

Figure 5-3 Flight 36.124 atmospheric transmission for solar emission lines. Dotted line represents MSIS prediction. In the left panels, solid lines are model predictions obtained by scaling MSIS O; in the right panels, solid lines are model predictions obtained by reducing MSIS F10.7 and, therefore, temperature. Crosses are measurements..... 155

Figure 5-4 Flight 36.124 atmospheric transmission for solar emission lines. Dotted line represents MSIS prediction. In the left panels, solid lines are model predictions obtained by scaling MSIS O; in the right panels, solid lines are model predictions obtained by reducing MSIS F10.7 and, therefore, temperature. Crosses are measurements..... 156

Figure 5-5 Flight 36.124 atmospheric transmission for solar emission lines. Dotted line represents MSIS prediction. In the left panels, solid lines are model predictions obtained by scaling MSIS O; in the right panels, solid lines are model predictions obtained by reducing MSIS F10.7 and, therefore, temperature. Crosses are measurements..... 157

Figure 5-6 Flight 36.098 atmospheric transmission for solar emission lines. Dotted line represents MSIS prediction. In the left panels, solid lines are model predictions

obtained by scaling MSIS O; in the right panels, solid lines are model predictions obtained by reducing MSIS F10.7 and, therefore, temperature. Crosses are measurements.....158

Figure 5-7 Flight 36.098 atmospheric transmission for solar emission lines. Dotted line represents MSIS prediction. In the left panels, solid lines are model predictions obtained by scaling MSIS O; in the right panels, solid lines are model predictions obtained by reducing MSIS F10.7 and, therefore, temperature. Crosses are measurements.....159

Figure 5-8 Flight 36.098 atmospheric transmission for solar emission lines. Dotted line represents MSIS prediction. In the left panels, solid lines are model predictions obtained by scaling MSIS O; in the right panels, solid lines are model predictions obtained by reducing MSIS F10.7 and, therefore, temperature. Crosses are measurements.....160

Figure 5-9 Flight 36.107 atmospheric transmission for solar emission lines. Dotted line represents MSIS prediction. In the left panels, solid lines are model predictions obtained by scaling MSIS O; in the right panels, solid lines are model predictions obtained by reducing MSIS F10.7 and, therefore, temperature. Crosses are measurements.....161

Figure 5-10 Flight 36.107 atmospheric transmission for solar emission lines. Dotted line represents MSIS prediction. In the left panels, solid lines are model predictions obtained by scaling MSIS O; in the right panels, solid lines are model predictions obtained by reducing MSIS F10.7 and, therefore, temperature. Crosses are measurements.....162

Figure 5-11 Flight 36.107 atmospheric transmission for solar emission lines. Dotted line represents MSIS prediction. In the left panels, solid lines are model predictions obtained by scaling MSIS O; in the right, solid lines are model predictions obtained by reducing MSIS F10.7 and, therefore, temperature. Crosses are measurements.....163

Figure 5-12 Typical flight profile for a solar x-ray photometer; the Al/Sc/C coated photodiode flown on 36.124 is shown. The period of lower count rate at apogee is the result of closing the door and placing a $MgF_2$ window in front of the photometer.....166

Figure 5-13 Convolution of 36.124 x-ray photometer sensitivities with reference solar spectrum.....167

Figure 5-14 Convolution of 36.107 x-ray photometer sensitivities with reference solar spectrum. The reference solar spectrum is shown for comparison.....168

Figure 5-15 Attenuation profiles of the Al/Sc/C coated photodiode flown on 36.107 and 36.124. Crosses are data points. Solid line is prediction using MSIS atmosphere with scaled O and solar irradiance using the derived scaling factors.....173

Figure 5-16 Raw 36.124 FUV airglow spectrum at 150 km. Emissions of OI, NI, and $N_2$ are labeled. Data between 142 and 147 nm are not shown due to a defect in the CODACON detector.....175

Figure 5-17 Raw 36.098 and 36.107 FUV airglow spectrum at 150 km. Data at longer wavelengths is not shown due to contamination by background signals. Some background signal is evident in the figure..... 176

Figure 5-18 Altitude profiles of $N_2$ and OI FUV airglow emissions for 36.124..... 179

Figure 5-19 Altitude profiles of $N_2$ and OI FUV airglow emissions for 36.098..... 180

Figure 5-20 Altitude profiles of $N_2$ and OI FUV airglow emissions for 36.107..... 181

Figure 6-1 Comparison of modeled and measured airglow for 36.124..... 186

Figure 6-2 Comparison of modeled and measured airglow for 36.098. Because no solar irradiance measurements were made below 30 nm, the SERF 1 model solar irradiance appropriate to the conditions of the rocket launch is used..... 188

Figure 6-3 Comparison of modeled and measured airglow for 36.098. Here, the SERF 1 model solar irradiance below 30 nm has been scaled by a factor of two..... 189

Figure 6-4 Comparison of modeled and measured airglow for 36.107..... 191

Figure 6-5 Comparison of modeled and measured airglow for 36.107. Here, the MSIS $O_2$ density has been scaled by a factor of two..... 193

Figure 6-6 LBH volume excitation rate as a function of solar irradiance wavelength and of altitude..... 197

Figure 6-7 LBH volume excitation rate as a function of solar irradiance wavelength, shown for 110, 150, and 200 km..... 198

Figure 6-8 Measured variability of the LBH (4,0) 150 km limb viewing brightness with solar activity. The linear relationship is demonstrated for integrated solar soft x-ray integrated irradiance, solar 30.4 nm irradiance, and for solar F10.7 cm flux... 199

Figure 6-9 Calculated variability of the LBH (4,0) 110 km limb viewing brightness with solar activity. The best fit linear relationship is demonstrated for integrated solar soft x-ray integrated irradiance, integrated solar 2-10 nm irradiance, and for solar F10.7 cm flux..... 201

Figure 7-1 A schematic representation of thermospheric NO chemistry..... 204

Figure 7-2 Total cross sections for ionization and dissociation of $N_2$ by photoelectron impact..... 210

Figure 7-3 Calculations of photoelectron impact ionization of $N_2$ from the */glow* and PEGFAC models. See Table 3-1 for geophysical conditions..... 211

Figure 7-4 Calculations of photoelectron impact dissociation of $N_2$ from the */glow* and PEGFAC models. See Table 3-1 for geophysical conditions..... 212

Figure 7-5 Predictions of NO density by the NOx 1-D model using */glow* and PEGFAC. See Table 3-1 for geophysical conditions..... 213

# Chapter I

# Introduction

## 1.1 Overview of Dissertation Topics

Photoelectrons are produced by energetic solar radiation which ionizes neutral species in the Earth's atmosphere. At short wavelengths, solar photons have more energy than is required to ionize, thus extra energy is carried by the electron produced by the photoionization. This electron is a photoelectron and further reacts with atmospheric constituents via excitation, dissociation, or ionization. The solar radiation responsible for generating the majority of the primary photoelectrons occurs mostly at wavelengths shorter than that needed to ionize molecular oxygen, 102.7 nm. The important spectral regions for the production of photoelectrons are the Extreme Ultraviolet (EUV) from 30 to 120 nm, and the soft x-ray from 2 to 30 nm.

One of the many applications of space technology is global remote sensing of the Earth's atmosphere. In particular, ultraviolet spectroscopy has been used as a tool to study the chemistry, structure, and dynamics of the thermosphere. An era is approaching when the Earth's Far Ultraviolet (FUV, 120 - 200 nm) spectrum will be routinely monitored (McCoy *et al.*, 1992, Paxton *et al.*, 1992). Because many of the FUV airglow emissions are excited by impact with photoelectrons, the magnitude and shape of the photoelectron spectrum must be known. Such knowledge can only be obtained through direct measurement or through calculations using solar EUV and soft x-ray irradiances. Unfortunately, the solar flux at these wavelengths is not well understood. Since there are no plans for continuous monitoring of solar or photoelectron spectra, a method of inferring them is required to interpret the airglow. A solution would be to find a terrestrial FUV emission which responds directly to changes in the solar irradiance.

PRECEDING PAGE BLANK NOT FILMED
PAGE 24 INTENTIONALLY BLANK

The Lyman-Birge-Hopfield (LBH) bands of $N_2$ are significant features in the Earth's dayglow spectrum. The LBH bands are optically forbidden and are therefore excited only by photoelectron impact. The relative lack of radiative transfer complications makes these emissions attractive as monitors of the photoelectron flux and solar energy deposition. This idea has been previously proposed (Meier and Anderson, 1983) and applied by several authors (see Section 1.1.3). These data sets, however, did not contain simultaneous measurements of the solar irradiance and the Earth's airglow. The analysis procedure was to scale a model solar or model photoelectron spectrum until the LBH brightnesses were reproduced. Previously, there has not been a simultaneous measurement of both the solar ultraviolet spectrum and the thermospheric LBH airglow emissions.

Results from three rocket experiments are described in this dissertation. These experiments measured both the terrestrial FUV airglow and the solar spectrum below 120 nm. The three flights occurred at different levels of solar activity. The data sets from these rocket flights are analyzed and used in conjunction with a model of photoelectron production and LBH brightness to answer the following questions: What is the variation of LBH brightness with solar activity? Does the accepted value of the LBH photoelectron excitation cross section, in conjunction with existing photoelectron models, reproduce the airglow measurements? To what wavelength intervals in the solar spectrum does the LBH brightness respond?

### 1.1.1 Solar Irradiance

Lean (1987) reviewed the history of solar irradiance measurements and the current understanding of the ultraviolet spectrum and its variability. The majority of knowledge on solar soft x-ray and EUV irradiance comes from the work of Hinteregger and coworkers (Hinteregger *et al.*, 1981) using measurements from the Atmospheric Explorer satellites and sounding rockets. These measurements occurred during the

minimum and rise to maximum of solar cycle 21. Hinteregger subsequently established a solar minimum reference spectrum (Hinteregger *et al.*, 1981) referred to as SC#21REFW. This reference spectrum can be obtained from the National Geophysical Data Center. The data file is labeled AES1REF.DAT and can be obtained at the following internet address:

gopher://gopher.ngdc.noaa.gov:70/11/NGDC%20%Data/Solar%20Terrestrial%20

Physics/SOLAR_DATA/SOLAR_UV_SERF2

Reviews of other measurements of the solar soft x-ray flux can be found in Manson (1976), Feng *et al.* (1989), Kreplin and Horan (1992), and their references.

Figure 1-1 displays the SC#21REFW reference solar spectrum; the spectral resolution is approximately 0.1 nm. Photons of wavelength less than approximately 60 nm possess enough energy to produce primary photoelectrons that can excite an FUV transition. Although the magnitude of the solar irradiance decreases with wavelength, the photons have increasing energy and therefore generate significant numbers of photoelectrons. Below 60 nm, the brightest solar emission is the HeII 30.4 nm line.

The limited amount of solar data made proxy models of the solar variability necessary. The first widely used model was that of Hinteregger *et al.* (1981). The proxies are the chromospheric Lyman ß (102.6 nm) and the coronal Fe XVI (33.5 nm) emissions. As measurements of these emissions are not typically available, they are correlated with the 10.7 cm radio flux and its 81 day average. Measurements of this solar emission are available on a daily basis. The Hinteregger model is referred to as SERF 1 by the Solar Electromagnetic Radiation Flux subgroup of the World Ionosphere-Thermosphere Study.

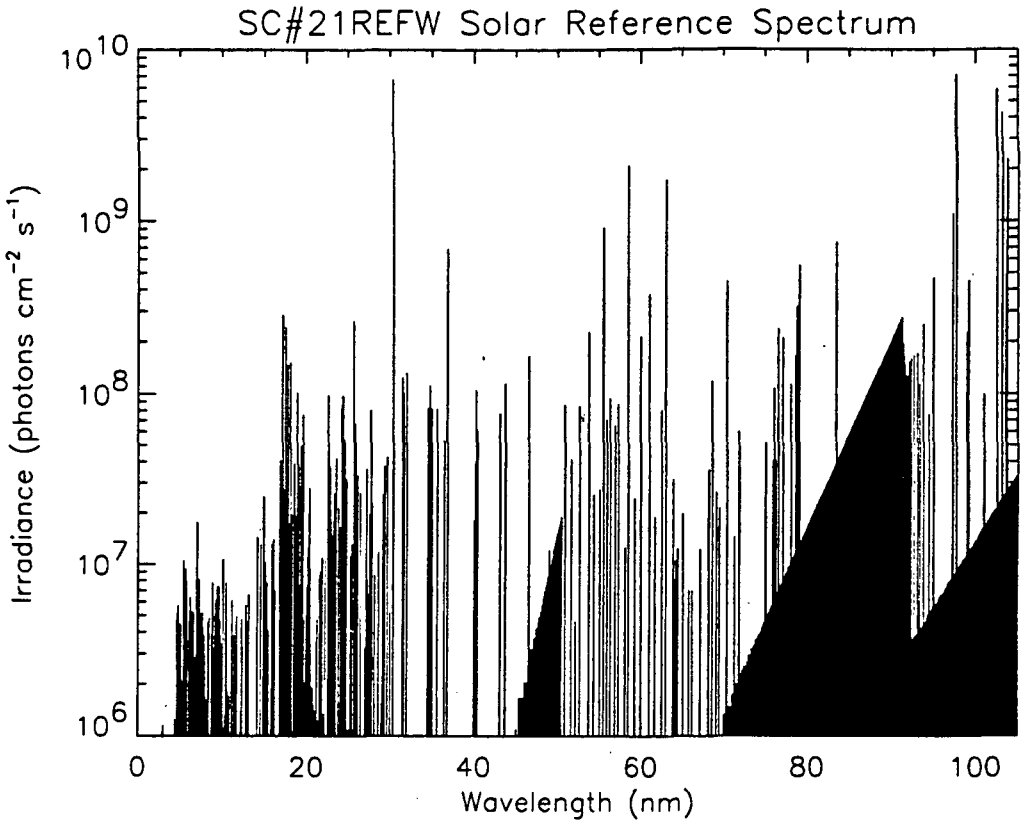


Figure 1-1 The SC#21REFW solar reference spectrum. This solar minimum reference spectrum is the basis for several models of solar variability.

Following the work of Hinteregger, Tobiska and Barth (1990) developed a new model of the solar flux, named SERF 2. Lean (1990) compared the results of SERF 1 and SERF 2 over time scales of the 27 day solar rotation and the 11 year solar cycle and concluded that the two models predicted significantly different variability. Tobiska (1991) revised the SERF 2 model. The new version was compared to SERF 1 and SERF 2 by Buonsanto *et al.* (1992) who concluded that, at soft x-ray wavelengths, the Tobiska (1991) model produced more flux than SERF 1.

Other atmospheric modeling efforts have addressed the magnitude of the solar soft x-ray and EUV irradiances. Richards and Torr (1984, 1985) studied the consistency of photoelectron measurements and calculations using measured solar soft x-ray irradiances values. They found agreement in the calculated and observed photoelectron fluxes if they scaled the solar irradiance below 25 nm by approximately a factor of two. Barth *et al.* (1988) and Siskind *et al.* (1990) found that in the wavelength range of 2-5 nm, an assumed order of magnitude variability of solar soft x-rays reproduced the large changes in the nitric oxide density observed by sounding rockets and by the Solar Mesosphere Explorer.

Previous work has demonstrated that the region of the solar spectrum responsible for most photoelectrons lies at and below 30.4 nm (Richards and Torr, 1984; Richards and Torr, 1985). The 30.4 nm emission comes from the solar chromosphere, whereas emissions shortward of 30.4 nm are from both the solar chromosphere and the solar corona. Chromospheric emission variability is better understood than coronal variability; chromospheric emissions are at longer wavelengths where there is more data and the emissions typically vary similarly over the solar cycle. Variability of the 30.4 nm feature has been observed by the OSO 4 spacecraft. Timothy and Timothy (1970) correlated the 30.4 nm irradiance with both the Zurich sunspot number and the F10.7 cm flux.

This dissertation represents the first analysis of simultaneous airglow and solar soft x-ray observations. Particular attention is paid to the effect of soft x-ray radiation on the thermosphere and how this effect can be inferred from measurements of the LBH bands.

### 1.1.2 Photoelectron Modeling

The importance of photoelectrons in the atmosphere was brought to attention by Hanson and Johnson (1961). Barth (1966) pointed out the utility of photoelectron impact excited emissions in the remote sensing of planetary atmospheres and described the necessary physics for interpreting the brightnesses of those emissions. Numerical modeling of photoelectron fluxes for calculating emission rates has progressed for nearly three decades. Early works include Dalgarno *et al.* (1963), Green and Barth (1967) and Dalgarno *et al.* (1969). Because calculations were computationally intensive, parameterizations were introduced (Stewart, 1970). As computers became faster and more available, numerical techniques were developed. Monte carlo methods were employed (Cicerone and Bowhill, 1971) and the equation of transfer was solved using two stream (Nagy and Banks, 1970; Stamnes, 1981a,b) and multistream methods (Strickland *et al.*, 1976; Oran and Strickland 1978; Link, 1982). Rapid calculation of photoelectron excitation rates was performed assuming the local approximation (Strickland and Meier, 1982; see Section 7.2.2). Cicerone *et al.* (1973) compared the application of several methods of photoelectron fluxes and found good agreement at altitudes where the local approximation applied. In the current era, computers are fast enough that photoelectron spectra and excitation rates can be computed rapidly without making the local approximation. Models using the above numerical techniques are described in Solomon *et al.* (1988), Richards and Torr (1990), Link (1992), and their references. Today, the numerical methods employed are relatively mature; any discrepancies among the various models are probably due to differences in the cross sections employed. For this work, the */glow* model (Solomon

*et al.*, 1988; Solomon and Abreu, 1989) will be used to calculate the photoelectron spectrum. The model follows a two stream formalism and includes electron transport.

### 1.1.3 Previous Analyses of FUV Airglow Data

The LBH bands are a prominent feature in the Earth's FUV dayglow and thus have been observed many times beginning in the 1960's (Barth and Schaffner, 1970). The first measurement of the LBH bands in the Earth's atmosphere was in 1960 during an auroral rocket experiment by Fastie and coworkers (Fastie *et al.*, 1961). A prediscovery identification of the LBH bands in the dayglow can be made in the data of Fastie *et al.* (1964); their work represents the first measurement of this emission attributable to photoelectron impact excitation. The first detailed analysis of LBH band measurements came from Prinz and Meier (1971) who analyzed data from the OGO 4 satellite. They concluded that the LBH emissions followed variations in the solar soft x-ray irradiance (Kreplin, 1970). Later studies, where LBH emissions were used as monitors of the solar energy input, were based on rocket data; these works are listed in Table 1-1. Also included in the table are: the excitation cross sections used; the source of solar irradiance values; and, any scaling factor used to achieve agreement between modeled photoelectron excitation and measured brightnesses. A scaling factor can apply to either the solar spectrum or the LBH excitation cross section because the measured brightness is proportional to both. The scaling factors are on the order of 30-40%. Several of the data sets have been analyzed more than once; varying results arise from different assumptions of cross sections or solar irradiances.

The present analysis is an improvement over those listed in Table 1-1 because the solar irradiance, as well as the LBH brightnesses and the neutral atmosphere, are measured quantities. Any scaling factor applied to match model with data is an implication about the excitation cross section and determines the relationship between solar irradiance and LBH brightness.

**Table 1-1 Analyses of $N_2$ LBH Emissions**

| Analysis | Data Set | Cross Section[1] | Solar Flux | Scaling Factor[2] |
|---|---|---|---|---|
| Prinz and Meier (1971) | OGO 4 | B+T 1970 | H 1965† | 1.0 |
| Takacs and Feldman (1977) | R1977a | F+D 1976 | AE-C‡ | - |
| Meier *et al.* (1980) | R1978b | O+S 1978 | AE-E‡ | 1.0 |
| Conway (1982) | R1978b | O+S 1978 | AE-E‡ | 0.7 |
| Meier *et al.* (1985) | R1978b | Borst 1972 | SC#21REFW | 1.5 |
| Meier *et al.* (1985) | R1980c | Borst 1972 | SC#21REFW | 2.4 |
| Morrison and Meier (1988) | R1978b | A+S 1985 | SERF1 | 1.3 |
| Morrison and Meier (1988) | R1980c | A+S 1985 | SERF1 | 0.9 |
| Link *et al.* (1988) | R1978b | A+S 1985 | SERF1 | 1.5 |
| Link *et al.* (1988) | R1980c | A+S 1985 | SERF1 | 1.0 |
| Morrison *et al.* (1990) | R1983d | A+S 1985 | SERF1 | 1.4 |
| Morrison *et al.* (1990) | R1985d | A+S 1985 | SERF1 | 1.4 |

† Hinteregger *et al.* 1965.

‡ Indicates use of measured photoelectron spectrum from AE-C or AE-E satellites.

[1] Cross section measurements are described in Chapter II, see Table 2-1 for results referred to above.

[2]See text for description of scaling factors.

[a] For a description of the experiment see Takacs and Feldman (1977).

[b] For a further description of the experiment see also Gentieu *et al.* (1979).

[c] For a further description of the experiment see also Christensen *et al.* (1982) and Eastes *et al.* (1985).

[d] For a further description of the experiment see also Bowers (1985) and Bowers *et al.* (1987).

In addition to the LBH bands, the FUV airglow spectrum contains features of atomic oxygen. The OI 130.4 nm emission is the brightest feature in the FUV airglow spectrum, followed by the OI 135.6 nm emission. Although resonant scattering of sunlight is responsible for some of the OI 130.4 nm excitation, both of the OI emissions are primarily excited by photoelectron impact and thus respond to variations in solar irradiance. The analyses listed in Table 1-1 also studied the OI emissions. An important distinction between the OI emissions and the LBH emissions is that the OI lines undergo multiple scattering in the atmosphere. Consequently, more complex radiative transfer algorithms are required to understand the measured OI brightnesses. In this dissertation, the OI 135.6 and 130.4 nm emissions are also studied.

## 1.2 Overview of Dissertation

The following chapters discuss the modeling and experimentation used to study the solar irradiance and the Earth's FUV airglow. Chapter II provides an overview of the spectroscopy and excitation of the emissions discussed in this dissertation. Particular emphasis is placed on the current state of knowledge of the electron impact excitation cross sections.

In Chapter III, the various models used in studying the airglow are described. Photoelectron fluxes are calculated with the */glow* model (Solomon *et al.*, 1988; Solomon and Abreu, 1989); radiative transport is calculated with the Feautrier solution of Gladstone (1982, 1988). The body of information required for these calculations is discussed.

Chapter IV describes the instrumentation and calibration procedures which are implemented in the rocket experiments. Two instruments are used to measure the solar irradiance; one FUV spectrograph is used to measure the Earth airglow. The uncertainties associated with each of the calibrations are discussed.

The three instruments used in the rocket experiments provide three unique sets of data. The analysis techniques vary widely among the instruments. Chapter V describes the techniques involved in reducing the data and converting it into physical units.

In Chapter VI, the measurements are compared with the results of model calculations. These comparisons demonstrate that the models are capable of reproducing the measured airglow, providing confidence that the FUV airglow emissions can be used for remote sensing of atmospheric processes.

Chapter VII discusses the further effects of solar soft x-ray radiation. As mentioned above, variability in solar soft x-rays is theorized to produce large variations in nitric oxide densities. The NOx 1-D model is described and updated to incorporate the */glow* model for photoelectron calculations. The ability of solar soft x-rays to produce nitric oxide is examined; It will be shown that lower solar soft x-ray irradiances than previously suggested are required to produce observed densities of nitric oxide.

Finally, in Chapter VIII, the conclusions from this dissertation are summarized. Suggestions for future work are also discussed.

Three appendices are included. Appendix A describes the analytical representations for electron impact cross sections which are used by the */glow* model. In Appendix B, ionization and absorption cross sections are tabulated along with the SC#21REFW reference solar spectrum. Appendix C lists the results of the solar irradiance measurements described in Chapter V.

# Chapter II

## Spectroscopy and Excitation of Terrestrial Far Ultraviolet Dayglow Emissions

### 2.1 Introduction

In this chapter the excitation mechanisms which create the emissions in the Earth's FUV spectrum are discussed. The chapter begins with a review of the notation used in atomic and molecular spectroscopy relevant to this work, and will lead to a discussion of the molecular spectroscopy of the LBH bands and to the calculation of synthetic spectra. The concept of a cross section will also be introduced, and the excitation cross sections of the important FUV emissions will be discussed. A central goal of this chapter is to review the previous work concerning the excitation of the FUV emissions.

### 2.2 Notation and Terminology of Spectroscopy

In discussing excitation of the various emissions, spectroscopic notation is used. Therefore it is useful to begin with a review of this notation. This review is intended to be brief and cover only the relevant details. For further information the reader is referred to the following books: *Spectrophysics*, by Anne P. Thorne (1988) and *Elements of Diatomic Molecules*, by H. Brian Dunford (1968). Two cornerstone texts in the field are *The Theory of Atomic Spectra*, by E. U. Condon and G. H. Shortley and *Spectra of Diatomic Molecules*, by Gerhard Herzberg (1989).

Spectroscopic notation describes the state of an electron, atom, or molecule; in particular, the energy, angular momentum, or spin characteristics of the particle. Since these and other properties are quantized (able to have only discrete values), they are typically described by quantum numbers. Quantum numbers describe the physical state of the electron and are usually integers or half integers. For a given property, a

quantum number is all that is needed to describe the state of the particle. For example, the orbital angular momentum of an atom $\boldsymbol{L}$, can be described by a quantum number $L$. The magnitude of the orbital angular momentum is $\sqrt{L(L+1)}\hbar$.

### 2.2.1 Atomic Spectroscopy

For each electron in an atom, there are four quantum numbers: $n$, $l$, $m_l$, and $m_s$. They are products of the solution of the Schrödinger equation for an electron trapped in a potential well (due to the nucleus of the atom). In solving the Schrödinger equation, constraints on the values of the quantum numbers are also produced.

The quantum number $n$ is the principal quantum number. It is related to the radial distance between the electron and the nucleus. The second quantum number, $l$, is related to the total orbital angular momentum of the electron. The third quantum number, $m_l$, is related to the angular momentum about one fixed axis, taken as the z axis. The final quantum number, $m_s$, describes the spin state of the electron. The following constraints are placed on the four quantum numbers:

$$n \geq l + 1,$$

$$l \geq 0,$$

$$|m_l| \leq l, \text{ and}$$

$$m_s = \pm\frac{1}{2}. \qquad \text{2-1}$$

Under these rules, for an electron of given $n$, there are $n$ possibilities for $l$ , and $2l+1$ possibilities for $m_l$.

The Pauli exclusion principle forbids any two electrons to have the same set of quantum numbers. Were it not for such a rule, all electrons of an atom would have $n$=1 and minimum energy. As it is, for a given $n$, the first electrons of an atom fill up the possible values of $l$, $m_l$, and $m_s$. The next electrons then fill up the possibilities for the next value of $n$. Electrons with the same $n$ form "shells"; electrons with identical $n$ and $l$

form "sub-shells". The "electron configuration" represents the values of $n$ and $l$ for all the electrons. In writing the configuration for an electron, the $l$ value is described by a letter, i.e. the letters for $l$ = 0,1,2,3,4,... are s,p,d,f,g,... Beyond g the letters are used alphabetically. The reason for such notation is historical. In the electron configuration $n$ is represented by its numerical value, followed by $l$ as described above. A superscript is written to the right of the letter designation for $l$; the value of the superscript represents the number of electrons in the sub-shell. An example of an electron configuration for an oxygen atom with eight electrons in their lowest energy states is $1s^2 2s^2 2p^4$. Should an outer electron be excited to 3s, the electron configuration would then be written $1s^2 2s^2 2p^3 3s$. Note that when a sub-shell contains only one electron, no superscript is used.

In describing the state of the atom, the interactions of all the atom's electrons must be accounted for. To do this, a new set of quantum numbers is used. The first of these is $L$, the quantum number describing the resultant angular momentum after the contributions of all the electrons are taken into account. The magnitude of the atom's angular momentum will have a value $\sqrt{L(L+1)}\hbar$. Note that the orbital angular momentum of two electrons can be equal and opposite and thus cancel each other out. Therefore, $L$ can take on values from zero through the sum of all $l$ values. The component of $L$ in the z direction can take on the $2L+1$ values of $L$ from $-L$ to $L$. Atomic states with different $L$ values are referred to as terms. Similar to $l$, $L$ values are labeled S,P,D,F,G,... for $L$ values 0,1,2,3,4,... In an analogous way to $L$, a quantum number $S$ can be defined which represents the total spin angular momentum. The total spin angular momentum is the vector sum of all the electron spin angular momenta, thus since values of $m_s$ are $\pm\frac{1}{2}$, $S$ can take on integral or half integral values.

A total angular momentum is formed from the vector addition of the orbital angular momentum and the spin angular momentum. The quantum number for total

angular momentum is $J$, which can take on values from $L+S$ to $L-S$, and therefore can have integral or half integral values. Note that $S$ determines the number of possible values for $J$, $2S+1$. This value is referred to as the multiplicity of states. For a state of given $L$ and $S$, the difference in energy of the states with differing $J$ values is very small. For this reason the splitting among $J$ states is referred to as fine structure.

When describing the state of an atom, the multiplicity is written as a superscript to the left of the $L$ designation. The $J$ value is written as a subscript to the right of the $L$ designation. For example the ground state of atomic oxygen is written $^3P_2$ for $L=1$, $S=1$, and $J=2$. Figure 2-1 is a term diagram for atomic oxygen. It shows all the possible states for O. The ordering of Figure 2-1 is such that multiplicity increases to the right, and energy increases upward, thus the difference in energy between two atomic states can be inferred by the difference in vertical position. The energy difference between some levels is labeled by the wavelength of emitted radiation (in units of Ångstroms).

Radiative transitions between different atomic states are the result of interactions between the atom and a radiation field. The radiation field is made up of electric and magnetic fields. The interactions are expanded and solved in order of strength. The most important component of the radiation field is the electric dipole field, then the magnetic dipole, followed by the electric quadrupole, and so on. In solving for probabilities of transitions, constraints are placed on how certain quantum numbers may change. These constraints are referred to as selection rules. If, for a given transition, a selection rule is violated, this transition becomes unlikely and is deemed forbidden. Transitions which do not violate selection rules are referred to as "allowed". It is possible, however, for a transition to be forbidden under electric dipole interactions, but allowed under magnetic dipole interactions. Thus, while the probability of transition is reduced, it is still possible. The molecular transition in $N_2$

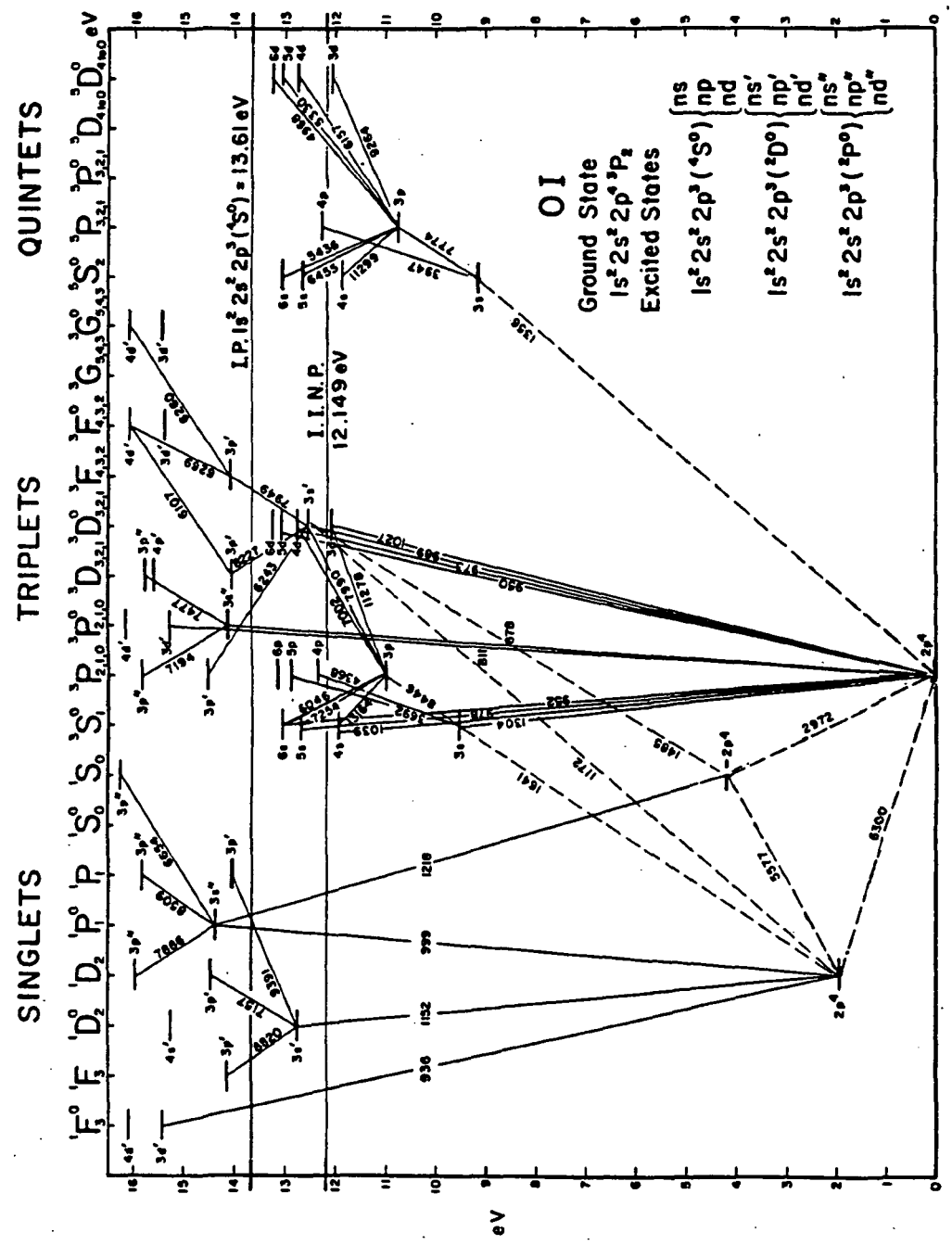


Figure 2-1 Energy level diagram for atomic oxygen, taken from Meier (1991).

which produces the LBH bands is an example of an electric dipole forbidden transition which is magnetic dipole and electric quadrapole allowed.

The selection rules for atomic transitions are as follows. The change in $S$ must be zero, or $\Delta S = 0$. For $L$ the selection rules are $\Delta L = 0$, or $\Delta L = \pm 1$; however, the transition from $L=0$ to $L=0$ is not allowed. The selection rules on $J$ are analogous to those for $L$, $\Delta J = 0$ and $\Delta J = \pm 1$, with $J=0$ to $J=0$ not allowed.

In writing an atomic transition the lower state is always written first. For example the 135.6 nm emission of atomic oxygen is written $2p^4\ ^3P - 3s\ ^5S$. Note that in writing the electron configuration with the atomic state, only the last subshell need be listed.

### 2.2.2 Diatomic Molecular Spectroscopy

The various states of a molecule are described by quantum numbers in much the same way as atoms. Just as in the atomic case, the quantum number for the total orbital angular momentum of the electrons is $L$. The component of the orbital angular momentum about the internuclear axis is $\Lambda=\Sigma m_l$. Possible values of $\Lambda$ range from 0 to $L$. In the molecular case, the vector orbital angular momentum is not always well defined, thus the quantum number $L$ cannot always be specified. Therefore the term values for molecules follow $\Lambda$. Similar to atoms, molecular terms are labeled $\Sigma$, $\Pi$,$\Delta$, and $\Phi$ for $\Lambda = 0,1,2,3$.

The quantum number for spin angular momentum S is defined for molecules in an identical way to atoms. The component of spin angular momentum about the internuclear axis has a quantum number $\Sigma$. Values of $\Sigma$ range from $-S$ to $S$, thus there are $2S+1$ possible values for $\Sigma$. It is unfortunate that the symbol $\Sigma$ is used for the $\Lambda=0$ term label as well as for a quantum number. Care must be exercised not to confuse the two uses.

The quantum number for the total angular momentum of the molecule about the internuclear axis is $\Omega$. The numerical value for $\Omega$ is $|\Lambda+\Sigma|$. For $\Lambda \neq 0$, there are $2S+1$ possibilities for $\Omega$. Thus, as in the atomic case, the value $2S+1$ is referred to as the multiplicity of the state. Terms contain the multiplicity as a superscript to the left of the $\Lambda$ designation. The value of $\Lambda+\Sigma$, which can be positive or negative, is written as a subscript to the right of the $\Lambda$ designation.

In addition to the above quantum numbers, there are two other labels of a molecular state. These describe the symmetry of the electronic wave functions about two planes. The first label applies only to homonuclear molecules and describes the symmetry of the wavefunction about the origin of the molecule. Terms are subscripted with *g* (gerade) or *u* (ungerade) for even and odd symmetry. The second label applies to both heteronuclear and homonuclear molecules, and describes the symmetry of the wavefunction through any plane containing both atoms. Terms are superscripted with + or - for even or odd symmetry.

Combining the above information, an example is the term designation for the ground state of $N_2$: $X^1\Sigma_g^+$. The X is the typical designation for the ground state. For higher energy states, those with the same multiplicity as the ground state have the designation A,B,C,... in ascending order of energy. For those states with differing multiplicities, the designations a,b,c,... are used. For example the excited state of the $N_2$ LBH bands has the term $a^1\Pi_g$.

Figure 2-2 shows an energy level diagram for $N_2$. The excited states and the transitions among them are all labeled. Transitions among molecular states are typically named for the researchers who discovered them. An example is the Lyman-Birge-Hopfield (LBH) emission.

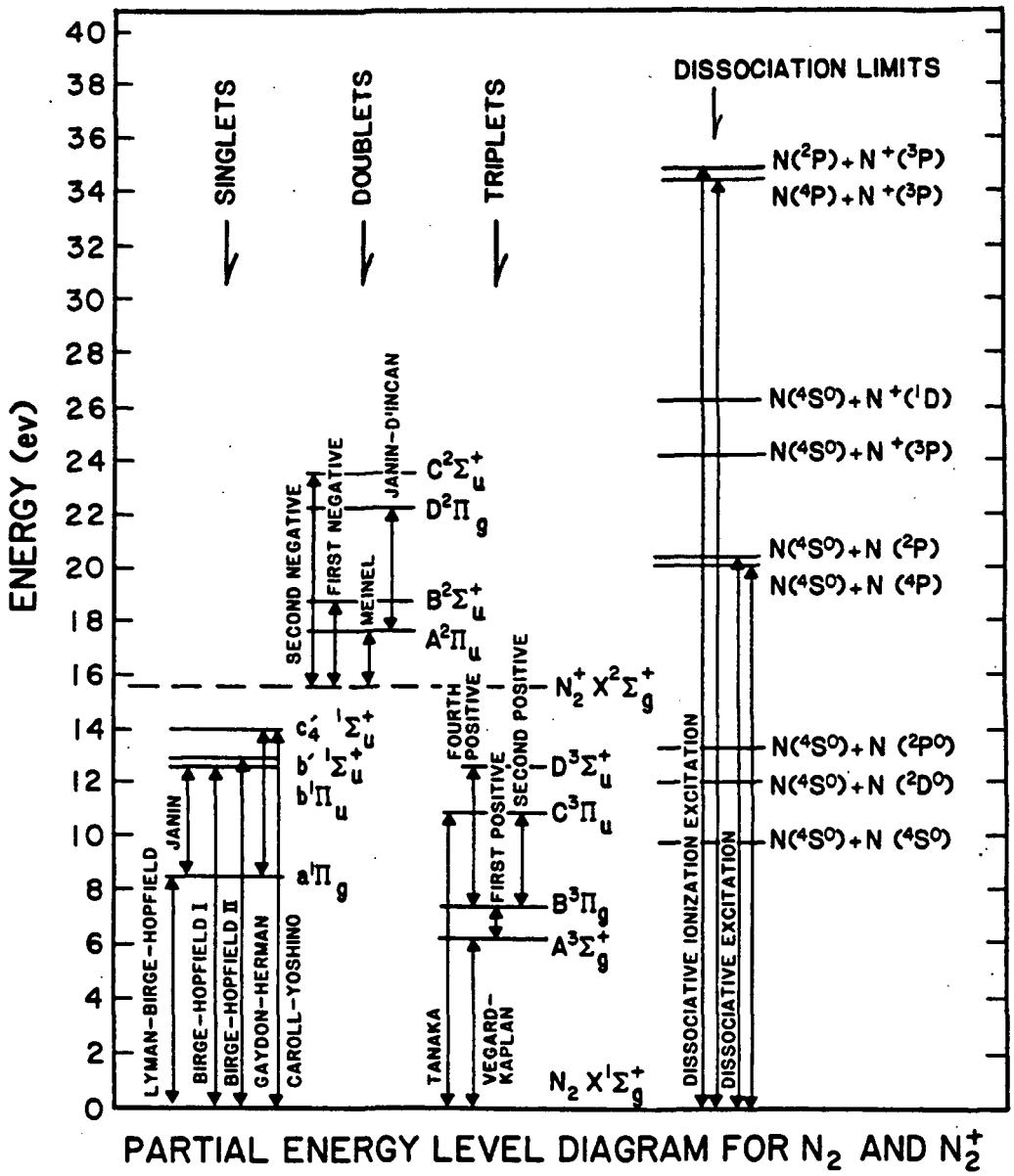


Figure 2-2 Energy level diagram for molecular nitrogen, taken from Meier (1991).

As with atoms, radiative transition in molecules must obey selection rules. Many selection rules for a given molecular transition depend upon how the angular momenta (orbital and spin) are coupled. These rules will be described as needed in later sections. For a detailed treatment of coupling schemes, the reader is referred to Herzberg (1989). At this point, the selection rules for dipoles governing changes in the symmetry of a state are listed. Transition from two + states or two - states are allowed, but + to - and - to + transitions are forbidden. Transitions from ungerade to gerade states are also allowed, but transitions between two ungerade states or two gerade states are forbidden. It is the last selection rule that makes the LBH transition forbidden.

When describing a radiative transition in a molecule, the upper state is written first. For example the transition resulting in a LBH band emission is $a^1\Pi_g - X^1\Sigma_g^+$. This is opposite to the convention for atomic transitions.

The above describes the state of a molecule due to interactions of orbiting electrons. A molecule is also characterized by how the two atoms interact. For instance the atoms may vibrate along the internuclear axis, thus changing the distance separating them. The atoms may also rotate about their center of mass. The vibrational and rotational states of a molecule determine the energy of a photon emitted by transition between electron states, and will be described further in Section 2.5. The vibrational state is denoted by the quantum number $v$, and the rotational state is denoted by the total angular momentum quantum number $J$.

The $a^1\Pi_g - X^1\Sigma_g^+$ transition in $N_2$ is an example of an electronic transition. Within each electronic transition, the transitions from upper electronic state vibrational levels to different vibrational levels in the lower electronic state yield photons of varying energies. Therefore each electronic transition in a molecule does not yield a line emission, but rather bands of emission. Each band is formed by many lines which are due to the different rotational states the molecules occupy in the upper and lower

electronic states. Different bands are due to the possible combinations of upper and lower vibrational states. A particular band is labeled by the vibrational state quantum numbers. For example the LBH (2,0) band at 138.3 nm is due to the transition from the v=2 vibrational level in the upper electronic state to the v=0 level in the lower state. Typically the upper state quantum number is given a single prime, and the lower state is given a double prime. Thus the (2,0) band has v"=2 and v'=0.

## 2.3 The Cross Section

A cross section for a given process is a measure of the efficiency of that process. Cross sections are typically used in radiative processes or processes describing the transport of energetic electrons. Consider a beam of photons or electrons of flux $\phi$ traveling through a column of gas of number density $n$ ($cm^{-3}$). The gas has some ability to absorb or scatter the photons or the electrons. The differential flux through the column will be proportional to the original flux, to the density of scatterers, $n$, and to the differential length of the column, $dz$ (cm). The differential flux can be written:

$$d\phi = -\phi n \sigma dz. \qquad 2\text{-}2$$

Examination of Equation 2-2 shows that the units for the value $\sigma$ are $cm^2$ or area. This value is referred to as a cross section; it can be imagined as the area of a scatterer as seen by a photon or electron. Equation 2-2 can be integrated to yield:

$$\phi(z) = \phi_{z=0} e^{-n\sigma z}. \qquad 2\text{-}3$$

This is Beer's law. It demonstrates that the cross section is a measure of the efficiency of a scattering or absorbing process. For an absorber with a large cross section, a lower density is required to perform the same amount of absorption as an absorber with a smaller cross section.

For photons, the exponent in equation 2-3 is referred to as the optical depth $\tau$:

$$\tau = \int n(z)\sigma dz. \qquad 2\text{-}4$$

For the transfer of electrons through a scattering medium, a similar term can be defined. The symbol $\tau_e$ can be used and referred to as electrical depth (Solomon, 1993). When $\tau$ becomes larger than unity, the medium is said to be optically or electrically thick, for $\tau$ less than unity, the medium is optically thin. Equation 2-4 assumes a single constituent medium; for a multi-constituent medium a sum over the constituents can be made.

Any scattering or absorbing process can have a cross section. The sum of these cross sections is the total cross section for scattering or absorbing. Cross sections are different for every scatterer and are typically functions of photon or electron energy.

## 2.4 Electron Impact Excitation Cross Sections

One of the most important parameters needed to calculate the photoelectron impact excitation rate of a particular band or atomic emission is the cross section. Cross sections can be measured or calculated theoretically. Cross sections for electron impact excitation are generally determined experimentally by electron energy loss measurements, metastable particle measurements, or absolute emission measurements. In energy loss experiments a beam of electrons of known energy is impacted onto a gas. The energy spectrum of the scattered electrons is measured at several scattering angles. This information is then used to calculate the cross section, using the determined pressure of the gas. A portion of the measured cross section is due to elastic scattering, which is determined by other means and subtracted out. In such measurements an angle of 0° means forward scattering, and 180° is backward scattering. Metastable particle experiments require that the lifetime of the excited state be sufficiently long that the particle can be collected before relaxation to the ground state. After impacting the gas with a beam of electrons, the gas particles are measured as a function of energy. By counting the number of excited particles, the cross section for excitation is deduced. An absolute emission experiment also begins by injecting a beam

of electrons into the system. In this case, the resulting photon emission due to the electron impact excitation is measured. The pressure inside the chamber is again determined and kept low enough that the gas is optically thin for the measured emission. The measured spectrum is used to calculate the cross section.

Each of these methods has advantages and disadvantages. Energy loss measurements can provide the angular dependence of the cross sections; however they include the portion of the cross section due to predissociation (which does not lead to an emission). They also suffer from the fact that the measurements are angle dependent and must be integrated to obtain the integral cross section used by aeronomers. This condition is not a problem in and of itself, however it is difficult to obtain data at high scattering angles because as 180° is approached, the detector interferes with the beam of electrons. Thus the data must be extrapolated to higher angles which can cause errors in the integration. The measurement of metastable particles is difficult because excited atoms or molecules can radiate or collisionally deactivate before collection. Absolute emission measurements more closely resemble the measurements made by aeronomers; however, the calibration of the system is difficult. This calibration problem can be overcome by making relative measurements and comparing to known cross sections. The predissociation cross section can be discerned by comparing absolute emission measurements and energy loss measurements, or by comparing the measured spectrum to a theoretical spectrum and observing which features are not present in the data.

### 2.4.1 The Excitation of the LBH Bands

The history of LBH photoelectron impact excitation cross section measurements is reviewed by van der Burgt *et al.* (1989) and Meier (1991). Table 2-1 lists the results of many such experiments. Although this list is not comprehensive, it does contain most of the results which have been used in previous

**Table 2-1 Measurements of the LBH Electron Impact Cross Section**

| Measurement | Type[a] | Peak Location (eV) | Peak Value[b] ($10^{-17}$ cm$^2$) |
|---|---|---|---|
| Ajello (1970) | PE | 16 | 3.85 |
| Brinkmann and Trajmar (1970) | ES | 17 | 4.5 |
| Borst (1972) | MP | 15.6 | 3.85 |
| Finn and Doering (1976) | ES | 17 | 3.6 |
| Cartwright *et al* (1977) | ES | 17 | 2.72[c] |
| Ajello and Shemansky (1985) | PE | 17 | 2.63[d] |
| Mason and Newell (1987) | MP | 17 | 3.50 |
| Zetner and Trajmar (1987) | ES | | 4.29 |
| Brunger and Teubner (1990) | ES | 17.5 | 4.24 |

[a] PE is a photoemission measurement, MP is a metastable particle measurement, and ES is an electron scattering measurement.
[b] All values represent electron impact excitation cross section and thus include the component due to predissociation.
[c] This value is the result of a scaling by a factor of 0.90 following the work of Trajmar *et al.* (1983).
[d] This value is the result of a scaling by a factor of 0.875 due to a reevaluation of the H Lyman-$\alpha$ standard (van der Burgt, 1989).

airglow analyses. Emission measurements have been made by several authors and most recently by Ajello and Shemansky (1985). Mason and Newell (1987) have made metastable particle measurements. The results from these two methods are in general agreement. Electron energy loss experiments have been made by Cartwright *et al.* (1977). Similar work to that of Cartwright *et al.* has been done by Brunger and Teubner (1990). The review of Trajmar *et al.* (1983) presented a downward revision of the Cartwright *et al.* results on the order of 10%. This adjustment is due to changes in the elastic scattering cross section standard used by Cartwright *et al.* The reported integrated cross sections of Brunger and Teubner at 15 eV differ from the peak value of Ajello and Shemansky by as much as 25%. Since the measurements of Cartwright *et al.* and Brunger and Teubner are energy loss measurements, the comparison to the work of Ajello and Shemansky is done after integration of the angle dependent differential cross section. Integrations performed by Cartwright *et al.* (1977) are in good agreement with those of Ajello and Shemansky (1985). The fact that the latest measurements by Brunger and Teubner are not in agreement is discussed here.

Cartwright *et al.*, measured cross sections from scattering angles of 10° to 138°, at incident energies of 10, 12.5, 15, 20, 30 and 50 eV. Brunger and Teubner made measurements at similar incident energies but at scattering angles of 10° to 90°. At incident energies above 12 eV the measurements of Ajello and Shemansky are in excellent agreement with the integrated data of Cartwright *et al.* The differential cross section measurements of Brunger and Teubner are in fair agreement with those of Cartwright *et al.* at the larger incident energies, but at 15 eV this agreement is not the case. The peak cross section value occurs at 18 eV (Ajello and Shemansky, 1985). Brunger and Teubner integrate their measurements at 15 eV only and arrive at an integrated cross section 40% larger than the peak value measured by Ajello

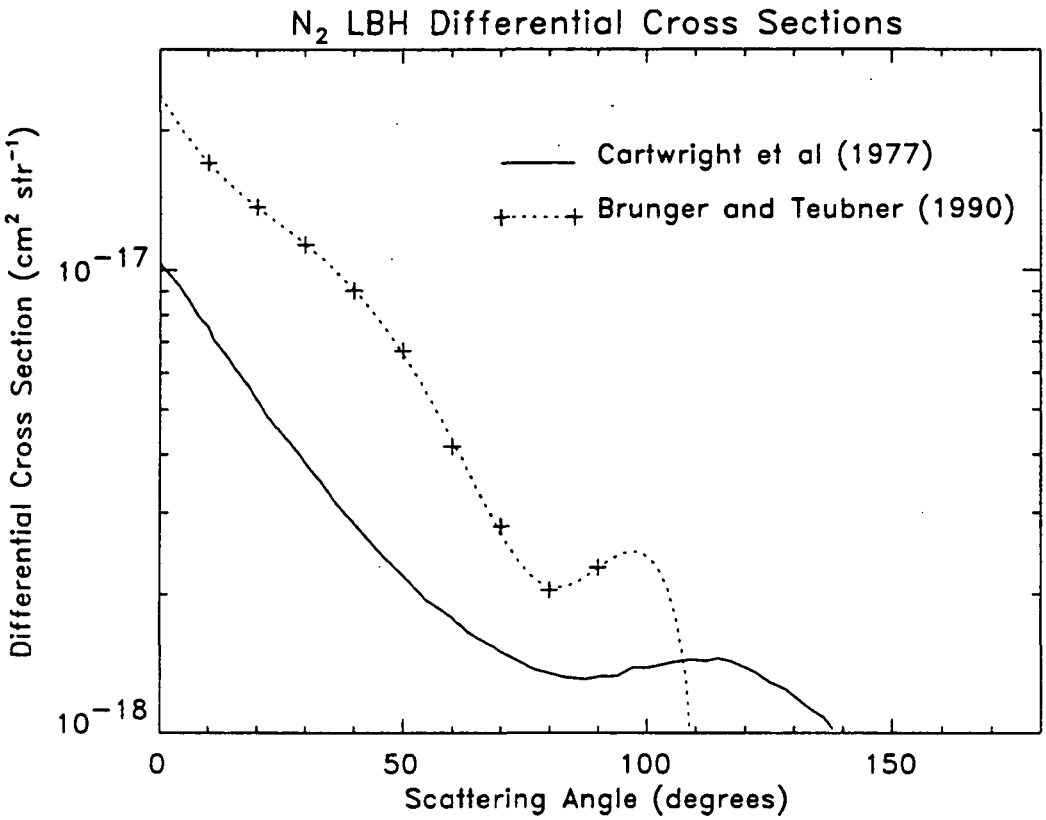


Figure 2-3 A comparison of differential cross section measurements for the LBH bands. Both measurements are made at an electron energy of 15 eV.

and Shemansky. Some of this disagreement is due to predissociation, but the discrepancy is at least 25%. Figure 2-3 shows a fit to the differential cross section data of Cartwright *et al.*

(1977) for an electron energy of 15 eV. Brunger and Teubner measured only to 90°; to perform the integration, a sixth order polynomial was fit to the data which was extrapolated to angles greater than 90°. Figure 2-3 also shows the results of a fit done to the Brunger and Teubner 15 eV data following the procedure they described. This graph shows that the cross section of Brunger and Teubner is higher than that of Cartwright *et al.* at smaller angles and is lower at larger angles. Integration of the fit to the Brunger and Teubner data yields a cross section of $4.19 \times 10^{-17}$ which is 25% (accounting for predissociation) higher than the peak value of Ajello and Shemansky. The conclusion is that although the other measurements (using different techniques) are in relative agreement, the measurements of Brunger and Teubner are not in agreement at lower energies. The fit to larger angles does not follow the shape or magnitude of the Cartwright *et al.* measurements. A small part of the discrepancy may be due to an inadequacy in the 6th order fit. It should be pointed out that the integrated cross sections of Zetner and Trajmar (1987) (See Table 2-1) support the Brunger and Teubner results. Thus from a laboratory perspective, there is still some disagreement as to the magnitude of the LBH cross section. The extent of the disagreement is demonstrated in Table 2-1.

When making an absolute emission cross section measurement, the technique usually involves two measurements. First a measurement is made using what is commonly referred to as the relative flow technique. This technique provides the ratio of the cross section of one emission in one gas to the cross section of a particular emission in a second gas. The emission from the second gas is referred to as a standard, meaning its cross section has an accepted value. Ajello and Shemansky used

the relative flow technique to measure the NI 119.99 nm cross section (energetic electrons on $N_2$) by referring it to the HI Lyman α 121.6 nm cross section (energetic electrons on $H_2$). The LBH spectrum thus included the 119.99 nm line and a ratio of the intensities of the LBH bands to the 119.99 line provided the LBH cross section. Since the work of Ajello and Shemansky, a new value of the Lyman α standard has been measured and has become the adopted value (van der Burgt, 1989). This results in a scaling of the cross sections of Ajello and Shemansky by 0.875. The values of Table 2-1 include to these scalings.

The model presented here currently uses this scaled version of the Ajello and Shemansky (1985) cross section as shown in Figure 2-4.

### 2.4.2 Excitation of the OI 135.6 nm Emission

The OI 135.6 nm transition is a doublet; the transitions are $2p^4\ ^3P_2 - 3s^5S_2$ and $2p^4\ ^3P_1 - 3s^5S_2$. This emission is spin forbidden ($\Delta S$=1), which, in conjunction with negligible solar 135.6 nm emission, means that photoelectron impact on O is the dominant excitation mechanism in the dayglow. A significant contribution comes from cascade from higher energy states. The most important contribution from cascade processes is the $^5P$ - $^5S$ transition which produces a photon at 777.4 nm. A comprehensive review of all the cascade transitions to the $^5S$ state is presented by Julienne and Davis (1976), and also tabulated in Table 2-2. Parameters of the $^3P$ - $^5S$ transition are presented in Table 2-3. In the nightglow, the OI 135.6 nm emission is excited by radiative recombination of $O^+$. This source is not typically accounted for in dayglow analyses; this point will be discussed further in Chapter VI.

Electron impact cross sections for the production of OI 135.6 nm emissions have been obtained from theory, measurement, and airglow observations of direct, cascade, and total excitation. Previous airglow observations did not have the simultaneous measurement of the solar irradiance. A detailed review of these cross

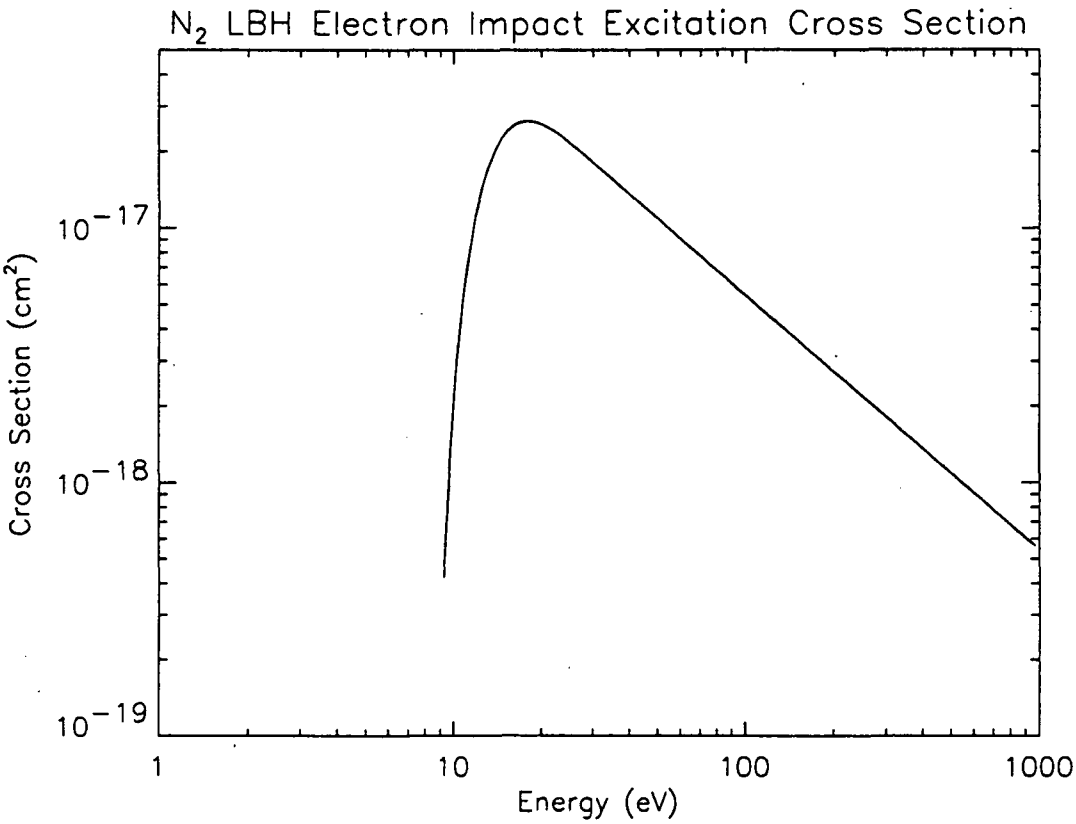


Figure 2-4 Cross section for photoelectron impact excitation of the LBH bands.

**Table 2-2 OI Electron Impact Emission Cross Sections[‡] for the OI 135.6 and 130.4 nm Emissions[†]**

| Feature | Optical Depth | Type[+] | Direct | | | | | | | | | Total Cascade | Total | Ref |
|---|---|---|---|---|---|---|---|---|---|---|---|---|---|---|
| | | | | 3s' | 3p | 3d | 4s | 4p | 4d | 4f | n=5 | | | |
| 135.6 | Thin | Thry | 2.9 | | 2.6 | 1.5 | 0.9 | 1.1 | 1.0 | 0.05 | 1.4 | 8.6 | 11.5 | 1 |
| (at 15 eV) | Thin | Lab | 3.1 | | 3.6 | | | | | | | | | 2,4 |
| | Thin | Lab | | | | | | | | | | | 9 | 3 |
| 130.4 | Thin | Thry | 7.1 | 0.7 | 5.7 | 0.5 | 0.2 | 0.5 | 0.1 | .004 | 0.3 | 8 | 15 | 1 |
| (at 20 eV) | Thick | Thry | 7.1 | 6.6 | 5.7 | 2.5 | 1.4 | 1.8 | 1.5 | .02 | 2.6 | 22 | 29 | 1 |
| Revised | Thin | Lab | 11 | $10^{-4}$* | 7.7 | 0.7 | (0.2) | (0.5) | (0.1) | (.004) | (0.3) | 9 | 20 | 2,4-6 |
| " | Thick | Lab | 11 | 0.6** | 7.7 | 2.4 | (1.4) | (1.8) | 1.3 | .02 | (2.6) | 18 | 29 | 2,4-6 |
| | Thin | Thry | 10.8 | | 11.3 | | | | | | | | | 7 |
| (Emission) | Thin | Lab | | | | | | | | | | | 17 | 8 |

References:
1 Julienne and Davis (1976)
2 Doering and Gulcicek (1989)
3 Stone and Zipf (1974) reduced by 0.36
4 Gulcicek *et al.* (1988)
5 Vaughan and Doering (1987)
6 Gulcicek and Doering (1988)
7 Tayal and Henry (1988)
8 Zipf and Erdman (1985)
* 5.4 (Ref. 4) x 2 x 10-5 (Erdman and Zipf [1983])
** 5.4 (Ref. 4) x 0.11
( ) Assumes ref. 1 values

[+] Thry implies theoretical calculation.
Lab implies measurement.

[†] After Meier (1991)

[‡] In units of $10^{-18}$ $cm^2$

**Table 2-3 OI Atomic Absorption and Emission Line Parameters at 1000K**

| $\lambda$ (nm) | $f_{12}$ | A ($s^{-1}$) | $\Delta\lambda_D$ (nm) | $\sigma_0$ ($cm^2$) |
|---|---|---|---|---|
| 135.85123 | $6.200 \times 10^{-02}$ | $1.207 \times 10^{+03}$ | $4.602 \times 10^{-04}$ | $1.242 \times 10^{-18}$ |
| 135.55977 | $1.250 \times 10^{-06}$ | $4.575 \times 10^{+03}$ | $4.592 \times 10^{-04}$ | $2.499 \times 10^{-18}$ |
| 130.60286 | $4.850 \times 10^{-02}$ | $6.400 \times 10^{+07}$ | $4.424 \times 10^{-04}$ | $9.340 \times 10^{-14}$ |
| 130.48575 | $4.850 \times 10^{-02}$ | $1.970 \times 10^{+08}$ | $4.420 \times 10^{-04}$ | $9.331 \times 10^{-14}$ |
| 130.21685 | $4.850 \times 10^{-02}$ | $3.290 \times 10^{+08}$ | $4.411 \times 10^{-04}$ | $9.331 \times 10^{-14}$ |

* Taken from Meier (1991)

section results is presented by Meier (1991), and a summary is also presented in Table 2-2.

Much of the cross section work for the 135.6 nm emission has been theoretical. The most comprehensive work is by Julienne and Davis (1976, see Table 2-2) who studied the direct excitation as well as all of the cascade contributions. Other theoretical work on direct excitation has been done by Rountree (1977) and Tayal and Henry (1988). Rountree (1977) found a strong resonance just above the threshold at 9.14 eV. This resonance does not appear in the other theoretical work and to date the experimental work has not been of sufficient resolution to make a determination as to the presence of such a feature. After summing the cross sections for direct excitation and all the cascade mechanisms, Julienne and Davis arrive at a peak cross section of $1.15 \times 10^{-17}$ cm$^2$ at 15 eV.

Measurements of the direct excitation cross section have been performed by Doering and Gulcicek (1989) and Gulcicek *et al.* (1988) using electron energy loss techniques. They measured a peak value of $3.1 \times 10^{-18}$ cm$^2$ at 15 eV. This value is in excellent agreement with the theoretical calculation of Julienne and Davis (1976); unfortunately the two works do not agree on the shape of the cross section. The Doering and Gulcicek measurement shows a much steeper decline at the higher energies.

Measurements of the total cross section (direct plus cascade) have been performed by Stone and Zipf (1974). While they measured a value of $2.5 \times 10^{-17}$ cm$^2$, revisions by Zipf and Erdman (1985) suggest that the $^5$S cross sections should be multiplied by a factor of 0.36 to a value of $9 \times 10^{-18}$ cm$^2$. Doering and Gulcicek (1989) point out that the factor of 0.36 scaling may not be appropriate. The scatter in the Stone and Zipf measurements makes it difficult to compare them accurately with the theoretical cross sections at larger energies; however, there is some difference near the

threshold energy. Stone and Zipf report that the electron beam in their measurements had a width of approximately 2 eV. This width renders approximately 1 eV error in determining the threshold energy and may be responsible for the differences at the lower energies.

The FUV dayglow analyses have been performed by several groups. These analyses attempted to find consistent pictures of the atmosphere by using the FUV emissions in conjunction with model atmospheres and model solar fluxes. Much of this work comes from analyses of two rocket flights made at high and low solar activity. The rocket flights are described by Gentieu *et al.* (1979) and Eastes *et al.* (1985). A review of the modeling of this data can be found in Meier (1991). Although earlier modeling of the data led to conclusions of large 135.6 nm cross sections (Meier *et al.*, 1985), more recent works concur that a value of $9 \times 10^{-18}$ $cm^2$ agrees well with the airglow data (Link *et al.*, 1988; Morrison and Meier, 1988). Other works analyzing more recent airglow data also agree with this result (Conway *et al.*, 1988; Morrison *et al.*, 1990).

Although the shape of the 135.6 nm excitation cross section at higher energies is still uncertain, there is general agreement as to the magnitude and the low energy shape. The difference between the experimental value of the peak total cross section of $9 \times 10^{-18}$ $cm^2$ and the theoretical value of $11.5 \times 10^{-18}$ $cm^2$ may be explained if the highest states in the Julienne and Davis analysis lead to autoionization rather than radiative relaxation. Currently the */glow* model uses the Julienne and Davis direct excitation cross section and the Julienne and Davis cascade contributions scaled to give a peak total cross section at 15 eV of $9 \times 10^{-18}$ $cm^2$. This cross section is shown in Figure 2-5.

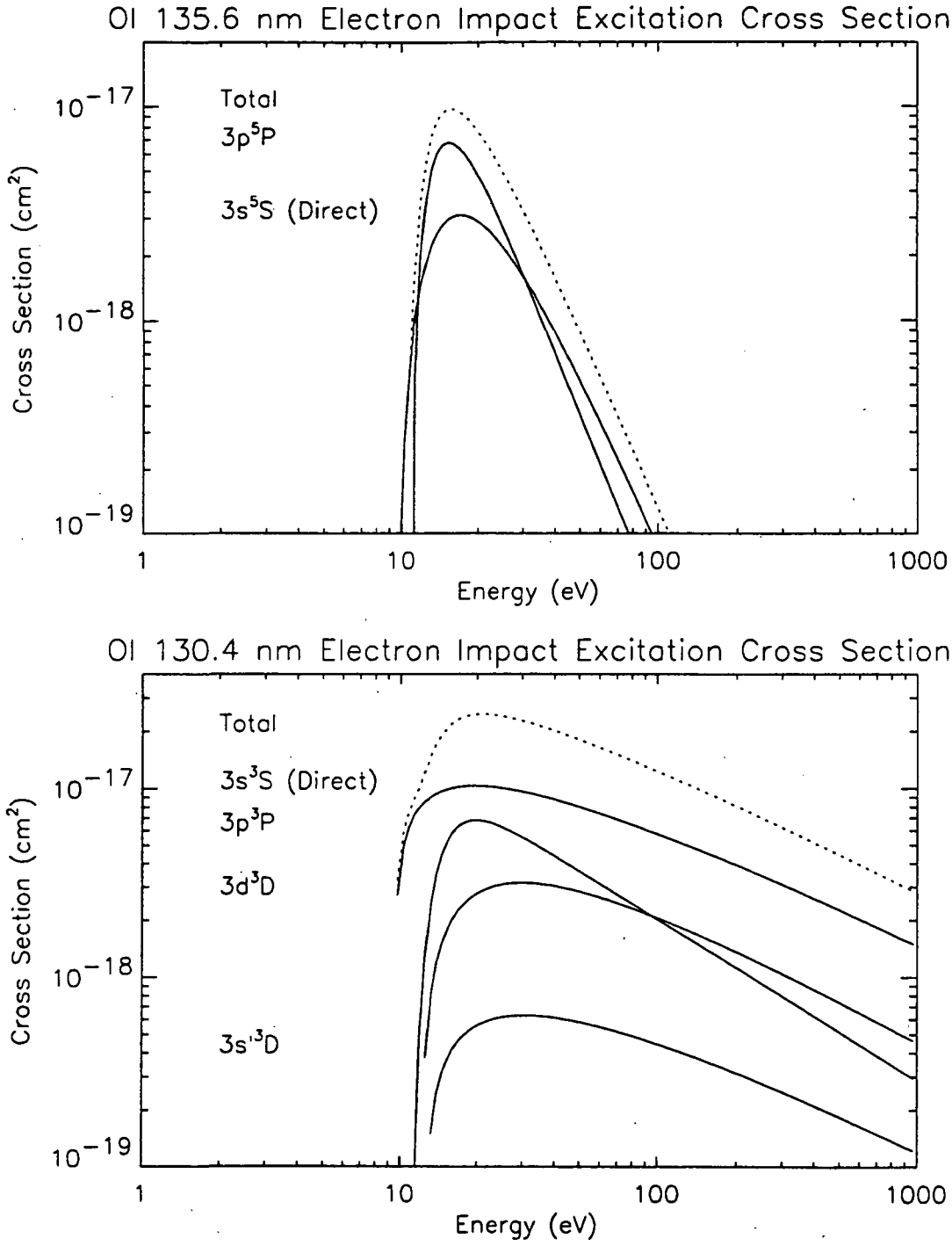


Figure 2-5 Photoelectron impact excitation cross sections, cascade and total, for the OI 135.6 and 130.4 nm emissions.

### 2.4.3 Excitation of the OI 130.4 nm Emission

The OI 130.4 nm emission is a triplet from the allowed transitions: $2p^4{}^3P_2$ - $3s^3S_2$ , $2p^4{}^3P_1$ - $3s^3S_2$ and $2p^4{}^3P_0$ - $3s^3S_2$. Because of the bright solar feature at 130.4 nm, there is significant resonant scattering of sunlight. This contribution is smaller than excitation by photoelectron impact; however, it cannot be neglected. Details of the transition are presented in Table 2-3.

#### 2.4.3.1 Photoelectron Impact Excitation

The OI 130.4 nm feature is one of the brightest in the Earth's UV dayglow spectrum. Measurements of this emission have been made for several decades. Given its prominence, there have been many attempts to measure the excitation cross section. A review of these measurements can be found in Meier (1991) and Cotton *et al.* (1993b). As with the 135.6 nm emission, there are contributions due to direct excitation and due to cascade from higher states. However in the atmosphere and often in the laboratory the 130.4 nm emission is optically thick ($\tau >> 1$), resulting in severe multiple scattering. Under optically thin conditions, a transition between the ground state and a higher electronic state has some finite probability of relaxing to the $^3S$ state; this is referred to as the branching ratio for that transition. Under optically thick conditions, there can be many transitions between the ground state and the upper state. Although the branching ratio may be small, the branch transition to the $^3S$ state will become significant after enough scatterings. For these reasons, cross sections may be referred to as "thin" when the extra cascade from multiple scatterings is not accounted, or "thick" when the multiple scattering is accounted. Julienne and Davis (1976) in their theoretical work used the term "thick" to describe the limiting case of infinite opacity described by assuming the branching ratio to be unity. Table 2-2 lists the cascading states and assesses the magnitudes of their contributions.

As with the OI 135.6 nm emission, the most comprehensive theoretical investigation of the 130.4 nm feature has been performed by Julienne and Davis (1976). Their work involves theoretical calculations of the direct cross section as well as all the cascade mechanisms for both thin and thick (infinitely thick) cases. For the thin case, they obtained a peak total excitation cross section (direct plus cascade) of 15 x $10^{-18}$ $cm^2$ at 20 eV and for the thick case a peak value of 29 x $10^{-18}$ $cm^2$. This result indicates an enhancement of nearly a factor of two due to infinite optical depth effects. Theoretical calculations of the direct excitation cross section have been performed by Rountree and Henry (1972) and Tayal and Henry (1988). The calculations of Rountree and Henry showed a resonance near threshold which was not found in the work of Julienne and Davis or Tayal and Henry. Tayal and Henry obtained a magnitude of 10.8 x $10^{-18}$ $cm^2$ compared to the 7.1 x $10^{-18}$ $cm^2$ found by Julienne and Davis (1976).

Electron energy loss measurements have been performed by Doering and coworkers (Vaughan and Doering, 1987; Gulcicek and Doering, 1988; Gulcicek *et al.*, 1988; Doering and Gulcicek, 1989). They have measured both the direct excitation cross section as well as several of the cascade state cross sections. Gulcicek and Doering (1988) found a value of 11.1 x $10^{-18}$ for the direct cross section in excellent agreement with the result of Tayal and Henry. The cascade cross sections are shown in Table 2-2. Following Meier (1991), the cross sections not measured are shown in parenthesis and are substituted by those of Julienne and Davis (1976). With the exception of the 3s' state, the measured cross sections are multiplied by the branching ratios used by Julienne and Davis for the thin case. Unity branching ratios are used for the thick case. Also following the nomenclature of Meier (1991), these cross sections are labeled "revised" in Table 2-2 to represent revisions to the theoretical work of Julienne and Davis. One should note that the total cascade and total cross sections of Table 2-2 are in general agreement.

A measurement of the total excitation cross section under optically thin conditions was performed by Stone and Zipf (1974). Their result was later scaled by a factor of 0.36 by Zipf and Erdman (1985), whose value of the total thin excitation cross section is 17 x $10^{-18}$ $cm^2$, in good agreement with the values of Julienne and Davis (15 x $10^{-18}$ $cm^2$) and the Doering group (20 x $10^{-18}$ $cm^2$).

Analyses of airglow data has also provided some insight into the magnitude of the total excitation cross section and the contribution due to optically thick conditions. Much of this work has come from the two rocket flights mentioned above and described by Gentieu *et al.* (1979) and Eastes *et al.* (1985). Meier *et al.* (1985) did the first comprehensive analysis of these data, and Morrison and Meier (1988) later revised their results. Morrison and Meier found that the total excitation cross section of Zipf and Erdman (1985) is consistent with the airglow data if it was scaled by a factor of 1.42. This enhancement would account for the optically thick atmosphere and represents a smaller contribution than predicted for an infinitely optically thick atmosphere (see Table 2-2). Conway *et al.* (1988) supported this result in analyses of S3-4 satellite data. On the other hand, Link *et al.* (1988b) analyzed the same rocket data as well as STP 78-1 satellite data (Link *et al.*, 1988a) and concluded that the Zipf and Erdman cross section is consistent with the data without scaling.

Extensive analyses of airglow data were performed by Cotton *et al.* (1993a, 1993b, 1993c). They modeled the radiative transfer of three important oxygen transitions which have branches to the 3s $^3S$ state. By calculating the multiple scattering accurately and storing the branched fraction of the production rate, they calculated the contribution to the final excitation rate of the 130.4 nm emission. The states they analyzed were the 3s' $^3D$, 3d $^3D$, and 4s $^3S$ which lead to emissions at 98.9, 102.7, and 104.0 nm respectively. Unfortunately, these are not all the states which can lead to 3s $^3S$ population. However, after accounting for all the excitation from these branches,

more excitation was still required to fit the data. An optically thick enhancement to the cross section of Zipf and Erdman (1985), as suggested by Morrison and Meier (1988), brought the model and data in near agreement. Cotton *et al.* point out that although the summed contribution of the branches are in near agreement with those of Meier (1991), the individual contributions differ. Therefore, simply applying a scaling factor to an optically thin cross section may not be appropriate.

While there is general agreement between theoretical calculations and laboratory measurements of the optically thin cross section, there is not general agreement as to the magnitude of the excitation of the OI 130.4 nm emission. For this work, the shape of the energy loss laboratory results of Doering and coworkers are assumed; these cross sections and their references are listed in Table 2-2. These cross sections are scaled so that the sum yields a magnitude equal to that recommended by Morrison and Meier (1988).

### 2.4.3.2 Resonant Scattering of Sunlight

The second source of OI 130.4 nm emission is resonant scattering of sunlight. The model for calculating emission rates from this source is described in Chapter III. The solar irradiance at 130.4 nm is divided approximately equally in the three OI 130.4 nm lines. The magnitude of the solar irradiance has been found to vary from 6 to 14 x $10^9$ photons $cm^{-2}$ $s^{-1}$ on rockets (Mount and Rottman, 1985) and from 6.6 to 8.6 x $10^9$ photons $cm^{-2}$ $s^{-1}$ by the Solar Mesosphere Explorer (SME) satellite (Rottman, 1985). Solar FUV irradiances are currently being monitored by the Solar Stellar Irradiance Comparison Experiment (SOLSTICE) on the Upper Atmosphere Research Satellite (UARS). The UARS solar measurements are available for the times of each of the rocket flights described in this work and are used in the emission rate calculations. The UARS SOLSTICE instrument is capable of separating the 130.2 nm line from the other two in the triplet, but it cannot completely resolve the three lines. The integrated

irradiance as measured by the SOLSTICE instrument is divided among the three lines according to the ratios listed in Gladstone (1992). The solar line shapes are taken from Gladstone (1992).

Solar irradiance contributes to the terrestrial 130.4 nm emission rate in a second way, due to a resonance between the singlet transition of the $2p^4\ ^3p$ - $3d\ ^3D^0$ multiplet and the solar Lyman β emission at 102.576 nm. The solar Lyman β feature excites oxygen atoms to the $3d\ ^3D^0$ state. From this state, there are branch transitions to $3s\ ^3S$; the branching probability is 29%. Meier *et al.* (1987) show that this mechanism represents approximately 10% of the total solar contribution to the OI 130.4 nm emission rate. This process is not included in this work.

## 2.5 Spectroscopy of the Lyman Birge Hopfield Bands of $N_2$

The LBH bands of $N_2$ are a very prominent feature in the FUV spectrum of the Earth's upper atmosphere. Several measurements have demonstrated this fact (Meier *et al.,* 1985; Eastes *et al.* 1985; Morrison *et al.*, 1990), thus several authors have published synthetic spectra for the LBH bands (Barth, 1965; Conway 1982; Cleary 1986). It will be assumed here that the population mechanism follows direct Franck-Condon theory. The validity of this assumption will be addressed later.

### 2.5.1 The Franck-Condon Principle

The Franck-Condon principle governs the population of the various vibrational levels upon an electronic transition. Franck-Condon theory allows the calculation of the relative populations of the vibrational levels given an original state. The results of such calculations are Franck-Condon factors. A Franck-Condon factor is usually designated with the symbol $q$, and subscripted with v' and v" for the transition. Thus for a transition from v' = 0, the populations of the upper states are proportional to the Franck-Condon factors $q_{v0"}$.

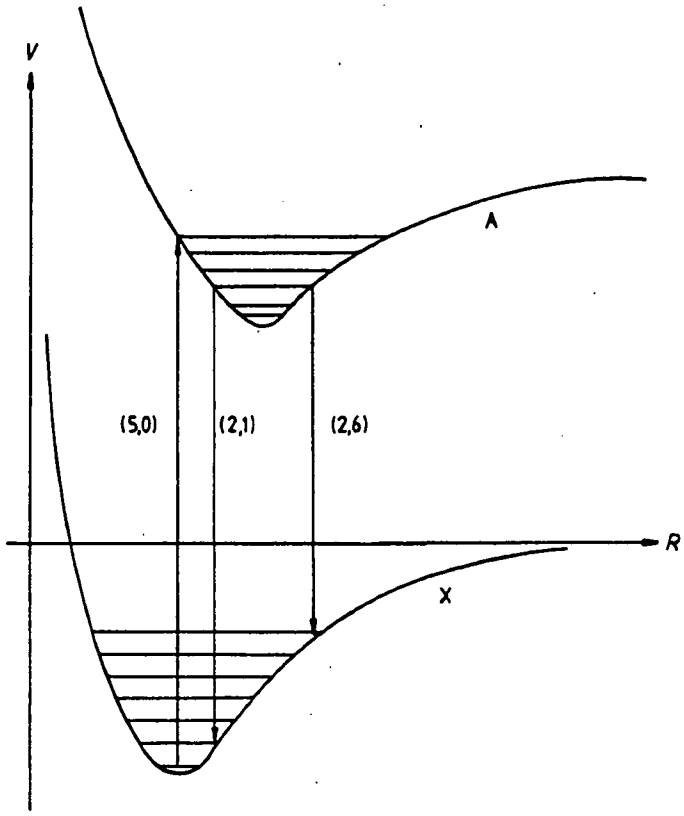


Figure 2-6 Illustration of the Franck-Condon principle. The most probable absorption from $v''=0$ is to $v' = 5$. The most probable emissions are from $v'=2$ are to $v''=1$ and $v''=6$. This figure is taken from Thorne (1988).

The calculation of Franck-Condon factors is not discussed in this work. However, the principle is illustrated in Figure 2-6 which shows potential curves for two electronic states. The X axis of Figure 2-6 is increasing radial distance between the two atoms of the molecule; the Y axis is increasing energy of the state. The steps in the potential well are vibrational states. The Franck-Condon principle states that for a transition between the two electronic states, the most likely new vibrational state is the one directly above (or below, depending on the direction of the transition) the original state. All other transitions are less likely. The probabilities of the various possible transitions are then proportional to overlap integrals of the wavefunctions for the two states.

### 2.5.2 Calculation of Synthetic LBH Spectra

There are three stages to calculating synthetic spectra: calculating the energy of each transition, calculating the transition probabilities, and populating the upper states. These will be addressed individually.

The three energy components of a molecular transition are the electronic transition, the vibrational transition, and the rotational transition. The energies are generally expressed as wavenumbers in units of $cm^{-1}$ and called terms. The term value of a given state is given by:

$$T = T_e + G(v) + F(J) \quad , \qquad 2\text{-}5$$

where $T_e$ is the term for the electronic state, $G$(v) is the term for vibrational state v, and $F(J)$ is the term for the rotational state with the total angular momentum quantum number $J$. The terms $G$ and $F$ are then calculated by:

$$G(v) = \omega_e(v+\frac{1}{2}) - \omega_e\chi_e(v+\frac{1}{2})^2 \quad , \qquad 2\text{-}6$$

$$F(J) = B_v J(J+1) - D_v J^2(J+1)^2 \quad , \qquad 2\text{-}7$$

where,

$$B_v = B_e - \alpha(v + \frac{1}{2}), \qquad 2\text{-}8$$

$$D_v \approx D_e. \qquad 2\text{-}9$$

The first term in equation 2-6 is the solution to the Schrödinger equation assuming the molecule vibrates as a simple harmonic oscillator. Although this assumption is a good approximation, it does not adequately reproduce the vibrational energy levels. Therefore the second term, called the anharmonicity term, is added and $\chi_e$ is the anharmonicity constant. Similarly in equation 2-7, the first term is the result of approximating the rotating molecule as a simple rotor. As this approximation is insufficient, the second term is incorporated. It should be noted that the rotational term is dependent upon the virbrational level, thus the vibrational and rotational levels are coupled. The constants $T_e$, $\omega_e$, $\omega_e\chi_e$, $B_e$,$\alpha_e$ and $D_e$ for both the upper and lower state are measured and can be found in Huber and Herzberg (1979). These are listed in Table 2-4.

**Table 2-4 Spectroscopic Constants of the $N_2$ $a^1\Pi_g$ - $X^1\Sigma_g^+$ Transition**

| | $X^1\Sigma_g^+$ | $a^1\Pi_g$ |
|---|---|---|
| $T_e$ | 0.0 | 69283.06 |
| $\omega_e$ | 2358.57 | 1694.2 |
| $\omega_e\chi_e$ | 14.324 | 13.949 |
| $B_e$ | 1.99824 | 1.6169 |
| $\alpha_e$ | 0.017318 | 0.01793 |
| $D_e$ | $5.76 \times 10^{-6}$ | $5.89 \times 10^{-6}$ |

The probability of transition from an upper vibrational state v ' to a lower one v" is written:

$$A_{v'v''} = \frac{64\pi^4}{3hc^3}\frac{\upsilon^3_{v'v''}}{d_{v'}}\left|R_e^D\right|^2 q_{v'v''} + \frac{32\pi^6}{5hc^3}\frac{\upsilon^5_{v'v''}}{d_{v'}}\left|R_e^Q\right|^2 q_{v'v''}, \qquad 2\text{-}10$$

where $\upsilon$ is the frequency of the band emission, $d_{v'}$ is the degeneracy of the upper level and $R_e$ is the electronic transition moment (superscripted D and Q for dipole and quadrapole transitions), assumed constant for all bands. The symbol $q_{v'v''}$ denotes the Franck-Condon factor for the transition from v=v' to v=v". The electronic transition moment has been measured in the laboratory (Shemansky, 1969; Pilling, 1971). Based on these measurements and other work (Freund, 1972), Conway (1982) writes the transition probability as:

$$A_{v'v''} = 4.373 \times 10^{-11}\, \upsilon^3_{v'v''}\, q_{v'v''} + 5.435 \times 10^{-22}\, \upsilon^5_{v'v''}\, q_{v'v''}. \qquad 2\text{-}11$$

The first term in Equations 2-10 and 2-11 corresponds to dipole transitions and the second to quadrupole transitions. Recalling that the LBH bands are optically forbidden, the observed lines are magnetic dipole and electric quadrapole transitions.

The population of the states is written by Tatum (1967) as

$$\frac{N(nvJ)}{N(nv)} = \frac{1+\delta}{3}(2J+1)\frac{hcB_\upsilon}{kT}\exp\left(-\frac{hc}{kT}F(J)\right), \qquad 2\text{-}12$$

where $\delta$ is 1 for symmetric levels and 0 for antisymmetric levels and $N(nvJ)$ reflects the number of atoms in electronic state $n$, vibrational state v, and total angular momentum state $J$. The symbols $B_v$ and $F(J)$ have already been defined, and $T$ is the temperature. The other symbols have their usual meanings.

The calculation of the emission rate proceeds with the equation:

$$E = P(n'v')\frac{N(n'v'J')}{N(n'v')}\omega_{v'v''}\frac{S(J'J'')}{2J'+1}, \qquad 2\text{-}13$$

where $\omega_{v'v''}$, the single scattering albedo, can be written:

$$\omega_{v'v''} = \frac{A_{v'v''}}{\sum A_{v'v''}}. \qquad 2\text{-}14$$

The single scattering albedo is necessary to account for loss to other transitions. The production rate to the $n'v'$ level, $P(n'v')$, is written:

$$P(n'v') = \phi\sigma q_{0v'}, \qquad 2\text{-}15$$

where $\phi$ is the photoelectron flux, $\sigma$ is the cross section for excitation to the $a^1\pi$ state by impact with photoelectrons, $q_{0v'}$ is the Franck-Condon factor for excitation from the v=0 state to the v' state, and $S(J'J'')$ is the line strength for the transition. Depending on the normalization, the line strength may be referred to as a Hönl-London factor. Tatum (1967) provides a discussion of this normalization. The product $\phi\sigma$ is calculated by the */glow* model as a function of altitude.

Synthetic spectra are generated by following the above procedure for all the relevant vibrational and rotational transitions, taking care that all selection rules are obeyed. For a harmonic oscillator, $\Delta v$ must be $\pm 1$, but for anharmonic oscillator $\Delta v$ may be $\pm 2$, $\pm 3$,... Thus the vibrational state may change by any integral value. The rules on $J$ are more complicated. For electric or magnetic dipole transitions, $\Delta J$ can be $\pm 1$ or 0. This rule is not true for $\Sigma$ - $\Sigma$ transitions. The emissions formed when $\Delta J=0$ comprise what is referred to as the Q branch. Lines where $\Delta J=-1$ form the P branch, and those where $\Delta J=+1$ form the R branch. For quadrupole transitions, $\Delta J=\pm 2$ are allowed. Where $\Delta J=-2$, the O branch is formed and $\Delta J=+2$ comprise the S branch. Thus, the LBH bands consist of a total of eight branches.

States higher than v'=6 and $J'=13$ have been observed to predissociate (Takacs and Feldman, 1977; Ajello and Shemansky, 1985) thus no emission is generated. Line

strengths can be found in Kovacs (1969) and Franck-Condon factors have been tabulated by Benesch *et al.* (1966) and Loftus and Krupenie (1977). The calculations described above have been compared to measured and calculated transition probabilities and wavelengths from Shemansky (1969) and Ajello and Shemansky (1985). All comparisons indicated agreement to better than 1%.

Figures 2-7 and 2-8 show examples of synthetic spectra calculated using the above theory. Figure 2-7 shows the LBH band spectrum from 125 to 180 nm. Figure 2-8 show the (2,0) band at 138.3 nm at two temperatures. The spreading of the band at higher temperatures can be used to deduce temperature from airglow measurements with sufficient spectral resolution.

### 2.5.3 Deviations from Franck-Condon Theory

In their work on cross sections, Ajello and Shemansky (1985) pointed out that the populations of the *a* state of $N_2$ should be different from the direct Franck-Condon theory due to the fact that the thresholds for excitation of the various vibrational levels are not the same and that they occur at energies where the photoelectron flux is increasing rapidly. The thresholds are separated by approximately 0.2 eV. Incorporating this effect into the modeling would require a separate cross section for each vibrational level. These cross sections would only differ at the lowest energies. In the present model, the total cross section of Ajello and Shemansky is used; no threshold effects are considered.

Cartwright (1978) used the measured excitation cross sections to calculate populations of the various electronic states of $N_2$ under auroral conditions. These calculations began with a measured photoelectron flux and a model atmosphere appropriate to the aurora. The equations of statistical balance were then solved using

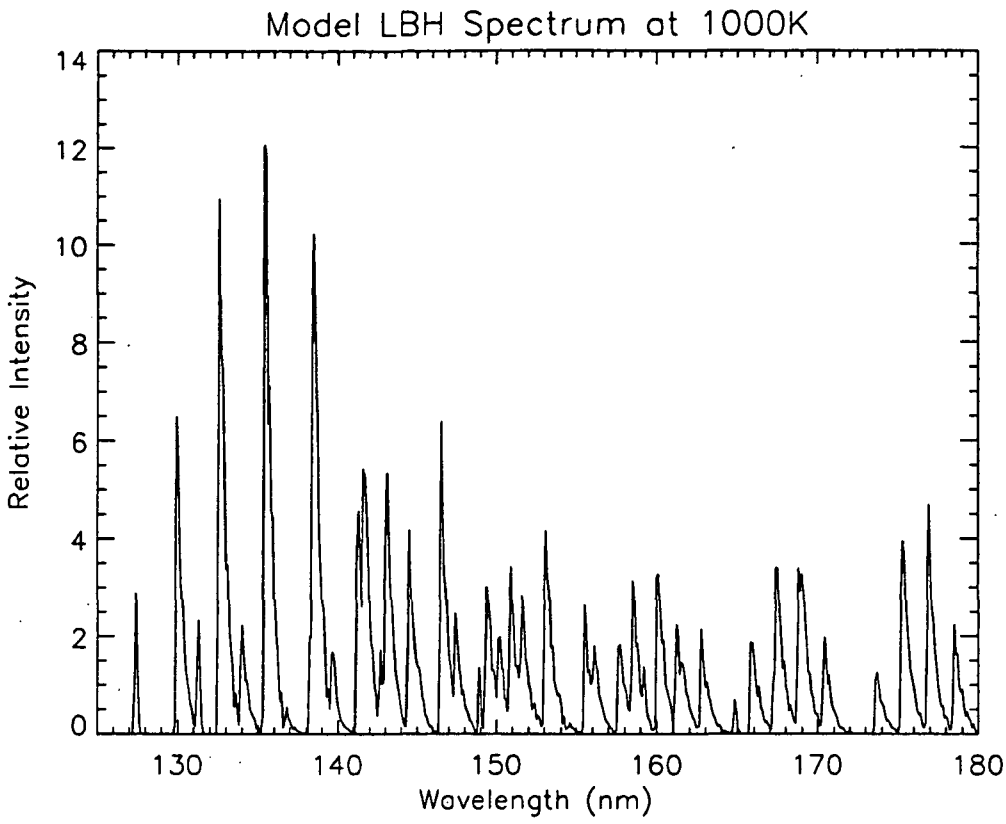


Figure 2-7 Synthetic LBH spectrum for 1000 K.

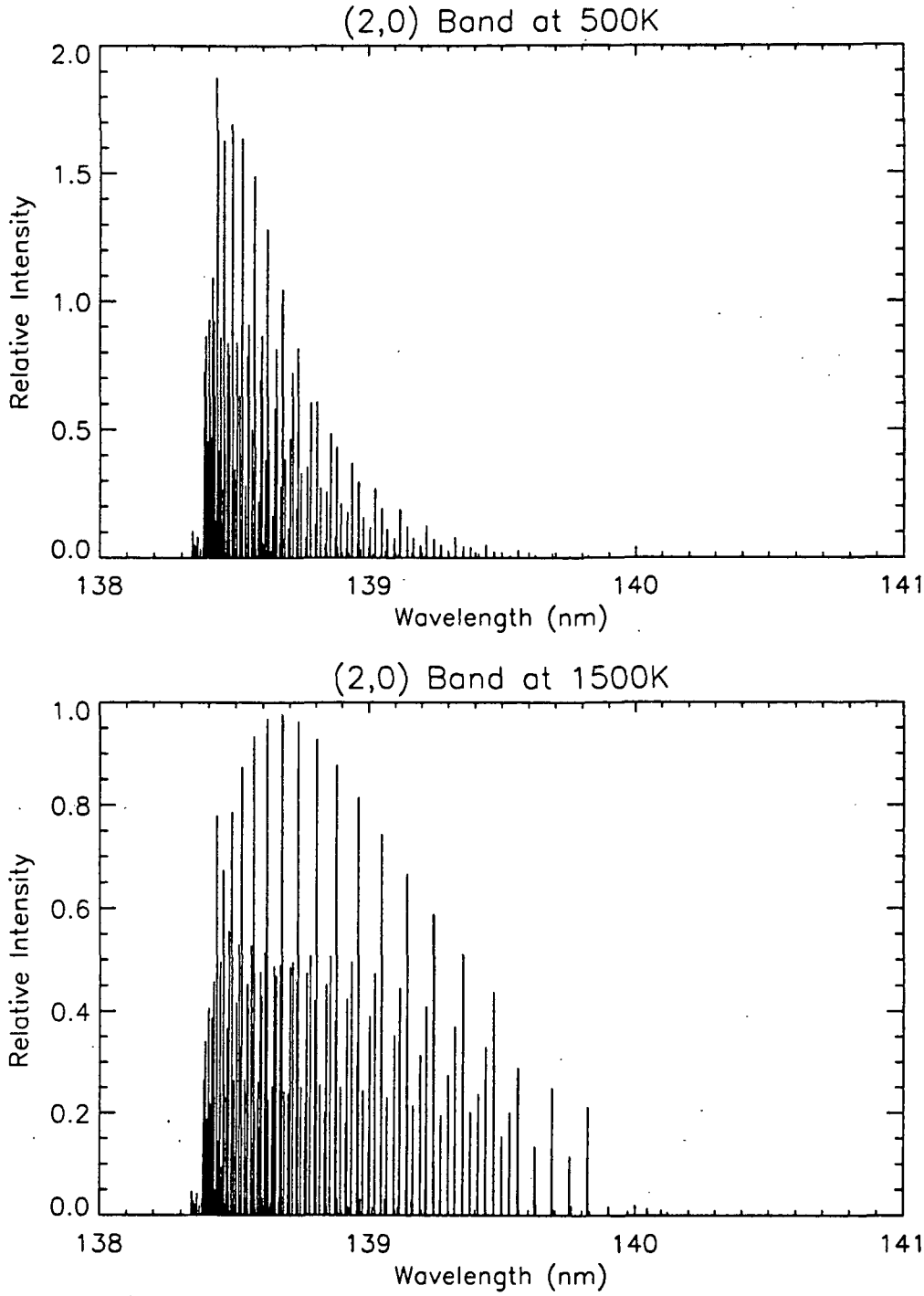


Figure 2-8 Synthetic LBH (2,0) bands at high resolution for temperatures of 500 and 1500K.

an iterative technique. The results of these calculations showed that an important mechanism to the population of the *a* state was cascade from the *a'* and the *w* states. These cascades would give a vibrational population different from that predicted by the direct Franck-Condon theory and would show up as such in airglow measurements. Ajello and Shemansky placed an upper limit of 5% on any cascade effects. Meier *et al.* (1985; Meier, 1991) compared the results of several experiments with the predictions of direct Franck-Condon theory. A 1980 dayglow observation (Meier *et al.*, 1980) observed an enhancement at low v' as would be predicted by Cartwright's analysis; however, similar experiments (Meier *et al.*, 1982; Meier *et al.*, 1985; Eastes and Sharp, 1987; Morrison *et al.*, 1990) did not reveal such an enhancement.

At v'=3, Meier *et al.* (1985) and Eastes and Sharp (1987) report a depletion; however, Morrison and Meier (1990) found a possible enhancement. Budzein *et al.* (1994) and Torr *et al.* (1994) also report virbrational distributions which differ from that predicted by Franck-Condon theory. Budzein *et al.* support Cartwright's conclusion of a cascade contribution to the LBH excitation. The experiments described above did not have a simultaneous measurement of the solar irradiance and so could not accurately determine the excitation due to photoelectrons. As will be shown in later chapters, there are not enough vibrational bands measured in this work to determine the vibrational distribution accurately. The populations of the vibrational states will be assumed to follow direct Franck-Condon theory.

## 2.6 Summary

The goal of this chapter was to discuss the spectroscopy and excitation of the airglow features observed by the experiments which will be described in Chapters IV and V. Particular attention was paid to prior studies of electron impact excitation cross sections. The details of calculating synthetic spectra of the LBH bands were discussed and controversies relating to the excitation of the LBH bands were mentioned.

Although these controversies will be discussed further, LBH excitation in this dissertation will be assumed to follow direct Franck-Condon theory. The LBH electron impact excitation cross section of Ajello and Shemansky (1985), scaled by 0.875 (van der Burgt, 1989), is assumed. For the OI 135.6 nm emission, the cross section of Julienne and Davis, scaled as described in Section 2.4.2, is used. The cross sections for excitation leading to the OI 130.4 nm emission are taken from the optically thick laboratory measurements of Table 2-2 and scaled to achieve the magnitude suggested by Morrison and Meier (1988).

# Chapter III

# Modeling of Photoelectron and Airglow Processes

## 3.1 Introduction

The energy deposited into the atmosphere by solar soft x-rays follows a complicated path. Photoionization produces photoelectrons which lead to further ionization, excitation, and dissociation. The energy manifests itself in the airglow spectrum and the structure of the ionosphere. This chapter describes the modeling which encompasses the study of these processes.

## 3.2 The */glow* Photoelectron Model

The */glow* model (Solomon *et al.*, 1988; Solomon and Abreu, 1989) is a comprehensive set of numerical routines which calculate photoelectron fluxes in the atmosphere and use them to derive profiles for a variety of atmospheric observables. The computer code is available as collaborative software. In this section the formalism used to calculate the flux of photoelectrons will be described. The method of calculation follows that outlined by Nagy and Banks (1970).

### 3.2.1 Model Formalism

The photoelectron flux calculation follows a two stream formalism. The basic premise of such a method is the assumption that the angular dependence of the problem can be simplified by making calculations along one particular path. This path is in a representative direction for which the results approximate the case where all angles are accounted for. The "two stream" name comes from the fact that calculations must be made in both the upward and downward directions. Because electrons travel along the Earth's magnetic field in a spiral motion, it is logical that the path of travel used here be at a representative pitch angle to the magnetic field. In the */glow* model, the path is along a pitch angle of 60°, more commonly referred to by its cosine

of 0.5. Note that this choice of pitch angle evenly divides the surface area of a hemisphere.

For the problem at hand we consider an atmosphere of molecular nitrogen ($N_2$), atomic and molecular oxygen (O and $O_2$), and nitric oxide (NO). Solar soft x-ray and EUV irradiance ionizes these gases creating energetic photoelectrons. These electrons can cause further ionization or excitation by impact with other atoms or molecules. The initial ionization by a solar photon results in a primary photoelectron. Photoelectrons created through ionization by other photoelectrons are called secondary photoelectrons. In an aurora, the deposition of energetic electrons into the atmosphere is a source of energy in addition to the solar irradiance. In this work, only solar irradiance is considered; however, the */glow* model is capable of handling the auroral case (Solomon *et al.*, 1988).

In the two stream formalism, the solar irradiance incident upon the atmosphere at some solar zenith angle is considered. A neutral atmosphere varying only with altitude is assumed and a slant path from the top of the atmosphere is followed. Along the path, electrons can be scattered out of the path by elastic collisions or they can undergo an inelastic collision resulting in ionization, dissociation, or excitation. The sum of these processes will be labeled $T_2$. Electrons can be scattered into the path via elastic collisions, these are labeled $T_1$. Both $T_1$ and $T_2$ are functions of altitude, and have units of $cm^{-1}$ corresponding to production or loss per unit length. The following forms are used:

$$T_1 = \sum_s b_s \sigma_s^{es} n_s, \qquad 3\text{-}1$$

$$T_2 = \sum_s (b_s \sigma_s^{es} n_s + \sigma_s^{is} n_s), \qquad 3\text{-}2$$

where $n$ is the number density of scattering atoms or molecules, $b$ is the backscatter probability, and $\sigma^{es}$ and $\sigma^{is}$ are the elastic and inelastic cross sections respectively. The

subscript $s$ stands for atmospheric species. For a two stream case, the backscatter probability is the probability of reversing directions after an elastic collision. In each energy bin, primary photoelectron production $q$ and cascade from higher energy photoelectrons in either stream undergoing elastic or inelastic collisions $Q$ are accounted for. Both $Q$ and $q$ have units of $cm^{-3}\ s^{-1}$. Defining $\mu$ as the cosine of the angle between the path and the magnetic field, $\phi$ as the flux of photoelectrons ($cm^{-2}\ s^{-1}$, a function of electron energy and altitude), + and - superscripts as the upward and downward directions, and $z$ as the distance along the field line, the two stream equations of electron transport are:

$$\mu\frac{d\phi^+}{dz} = -T_2\phi^+ + T_1\phi^- + Q^+ + \frac{q}{2}, \qquad 3\text{-}3$$

$$-\mu\frac{d\phi^-}{dz} = -T_2\phi^- + T_1\phi^+ + Q^- + \frac{q}{2}. \qquad 3\text{-}4$$

Taking the derivative of Equation 3-4 gives:

$$-\mu\frac{d^2\phi^-}{dz^2} = -T_2\frac{d\phi^-}{dz} - \phi^-\frac{dT_2}{dz} + T_1\frac{d\phi^+}{dz} + \phi^+\frac{dT_1}{dz} + \frac{dQ^-}{dz} + \frac{1}{2}\frac{dq}{dz}. \qquad 3\text{-}5$$

Substituting 3-3 into 3-5 yields:

$$-\mu\frac{d^2\phi^-}{dz^2} = -T_2\frac{d\phi^-}{dz} - \phi^-\frac{dT_2}{dz} + \frac{T_1}{\mu}\left[-T_2\phi^+ + T_1\phi^- + Q^+ + \frac{q}{2}\right] + \phi^+\frac{dT_1}{dz} + \frac{dQ^-}{dz} + \frac{1}{2}\frac{dq}{dz}. \qquad 3\text{-}6$$

Solving 3-4 for $\phi^+$ gives:

$$\phi^+ = \frac{1}{T_1}\left[-\mu\frac{d\phi^-}{dz} + T_2\phi^- - Q^- - \frac{q}{2}\right]. \qquad 3\text{-}7$$

Finally, substituting 3-7 into 3-6 results in the equation:

$$\frac{d^2\phi^-}{dz^2} + \alpha\frac{d\phi^-}{dz} + \beta\phi^- + \gamma = 0. \qquad 3\text{-}8$$

Here $\alpha$, $\beta$, and $\gamma$ are collected terms in $T_1$, $T_2$, $q$, $Q$, and their spatial derivatives. Thus $\alpha$, $\beta$, and $\gamma$ have the forms:

$$\alpha = -\frac{1}{\mu}\left(2T_2 + \frac{\mu}{T_1}\frac{dT_1}{dz}\right), \qquad 3\text{-}9$$

$$\beta = \frac{1}{\mu}\left(\frac{T_1^2}{\mu} + \frac{T_2^2}{\mu} + \frac{T_2}{T_1}\frac{dT_1}{dz} - \frac{dT_2}{dz}\right), \qquad 3\text{-}10$$

$$\gamma = \frac{1}{\mu}\left[\frac{T_1 Q^+}{\mu} - \frac{T_2 Q^-}{\mu}\right] + (T_1 - T_2)\frac{q}{2\mu} - (Q^- + \frac{q}{2})\frac{1}{T_1}\frac{dT_1}{dz} + \frac{dQ^-}{dz} + \frac{1}{2}\frac{dq}{dz}. \qquad 3\text{-}11$$

Equation 3-8 is a second order ordinary differential equation. In the */glow* model, the equation for $\phi^-$ is solved using the steady state Crank-Nicholson numerical technique. This method is generally applicable to parabolic partial differential equations, using an iterative approach. For the steady state case at hand, a solution can be obtained in only one iteration. A complete description can be found in Von Rosenberg (1969). Once $\phi^-$ has been calculated at all altitudes, $\phi^+$ is obtained by integrating (3-5) from the lower boundary to the upper. Two boundary conditions are required to obtain a solution. At the top of the atmosphere, the downward flux is a given value appropriate for the particular problem, such as an auroral electron spectrum or a conjugate electron spectrum. Conjugate electrons are produced at a given location and follow magnetic field lines to their conjugate position on the Earth. At the bottom of the atmosphere, the upward flux and the downward flux are set equal. The lower boundary of the altitude grid is selected such that these fluxes are zero or very small.

In the above method, the highest electron energy bin is solved first, the cascade terms are then calculated, and the process is repeated for the next highest energy bin. Thus the loop structure is over electron energy and then altitude. Photoelectron production through photoionization is calculated at each altitude prior to beginning the main loop. The altitude and electron energy bin sizes are variable; at low altitude or

energy the bins are smaller than at high altitude and high energy. There are 81 bins in altitude ranging from 86 km to 1000 km. There are 112 bins in electron energy ranging from 0.1 to 1000 eV. The selection of bin size for solar irradiance, and therefore photoabsorption and photoionization cross sections, can be important. This will be discussed in a later section.

The calculation of photoelectron fluxes requires knowledge of many parameters. These fall into three classes: energy deposition, such as solar irradiance; atmospheric composition, including density and temperature; and physical parameters of the atmospheric constituents. Solar irradiances and the neutral atmosphere are used to calculate the photoelectron profile. These are then used in conjunction with the chemistry to calculate volume emission rates for many emissions.

The solar emission data required for these calculations range in wavelength from the EUV downward to the x-ray region of the spectrum. Works published in the field have used solar fluxes from models and past measurements (Hinteregger *et al.*, 1981; Woods and Rottman, 1990; Tobiska, 1991). For a typical */glow* model run, the EUV irradiance model of Hinteregger *et al.* (1981) is used. To account for solar activity, this model varies the SC#21REFW reference spectrum according to the solar 10.7 cm flux value. For wavelengths longer than 120 nm, a similar scaling is used based on spectra from the SME satellite (Rottman, 1985). Measured solar irradiances can also be used, as is the case for the sounding rocket measurements described in this work.

For a typical run of the */glow* model, a complete model atmosphere is obtained from two sources. Profiles for the neutral species and temperatures are obtained from the Mass Spectrometer Incoherent Scatter model (MSIS) (Hedin, 1987). Electron and ion densities and temperatures are obtained from the International Reference Ionosphere (Belitza, 1986). Measured atmospheric profiles can also be accommodated.

In order to calculate the rates of elastic and inelastic collisions, the */glow* model incorporates a large body of cross section data. Appendix 1 of Solomon *et al.* (1988) details the many cross sections used. The inelastic cross sections are fitted with analytical curves. For excitation, the Green and Stolarski (1972) method is used; for ionization and secondary electron production, the formula of Jackman *et al.* (1977) is used. Elastic cross sections are obtained through interpolation of published theoretical and experimental work. Much of this experimental data can be found in Trajmar *et al.* (1983). Appendix A describes the fitting algorithms and provides a table of the fit parameters for each cross section. Some updates to the cross sections referenced above will be described in the following sections of this chapter, specifically these are the $N_2$ LBH, and the OI 130.4 and 135.6 nm electron impact excitation cross sections.

Figures 3-1 and 3-2 show examples of photoelectron spectra calculated at different altitudes. Figure 3-1 is for times of high solar activity (solar maximum) and Figure 3-2 for times of low activity (solar minimum). The parameters used in the MSIS model atmosphere are listed in Table 3-1 for both cases. Note that these are the same cases used as examples in the review of Meier (1991); these cases will be used for other examples throughout this chapter and Chapter VII. The solar irradiances for the sample calculations are taken from the SERF 1 solar irradiance model (Hinteregger *et al.*, 1981; see also Section 1.1.1) appropriate to the conditions of Table 3-1.

The general trend in Figures 3-1 and 3-2 is increasing photoelectron fluxes toward lower electron energies. This is because the photoelectrons tend to cascade towards lower energies as they collide with the atmospheric constituents. Each collision leads to an ionization, dissociation, or excitation of that species, which reduces the energy of the electron. Therefore, as each electron eventually transfers its energy to the

**Table 3-1 MSIS Model Atmosphere Parameters**

| Parameter | Solar Min | Solar Max |
|---|---|---|
| Date | 21 March 1976 | 21 March 1980 |
| Latitude | 32° | 32° |
| Longitude | 254° | 254° |
| Local Solar Time | 10:00 | 10:00 |
| Solar Zenith Angle | 42.4° | 42.4° |
| Solar 10.7 cm Flux | 71 | 188 |
| - 81 Day Average | 71 | 188 |
| - Prior Day | 86 | 163 |
| Ap | 6 | 18 |
| $T_{exospheric}$ | 816K | 1191K |
| Solar 130.4 nm Flux | $6 \times 10^9$ ph $cm^{-2}$ $s^{-1}$ | $10 \times 10^9$ ph $cm^{-2}$ $s^{-1}$ |

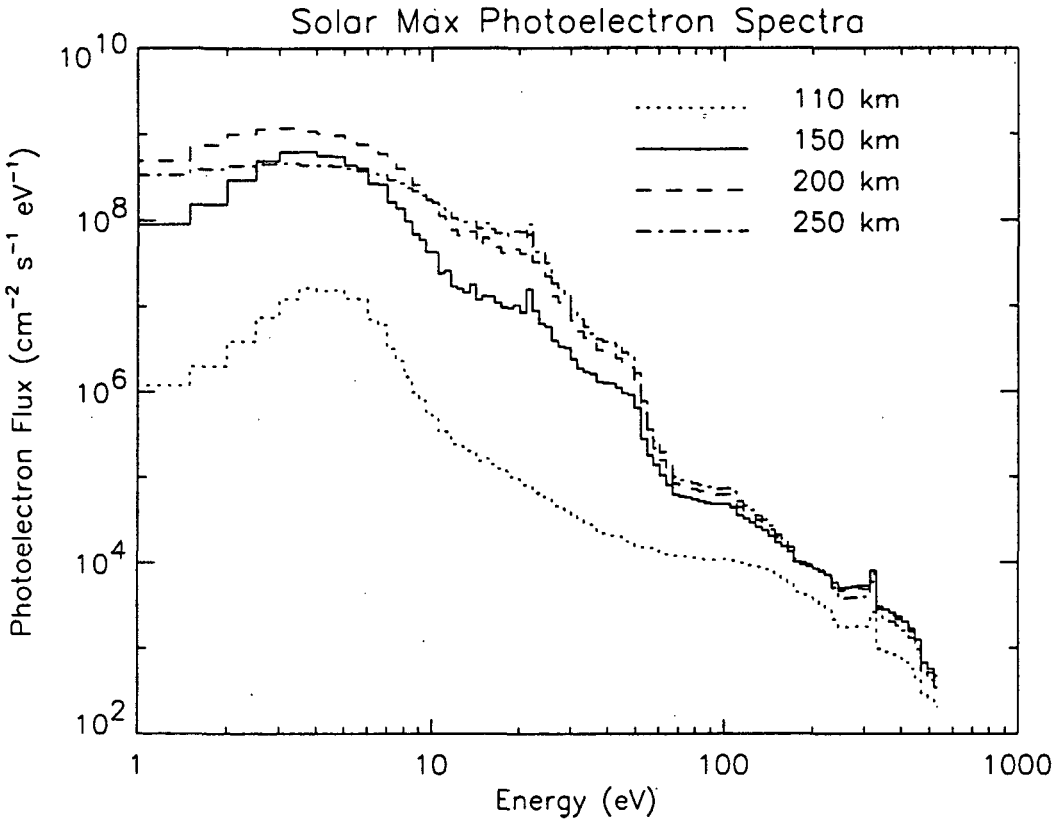


Figure 3-1 Photoelectron spectrum calculated by the */glow* model for the solar maximum conditions described in Table 3-1.

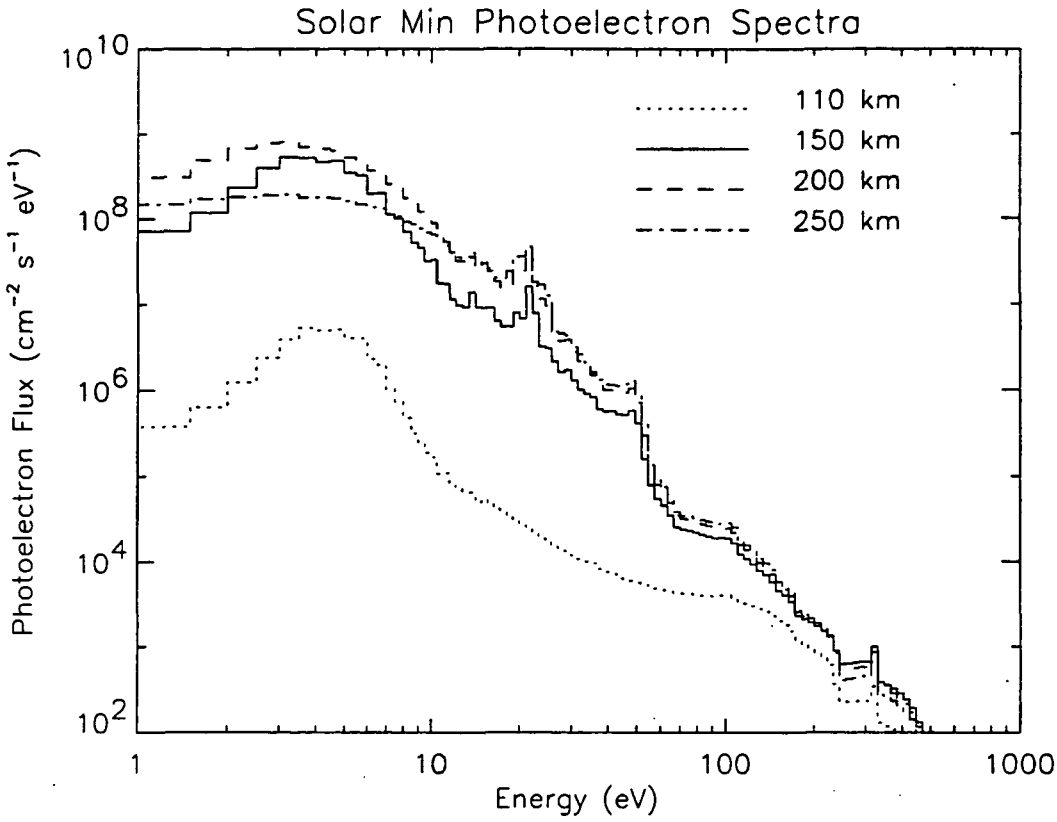


Figure 3-2 Photoelectron spectrum calculated by the */glow* model for the solar minimum conditions described in Table 3-1.

atmosphere, any snapshot of the photoelectron spectrum shows only a few high energy electrons and increasing numbers of electrons towards the lowest energies as they transfer their energy to the atmosphere. Below 3 eV, a dip appears in the photoelectron spectrum, this dip is due to vibrational excitation of $N_2$ for which there is a large cross section at these energies.

Some peaks also occur in the photoelectron spectra. The most obvious are at 25 and 335 eV. The feature at 25 eV is due to the very bright solar HeII emission at 30.4 nm. This feature is nearly an order of magnitude brighter than the emissions surrounding it in the solar spectrum. The energy of a 30.4 nm photon is about 40 eV; the ionization energy of O or $N_2$ is about 15 eV. Therefore, we expect a peak near 25 eV. The peak at 335 eV is due to Auger ionization of $N_2$, a process which will be described in Section 3.3.3.

Once the photoelectron spectrum is found, ionization, dissociation, or excitation rates by electron impact can be calculated by the following integration:

$$\int_0^\infty \phi(E,z)\sigma(E)n_s(z)dE. \qquad 3\text{-}12$$

Here $\phi$ is the photoelectron flux, $\sigma$ is the cross section for the process under consideration, $E$ is electron energy, and $n_s$ is the number density of the atmospheric species undergoing the process.

### 3.2.2 Photoabsorption and Photoionization Cross Sections

The original photoabsorption and photoionization cross sections for the */glow* model were taken from Kirby *et al.* (1979). Branching ratios for ionization to the various ion states were also taken from this work. The cross sections have been updated to those of Fennelly and Torr (1992). The branching ratios are taken from Conway (1988). The compilation of Fennelly and Torr uses more recent measurements of cross section values, and uses more data points. This is important in regions where

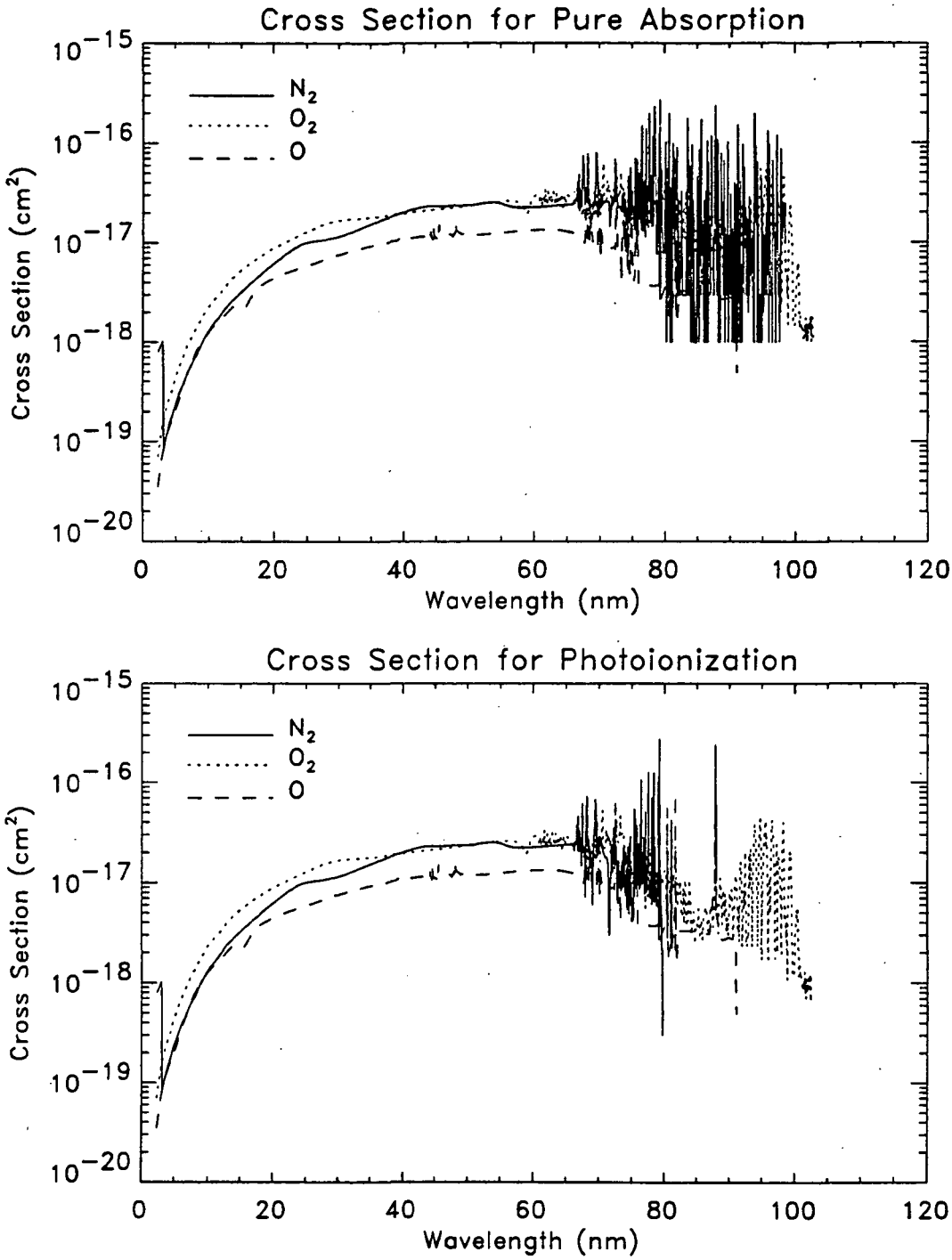


Figure 3-3 Cross sections for photoionization and pure absorption by O, $O_2$, and $N_2$.

the cross sections are varying rapidly. An important example is the $N_2$ absorption at wavelengths above 70 nm. These cross sections are displayed in Figure 3-3.

When incorporating the photoabsorption and photoionization cross sections into the photoelectron calculation, they must be binned in the same manner as the solar irradiance. The effect of binning the solar irradiance is discussed in Section 3.5. Rather than averaging each cross section over a wavelength bin, the cross sections are weighted according to the shape of the solar spectrum within that bin. The shape of the solar spectrum is taken from the SC#21REFW reference spectrum (Hinteregger *et al.*, 1981). The weighted cross sections and branching ratios are listed in Appendix B along with the binned SC#21REFW solar spectrum.

### 3.2.3 Auger Ionization

An important contribution to the photoionization term of Equation 3-2 is due to Auger electrons. The effects of Auger ionization were first calculated by Avakyan *et al.* (1977). The first measurements to demonstrate their importance were from the Dynamics Explorer 2 satellite (Winningham *et al.*, 1989). A detailed description of Auger processes can be found in Berkowitz (1979). The process of Auger ionization occurs when the impinging photon has enough energy to remove a K-shell electron from the atom or molecule with which it collides. Since the removal of the inner electron takes a great deal of energy (360 eV for $N_2$), the electron produced typically has very little energy. The interesting aspect of Auger ionization, however, is what occurs after the K-shell electron is released. The vacancy in the K-shell is immediately filled, so an outer electron takes its place. In doing so, the atom gives up the same amount of energy that was required to break free the K-shell electron. This energy is released with another outer shell electron. For molecules comprised of elements with atomic numbers less than 20, this process also dissociates the molecule (Berkowitz, 1979). The Auger process is written symbolically for $N_2$ in the following way:

$$N_2 + h\upsilon(> 400eV) \rightarrow N + N^{++} + e(400eV - 25.8eV) + e(h\upsilon - 400eV). \quad 3\text{-}13$$

The 25.8 energy in Equation 3-13 is the 10 eV needed to dissociate the molecule and the 15.8 eV needed to remove the outer shell electron. The process is similar for $O_2$ and O, except there is no dissociation involved with atomic oxygen. The dissociation, ionization, and Auger ionization energies are listed in Table 3-2.

Auger ionization is incorporated into the */glow* model as described above. Auger ionization is important in the lower thermosphere for the production of Nitric Oxide molecules. This effect is demonstrated in Section 3.4.3.

## 3.3 Radiative Transfer

Once the above methods are used to generate volume emission rate profiles, a radiative transfer algorithm must be employed to integrate these profiles along the line of sight of the observer. As measurements are made from varying geometries, this algorithm is designed to be capable of handling an arbitrary geometry. It is assumed that the volume emission rate profiles vary only in altitude and do not vary horizontally. The atmosphere is divided into spherical shells of constant emission rate.

### 3.3.1 Optically Thin Emissions

For the LBH bands, pure absorption by $O_2$ is accounted for but no multiple scattering effects are included. Conway (1982) has shown that self absorption is not important for the LBH bands except for the (6,0) band where attenuation can become as large 20%.

The integration follows the formalism:

$$4\pi I(s_0, \lambda) = \int_0^\infty j(s, \lambda) e^{-n\sigma(\lambda)s} ds \quad 3\text{-}14$$

where $4\pi I$ is the brightness in units of Rayleighs, $j$ is the volume excitation rate in units of $10^6$ cm$^{-3}$ s$^{-1}$, $s$ is the distance along the line of sight, $s_0$ defines the point of

**Table 3-2 Ionization and Dissociation Energies (eV)**

| Gas | First Ionization[†] | K-shell Ionization[‡] | Dissociation[†] |
|---|---|---|---|
| O | 13.61 (91.11) | 532 (2.33) | - |
| $N_2$ | 15.581 (79.58) | 402 (3.10) | 9.759 (127.1) |
| $O_2$ | 12.071 (102.7) | 532 (2.33) | 5.115 (242.4) |
| NO | 9.264 (133.9) | 402 (3.10) | 6.496 (190.9) |

[†]Values are taken from Huber and Herzberg (1979) for molecules and Zombeck (1990) for atomic oxygen.

[‡]Values are taken from Zombeck (1990).

observation, $n$ is the number density of absorbers ($O_2$ in this case), and $\sigma(\lambda)$ is the wavelength dependent cross section for pure absorption. Temperature dependence of the cross section for pure absorption by $O_2$ is not included. This dependence will be described in Section 3.3.3. The line of sight is referenced to the zenith by the angle $\theta$ called the observation zenith angle.

The numerical scheme employed is a Riemann or rectangular integration; other methods were tested but no significant improvement in accuracy or efficiency was obtained. Testing has also shown that increments in $s$ of 2 km give satisfactory results. Interpolation of the volume emission rate and $O_2$ number density is performed at each step. Integration continues until the contribution to the intensity becomes vanishingly small.

### 3.3.2 Optically Thick Emissions

The FUV resonant oxygen lines at 130.4 and 135.6 nm are optically thick to resonant fluorescent scattering in the Earth's atmosphere. Therefore, unlike the $N_2$ emissions described above, multiple scattering must be accounted for. For the OI 135.6 nm line, vertical optical depths are on the order of 1, whereas for the OI 130.4 nm line they can be as large as $10^5$ or more. The effect is therefore much stronger for the 130.4 nm emission.

The multiple scattering is calculated using the Feautrier numerical solution of Gladstone (1982, 1988). This matrix solution is described by Mihalas (1978). The equation to be solved is:

$$\frac{\mu}{E(z,x)}\frac{dI}{dz}(z,\mu,x) = -I(z,\mu,x) + \frac{n^a(z)}{2E(z,x)}\int_{-\infty}^{\infty}\sigma^a(z,x')r(z,x,x')\int_{-1}^{1}I(z,\mu',x')d\mu'\,dx' + \frac{n^s(z)}{4E(z,x)}\int_{-\infty}^{\infty}\sigma^s(z,x')r(z,x,x')F(x')\exp\left[-\int_{z}^{\infty}E(z,x')\frac{dz}{\mu_0}\right]dx' + \frac{V(z,x)}{4\pi E(z,x)} \quad 3\text{-}15$$

Where $z$ is the altitude, $\mu$ is the cosine of the zenith angle, and $x$ is the frequency in Doppler units from line center. This frequency is calculated by:

$$x = \frac{\upsilon - \upsilon_0}{\Delta\upsilon_D} \quad 3\text{-}16$$

The Doppler width of the line $\Delta\upsilon_D$ is:

$$\Delta\upsilon_D = \frac{\upsilon_0}{c}\sqrt{\frac{2kT}{m}} \quad 3\text{-}17$$

where $m$ is the mass of the scattering particle and $T$ is temperature. From Equation 3-15, $I$ is the specific intensity in units of photons $cm^{-2}$ $s^{-1}sr^{-1}$ $\Delta\upsilon_D{}^{-1}$. The total extinction per unit length $E$ is calculated by:

$$E(z,x) = n^s(z)\sigma^s(z,x) + n^a(z)\sigma^a, \quad 3\text{-}18$$

where $n^s$ and $n^a$ are the number densities of the scattering and absorbing constituents respectively, and $\sigma^s$ and $\sigma^a$ are the scattering and absorbing cross sections. For the OI emissions discussed in this work, atomic oxygen is the scatterer and molecular oxygen is the pure absorber.

The second term on the right hand side of Equation 3-15 represents the contribution from scattered photons; the third term is the contributions from an external source of photons, $\pi F(x)$; and the final term is the contribution from an internal source, $V(z,x)$. The OI 130.4 nm line is an allowed transition and the solar 130.4 nm feature is

bright, therefore some of the observed emission is the scattering of solar photons. This represents an external source of photons. The terrestrial 130.4 nm emission is also excited by photoelectron impact and represents an internal source. The OI 135.6 nm line is optically forbidden and so only the external source or photoelectron excitation is important. Initial excitation rates for excitation by photoelectron impact are calculated by */glow*.

The redistribution function determines the frequency of the new photon after scattering. The normalized redistribution function is the general redistribution function $R$ divided by the Voigt line shape function (Gladstone, 1982). In general $R$ is defined such that $R d\upsilon d\upsilon' d\Omega d\Omega' /(4\pi)^2$ is the probability that a photon of frequency between $\upsilon$ and $\upsilon+d\upsilon$ from direction $\mathbf{n}$ in solid angle $d\Omega$ is scattered with a frequency between $\upsilon'+d\upsilon'$ in the direction $\mathbf{n'}$ in the solid angle $d\Omega'$ (Hummer, 1962, 1969). An integration of $R$ over all independent variables yields unity. When the upper and lower states for the transition are discrete and the scattering is coherent, $R\equiv 1$. However, in reality it cannot be assumed that the upper state is discrete. The finite lifetime of the upper state to radiative decay leads to a Lorentzian line profile. Although scattering is coherent in the reference frame of the scattering atom, the atom has a finite velocity relative to the photon and therefore sees the photon at a Doppler shifted wavelength. The shape of the redistribution function is then determined by the distribution of velocities and by the Lorentzian lineshape due to the diffuse upper state.

The above description of redistribution is referred to as Partial Frequency Redistribution (PFR). The simplifying assumption can be made that the scattering is completely incoherent. Thus, the frequency of the scattered photon does not depend on the original frequency, which makes the redistribution function separable and can greatly simplify the solution of the radiative transfer equation. This assumption is referred to as Complete Frequency Redistribution (CFR). The assumption of CFR can

lead to errors as the vertical optical depth for scattering gets larger than ~200 (Meier 1991). An intermediate assumption between CFR and PFR is called Angle Averaged Partial Frequency Redistribution (AAPFR), where the dependence of $R$ on scattering angle is neglected. This assumption is valid for an isotropic radiation field. The technique used in this work assumes the AAPFR approximation, as developed by Ayres (1985). This assumption is made for both the OI 135.6 nm and the OI 130.4 nm emissions; although, CFR is an acceptable assumption for the 135.6 nm line (Strickland and Anderson, 1983; Meier, 1991).

To solve Equation 3-15, it is first discretized, leaving a tridiagonal system of matrix equations. This system of equations can then be solved by following the procedure described in Mihalas (1978). The calculation proceeds under the assumption of a plane-parallel atmosphere with temperature a function of altitude. The line shapes are divided into 12 nonuniform divisions: $x$ varies from 0 to 60 Doppler units for an external source and 0 to 15 Doppler units for an internal source. The extra linewidth for an external source is due to relatively wide solar lines. Boundary conditions must be supplied at the upper and lower boundaries. At the top of the atmosphere it is assumed that the downward diffuse flux is zero. At the lower boundary it is assumed that there is no upward flux. In practice, this calculation is performed to solve for the final source function:

$$S(z) = \int_{-\infty}^{\infty} \int_{-1}^{1} I(z, x', \mu') dx' \, d\mu' \qquad 3\text{-}19$$

The observed brightness can then be calculated from the formal solution to the equation of radiative transfer:

$$4\pi I(s_0) = \int_{0}^{\infty} S(s) e^{-n\sigma(\lambda)s} ds \qquad 3\text{-}20$$

The purpose of this procedure is to increase accuracy, because the sphericity of the Earth can be incorporated easily into the integration of 3-20.

Figures 3-4 and 3-5 show initial volume excitation rates for the LBH bands and the OI 135.6 and 130.4 nm emissions. The initial excitation rates are those calculated by */glow* using Equation 3-12. The final volume excitation rates (when multiple scattering is important) are produced by the Feautrier model. The limb brightnesses are then calculated by Equation 3-20, assuming the geometry of a rocket traveling through the atmosphere and viewing the horizon. This geometry will be further described in Chapter V. Note that this observing geometry is different than that used in Meier (1991), preventing direct comparison. The excitation rates, however, can be compared directly.

Figures 3-4 and 3-5 show that the difference in excitation and limb brightness from solar maximum to solar minimum is approximately a factor of 2 or 3. The figures also show that the excitation profiles have two peaks. The higher altitude peaks are primarily due to solar irradiance from 17 nm up to and including the bright HeII 30.4 nm feature. The solar irradiance has a dip from 10 to 17 nm where there is relatively little energy. Below 10 nm there is more irradiance and the solar emission from 1.8 to 10 nm generates the secondary, lower altitude peak. As wavelengths become shorter, absorption cross sections get smaller, allowing the solar irradiance to penetrate deeper into the atmosphere. This mechanism explains the separation of the peaks.

Figures 3-6 and 3-7 show the effect of multiple scattering on the OI emissions. Although the effect is small for the 135.6 nm emission, it is tremendous for the 130.4 nm emission. This is due to the large optical depth ($\sim 10^4$ - $10^5$) for resonant scattering. The internal (photoelectron impact) and external (resonant scattering of sunlight) sources produce very different shapes in excitation and limb brightness.

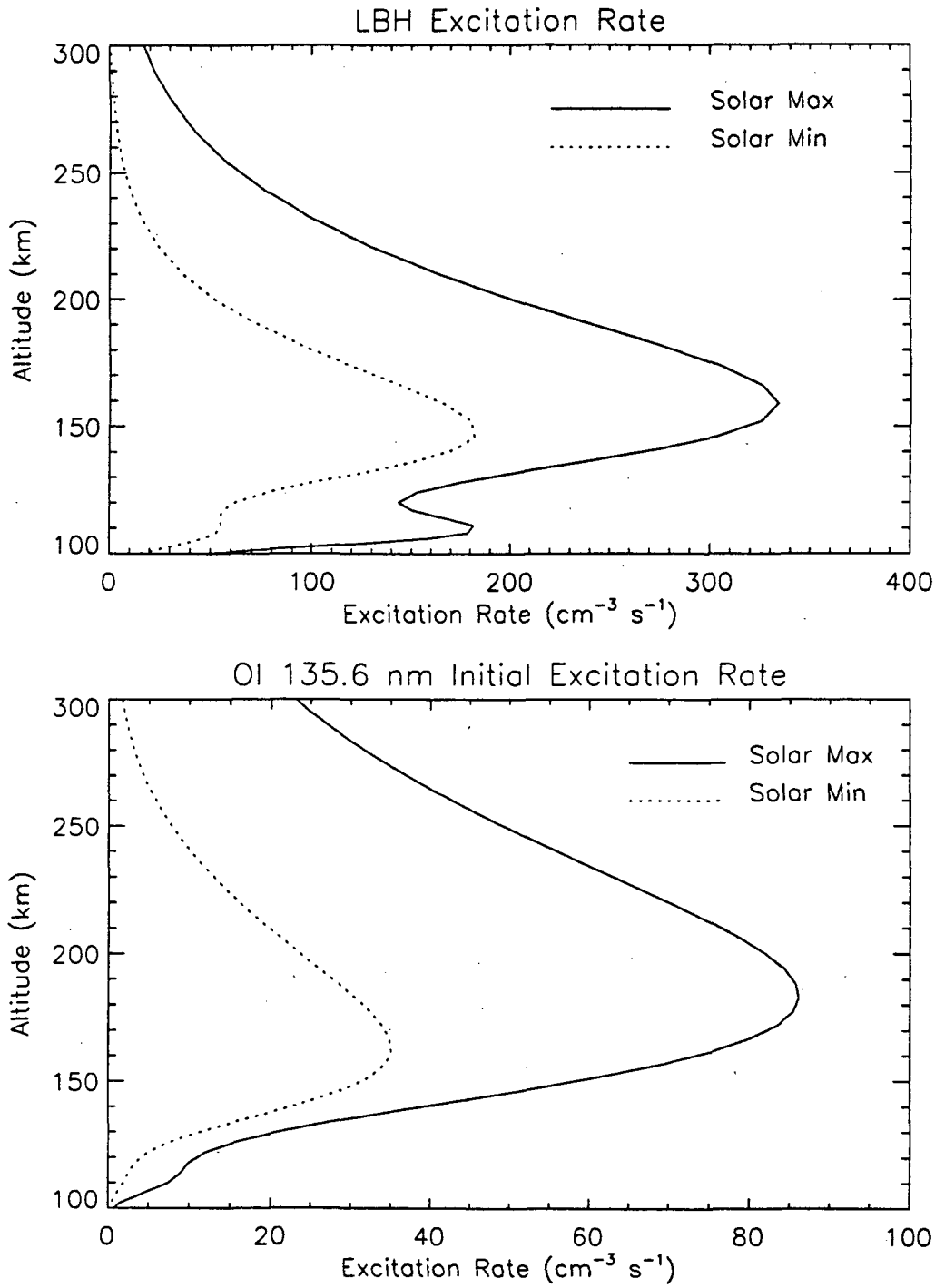


Figure 3-4 Initial volume excitation rate for the LBH bands and the OI 135.6 nm emission calculated by the */glow* model for the conditions described in Table 3-1.

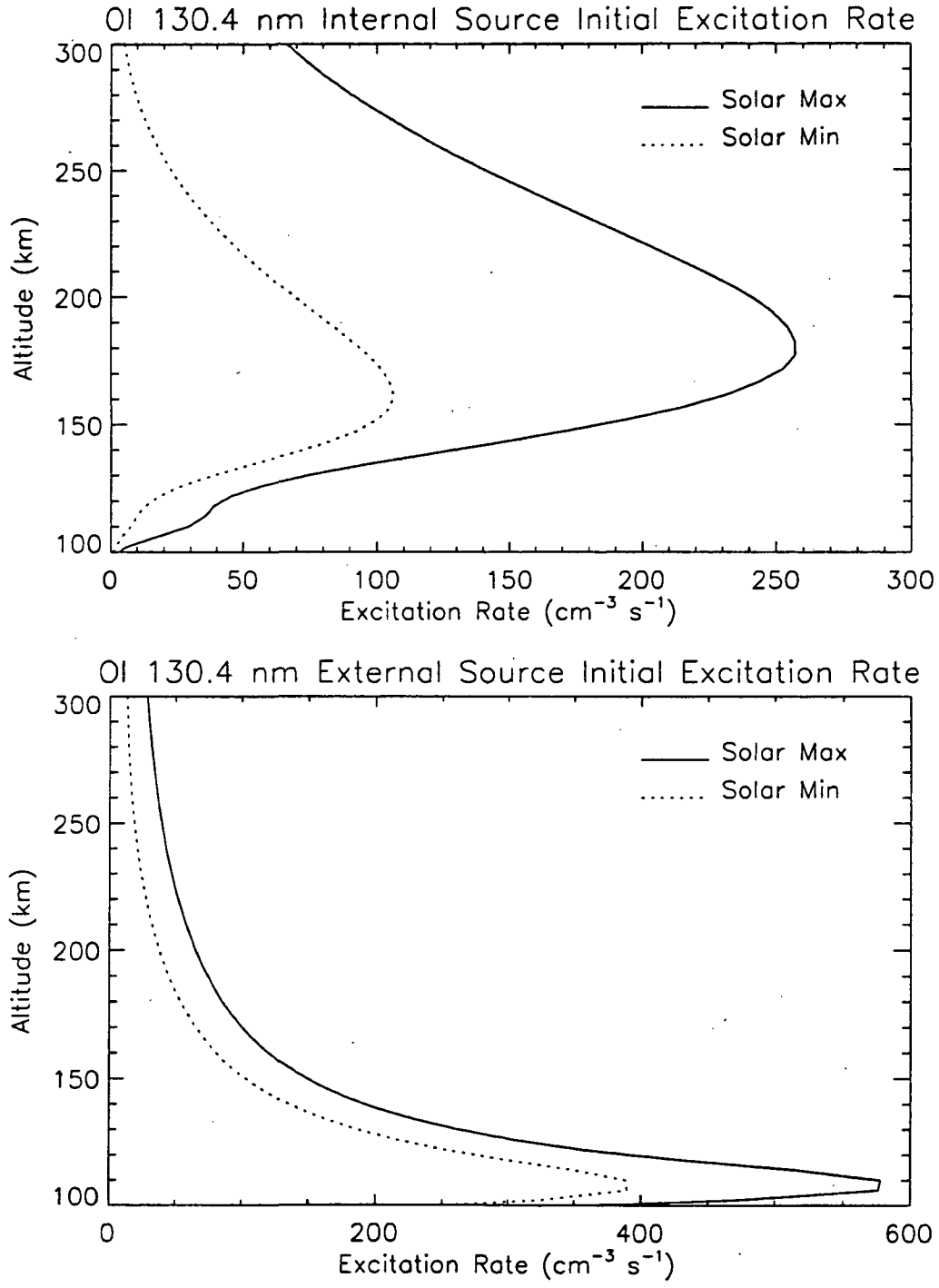


Figure 3-5 Initial excitation rate for the OI 130.4 nm emission calculated by the */glow* model for the conditions described in Table 3-1.

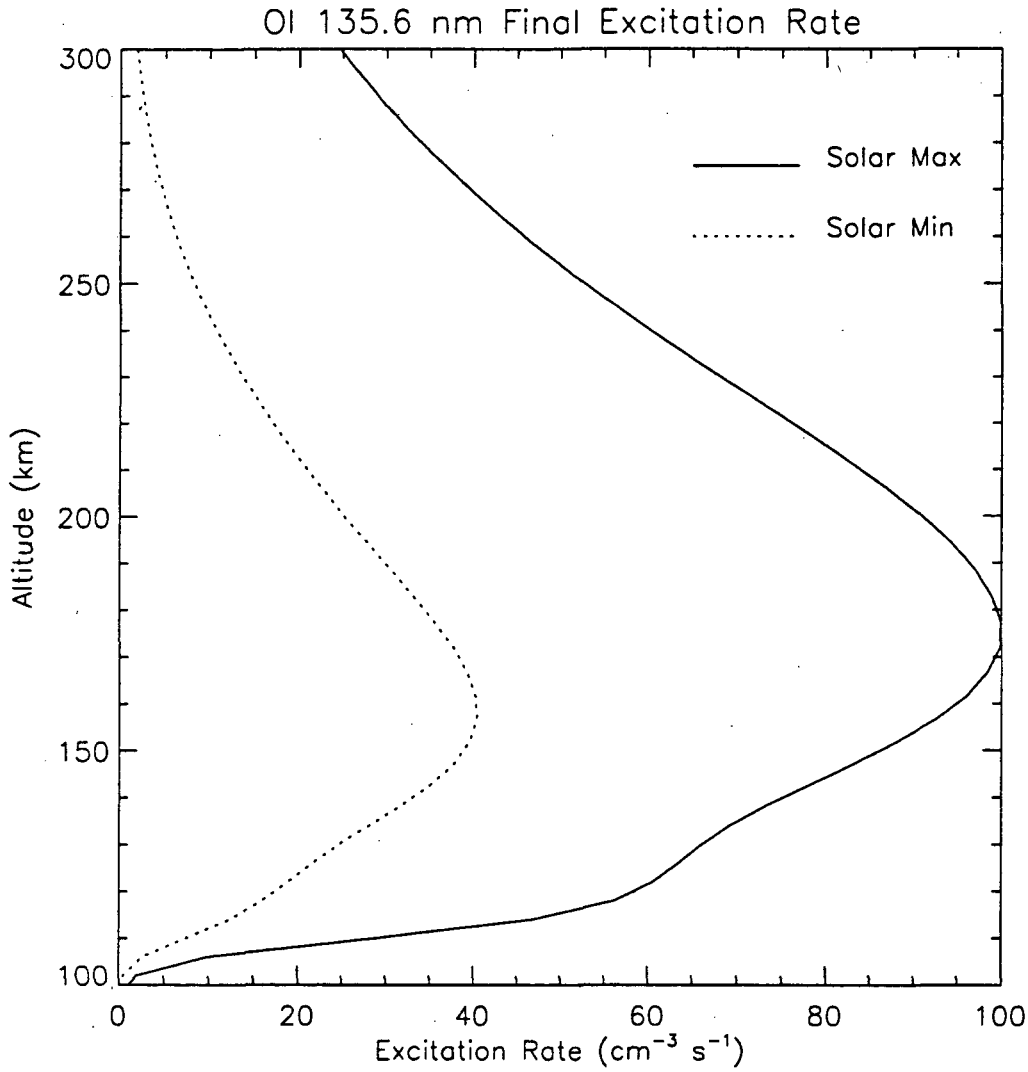


Figure 3-6 Final excitation rate for the OI 135.6 nm emission calculated by the Feautrier radiative transfer model for the conditions described in Table 3-1. The initial excitation rate calculated by the */glow* model is shown in Figure 3-3.

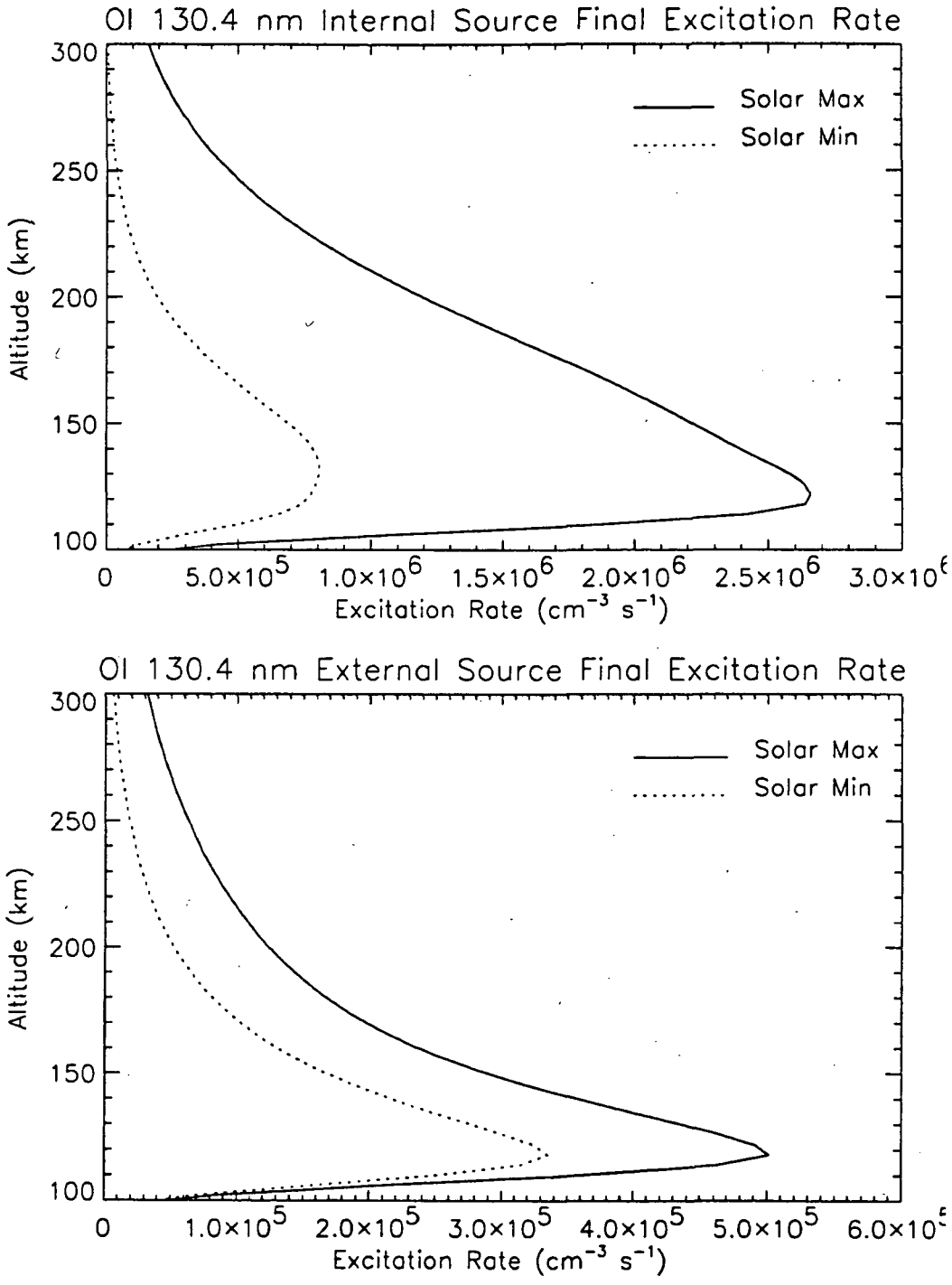


Figure 3-7 Final excitation rate for the OI 130.4 nm emission calculated by the Feautrier radiative transfer model for the conditions described in Table 3-1. The initial excitation rate calculated by the */glow* model is shown in Figure 3-4.

Figures 3-8 through 3-10 show limb brightness calculations for the LBH and the OI 135.6 and 130.4 nm emissions. The latter are calculated by the integral of Equation 3-20, the former is calculated by 3-14.

### 3.3.3 Cross Section for Pure Absorption by $O_2$

In the wavelength range 125 to 175 nm, $O_2$ absorbs in what is known as the Schumann-Runge continuum. This absorption arises from the $B^3\Sigma_u^-$ - $X^3\Sigma_g^-$ transition. The $B^3\Sigma_u^-$ state is above the dissociation limit of $O_2$, thus the absorption leads to dissociation. For cross section measurements made at room temperature, the absorption is typically due to transitions from the lowest vibrational level of the ground state. At thermospheric temperatures (~1000K), the higher vibrational levels are more significantly populated, leading to a temperature dependence of the cross section. The temperature dependence at wavelengths from 140 to 175 nm has been examined by Lean and Blake (1981) and Gibson *et al.* (1983). At 140 nm Gibson *et al.* found only an approximately 1% change in cross section value from 295K to 575K, but the effect was enhanced at longer wavelengths. Wang *et al.* (1987) extended the work of Gibson *et al.* down to 130 nm. In the region from 130 to 140 nm their data showed significant structure in the temperature dependence.

The temperature dependence of the $O_2$ photoabsorption cross section is not included in this work. The cross section measurements of Wang *et al.* (1987) at room temperature are used. This cross section is plotted in Figure 3-11. Pure absorption by $O_2$ is considered for each emission studied in this work. In most cases the effect is negligible; however, the $N_2$ LBH (2,0) band at 138.3 nm is significantly absorbed.

## 3.4 Effect of Solar Irradiance Bins on Model Calculations

The width of the solar irradiance bins in wavelength must be chosen carefully. Since photoelectron production at each altitude begins with photoionization, the CPU time for the calculation is roughly proportional to the number of bins in the solar

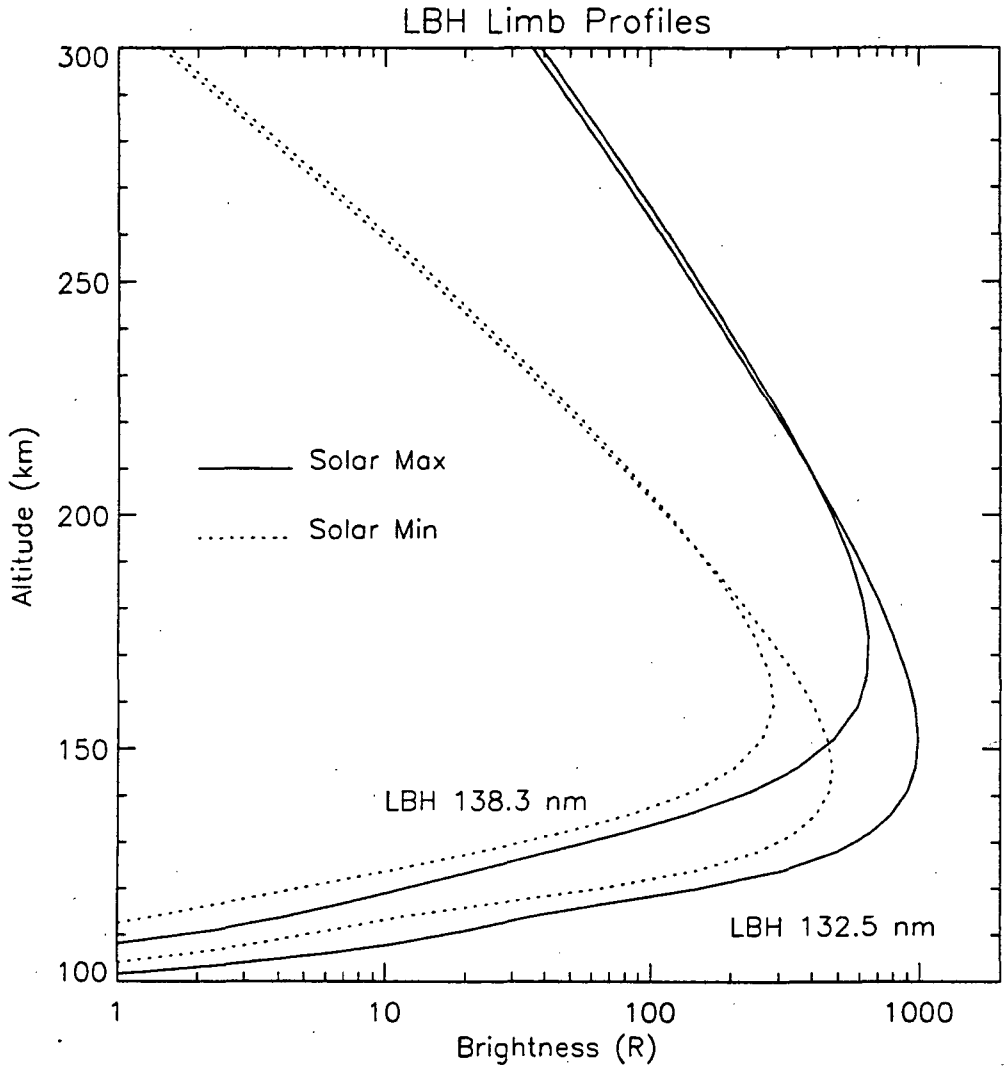


Figure 3-8 LBH limb brightness calculated by the optically thin radiative transfer model using initial excitation rates from */glow* (Figure 3-4). The geophysical conditions are listed in Table 3-1.

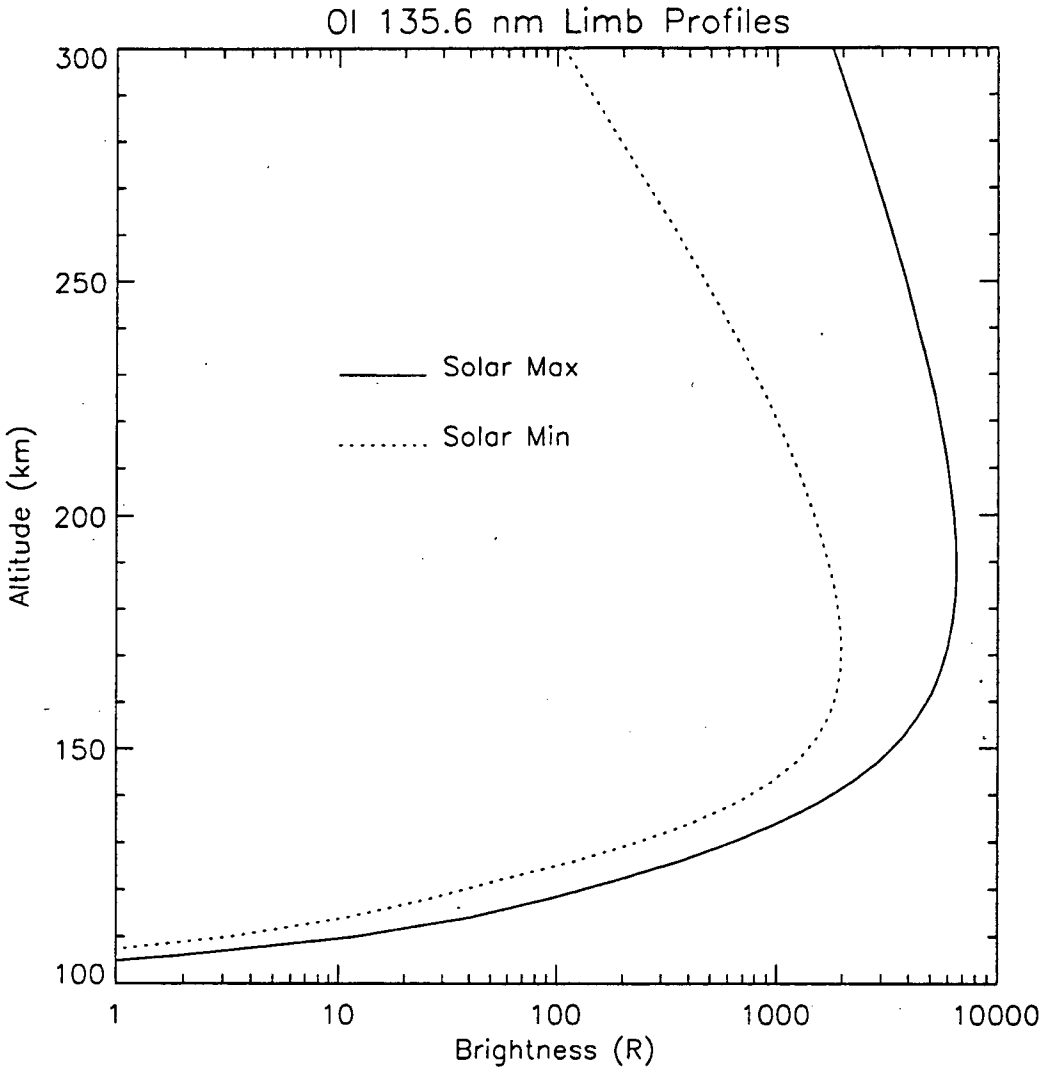


Figure 3-9 Limb brightness of the OI 135.6 nm emission calculated by the Feautrier radiative transfer model using initial excitation rates from */glow* (Figure 3-4). The geophysical conditions are listed in Table 3-1.

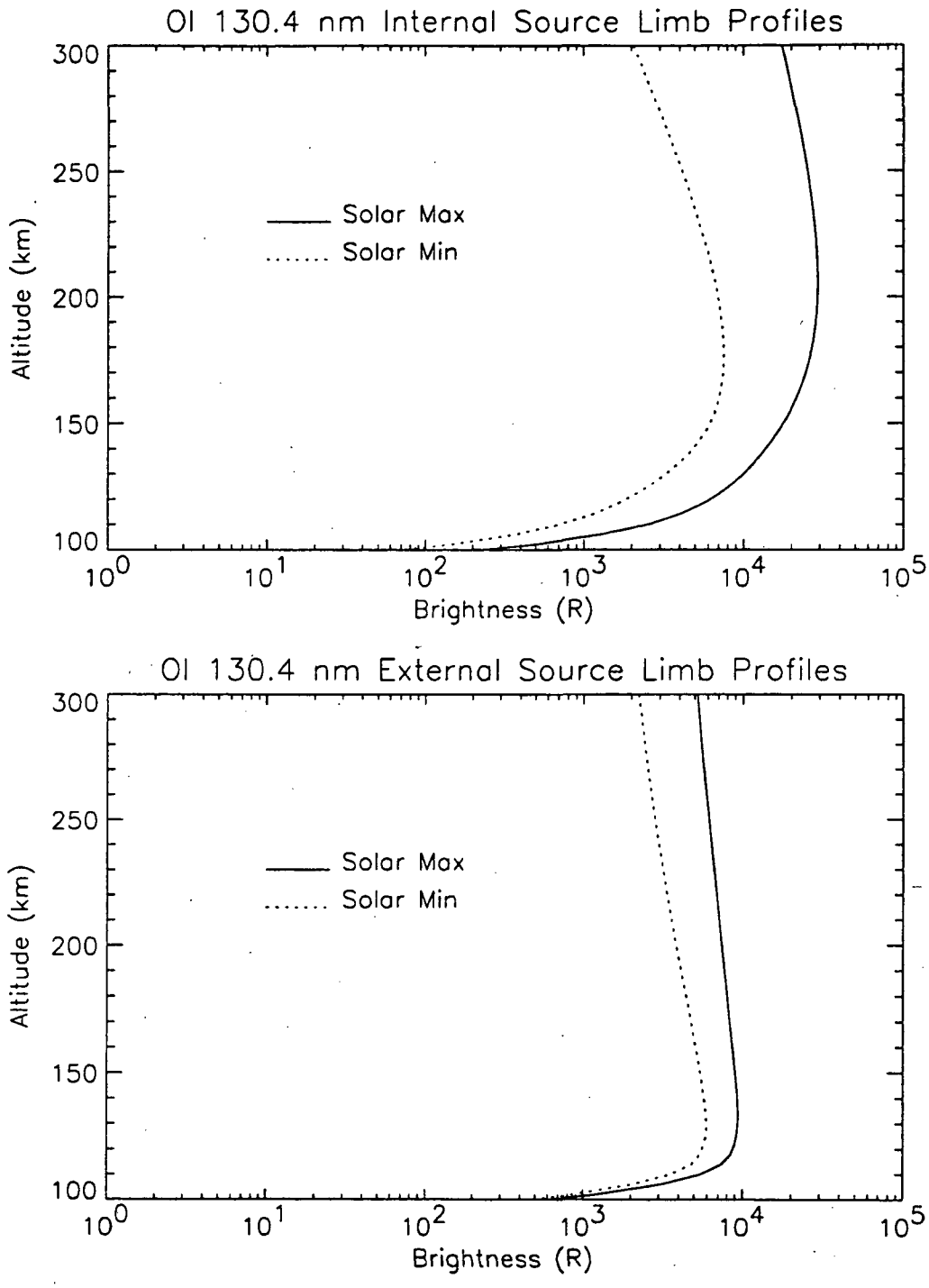


Figure 3-10 Limb brightnesses of the OI 130.4 nm emission calculated by the Feautrier radiative transfer model using initial excitation rates from */glow* (Figure 3-4). The geophysical conditions are listed in Table 3-1.

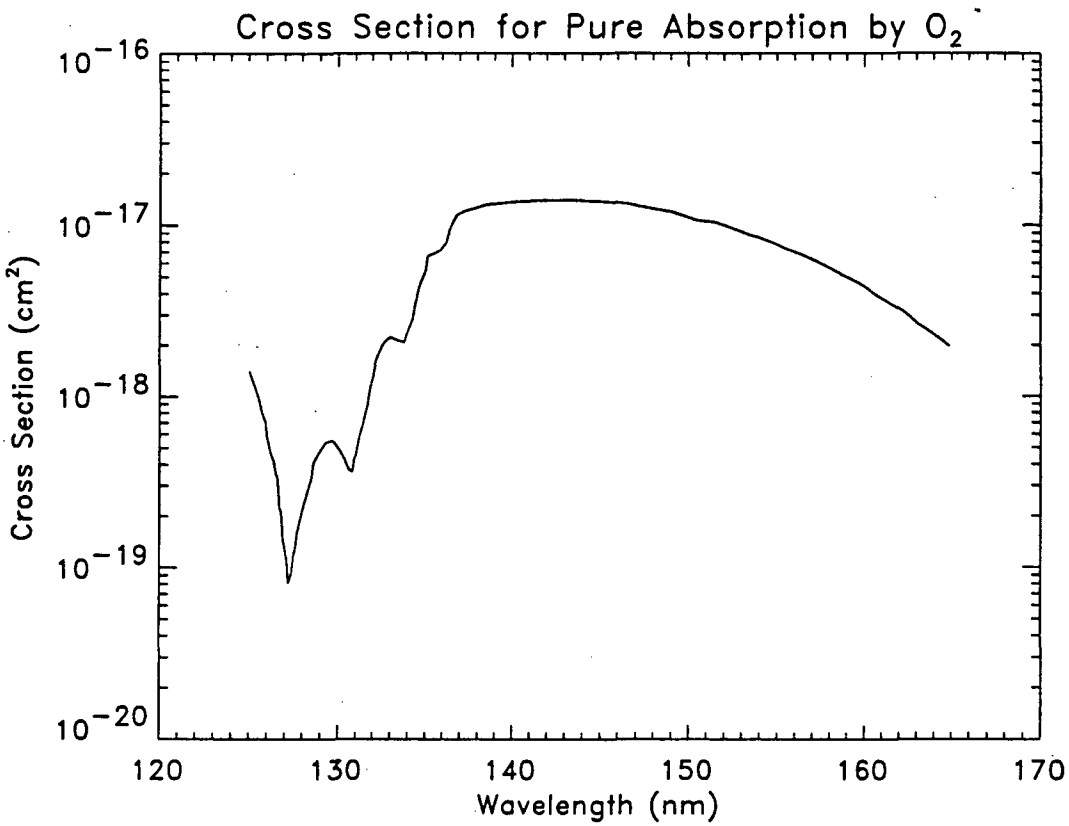


Figure 3-11 Cross section for pure absorption by $O_2$.

spectrum. The SC#21REFW (Hinteregger *et al.*, 1981; see also Section 1.1.1) spectrum contains approximately 1200 features, whereas the binned irradiance used by Torr *et al.* (1979) contained only 37 bins. Thus, roughly an order of magnitude of CPU time can be saved by binning the solar irradiance, however this binning affects the energy assigned to the photons and the cross section values because they must now be averaged over a bin. The effect must be quantified.

As shown in Chapter I, the nature of the solar spectrum is very complicated, with lines superimposed on continua. In the photoelectron calculation, the energy of the photoelectron is the difference between the energy of the ionizing photon and the energy required to photoionize. If the solar irradiance bins are too wide, and the solar flux varies widely over the bin, then the assumed average energy of photons may not accurately represent the energy of most of the photons. This can lead to errors in the photoelectron spectrum. Also, in a region where the absorption cross sections vary rapidly with wavelength, even the flux weighted cross sections can generate errors in the absorptive properties of the atmosphere. This has the effect of depositing energy into the wrong altitude.

The most common binning scheme is taken from the work of Torr *et al.* (1979). They binned the solar irradiance for several levels of solar activity and also tabulated flux weighted photoabsorption and photoionization cross sections for the bins. The scheme consisted of 5 nm bins from 5 nm to 105 nm and included separately many of the bright lines in the solar spectrum. The original */glow* model used this binning scheme with more bins added at shorter wavelengths.

For this work, the effect of binning is examined. The high resolution SC#21REFW reference spectrum is binned in two different ways. The first is the 5 nm bins plus lines (BPL) method of Torr *et al.* but with more lines used. The second method is 1 nm bins with no isolated lines. Model calculations (photoionization,

photoelectron impact dissociation, and photoelectron impact excitation) are performed using both of these schemes and with the complete SC#21REFW spectrum. The results of the three sets of calculations are then compared to determine the effect of binning the solar spectrum. Below 5 nm the same bins are used in both binning cases. These bins are approximately 1 nm, but the bin centers are chosen to best overlap regions where the cross sections change rapidly. For example, there are bin edges at the thresholds for Auger ionization of O, $O_2$, and $N_2$. The binned solar irradiance (SC#21REFW), cross sections, and branching ratios for both cases can be found in Appendix B.

For each wavelength bin, the cross sections are weighted according to the SC#21REFW solar reference spectrum to yield an effective cross section $\sigma_{eff}$ defined by:

$$\sigma_{eff} = \frac{\int_{\lambda_{min}}^{\lambda_{max}} I_{sun}(\lambda)\sigma(\lambda)d\lambda}{\int_{\lambda_{min}}^{\lambda_{max}} I_{sun}(\lambda)d\lambda}. \qquad 3\text{-}21$$

In Equation 3-21, $\lambda_{min}$ and $\lambda_{max}$ are the wavelength bin boundaries, $I_{sun}$ is the SC#21REFW irradiance, and $\sigma(\lambda)$ represents the high resolution cross section data.

Figures 3-12 through 3-14 show the results of this comparison. In each of the figures the solid line assumes the high resolution SC#21REFW solar spectrum, which is taken as the true representation. Figures 3-12 and 3-13 show similar results for electron impact excitation, dissociation, and photoionization of $N_2$. The 1 nm bins agree very well with the high resolution binning but the BPL tend to underestimate production; the discrepancy is on the order of 10%. This is a result of the continuum bins being too large over regions where both the cross sections and the solar irradiances are changing rapidly, which this is especially true below 31 nm. The smaller 1 nm bins fit better than the 5 nm bins even with the important lines treated separately.

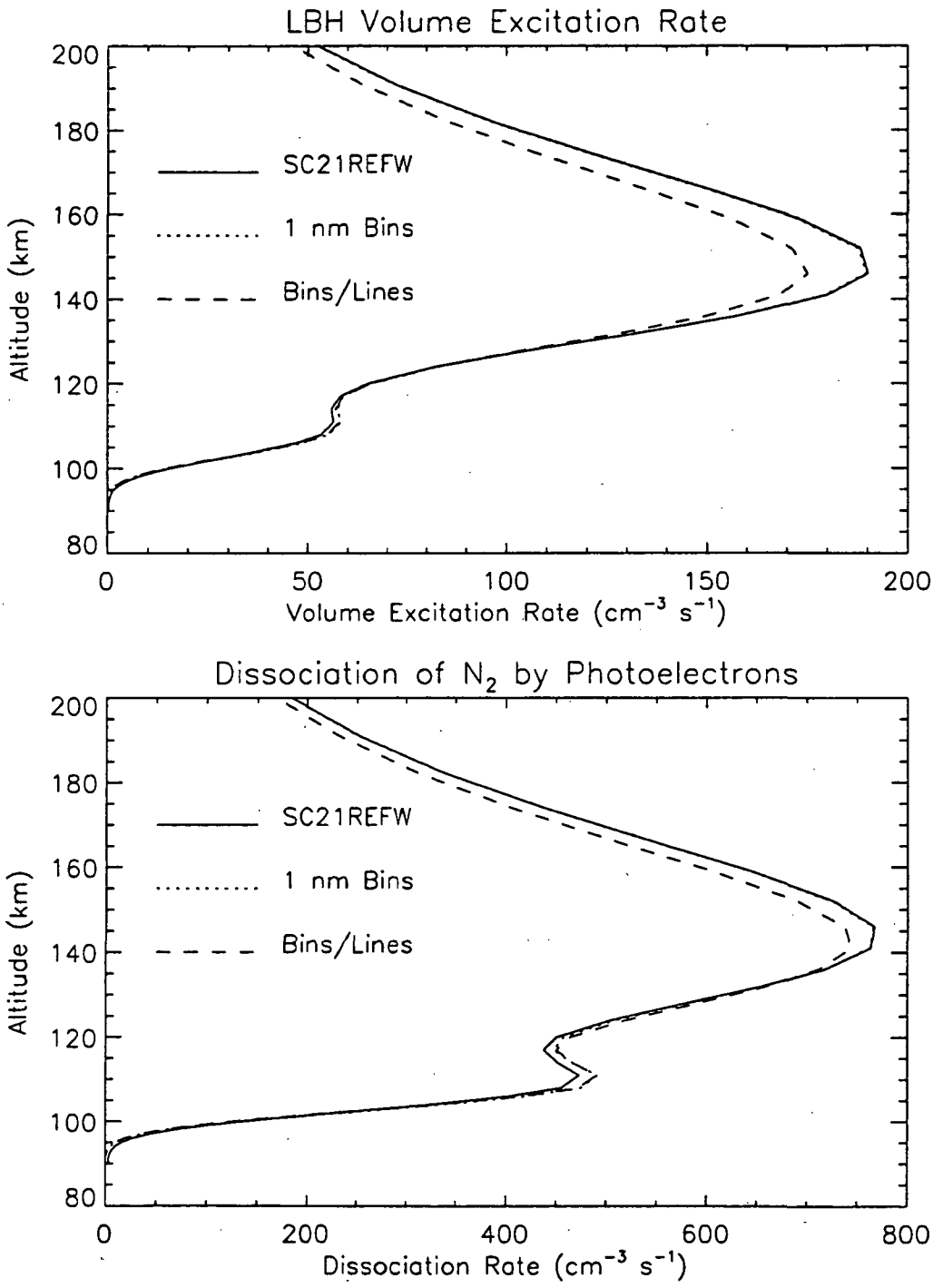


Figure 3-12 The */glow* calculations of LBH volume excitation rate and $N_2$ photoelectron dissociation rate using various solar irradiance binning schemes described in the text.

C-2

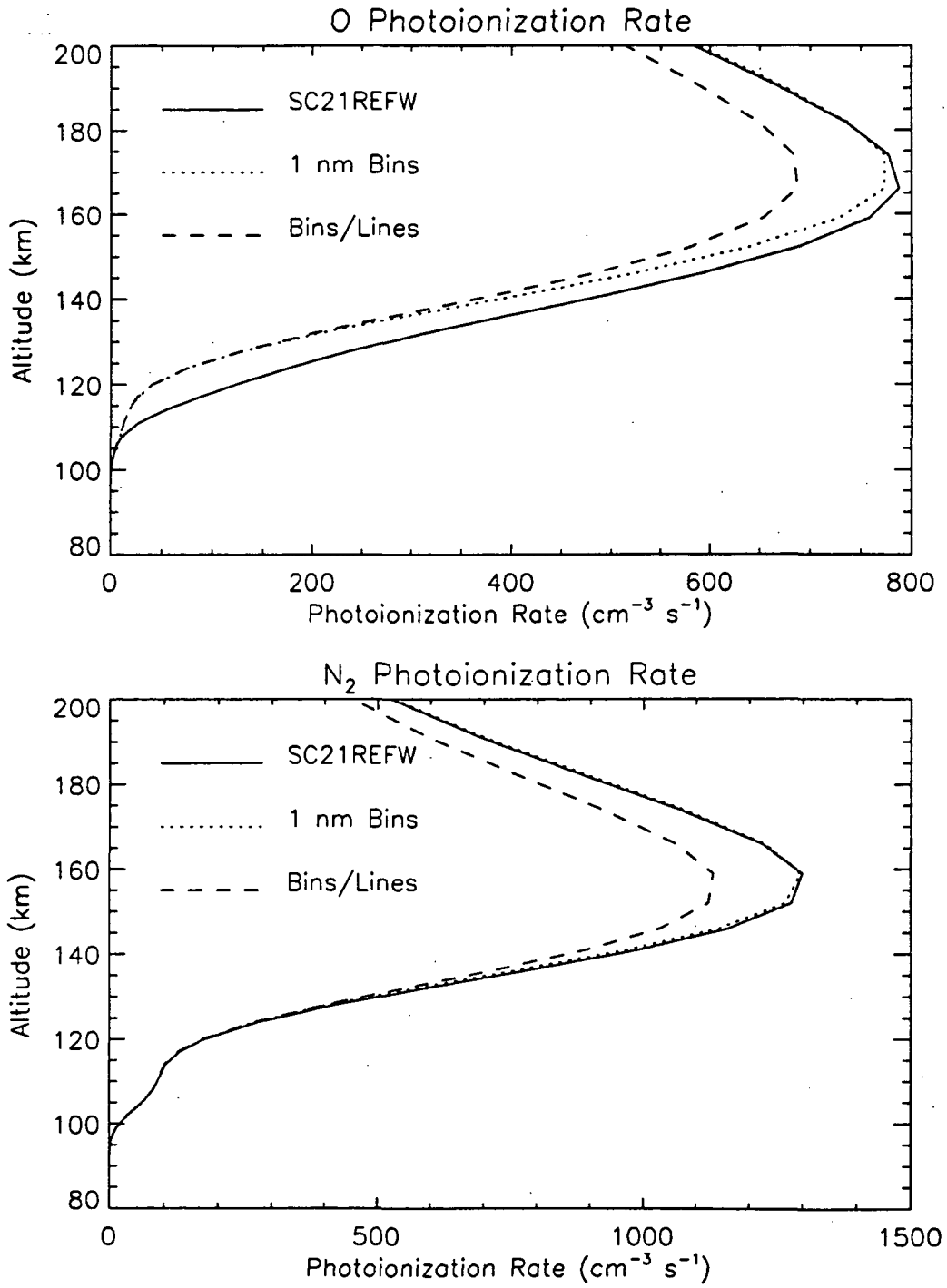


Figure 3-13 The */glow* calculations of O and $N_2$ photoionization using various solar irradiance binning schemes described in the text.

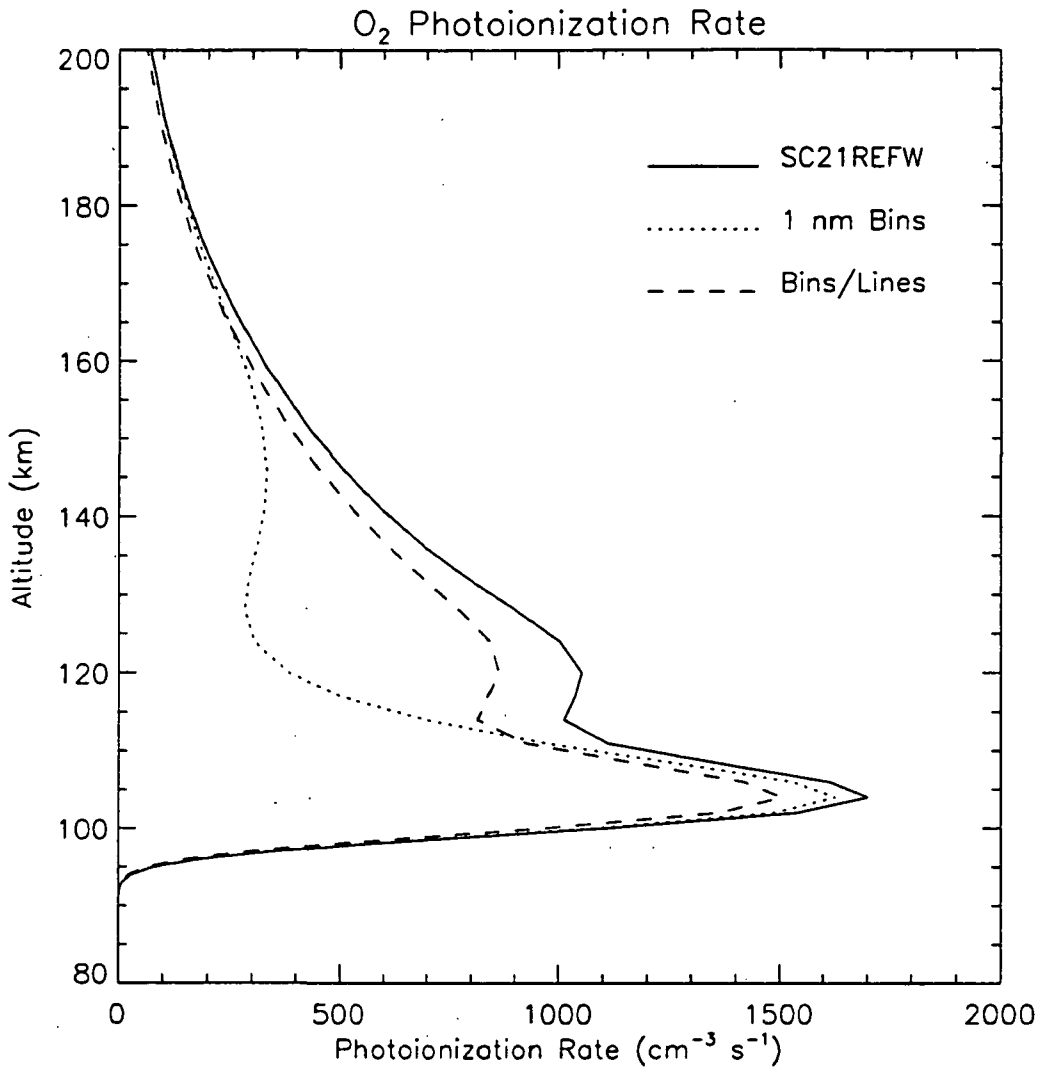


Figure 3-14 The */glow* calculations of $O_2$ photoionization using various solar irradiance binning schemes described in the text.

The more striking results of this comparison are photoionization of O and $O_2$ shown in Figure 3-14. For photoionization of $O_2$, neither binning scheme does a good job of reproducing the high resolution results. The comparison with the 1 nm bins is especially poor. The reason has to do with $N_2$ absorption at long wavelengths. The bright solar feature of CIII at 97.701 nm has an $N_2$ absorption cross section of 22 x $10^{-18}$ $cm^2$ (Fennelly and Torr, 1992) and a solar minimum irradiance of 6 x $10^9$ photons $cm^{-2}$ $s^{-1}$ (Hinteregger *et al.*, 1981). The weaker solar feature of HI at 97.254 nm has a much larger cross section of 117 x $10^{-18}$ $cm^2$ (Fennelly and Torr, 1992), which is two orders of magnitude larger that that for CIII, and a solar irradiance of only 0.8 x $10^9$ photons $cm^{-2}$ $s^{-1}$ (Hinteregger *et al.*, 1981), which is one order of magnitude smaller than that for CIII. After flux weighting into a 1 nm bin, the effective cross section becomes 16 x $10^{-18}$ $cm^2$, which is a factor of 10 too large for the bright CIII feature. In the model then, for the 1 nm bin case, $N_2$ absorbs the CIII photons high in the atmosphere before they can reach the lower altitudes where there $O_2$ densities increase. Since CIII accounts for much of the $O_2$ photoionization, the 1 nm binning leads to a large underestimate in $O_2^+$ production.

The result is that 1 nm bins work well for photoelectron processes but leads to errors in photoionization calculations, and the BPL scheme leads to an underestimate of photoelectron processes as well as photoionization. While neither binning scheme is entirely satisfactory, this work is primarily concerned with photoelectron processes and so the 1 nm bins are used for the remainder of this dissertation.

## 3.5 Summary

The purpose of this chapter was to describe the models used in photoelectron and airglow calculations. The details of the */glow* photoelectron model were described; this model follows a two stream formalism and includes electron transport. A large body of cross section data is required and this data is described both in this chapter and

Appendices A and B. The Feautrier solution to the radiative transfer equation, as developed by Gladstone (1982, 1988), was described. This calculation is used for the OI emissions which are optically thick to resonant scattering in the Earth's atmosphere. The effects of binning solar irradiance on model calculations were studied. It was shown that binning mechanisms can produce large errors in photoionization calculations. For this work, 1 nm bins throughout the soft x-ray and EUV are used.

# Chapter IV

## Sounding Rocket Instrumentation and Calibration

### 4.1 Introduction

In order to study the effects of solar radiation on the Earth's atmosphere, the best approach is to make simultaneous solar and terrestrial measurements. This approach is the goal of the experiments described in this work. An identical rocket payload was flown three times. The payload contains instrumentation for measuring both solar irradiance and terrestrial airglow. The simultaneous measurements allowed for a study of the response of the airglow to solar variability.

### 4.2 CODACON Array Detectors

The detector used for several of the rocket instruments is the photon-counting CODACON array detector which was developed by Dr. George Lawrence at the University of Colorado (McClintock *et al.* 1982). Both one-dimensional and two-dimensional versions of the CODACON detector have flown numerous times on previous sounding rocket payloads. These detectors consist of a microchannel plate (MCP) and a multi-anode "code plate". When a photon releases an electron from the photocathode on top of the MCP, the MCP amplifies the electron with a gain of approximately $10^6$. The resulting packets of electrons impinge on the anodes which are coded to have $n$ bits, where $2^n$ equals the total number of anodes along one axis. The $n$ bits form an address of the location of the electron event. The signal from each anode is activated by the capacitance between one large anode and a coded anode array, requiring only two charge amplifiers per bit. Thus, only 20 charge amplifiers are required for a 1 x 1024 CODACON detector, and 32 amplifiers are needed for a 256 x 256 CODACON. The coded anode data are either accumulated by a memory logic

PRECEDING PAGE BLANK NOT FILMED
PAGE 108 INTENTIONALLY BLANK

board for making a spectrum, or stored in FIFO (first in first out) electronics for buffering single photon events.

### 4.3 The Solar EUV Irradiance and Terrestrial Airglow Experiment

The Solar EUV Irradiance and Terrestrial Airglow Experiment (PI: Dr. T. N. Woods) is a sounding rocket experiment designed to measure the solar extreme ultraviolet (EUV: below 120 nm) irradiance simultaneously with the terrestrial far ultraviolet (FUV: 120 - 200 nm) airglow. Solar irradiance is measured from x-ray through EUV wavelengths at varying resolution with photometric and spectrometric instrumentation. An FUV spectrograph is used to measure the terrestrial airglow. The simultaneous measurements can then be used to study quantitatively the relationship between solar irradiance and the Earth's airglow.

Figure 4-1 shows a layout of the rocket payload. At the aft end of the payload is an evacuated section containing the solar pointing instruments. For the first two flights of the payload, one half of this section was occupied by an experiment developed by Boston University (PI: Supriya Chakrabarti, formerly at the University of California at Berkeley). The section is evacuated to ensure low pressure when applying high voltages to the windowless detectors on the instruments. Evacuation also helps to keep the payload free of contaminants which may condense on optics and lead to instrument degradation when exposed to EUV radiation. Forward of the solar section is the airglow section of the rocket. This section contains the airglow spectrograph and a TV camera. The TV camera is co-aligned with the airglow spectrograph to view the horizon; the TV signal is telemetered to the ground and used for real time attitude verification. Both the TV camera and the airglow spectrograph view through a deployable door in the skin of the rocket. As the solar instruments point at the sun, the rocket is rolled so that the airglow spectrograph views the limb of the Earth. The final section of the experiment contains the power and relay control electronics. Beyond the

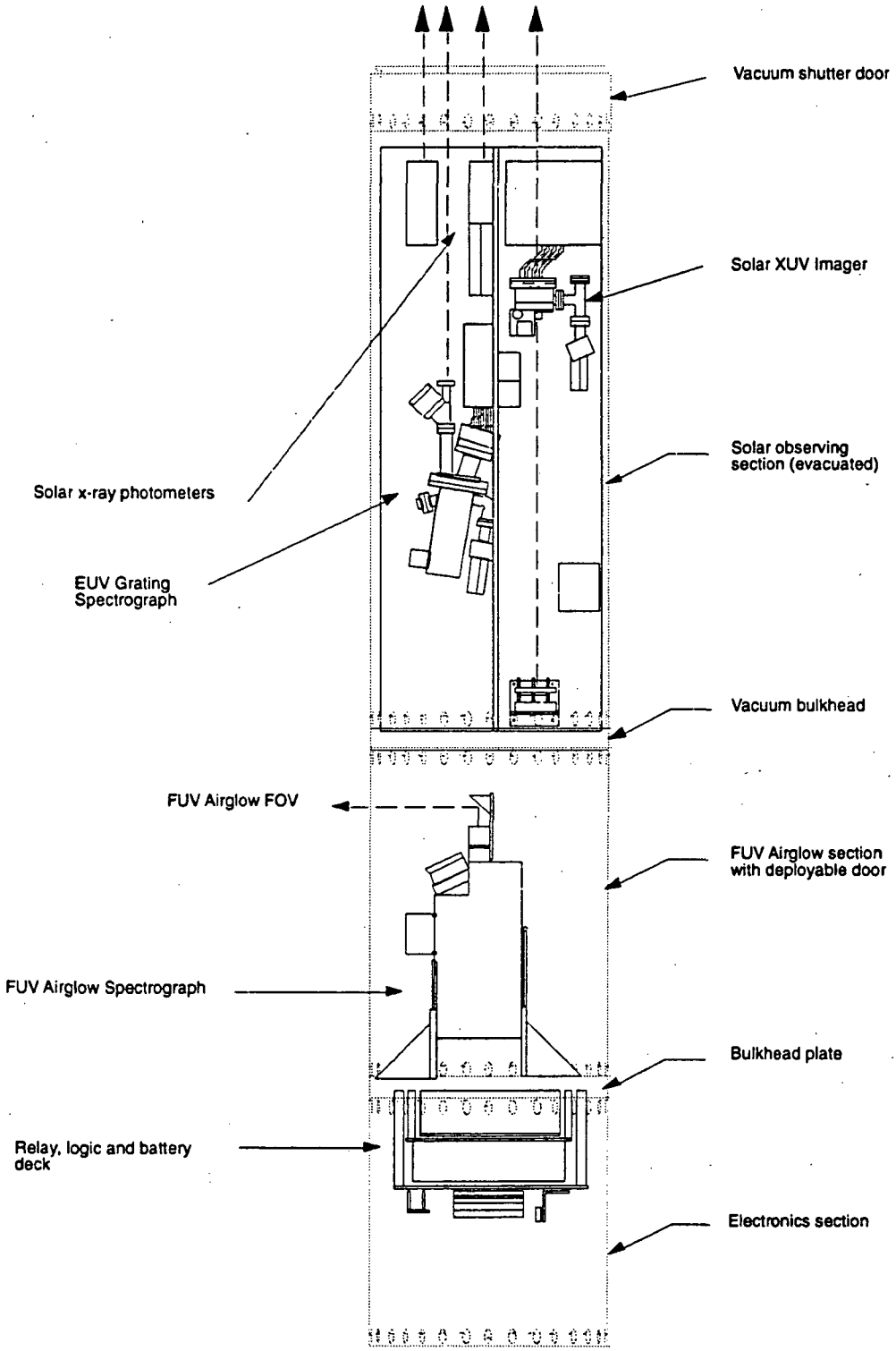


Figure 4-1 Layout of the Solar EUV Irradiance and Terrestrial Airglow Experiment. The arrows point in the aft direction during launch and toward the sun for an observing period of approximately 5 minutes during flight.

experiment sections are the NASA sections for telemetry, Attitude Control System (ACS), S-19 guidance, and recovery subsystems. The ACS is provided by the Lockheed Corporation. The SPARCS ACS provides solar pointing to within several arc seconds and roll control to 5° accuracy.

This payload has been flown three times. The data from each of these flights are analyzed in this work. The flights are referred to by their NASA identification numbers, 36.098, 36.107, and 36.124. The number 36 refers to the vehicle used, which is a Terrier Black Brant. The number after the decimal identifies the selection number of the vehicle. For example, 36.098 was the 98th selection of a Terrier Black Brant for flight. Chapter V will discuss the geophysical conditions for each of these flights. The dates of the flights were: October 27, 1992; October 4, 1993; and November 3, 1994. In the following sections the instrumentation is described.

### 4.3.1 EUV Grating Spectrograph (EGS)

The EUV Grating Spectrograph (EGS) consists of a 1/4 m EUV spectrograph used for obtaining full-disk solar irradiance. The optical layout of the instrument is shown in Figure 4-2. The 1/4 m spectrograph is a normal-incidence Rowland circle spectrograph with a windowless 1 x 1024 CODACON detector. The entrance slit is 9.14 μm wide by 0.995 mm long. The instrument has a spectral coverage of 25 to 120 nm with a 0.1 nm bandpass per anode on the detector, and an overall spectral resolution of about 0.3 nm. The concave diffraction grating is a tripartite (three ruling panels) grating with a ruling density of 1028 lines/mm. The grating is gold coated for increased reflectivity in the EUV. The instrument is equipped with a 2 liter/s Vac Ion Pump (VIP) to maintain evacuation to less than $1 \times 10^{-7}$ Torr. A complete solar spectrum scan is possible in less than 1 second due to the use of the array detector; therefore, atmospheric absorption information at all wavelengths is available on ≈1 km intervals. This spectrograph has twice been flown previous to the flights described in this work,

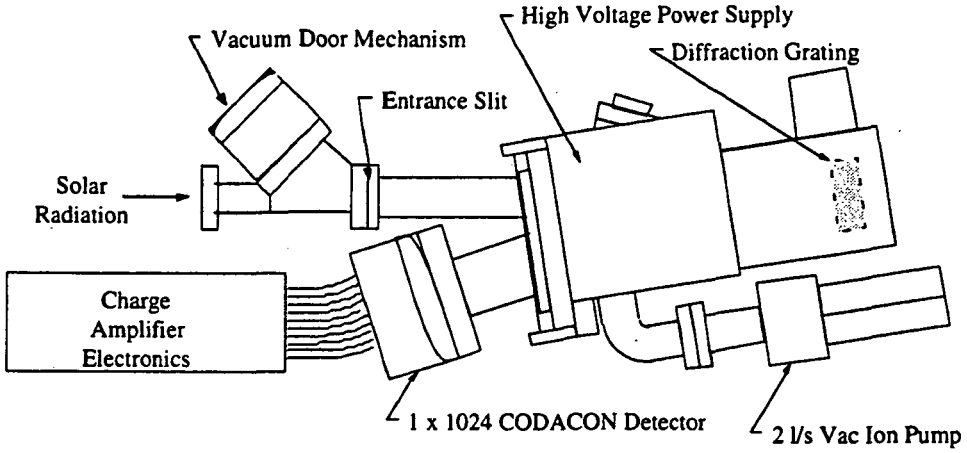


Figure 4-2 Optical layout of the EUV Grating Spectrograph (EGS). The EGS is a Rowland circle grating spectrograph with a 1 x 1024 CODACON array detector.

once in 1988 and once in 1989. Some of those results are described in detail by Woods and Rottman (1990). For the flights described here, no modifications were made to the optical system. For flight 36.098, a wire mesh was placed in front of the detector. The mesh had ~50% transmission and was used to lower the number of photons impinging on the CODACON and to prevent saturation of the microchannel plate pores at the brightest solar emission features. Typically, saturation occurs at ~5 counts per second per pore. No scattered light or other side effects were caused by the mesh. For the later flights which took place at lower solar activity, this mesh was removed. After the first flight a baffle was replaced inside the spectrograph. This baffle was used to prevent the bright solar Lyman $\alpha$ line at 121.6 nm from scattering inside the spectrograph and reaching the detector. Calibrations were performed before each rocket flight to assure consistency between the measurements.

### 4.3.2 Calibration of the EGS Using a Synchrotron Light Source

A technique is now presented for calibrating instrument sensitivity at different diffraction orders using the Synchrotron Ultraviolet Radiation Facility (SURF) at the National Institute for Standards and Technology (NIST). The application of this technique to the EGS has been described by Woods and Rottman (1990) and Bailey and Woods (1993). The SURF facilities are described by Furst and Graves (1993). Because the intensity of the SURF synchrotron radiation is known to an accuracy of better than 2% ($\lambda$>10 nm, Furst and Graves, 1993), the SURF has proven to be an ideal source for the calibration of the EGS. Measurements made on Beamline 2 of SURF provide data for wavelength, sensitivity, scattered light, and linearity calibrations. These procedures are discussed for the EGS spectrograph, which has been calibrated several times at SURF. Calibration of multiple diffraction orders is achieved by taking data with several different electron beam energies. Each SURF electron beam energy provides a unique synchrotron reference spectrum which is needed to distinguish between photons from different diffraction orders. A careful analysis of the

instrument's scattered light properties, also crucial to this linear regression problem, is discussed.

Because the SURF beam is highly polarized, the instrument must be calibrated at two different orientations 90° apart to average any instrumental polarization response. Measurements are made at nine positions over a field of view of 1° x 1°. Although, the field of view of the instrument is 3° x 3°, only 1° x 1° is required for calibration because the SPARCS is capable of solar pointing to within 5 arc seconds.

A wavelength calibration at SURF is important because the grating may move during flight or transport. Although the SURF beam is a continuum, filters can be placed in the beam. If the transmission versus wavelength of these filters is well known they can be used for a wavelength calibration. Filters of Tin Germanium (SnGe) and Lithium Fluoride (LiF) are used for wavelength calibration. Figure 4-3 shows the transmission of the SnGe filter. The transmission of these filters falls off sharply at their short cut-off wavelengths which serve as reference wavelengths. Thus, by making SURF measurements with and without the filters in front of the EGS, the anode value of the cut off can be found. Using several different filters, the anode values for several wavelengths can be found. By assuming a linear relationship between anode location and wavelength, a function can be constructed which will give the wavelength for any anode value. The slope of this function is the bandpass per anode on the detector. The result is about 0.1 nm per anode. The solar spectrum contains many bright lines; because line positions are well known, they can be used to verify the wavelength to anode relationship. The purpose of the above procedure is to check for shifts in the wavelength scale due to transport or launch vibrations. During the three flights analyzed here, the wavelength scale has shifted less than one anode.

The quantum throughput of the instrument is obtained in multiple grating orders by observing synchrotron radiation at different energies. The different beam energies

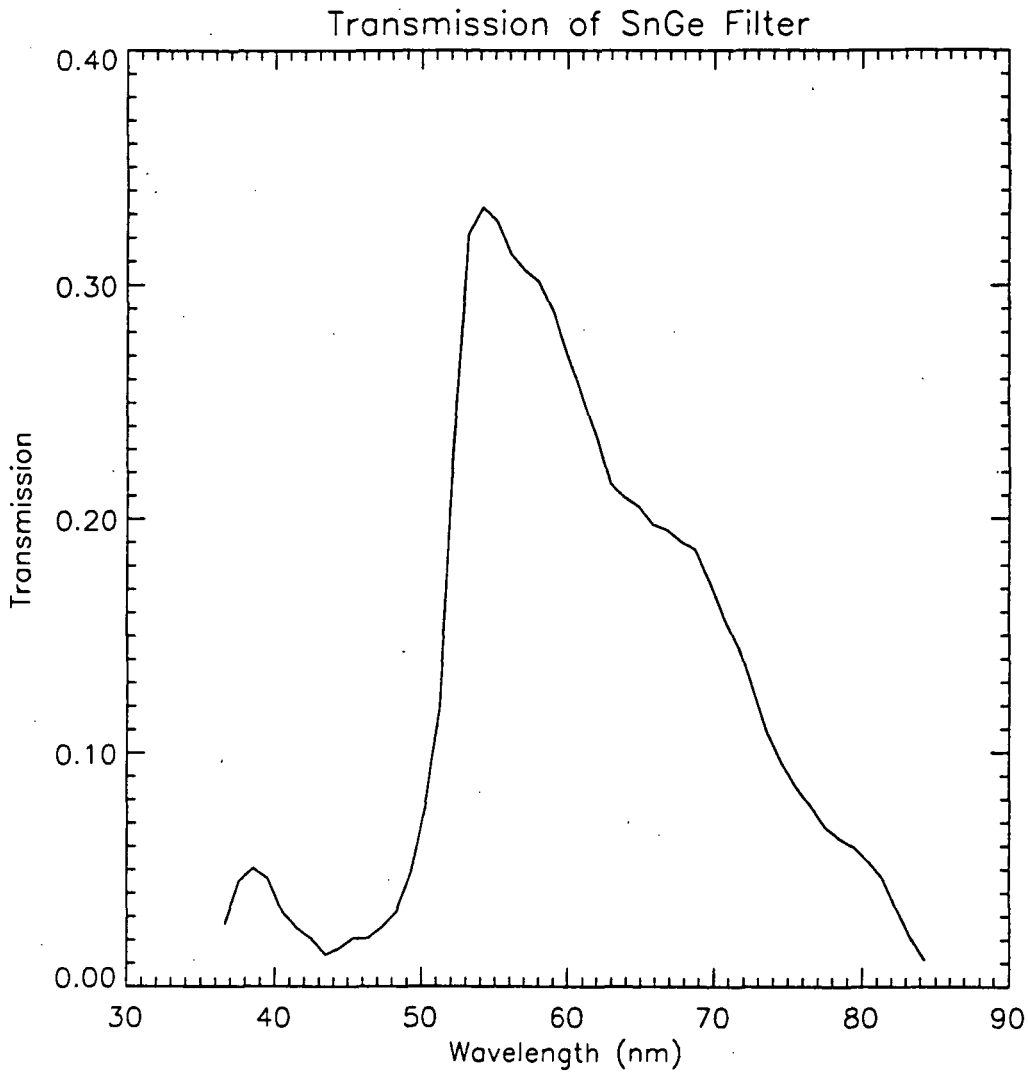


Figure 4-3 Transmission of SnGe foil filter. This filter is used to determine wavelength and second order grating contributions during the SURF calibration of the EGS.

provide different spectral shapes, as shown in Figure 4-4 for beam energies of 180 and 284 MeV (Furst and Graves, 1993). Assuming only two grating orders contribute, the quantum throughput can be calculated by:

$$\frac{C_e(\lambda)}{I_e A \Delta t \Delta\lambda} = F_e(\lambda) QT_1(\lambda) + \frac{1}{2} F_e(\frac{\lambda}{2}) QT_2(\frac{\lambda}{2}), \qquad 4\text{-}1$$

where the subscript $e$ denotes beam energy (180 or 284 MeV) and the subscripts 1 and 2 denote first and second order respectively. Measured counts are denoted by $C_e$, $I$ is the synchrotron beam current, $A$ is the area of the instrument's entrance slit, $\Delta t$ is the integration time, $\Delta\lambda$ is the spectral bandpass in first order, $F_e$ is the SURF flux, and $QT$ is the quantum throughput. The factor of 1/2 in the second term on the right hand side of Equation 4-1 accounts for the fact that $\Delta\lambda$ for second order is one half of that for first order. For two beam energies, there are then two equations for the two unknowns, $QT_1$ and $QT_2$. This matrix can be solved for the following result:

$$QT_1(\lambda) = \frac{\Gamma_{284} F_{180}(\frac{\lambda}{2}) - \Gamma_{180} F_{284}(\frac{\lambda}{2})}{F_{284}(\lambda) F_{180}(\frac{\lambda}{2}) - F_{180}(\lambda) F_{284}(\frac{\lambda}{2})}, \qquad 4\text{-}2a$$

$$QT_2(\lambda) = \frac{2\{\Gamma_{180} F_{284}(\frac{\lambda}{2}) - \Gamma_{284} F_{180}(\frac{\lambda}{2})\}}{F_{284}(\lambda) F_{180}(\frac{\lambda}{2}) - F_{180}(\lambda) F_{284}(\frac{\lambda}{2})}, \qquad 4\text{-}2b$$

where,

$$\Gamma_e = \frac{C_e(\lambda)}{I_e A \Delta t \Delta\lambda}. \qquad 4\text{-}3$$

Note that for third or higher grating orders, this method could still be applied if data were taken at three or more beam energies. Past experience with three beam energies has shown that higher orders are negligible for the EGS (Woods and Rottman, 1990).

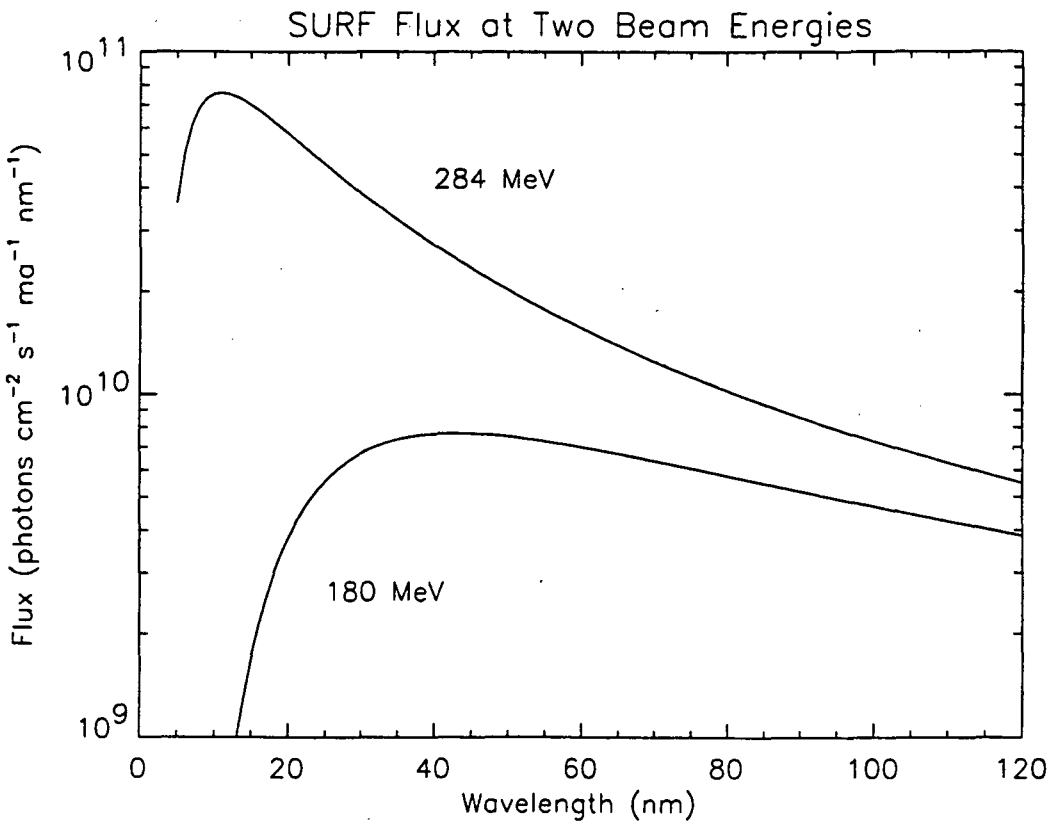


Figure 4-4 SURF fluxes for 180 and 284 MeV beam energies.

In practice, it is crucial that dark counts and scattered light be removed from the measured counts before the throughput is calculated. The scattered light correction can be inferred in the following manner. At wavelengths where second order is negligible (below 90 nm for this instrument), the quantum throughput can be found by:

$$QT = \frac{C_e(\lambda) - d - SL}{F_e(\lambda) I_e \Delta t \Delta\lambda}, \qquad 4\text{-}4$$

where $d$ denotes dark counts and $SL$ scattered light. The result must be the same for either beam energy. It is assumed that the scattered light component, $SL$, is the product of the total of the measured counts and a function $g(\lambda)$,

$$SL = Total(C_e) g(\lambda). \qquad 4\text{-}5$$

Using 4-4, the $QT$ calculated from two different beam energies can be equated to solve for $g(\lambda)$:

$$g(\lambda) = \left[\frac{C_{284}}{F_{284}} - \frac{C_{180}}{F_{180}}\right] \frac{1}{\frac{Total(C_{284})}{F_{284}} - \frac{Total(C_{180})}{F_{180}}}. \qquad 4\text{-}6$$

The calculated $g(\lambda)$ is valid only where second order is negligible. At this point in the calculations, the scattered light is assumed to be a Lorentzian function of wavelength. A fit is then performed to find the parameters of the Lorentzian. Once g(λ) is known, the scattered light can be accounted for.

Although the above procedure has been used successfully in the past, a newer procedure has been developed which is used in the present calibrations. This procedure is described in detail by Woods *et al.* (1994).

A final calibration performed at SURF is a measurement of the instrument's linearity. The SURF beam current can be varied to emit different magnitudes of flux. By varying the beam current over a large enough range, the response of the instrument can be observed into the region where count rates vary nonlinearly with illumination.

Such nonlinearity is primarily due to microchannel plate saturation, but can also be due to the dead time of the detector electronics at count rates of greater than 50,000 counts per second.

The average uncertainty in the sensitivity calibrations at SURF is about 6%, being better at wavelengths of increased sensitivity and poorer where the grating reflectivity is low. This uncertainty assumes a 1.3 % error in the calculated SURF fluxes and measured beam current (Furst and Graves, 1993) and a 2% uncertainty for averaging over the instrument's field of view. Photon counting statistics account for the remainder of the error.

The above description of the EGS calibration is the procedure followed for the first two rocket flights. In more recent calibrations, second order contributions have been derived in another way. By placing a SnGe filter of known transmission into the beam, there are no contributions to the signal from below the SnGe cut off wavelength (approximately 52 nm). Therefore, there can be no contributions from second order; this allows a calibration with only one SURF beam energy. Calibrations are made with and without the SnGe filter. By differencing the results, after accounting for the transmission of SnGe, the contribution from second order can be determined.

The result of the first order calibration for the 36.124 flight is shown in Figure 4-5. The scatter in the result is due to the flat field of the CODACON and is not a reflection of counting statistics or uncertainty. The sharp drop at short wavelengths is due to the rapidly decreasing reflectivity of the grating and due to vignetting of light by the zeroth order trap.

### 4.3.3 Solar X-ray Photometers (SXP)

The detectors for the Solar X-ray Photometers (SXPs) are silicon (Si) XUV photodiodes which are available commercially and discussed in detail by Korde and Geist (1987) and Korde *et al.* (1988). Their response at short wavelengths is near the

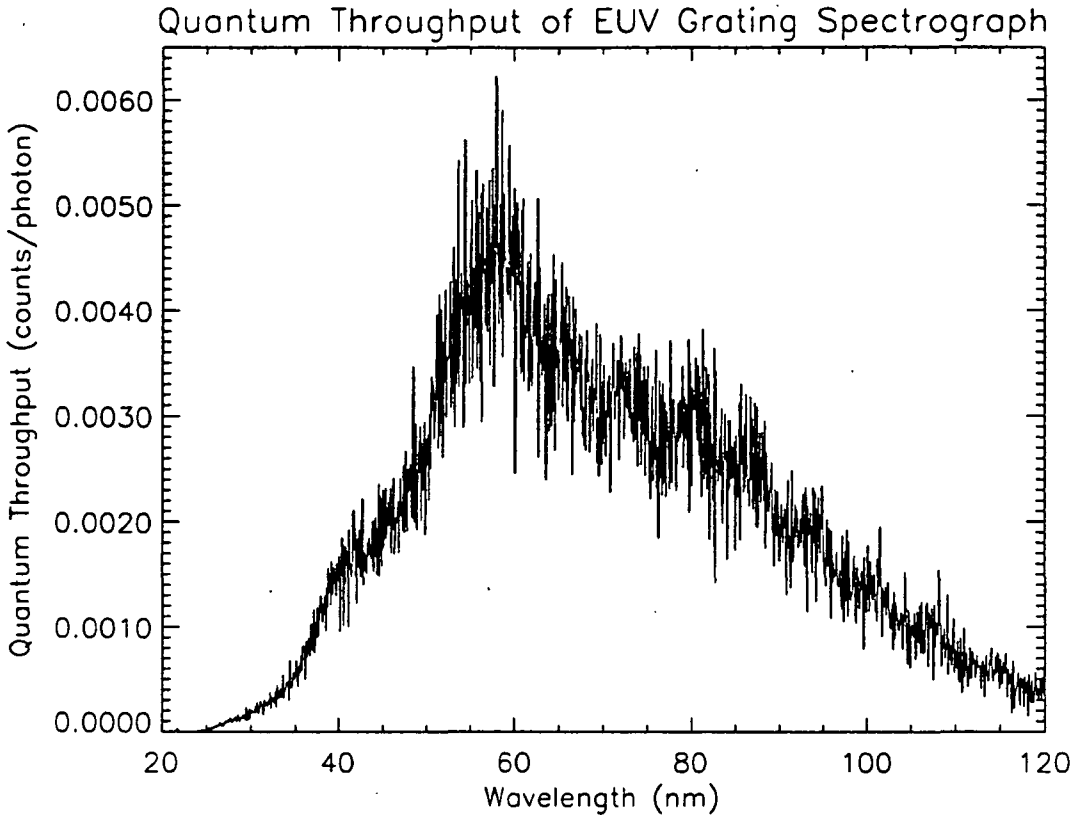


Figure 4-5 Quantum throughput of the EGS spectrograph. The scatter in the result is due to the flat field of the detector and is not due to counting statistics.

theoretical response for silicon. The sensitivity of a bare diode is about 1 electron per photon at 100 nm and increases proportionally at a rate of 1 electron per 3.63 eV of photon energy (Korde and Canfield, 1989). Thus, at 10 nm there are approximately 10 electrons per photon. The sensitivity has been shown to be highly stable for large levels of radiation (Canfield *et al.*, 1989). The National Institute of Standards and Technology has adopted these Si XUV photodiodes as a standard soft x-ray and EUV detectors. A solar photometer using an Si XUV photodiode has been flown previously and is described by Ogawa *et al.* (1990).

The photometer passband is determined from thin film filters deposited directly on the photodiode. The particular material and thickness in conjunction with the bare photodiode sensitivity, determine the wavelength region of sensitivity for each photometer. The use of several photometers with different filters yields the desired wavelength coverage. Table 4-1 lists the filter materials and thicknesses for each photodiode. A total of six photometers can be flown on the rocket payload; Table 4-1 lists only those photometers for which data are analyzed in this work. Oxide layers which grow on the metals are taken into account. Transmissions of the various metals used in this study are available for modeling (Henke *et al.* 1982, 1988; Powell *et al.*, 1990).

The electronics for the x-ray photometer are shown in Figure 4-6. The current from the photodiode is converted to a voltage through an operational amplifier circuit. A voltage to frequency converter then translates this voltage into a system of digital pulses such that the frequency is proportional to the original current. Outside the photometer electronics, in the telemetry section of the rocket, are pulse counters which count the pulse rate which is then telemetered to the ground. This method allows for a larger dynamic range as well as a much smaller susceptibility to random noise in the

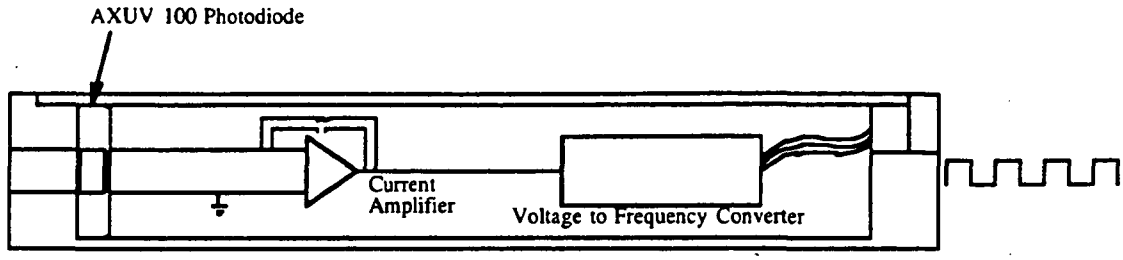


Figure 4-6 Schematic of the solar x-ray photometer electronics. Current from the photodiode is converted to a series of pulses such that the frequency of the pulses is proportional to the original current.

**Table 4-1 Photodiode Coatings used in Rocket Flights**

| Flight - ID Number | Coating | Thickness (Å) | Aperture Size ($cm^2$) |
|---|---|---|---|
| 36.107 - 3 | Ti | 5000 | 0.446 |
| | TiO | 5000 | |
| | $SiO_2$ | 50 | |
| 36.107 - 4 | Al | 1500 | 0.221 |
| | Sc | 500 | |
| | C | 450 | |
| | $SiO_2$ | 50 | |
| 36.107 - 6 | Al | 2000 | 0.198 |
| | C | 850 | |
| | $SiO_2$ | 100 | |
| 36.124 - 1 | Zr | 1900 | 0.178 |
| | Ti | 200 | |
| | C | 200 | |
| | TiO | 100 | |
| | $SiO_2$ | 50 | |
| 36.124 - 2 | No Coating | - | $1.135 \times 10^{-6}$ |
| 36.124 - 3 | Same as 36.107 | Same as 36.107 | Same as 36.107 |
| 36.124 - 4 | Same as 36.107 | Same as 36.107 | Same as 36.107 |
| 36.124 - 5 | Ti | 3100 | 0.178 |
| | TiO | 100 | |
| | $SiO_2$ | 50 | |
| 36.124 - 6 | Same as 36.107 | Same as 36.107 | Same as 36.107 |

measurements. The range of measurable currents for this electrometer system are 1 x $10^{-12}$ amperes to 2 x $10^{-8}$ amps, producing frequencies of 50 Hz to 1 MHz.

The major difficulty in these measurements is the rejection of intense visible light. There are nearly 10 orders of magnitude more photons in the visible than in the soft x-ray region of the solar spectrum; a bare silicon XUV photodiode has about the same sensitivity in the visible as it does in the soft x-ray region of the spectrum. The filters are designed to have sufficient soft x-ray transmission and to have the required level of rejection to visible light. However, deposition of a metal film over the entire area of a photodiode causes a short circuit between the anode and cathode of the photodiode. Therefore, the thin film is deposited on the active area and a mask is used to prevent visible radiation from reaching the uncoated regions. The mask complicates the fabrication process but this technique is still preferable to using thin foil filters. Foils are easily damaged and susceptible to pinholes and thus are not well suited for use in space. The mask dramatically reduces the visible light and makes solar soft x-ray measurements possible. For some photodiodes a visible background signal still exists at a lower level and is due to pinholes in the coating. These pinholes come from the deposition process, not from handling. In practice several photodiodes are coated and the best are chosen for flight. It is anticipated that improved deposition techniques will yield pinhole-free coatings.

While the dark current of the Si XUV photodiodes is usually negligible (less than $10^{-13}$ Amperes) compared to solar soft x-ray signals, the visible contribution to the background signal can be significant and must be measured in conjunction with the solar soft x-ray measurements. The background measurement is accomplished in flight by moving long pass Magnesium Fluoride ($MgF_2$) filters in front of the photometers for a short time near apogee. The $MgF_2$ passes UV and visible radiation but not soft x-ray or EUV. Therefore, these filters give the magnitude of background signal that is due to

visible radiation and any dark current. A correction must be made as the transmission of $MgF_2$ is slightly less than 100%. The transmissions of the filters are measured in the laboratory with a tungsten lamp and are typically about 96% at visible wavelengths.

### 4.3.4 Calibration of the Solar X-ray Photometers

Calibration of the photodiodes is performed primarily at SURF by Randy Canfield of NIST and the procedures are described in detail by Canfield (1989). Calibrations are performed from 5 to 50 nm. The only calibrations below 5 nm are done with a Fe-55 radioactive source. Thus, the region below 5 nm requires models of the photodiode sensitivity. This use of sensitivity calculations is possible because the sensitivity of the bare photodiode is well known (Korde and Canfield, 1989); absorption coefficients for all the coating materials are found in the literature (Henke *et al.*, 1982, 1988; Powell *et al.* 1990;). An added advantage is that the material thickness is measured as the material is deposited onto the photodiode. The transmission of the coating material is related to material thickness in the following way:

$$T = e^{-\mu\tau}, \qquad 4\text{-}7$$

where $T$ is the transmission, $\mu$ is the absorption coefficient for the material, and $\tau$ is the thickness. The product of the modeled transmission and the bare photodiode sensitivity gives the sensitivity of the coated photodiode. The procedure is then to perform a calibration at NIST over as broad a wavelength range as possible. This calibration is compared to a model of the sensitivity based on the material thicknesses. Included in the model are estimates for the thickness of the oxide layer, if any, which grows on most thin films after deposition. The thin film thicknesses are then adjusted to achieve the best possible match between the modeled and measured sensitivities. The modeled sensitivities are used for the full wavelength range. Figures 4-7 and 4-8 show the results of this procedure for the photodiodes presented in this work. The plots can be compared with the plot of the sensitivity of an uncoated photodiode, also shown in

Figure 4-7. Figures 4-7 and 4-8 show the measured calibrations with error bars which represent two sigma uncertainty. These uncertainties are provided by NIST.

### 4.3.5 FUV Airglow Spectrograph

The FUV Airglow spectrograph consists of a Wadsworth spectrometer, a telescope, and a 1 x 1024 CODACON detector with a Cesium Iodide (CsI) photocathode. An optical layout is presented in Figure 4-9. The telescope is an f/2 Calcium Fluoride ($CaF_2$) plano-convex lens. The transmission function of $CaF_2$ is appropriate in this application since its throughput is low at 130 nm and increases rapidly above 140 nm. The bright atomic oxygen emissions at 130.4 and 135.6 nm are prevented from saturating the detector, while the dimmer LBH emissions at longer wavelengths are not severely affected.

The Wadsworth mount consists of an off-axis parabolic mirror and a concave grating. The parabolic mirror is f/2 with a focal length of 152 mm. The concave grating is holographically ruled with a 600 mm radius of curvature and a ruling density of 2083 lines/mm. The instrument covers from 130 to 160 nm in wavelength with a resolution of approximately 0.3 nm.

The spectrograph flew in the same configuration for each of the three flights. For 36.098, the telescope contained an extra $CaF_2$ filter. This was used to ensure that the bright OI 130.4 nm emission would not saturate the detector. The filter was removed for the later flights. After the second flight, the telescope lens was replaced with an identical lens; the original lens suffered degradation during the first two flights.

Altitude resolution is determined by the field of view of the telescope, observing conditions, and the velocity of the rocket. At altitudes where count rates are low, data can be summed along altitude bins to obtain better counting statistics; however, altitude resolution is degraded. If the lens were in perfect focus at the entrance slit of the spectrograph, the field of view of the instrument would be approximated by:

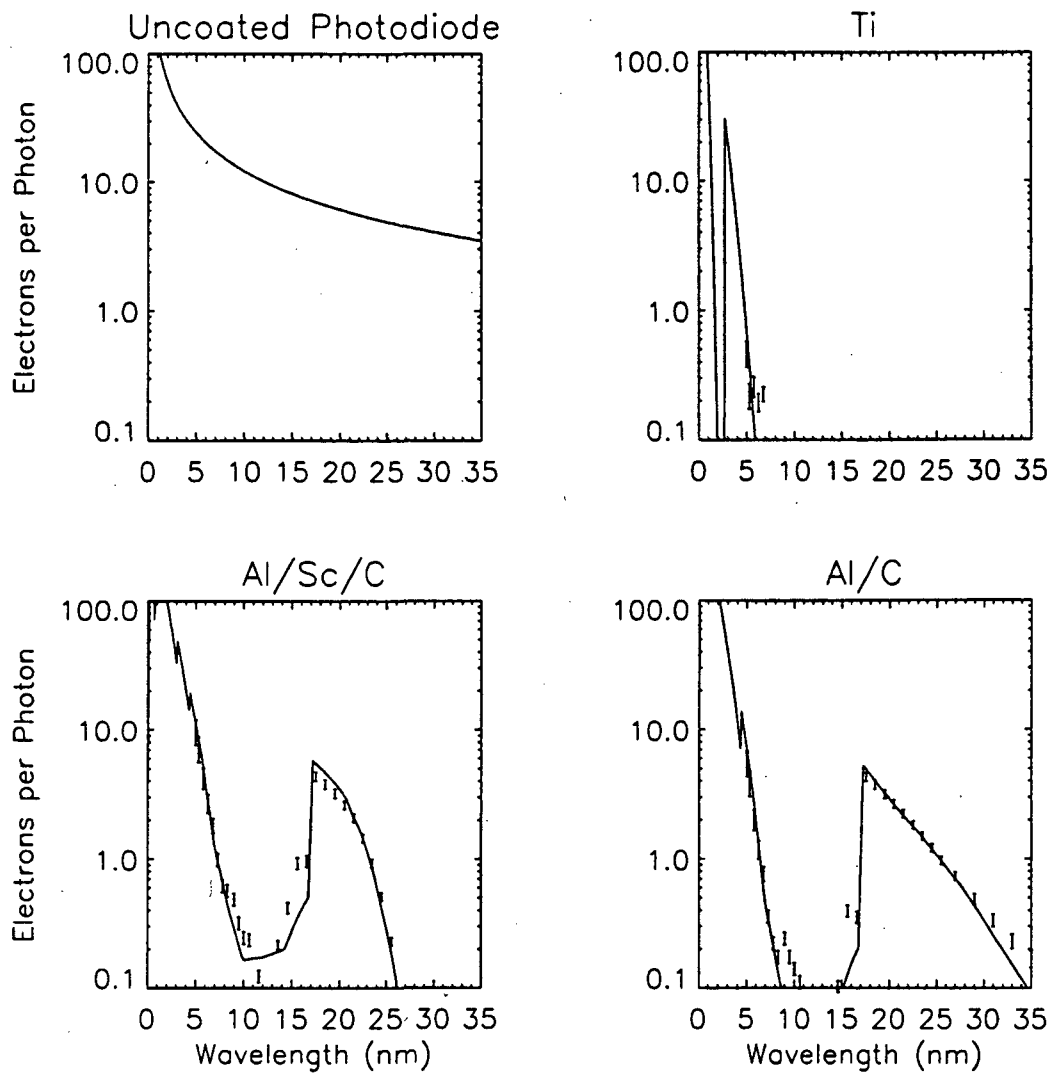


Figure 4-7 Sensitivity of the coated photodiodes flown on 36.107. An uncoated photodiode is shown for comparison. Error bars are discussed in the text.

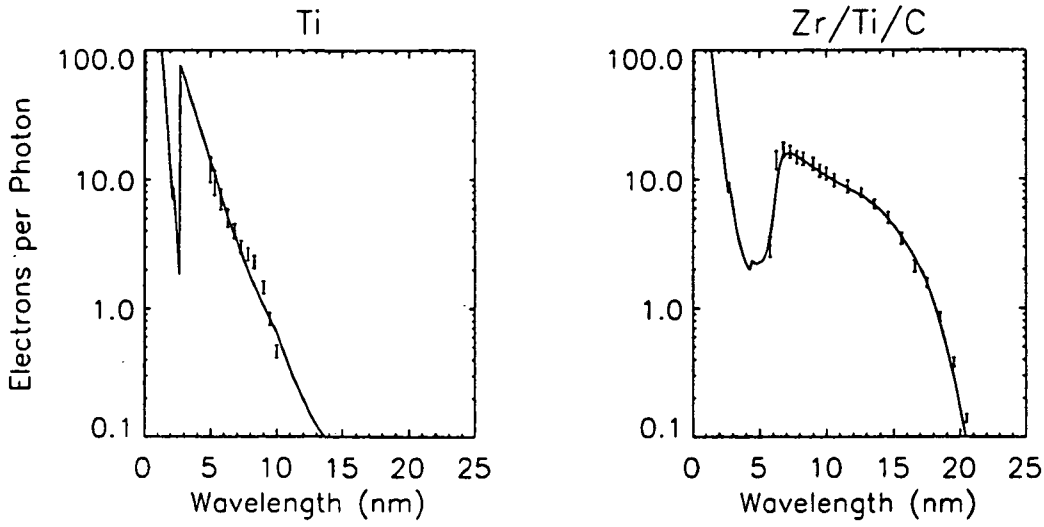


Figure 4-8 Sensitivity of the coated photodiodes flown on 36.124. Those photodiodes which were also flown on 36.107 are not shown. Error bars are discussed in the text.

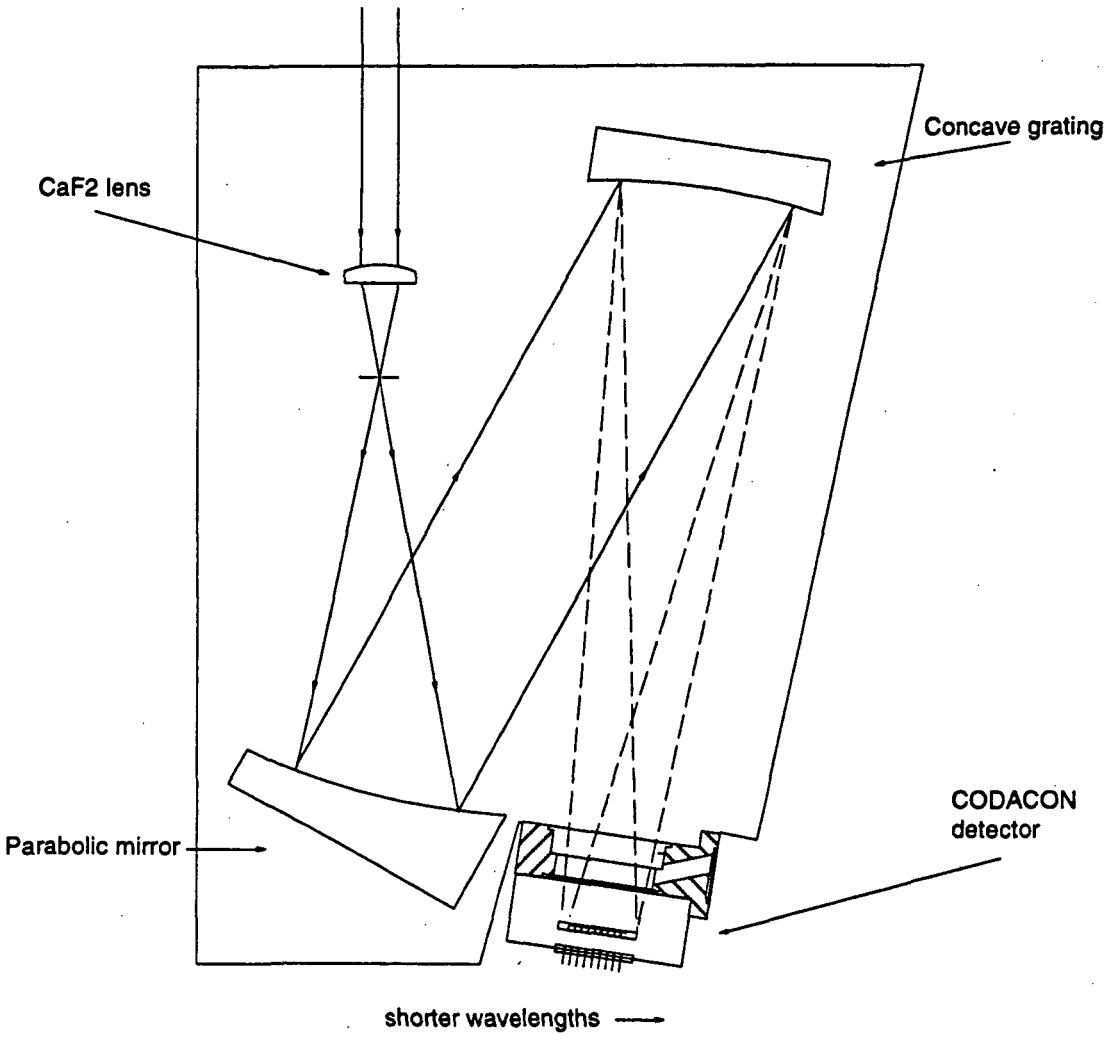


Figure 4-9 Optical layout of the FUV airglow spectrograph. The spectrometer is a Wadsworth mount.

$$\Omega = \frac{A}{f^2}, \qquad 4\text{-}8$$

where $\Omega$ is the field of view in steradians, $A$ is the area of the entrance slit, and $f$ is the focal length of the lens. For flights 36.107 and 36.124 the entrance slit was 0.156 mm wide by 2.664 mm long; for 36.098 the slit was 0.088 mm wide by 2.67 mm long. The focal length of the lens is 27.65 mm, and will be discussed further in the following paragraphs. Thus, the field of view of the instrument is 5.43 x $10^{-4}$ steradians for the latter rocket flights and 3.07 x $10^{-4}$ steradians for 36.098. These values represent fields of view of 0.32° by 5.52° and 0.18° by 5.53° respectively. The airglow instrument is pointed in flight so that the long axis of the slit is parallel to the horizon. To calculate the altitude resolution for a stationary instrument we can use the following property of the lens:

$$\frac{H_I}{S} = \frac{H_s}{f_{lens}}, \qquad 4\text{-}9$$

where $S$ is the pathlength through the atmosphere, $H_s$ is the height of the slit, and $f_{lens}$ is the focal length of the lens. The altitude resolution $H_I$ is the height of the image of the slit on the atmosphere. The pathlength $S$ is approximated by the horizontal distance to the point where the altitude is one scale height higher than that of the observation point. A scale height is a characteristic distance in altitude over which the atmospheric density decreases by a factor of $1/e$. The scale height at an altitude of 150 km is approximately 45 km which results in a pathlength of approximately 750 km. Applying this result to Equation 4-7 yields 4 km altitude resolution.

The above calculation of altitude resolution assumes the telescope is in perfect focus. The index of refraction of $CaF_2$ changes rapidly below 160 nm. Consequently, the focal length of the lens also changes. The distance between the lens and the entrance slit is chosen to be the average focal length over the passband. The result, however, is

that some wavelengths are not in focus at the entrance slit. Thus, the altitude resolution is degraded for these wavelengths.

The index of refraction of $CaF_2$ in the ultraviolet has been measured by Malitson (1963) and Handke (1898). The following fit can be applied to the results of Malitson:

$$n^2 - 1 = \frac{0.5675888\lambda^2}{\lambda^2 - 0.50263605^2} - \frac{0.4710914\lambda^2}{\lambda^2 - 0.1003909^2} - \frac{3.8484723\lambda^2}{\lambda^2 - 34.649040^2}. \qquad 4\text{-}10$$

This reproduces the results of Handke to within 1%. The expression was provided by the Ealing Optics company from whom the $CaF_2$ lens was purchased. Based on Equation 4-10, a calculation the focal length of the lens is shown in Figure 4-10. The thickness of the lens, 6.3 mm at the center and 2 mm at the edges, is accounted for in the figure. In the airglow spectrograph, the distance between the lens and the entrance slit is 27.65 mm, which gives best focus at approximately 141 nm. From Figure 4-10 it can be seen that at short wavelengths, the entrance slit is more than 1 mm from the focal point of the lens. For a 10 mm lens diameter (f/3 telescope) this results in a 300 micron diameter image on the slit. Thus, for normal incidence on the telescope, when a circular image is made on the slit, the image is wide compared to the height of the slit. For non-normal incidence, the circular image is displaced from the center of the slit according to the product of the distance between the real focus and the slit and of the tangent of the angle of incidence. The field of view is then determined by calculating the overlap area of the circular image and the slit. Dividing the overlap area by the area of the circular image gives a differential field of view $\omega(\theta)$ for the vertical direction. This is a dimensionless value and is an indicator of the ability of the instrument to view radiation incident at an angle $\theta$, which is defined as relative to the horizontal. The results of such a calculation are shown in Figure 4-11 for the wavelengths of the four most important features in the FUV airglow. The Y axis of Figure 4-11 shows $\omega$ as a function of $\theta$ and of altitude relative to the horizontal. The altitude is described by a ray extended out 750 km along the horizon at an angle $\theta$. For 138.3 nm, the telescope is in near focus and an

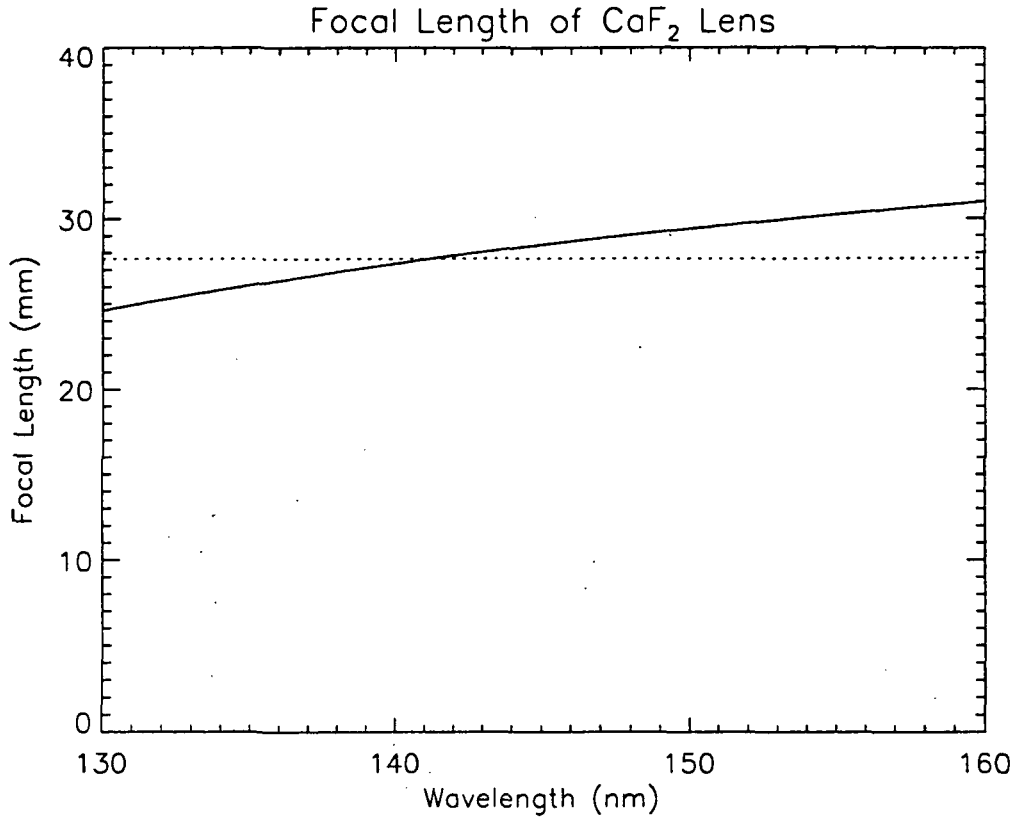


Figure 4-10 Focal length of $CaF_2$ lens as a function of wavelength. The focal length is measured from the back (exit) side of the lens. The dotted line shows the 27.65 mm chosen as the focal length used in the telescope.

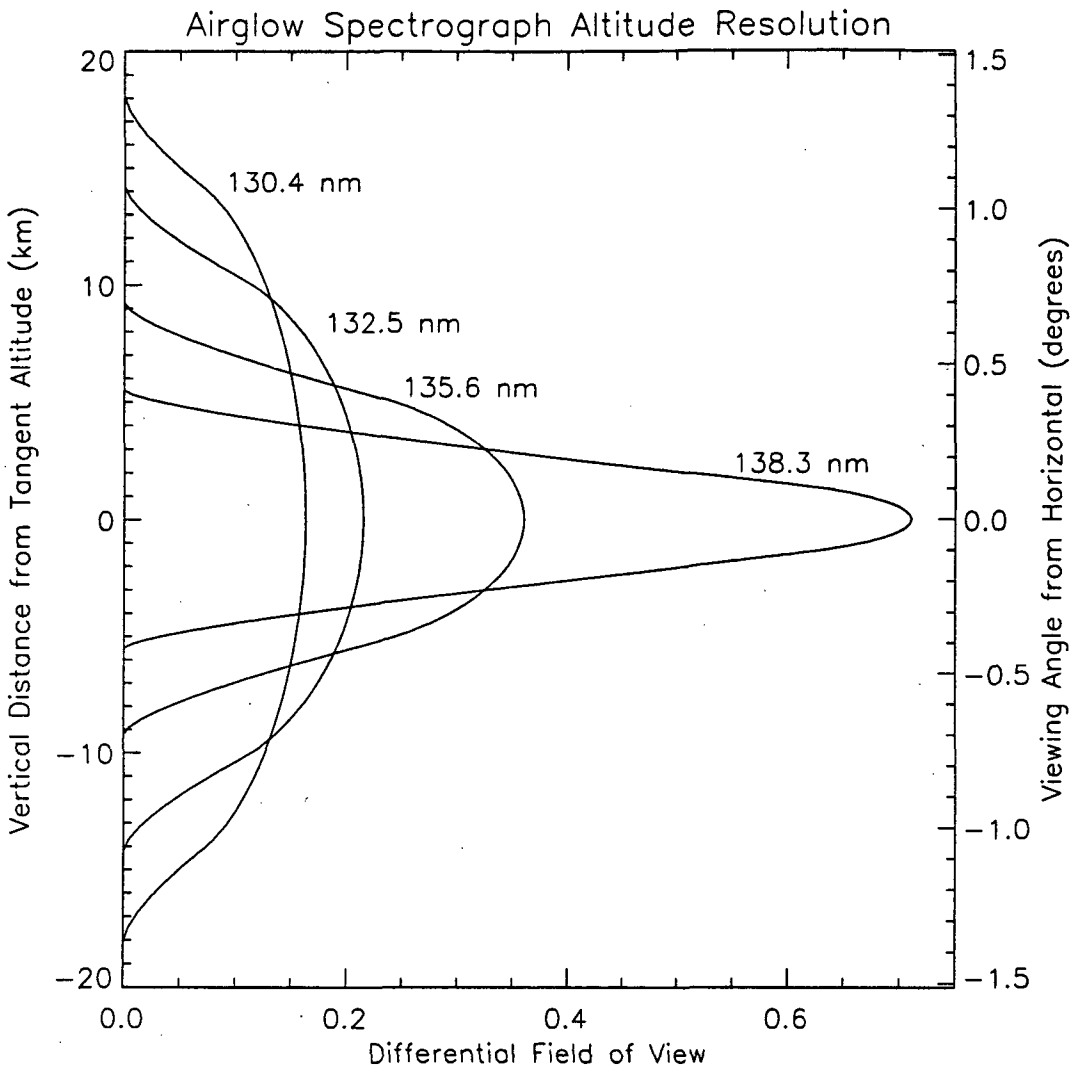


Figure 4-11 Altitude resolution of the telescope for the FUV airglow instrument shown for various wavelengths. At 138.3 nm the telescope is in near perfect focus. The observation angles, relative to the horizon, represented by the altitudes are also shown. Note that the area under each curve is the same.

altitude resolution of 6 km (full width at half maximum) is obtained. By 130.4 nm, this is degraded to approximately 25 km. As a test on the accuracy of the above calculation, $\omega$ can be integrated over $\theta$. At each wavelength the result of the integration should be, and is, equal. This is valid because defocusing the telescope cannot add or take away any extra light from the system. Rather, the effect is to spread out the ability of the instrument to view the atmosphere.

Given the above description of altitude resolution, it is now useful to describe how this is incorporated into the data analysis. As was mentioned, altitude resolution is determined by the time interval over which data is integrated as well as by the properties of the telescope. In Chapters V and VI the measured airglow profiles are compared to model airglow profiles. These model profiles are obtained by integrating calculated volume emission rates along the line of sight of the instrument. To properly account for the effects of the telescope on the field of view, the volume emission rates must be integrated as a function of the angle $\theta$ and then scaled according to $\omega(\theta)$.

### 4.3.6 Laboratory Calibration of the FUV Airglow Spectrograph

The airglow spectrograph is not easily calibrated at SURF. The solar instruments measure irradiance and are concerned with point source illumination. The light entering the instrument is essentially parallel and is incident upon the grating at a uniform angle. For an airglow instrument, the emission source is now extended and the grating is fully illuminated at all angles of incidence within the field of view. Therefore, the SURF beam better resembles the solar source than the airglow source. For the airglow instrument, an extended source is required for calibration.

For the airglow spectrograph calibration, the Calibration Test Equipment - 2 (CTE-2) at the High Altitude Observatory (HAO) was used. The facility is an evacuated chamber with an Acton VM 502 monochromator mounted on one end. The layout of the vacuum chamber is shown in Figure 4-12. A concave mirror and a flat mirror are

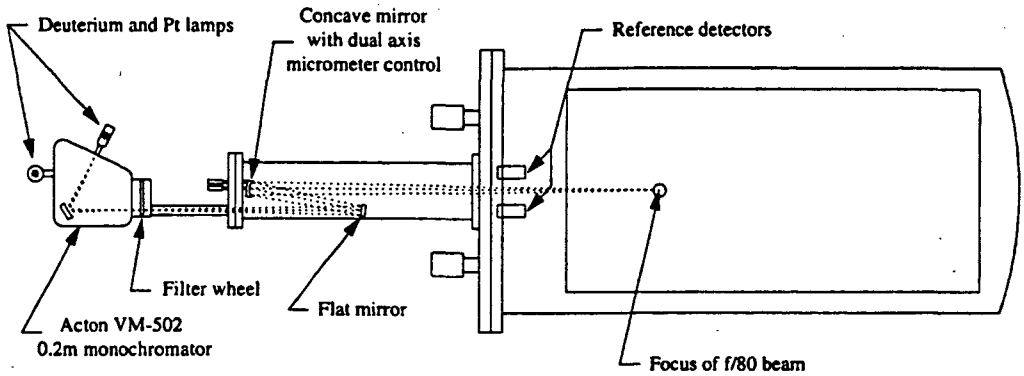


Figure 4-12 Layout of the Calibration - Test - Equipment (CTE) facility. Instruments can be placed in the test chamber (to the right) to view the monochromator output. A scattering screen can also be placed inside the vacuum chamber to simulate an extended source. This requires a calibration lamp to be mounted to a vacuum port at the top (coming out of the page) of the chamber.

used to focus the exit slit of the monochromator into the test chamber. The concave mirror can be manually tilted to allow the focal point to move horizontally and vertically. Reference photomultiplier tubes are also present in the test chamber. The photomultiplier tubes are calibrated relative to NIST standard photodiodes. The combination of NIST reported uncertainty in their photodiode calibration and the uncertainty in transferring the calibration to the photomultiplier tubes results in a two sigma uncertainty of 15%. Calibration lamps mount onto the monochromator at the entrance slit. Typical light sources used for calibrations are platinum (Pt) hollow cathode lamps for line emissions, and deuterium discharge lamps for continuum emission above 190 nm and band emission below 170 nm. The spectral bandpass of the Acton monochromator is 4 nm per 1 mm width of the exit slit. The slit width is manually adjustable to limit the bandpass and also to control the intensity of the beam.

The sensitivity of the airglow instrument follows the equation:

$$S = \frac{10^6}{4\pi} T_T QT_S \frac{RQT_F}{RQT_S} A\Omega. \qquad 4\text{-}11$$

Here $S$ is the sensitivity in units of counts per second per Rayleigh. The throughput of the telescope and the spectrograph are $T_T$ and $QT_S$ respectively, $A$ is the area of the entrance slit, and $\Omega$ is the field of view of the instrument in steradians. The ratio of $RQT_F$ to $RQT_S$ is the ratio of relative quantum throughput measurements with full and small fields of view. The product of this ratio and the absolute measurement of the quantum throughput of the spectrograph, $QT_S$, yields the efficiency of the spectrograph when fully illuminated. The field of view $\Omega$ is calculated by Equation 4-8. The quantum throughput of the telescope includes the transmission of the $CaF_2$ lens and the $CaF_2$ filter, if present. For the spectrograph, $QT_S$ is the product of the reflectivity of the parabolic mirror, the efficiency of the grating, and the quantum efficiency of the CODACON detector. The efficiency of the grating must be an average over the entire

active area of the grating and over all possible angles of incidence. The values $A$ and $\Omega$ are known properties of the instrument; the calibration procedure must measure the values of $T_T$ and $QT_S$ as a function of wavelength.

The calibration procedure has three steps. The first is the measurement of $T_T$. The second is an absolute measurement of $QT_S$ for a small field of view (FOV). The final step is to measure the relative $QT_S$ for the full FOV and a small FOV. The ratio of relative full FOV $QT_S$ to the relative small FOV $QT_S$ can then be multiplied by the result of the absolute $QT_S$ for the small FOV to yield the true $QT_S$ for an extended source, i.e. full FOV. This process is necessary because the monochromator can only provide a small FOV. The three measurements are described below. The quoted uncertainties are two sigma values.

The detector for the airglow spectrograph has poor response in the center of the active area; several anodes have no sensitivity due to a defect in the code plate. Thus, no results are shown for wavelengths between 142 and 147 nm.

Measurement of $T_T$ is relatively simple. A photomultiplier tube is placed just behind the focus of the CTE. The telescope is placed on a translation stage such that the telescope can be moved to the focus, or removed from the light path. At one position of the translation stage, the photomultiplier tube measures the light which passes through the telescope. At the second position, the unattenuated beam of light reaches the photomultiplier tube. A ratio of these two measurements provides the transmission of the telescope. This is repeated at several wavelengths to find $T_T$ as a function of wavelength. The Pt lamp is used; measurements are made at each of the bright lines of Pt within the instrumental passband. The unattenuated CTE beam is measured both before and after the telescope beam to account for any variations in the lamp output. On the time scale of a measurement at one wavelength, the lamps are not shown to vary. Figure 4-13 shows the results for the $CaF_2$ lens used on flight 36.124. Rather than

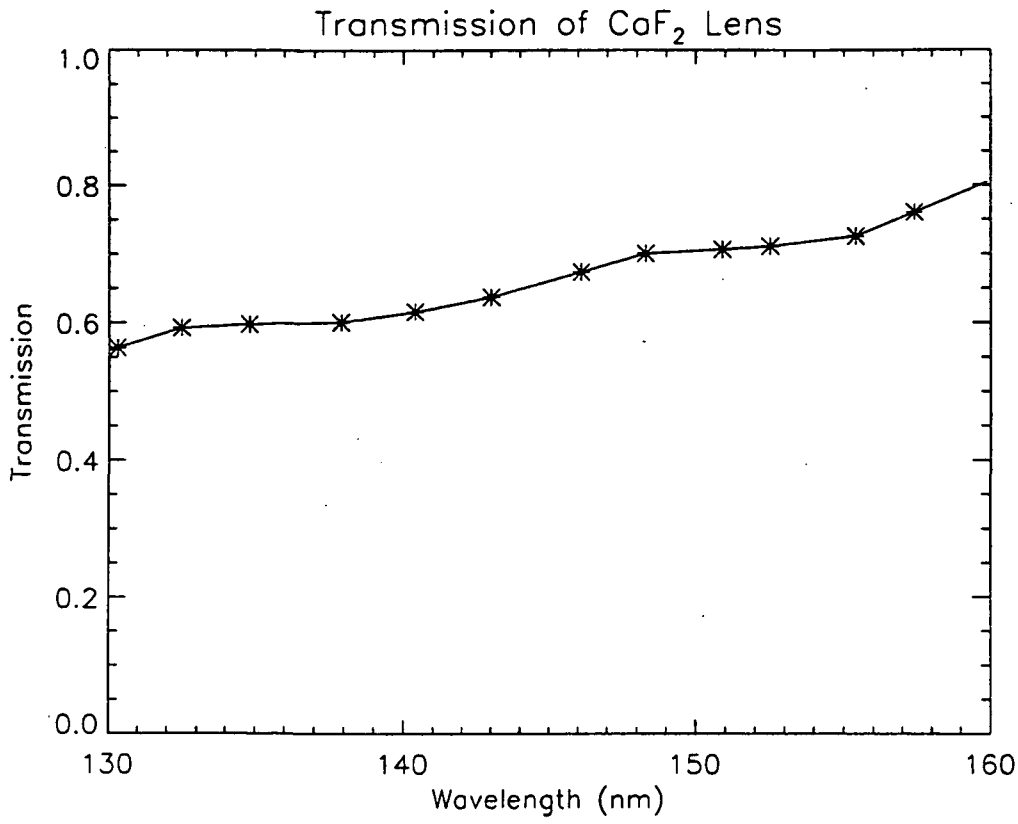


Figure 4-13 Transmission of the $CaF_2$ lens used in the airglow spectrograph telescope. Transmission of the $CaF_2$ filter is similar.

calibrate the assembled telescope, the lens and filter are measured individually. Table 4-1 lists the uncertainties in these values. The filter transmissions are very accurate as they depend only on counting statistics. The count rates in these experiments are typically on the order of several thousand per second, which yields low uncertainty while not operating the photomultiplier tube at such a high rate that it responds nonlinearly. For the lens, the uncertainties are larger because the focal length of the lens changes with wavelength. This effect has the result that at each wavelength, the light is focused to a different area of the photomultiplier tube. Because photomultiplier tubes exhibit some variation in sensitivity over the active area, there is uncertainty in this measurement. A two sigma uncertainty of 5% is attributed to this effect.

The absolute quantum efficiency of the spectrograph is measured at the center of its FOV, with the small FOV defined by the CTE monochromator. The entrance aperture of the spectrograph is placed at the focus of the CTE, but the entrance slit is removed so that the entire beam of the CTE enters the instrument (the focused beam has the size of the exit slit of the Acton monochromator). The height of the CTE monochromator exit slit is set at 2 mm, which is less than the 6 mm height of the active area of the CODACON. For this calibration it is important to not overfill the active area so that all photons can potentially reach the detector. The platinum lamp is again used. The focus of the CTE is moved between the spectrograph and the calibrated reference PMT. The PMT measurements are used to calculate the number of photons in the CTE beam. Comparing this value to count rates from the spectrograph yields the quantum throughput. Care is taken so that the instrument is aligned properly to the beam of the CTE. The result of this measurement is shown in Figure 4-14, and has been made before each of the three rocket flights. No changes were detected which were not attributable to experimental uncertainties or to improved procedures which lowered uncertainty in the measurements. Table 4-2 lists the uncertainties in these measurements. High count rates, but not so high to produce nonlinearity in the

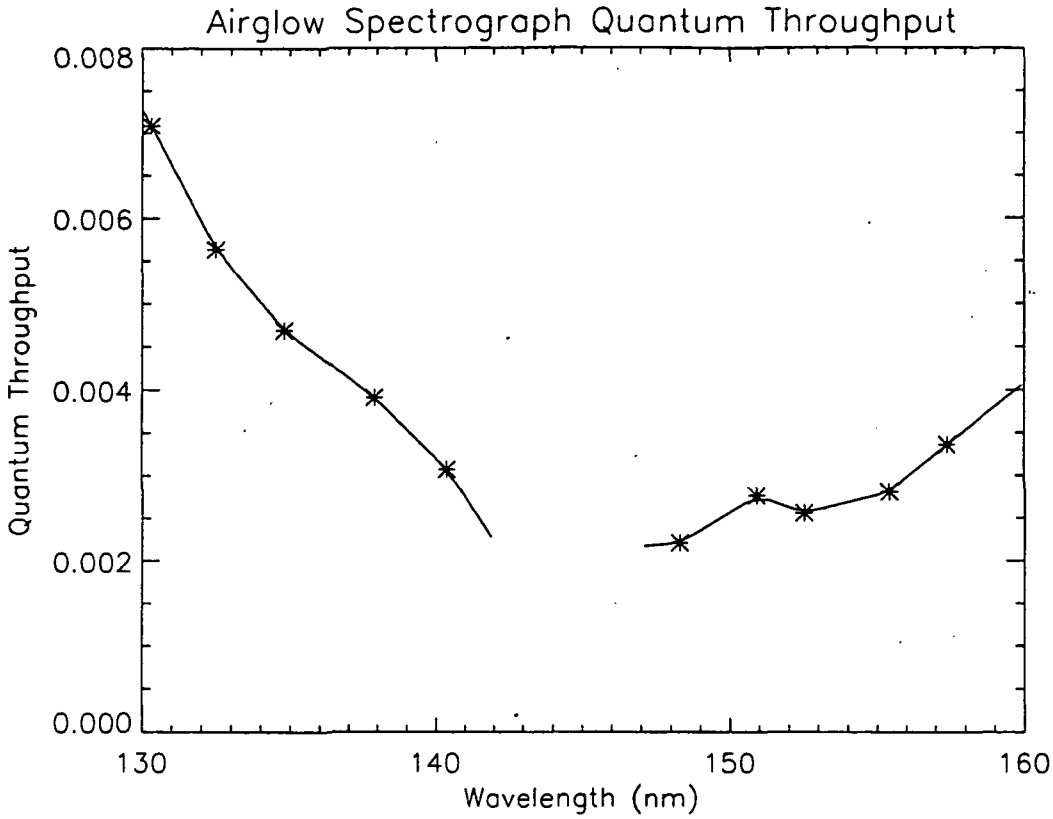


Figure 4-14 Quantum throughput of the airglow spectrograph. This *QT* is at the center of the spectrograph and over a small FOV defined by the CTE monochromator. Results are not shown for the wavelength region between 142 and 147 nm where the CODACON detector has several defective pixels.

**Table 4-2 Calibration Uncertainty for the FUV Airglow Spectrograph**

| Measurement | Uncertainty† | Major Cause of Uncertainty |
|---|---|---|
| Transmission of Telescope ($T_T$) | | |
| Lens Transmission | 5% | Changing Focus of Lens |
| Filter Transmission | 1% | Counting Statistics |
| Absolute *QT* of Spectrograph ($QT_S$) | | |
| Reference PMT *QT* | 15% | Uncertainty from NIST |
| Precision of Measurement | 2% | Counting Statistics |
| Ratio of Full to Small FOV Relative *QT* | | |
| Uncertainty Due to Technique | 10% | Misalignment/Averaging |
| Precision of Measurement | 12% | Counting Statistics |
| Total Uncertainty (rms) | 22% | |

† Estimated two sigma uncertainties.

detectors, can be maintained; therefore, counting statistics represent a small part of the uncertainty. Most of the uncertainty is in the transfer of the NIST photodiode calibration to the reference PMT.

The final step in the calibration requires use of an extended source. An aluminum plate is bead blasted to roughen the metal and make a Lambertian surface, ie. one which reflects in all directions. When illuminated, the roughened plate provides an extended source. The instrument is placed to view the sheet illuminated by a deuterium lamp, placed at an upper port in the CTE, via a concave mirror near the lamp. The focal length of the mirror is much shorter than the distance to the sheet to ensure that the sheet is uniformly filled. When viewing a perfectly uniform extended source which fills the instrument FOV, the number of photons entering the instrument should not vary with distance from the source or with viewing angle to the source. This condition is verified by scanning the instrument across the sheet, confirming that the count rates do not vary. When the setup is complete, measurements are made with the fully assembled spectrograph and telescope. One measurement is made with the full FOV. Because neither the deuterium lamp nor the mirror and aluminum plate are calibrated, these measurements only provide relative results. The next measurement is made with a small aperture in front of the telescope to simulate the small FOV used in the absolute *QT* calibrations. The ratio of the full FOV relative *QT* to the small FOV relative *QT* are needed to correct the absolute *QT* for the full FOV. This ratio is shown in Figure 4-15. The scatter in the measurements is noise related to the low count rates obtained during the small FOV relative *QT* measurements. The fit to the ratio shown in Figure 4-15 is the result used in the final calibration. Table 4-2 lists the uncertainties in this measurement. The largest fraction of the uncertainty is the counting statistics due to the low count rates obtained with the masked telescope in the small FOV calibration. Another component to the uncertainty is attributed to technique. The round aperture on the telescope has a diameter of about 3 mm; a smaller diameter would yield

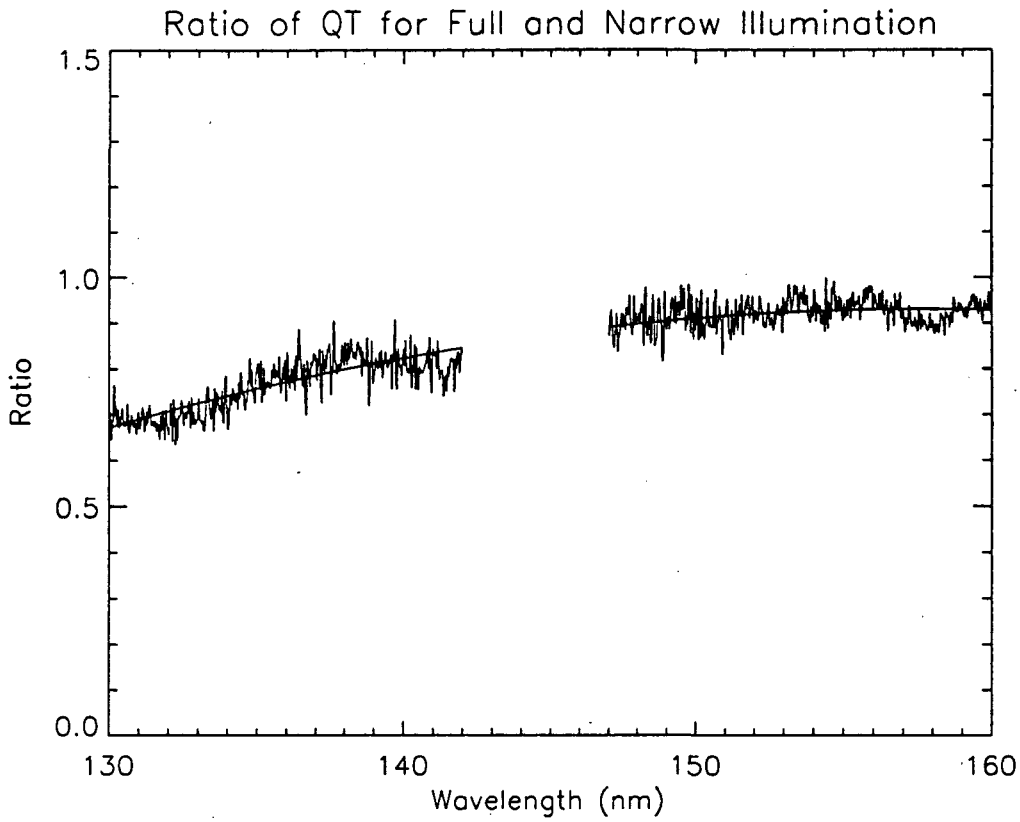


Figure 4-15 Ratio of relative *QT* for Full FOV to small FOV for the airglow spectrograph. Results are not shown for the wavelength region between 142 and 147 nm where the CODACON detector has several defective pixels.

unacceptably small count rates. The 3 mm aperture results in an illumination on the grating which is comparable in area to that used in the absolute *QT* measurement; however, they are different in shape and cover a slightly different area on the grating. Also, any misalignments can result in the absolute and relative *QT* measurements being made on slightly different parts of the grating. Experience with this spectrograph indicates that most of the variation along the FOV comes from one panel of the tripartite grating. Therefore, as long as the aperture is not so big that the image covers more than the panel used in the absolute *QT* measurement, this technique should be accurate. A conservative estimate of the uncertainty due to these effects is 10%.

The sensitivity of the instrument as calculated by Equation 4-11 is shown in Figure 4-16. The shape of the sensitivity is largely due to the absolute *QT* curve. The grating is ruled to have a peak efficiency at 90 nm; therefore, peak efficiency is at a lower wavelength than those wavelengths of concern. The microchannel plate in the CODACON is coated with a cesium iodide photocathode. The response of this photocathode peaks near 150 nm. The application of this sensitivity to measured airglow spectra will be discussed in Chapter V.

## 4.4 Summary

This chapter described the instrumentation used to measure the solar irradiance and terrestrial airglow. For each rocket flight the instrumentation was identical. The details of calibrations involving SURF measurements were described for the EUV grating spectrograph and the solar x-ray photometers. A laboratory technique was also presented for the calibration of the FUV airglow spectrograph; this calibration is referenced to standard photodiodes purchased from NIST. For each instrument, two sigma uncertainties in the calibration measurements were discussed.

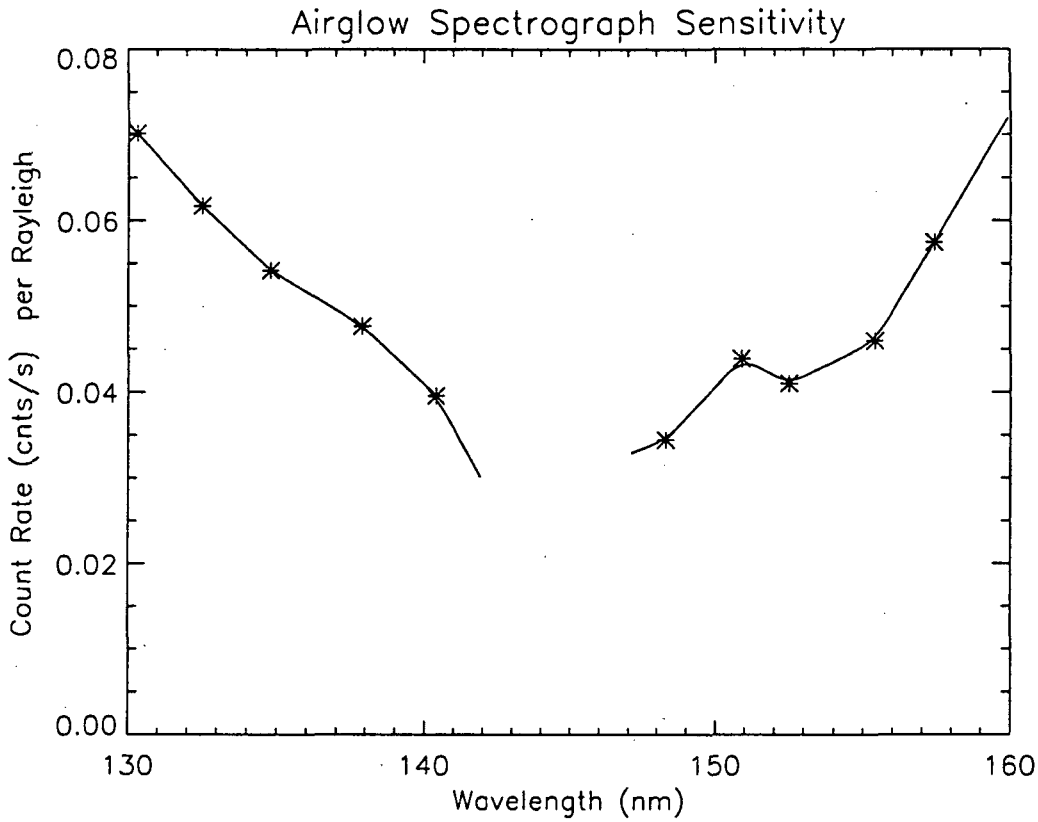


Figure 4-16 Sensitivity of the airglow spectrograph. The sensitivity, as calculated by Equation 4-11, is the product of the results presented in the last three figures. Results are not shown for the wavelength region between 142 and 147 nm where the CODACON detector has several defective pixels.

# Chapter V

# Reduction and Analysis of Rocket Data

## 5.1 Introduction

The rocket payload described in Chapter IV has been flown three times. The results of these flights are used to study the response of the upper atmosphere to the different levels of solar activity at which the payload was flown. In order to compare with the models described in Chapter III, the data must be converted from instrument units to physical units. In this chapter the data and the process of reducing the data are described.

## 5.2 The Solar EUV Irradiance and Terrestrial Airglow Experiment

The solar irradiance and terrestrial airglow experiment has been flown three times, each successfully. The physical and geophysical conditions of these launches are listed in Table 5-1. As described in Chapter IV, the instruments on the payload measured the solar irradiance at EUV and soft x-ray wavelengths and measured the Earth's airglow at FUV wavelengths. In the following sections, conversion of the solar data into irradiance units and airglow data into altitude profiles of brightness is described. Attenuation of the solar data is used to infer the densities of the major thermospheric constituents.

### 5.2.1 Reduction of EUV Grating Spectrograph Data

The EUV grating spectrograph (EGS) measures the solar irradiance from 25 to 120 nm. The measurements are made as the rocket ascends and descends through the atmosphere; as a result, the instrument also determines the attenuation of the solar irradiance. Attenuation profiles can be used with absorption cross sections to infer the densities of the major species in the thermosphere. The following sections describe the

**Table 5-1 Conditions for Rocket Flights**

| | 36.098 | 36.107 | 36.124 |
|---|---|---|---|
| Launch Date | Oct. 27, 1992 | Oct. 4, 1993 | Nov. 3, 1994 |
| Day of Year | 301 | 277 | 307 |
| Local Time | 11:30AM | 11:45AM | 11:45AM |
| Universal Time (s) | 63000 | 63900 | 67500 |
| Latitude | 32° | 32° | 32° |
| Longitude | 254° | 254° | 254° |
| Solar Zenith Angle | 48.7° | 39.9° | 47.2° |
| F10.7 cm flux | 168.9 | 121.0 | 84.6 |
| F10.7 (prior day) | 167.9 | 125.1 | 89.6 |
| F10.7 (81 day ave.) | 132.6 | 93.1 | 85.6 |
| Ap | 31 | 6 | 12 |
| Solar 130.4 nm Irradiance† | $8.7 \times 10^9$ | $7.7 \times 10^9$ | $7.8 \times 10^9$ |

† Values represent integration over the three lines of the triplet, measured by the SOLSTICE instrument on board the UARS satellite (T. N. Woods, private communication, 1995)

determination of absolute solar irradiances and the inference of the thermospheric density profiles.

### 5.2.2 Absolute Solar EUV Irradiances

Using the symbols of Chapter IV, the measured count rate, $C(\lambda)$, can be converted to solar irradiance $I(\lambda)$ (ph $cm^{-2}$ $s^{-1}$) using the following equation:

$$I(\lambda) = \frac{C(\lambda) - D - S}{A \Delta t Q T f_a \Delta\lambda}. \qquad 5\text{-}1$$

Chapter IV described the calibration of the EGS. Data from the most recent flight, 36.124, is shown in Figure 5-1. The factor $f_a$ is a correction to account for absorption at altitudes higher than the apogee of the rocket. To calculate $f_a$, the MSIS 86 (Hedin, 1987) model atmosphere is used along with the absorption cross sections described in Chapter III. Section 5.2.3 details the attenuation calculation. Equation 5-1 assumes only first order contributes. For the EGS, second order is only important at wavelengths longer than 90 nm because of poor grating reflectivity at short wavelengths. The irradiance between 45 and 90 nm can be calculated by Equation 5-1, and this irradiance and the second order sensitivity derived in Chapter IV can be used to calculate second order contributions at longer wavelengths. These contributions are subtracted out of the measured spectrum to leave only first order contributions. Equation 5-1 can thus be used to calculate irradiance at wavelengths longer than 90 nm. In application of the above process, dark counts $D$ measured at the lowest altitudes and scattered light contributions $S$ are subtracted from the measured count rate. The data is binned in 5 km intervals.

Application of the above method has been performed by Dr. T. N. Woods. A more detailed description of the procedure is described by Woods and Rottman (1990). Results are tabulated in Appendix C; for the tabulation, the irradiance is binned into 1 nm bins which are used for model calculations.

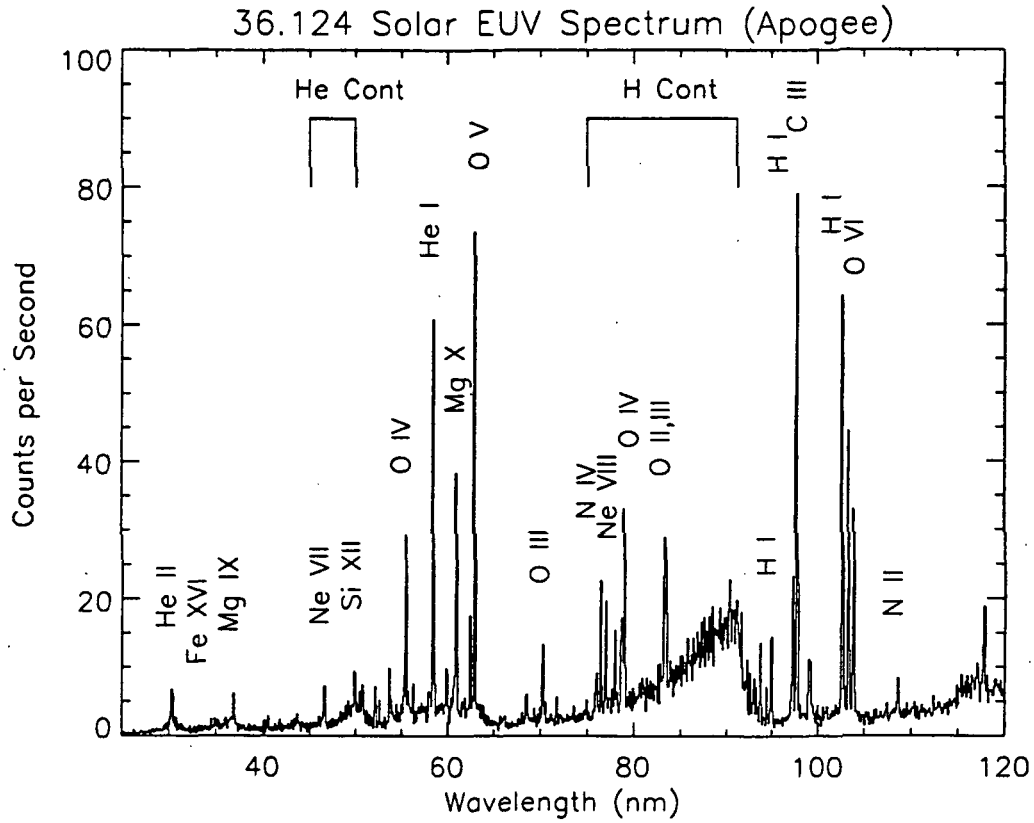


Figure 5-1 Raw spectrum from the EGS on flight 36.124, taken at apogee.

### 5.2.3 Attenuation of the Solar Irradiance

The solar EUV spectrum is comprised of several continua and many emission lines. An ideal candidate for attenuation studies is an emission line which stands out above the continua and is well separated from nearby emission lines. High count rates with good counting statistics are desired; however, lines which approach the saturation level of the microchannel plate suffer count rates which vary nonlinearly with irradiance. It is also important that the line occur in a wavelength region where the absorption cross sections are well understood. Because the structure in the cross section is due to the vibrational and rotational structure of the absorbing states, the absorption cross section of $N_2$ becomes complicated beyond 70 nm. The population of the levels is dependent on temperature; the absorption cross section will have a similar dependence. Because this temperature dependence is not well known, attenuation studies are made at wavelengths below 70 nm.

Given the above criteria, five lines are chosen for analysis. These are the 55.4 nm emission of OIV, the 58.4 nm emission of HeI, the 61.0 and 62.5 nm emissions of Mg X, and the 63.0 nm emission of OV. The cross sections for pure absorption by atmospheric species are shown in Figure 3-3.

The procedure begins with obtaining altitude profiles for the various emissions, which are in instrument units and binned into 5 km altitude intervals. To examine attenuation, the profiles are plotted in terms of transmission. Transmission is calculated by first assuming a model atmosphere, which is assumed to correctly represent the atmosphere above the apogee of the rocket. The transmission, $T$, of the atmosphere at the apogee is calculated by:

$$T(\lambda) = e^{-\tau(\lambda)}, \qquad 5\text{-}2$$

where,

$$\tau(\lambda) = \sum_i \int_z^\infty n_i \sigma_i(\lambda) \cos(\chi) dz. \qquad 5\text{-}3$$

Here, $\tau$ is optical depth, $n_i$ is number density of species $i$, $\sigma$ is the cross section for pure absorption at wavelength $\lambda$, $\chi$ is the solar zenith angle, and $z$ is altitude. The integration over $z$ yields the absorption by a column of gas from the observer to the sun. The summation is performed for O, $O_2$, and $N_2$. To account for absorption above the apogee of the rocket, the measured absorption profile is scaled so that the value at apogee is equal to the model transmission (calculated by Equations 5-2 and 5-3) at apogee. This process yields a measured absorption profile which can be compared to a model absorption profile. The model profile is obtained by solving Equations 5-2 and 5-3 at each altitude.

Figure 5-2 shows the result of the above procedure for the 55.4 nm emission measured during the 36.124 flight. The crosses represent the measured count rates at each altitude scaled to represent the transmission of the atmosphere. The solid line is the transmission as calculated using the MSIS prediction. Agreement at apogee is achieved since the measured profile is scaled to agree with the model at high altitudes. At lower altitudes the model falls off more rapidly than the data. This indicates that the MSIS model atmosphere is predicting larger atmospheric densities than are present. Between 150 and 300 km, O is the dominant constituent and, due to its lower mass, its scale height is approximately twice that of $N_2$ or $O_2$. Thus, most of the attenuation through the atmosphere is due to O. It follows that the large atmospheric density is an over prediction of the O density by the MSIS model. Performing the same comparison using scalings of 0.5 and 2.0 in $N_2$ produces negligible changes in Figure 5-2. An overabundance in O could be the result of a simple scaling in MSIS or an indication that the temperature predicted by MSIS is too large. To determine the proper interpretation, the absorption profiles are compared to model profiles using scaled O densities and reduced temperatures. To lower the MSIS temperature, the F10.7 cm flux input is

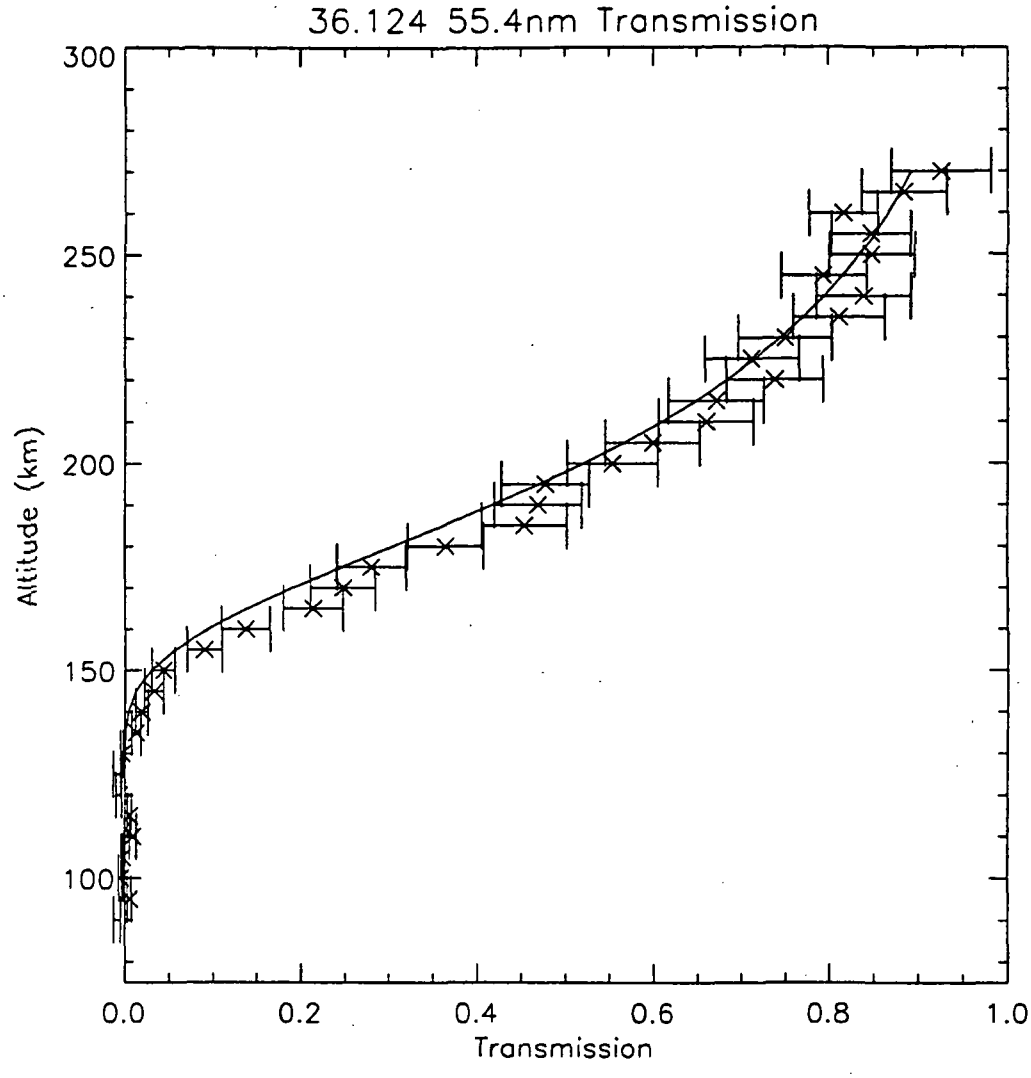


Figure 5-2 Attenuation of the 55.4 nm solar emission. Crosses are measurements, solid line is MSIS prediction. Data and MSIS prediction are shown in units of transmission of the atmosphere.

lowered. Figure 5-3 compares 36.124 55.4 nm absorption profiles using the original MSIS prediction, the MSIS prediction with O scaled by 0.5, and the MSIS prediction with F10.7 = 55. Although this value of F10.7 is unrealistic, it does provide a temperature profile which agrees well with the data. Figure 5-3 shows that the measured absorption profile can be reproduced with either a lower temperature or a scaling of O. This is unfortunate because a modification in temperature results in a modification in the $N_2$ and $O_2$ densities as well. Figures 5-3 through 5-5 show the same comparisons for the other emissions listed above. These figures demonstrate that both a 0.6 scaling of O and an F10.7 = 55 reproduce the data. This result is less true for the 58.4 and 63.0 emissions, but these emissions had count rates which approached the saturation of the CODACON detector during the 36.124 flight. Nonlinearities in the count rate are not accounted for in these figures. The count rates did not approach saturation during the 36.098 and 36.107 flights.

To understand which modified model atmosphere is correct, an emission which is principally absorbed by $N_2$ would be useful. Such emissions can be found at wavelengths longer than the photoionization threshold of O. Unfortunately, the absorption cross section of $N_2$ is complicated in this wavelength region, and also a function of temperature. No studies of this temperature dependence have yet been made; therefore, a study of the longer wavelength emissions is premature.

Figures 5-6 through 5-11 show the results of the same analysis for the 36.107 and 36.098 flights. A consistent result is obtained in that MSIS predicts a more dense atmosphere. Determinations of whether the dense atmosphere is due to an improper scaling of O densities or to a large temperature cannot be answered with this data and the current knowledge of $N_2$. The temperatures required to reproduce the 36.107 and 36.124 attenuation profiles are low exospheric temperatures and F10.7 values of 55 are unreasonable. Given that the temperature structure of the thermosphere is better

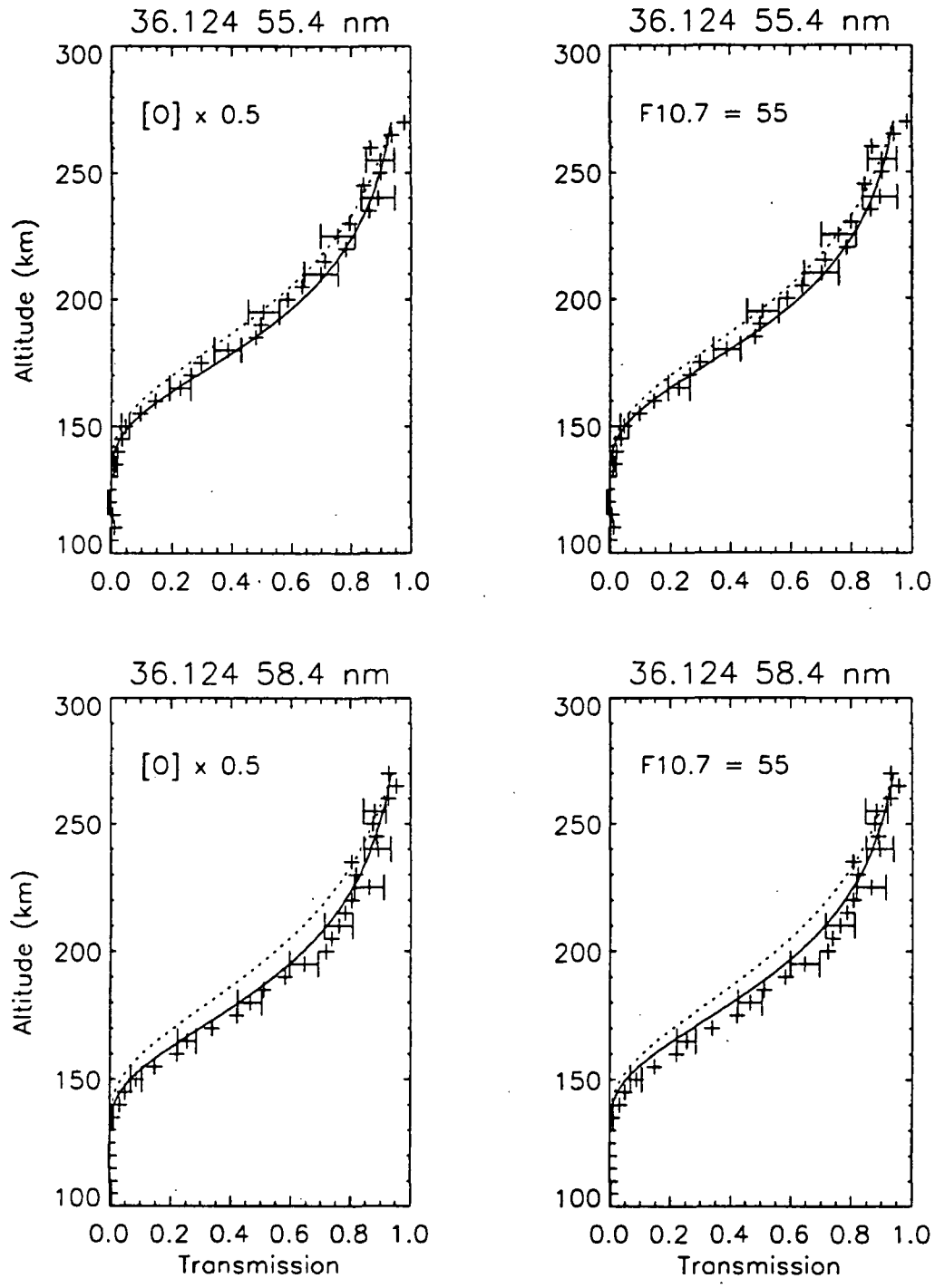


Figure 5-3 Flight 36.124 atmospheric transmission for solar emission lines. Dotted line represents MSIS prediction. In the left panels, solid lines are model predictions obtained by scaling MSIS O; in the right panels, solid lines are model predictions obtained by reducing MSIS F10.7 and, therefore, temperature. Crosses are measurements.

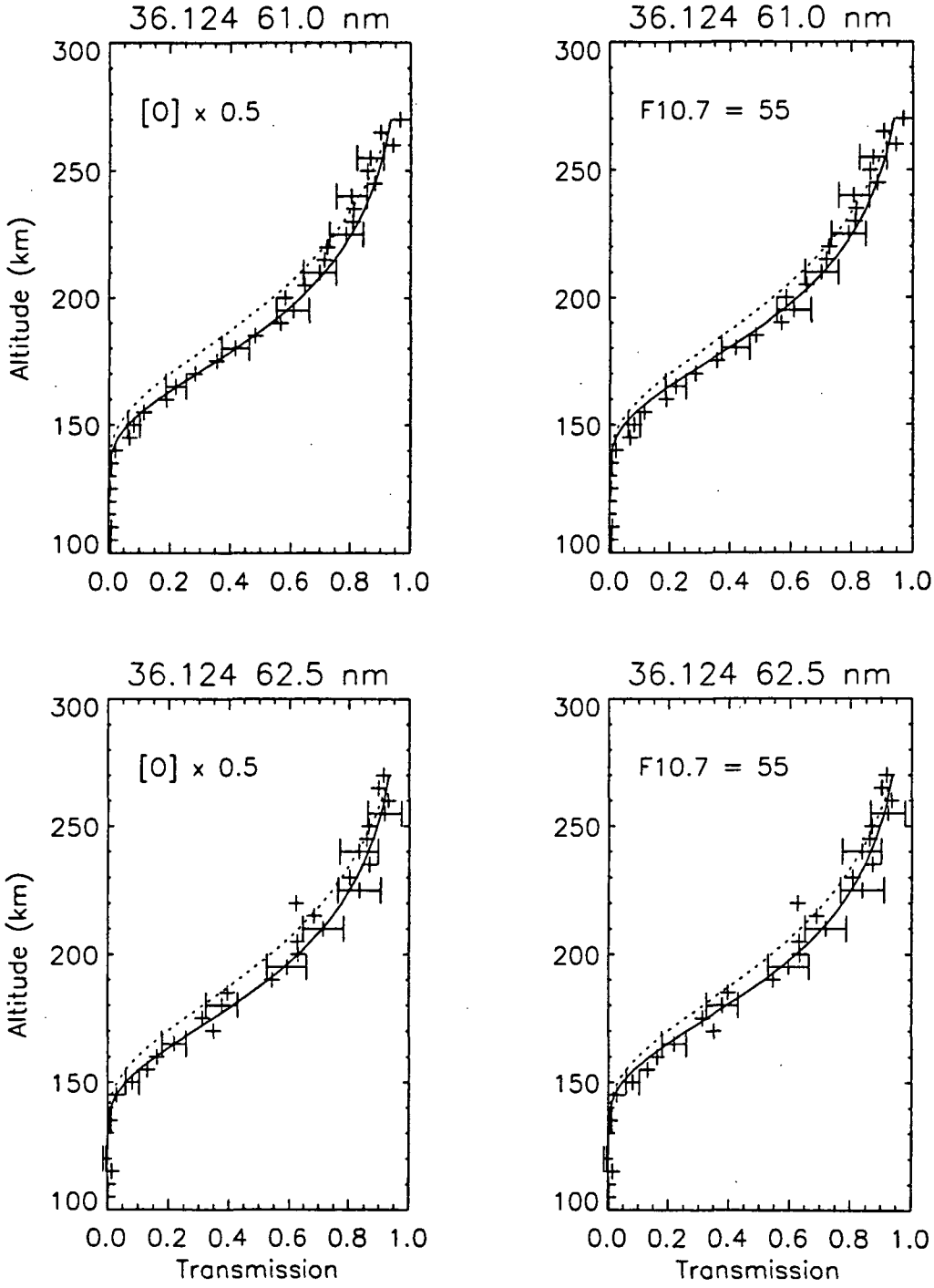


Figure 5-4 Flight 36.124 atmospheric transmission for solar emission lines. Dotted line represents MSIS prediction. In the left panels, solid lines are model predictions obtained by scaling MSIS O; in the right panels, solid lines are model predictions obtained by reducing MSIS F10.7 and, therefore, temperature. Crosses are measurements.

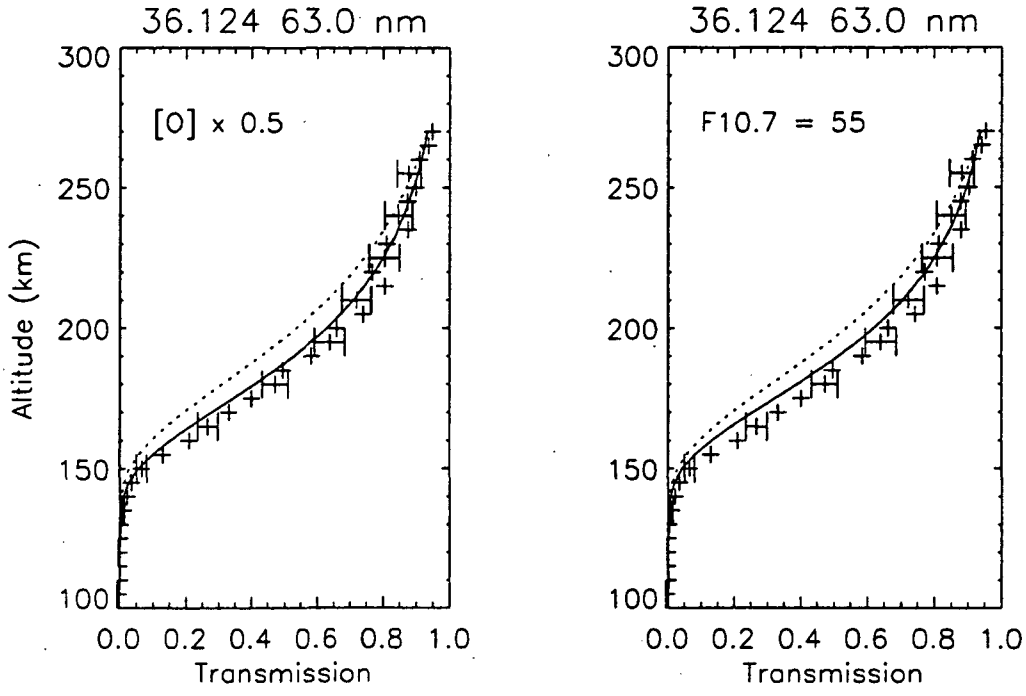


Figure 5-5 Flight 36.124 atmospheric transmission for solar emission lines. Dotted line represents MSIS prediction. In the left panels, solid lines are model predictions obtained by scaling MSIS O; in the right panels, solid lines are model predictions obtained by reducing MSIS F10.7 and, therefore, temperature. Crosses are measurements.

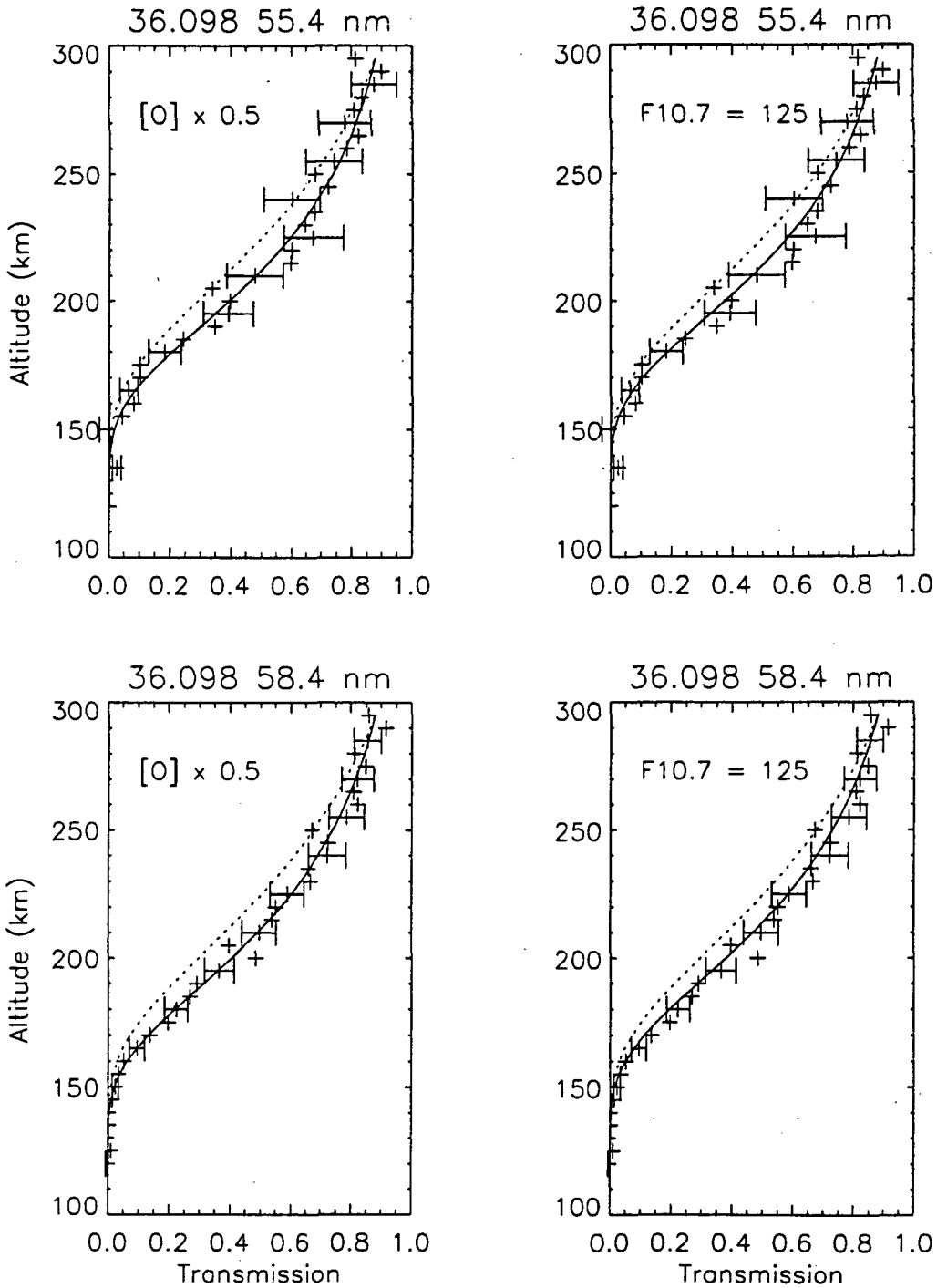


Figure 5-6 Flight 36.098 atmospheric transmission for solar emission lines. Dotted line represents MSIS prediction. In the left panels, solid lines are model predictions obtained by scaling MSIS O; in the right panels, solid lines are model predictions obtained by reducing MSIS F10.7 and, therefore, temperature. Crosses are measurements.

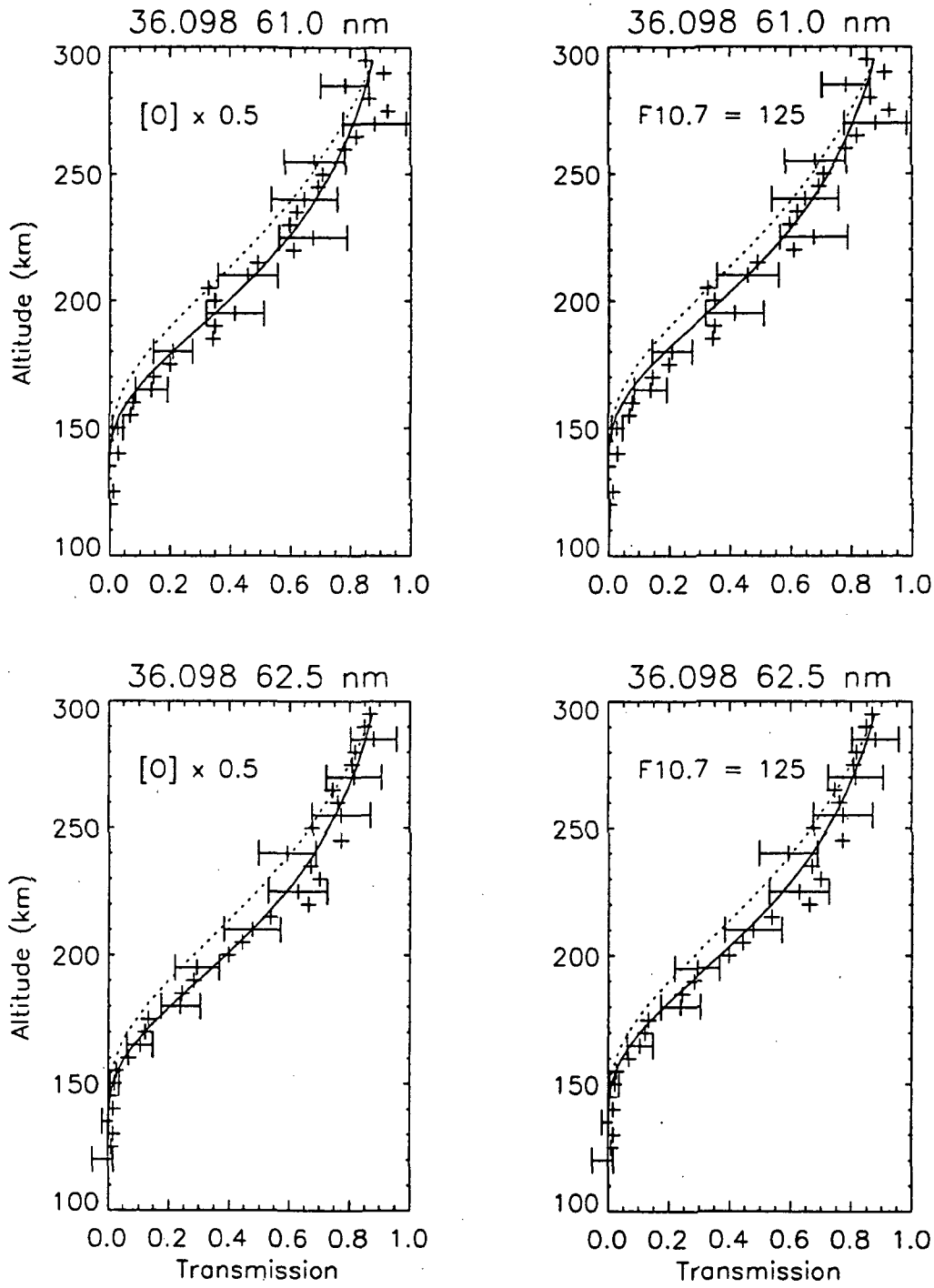


Figure 5-7 Flight 36.098 atmospheric transmission for solar emission lines. Dotted line represents MSIS prediction. In the left panels, solid lines are model predictions obtained by scaling MSIS O; in the right panels, solid lines are model predictions obtained by reducing MSIS F10.7 and, therefore, temperature. Crosses are measurements.

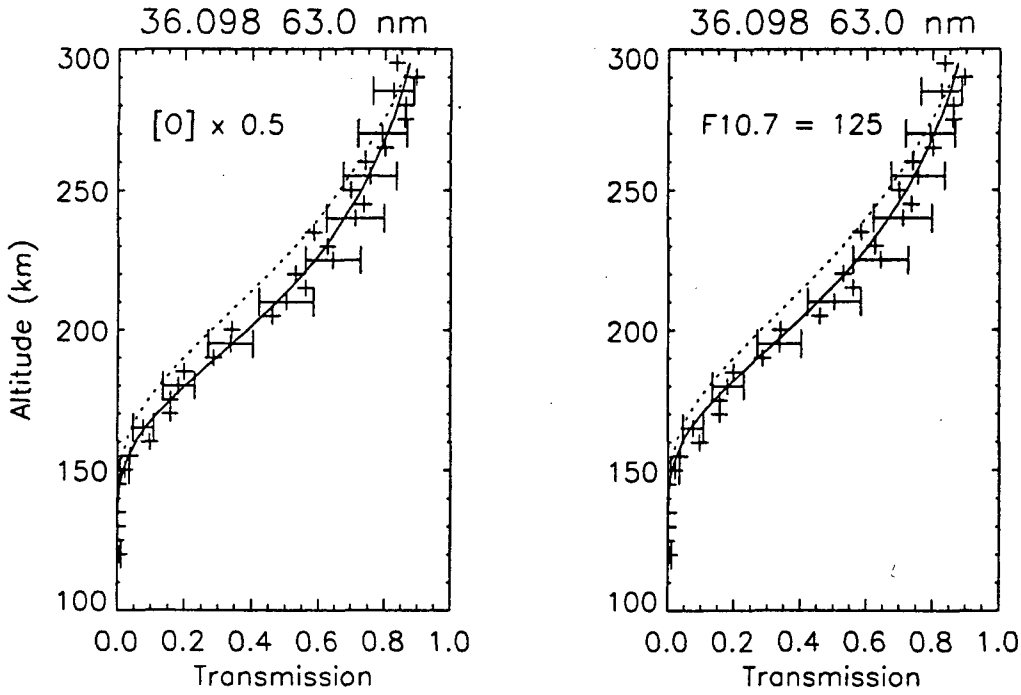


Figure 5-8 Flight 36.098 atmospheric transmission for solar emission lines. Dotted line represents MSIS prediction. In the left panels, solid lines are model predictions obtained by scaling MSIS O; in the right panels, solid lines are model predictions obtained by reducing MSIS F10.7 and, therefore, temperature. Crosses are measurements.

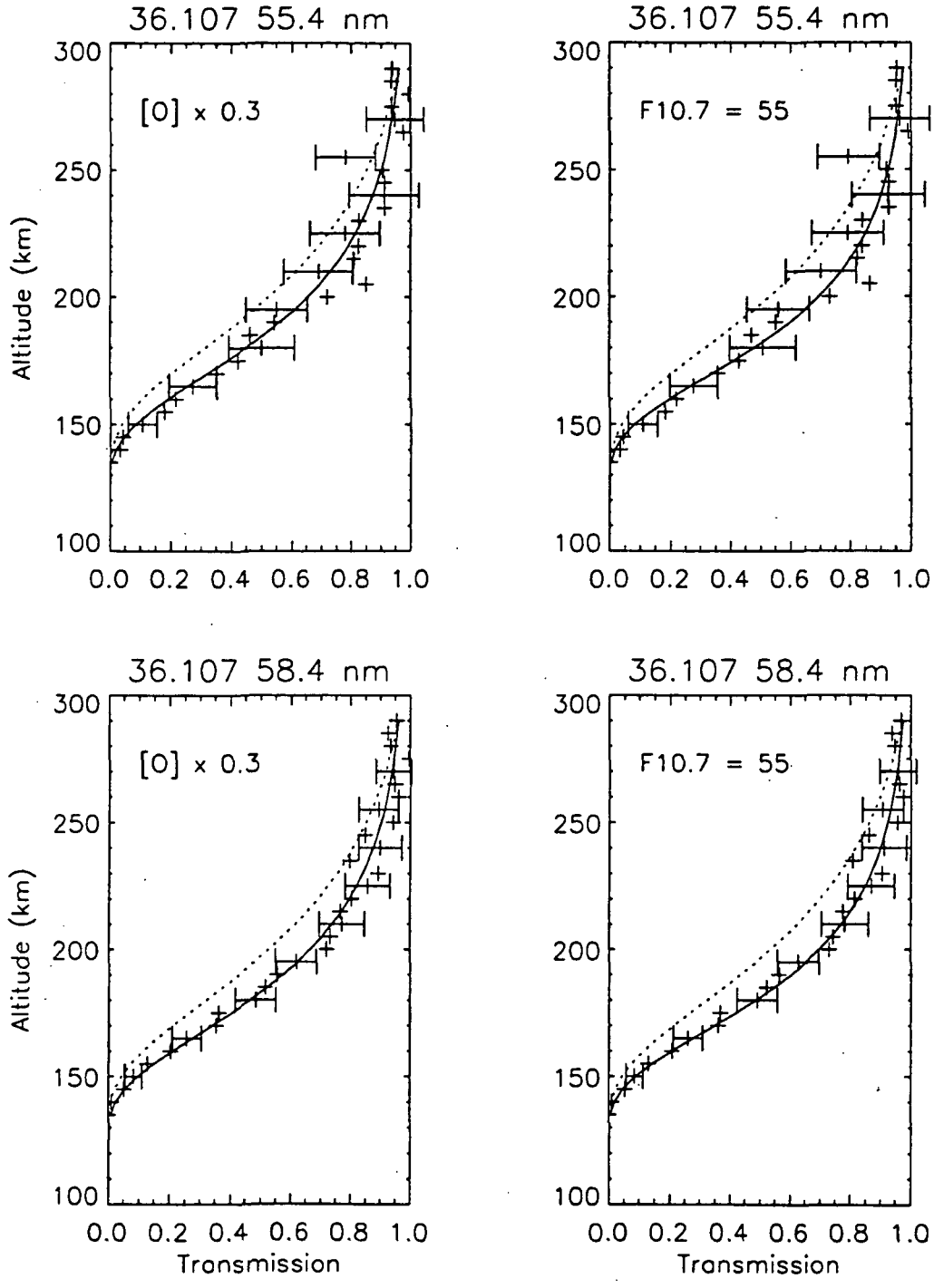


Figure 5-9 Flight 36.107 atmospheric transmission for solar emission lines. Dotted line represents MSIS prediction. In the left panels, solid lines are model predictions obtained by scaling MSIS O; in the right panels, solid lines are model predictions obtained by reducing MSIS F10.7 and, therefore, temperature. Crosses are measurements.

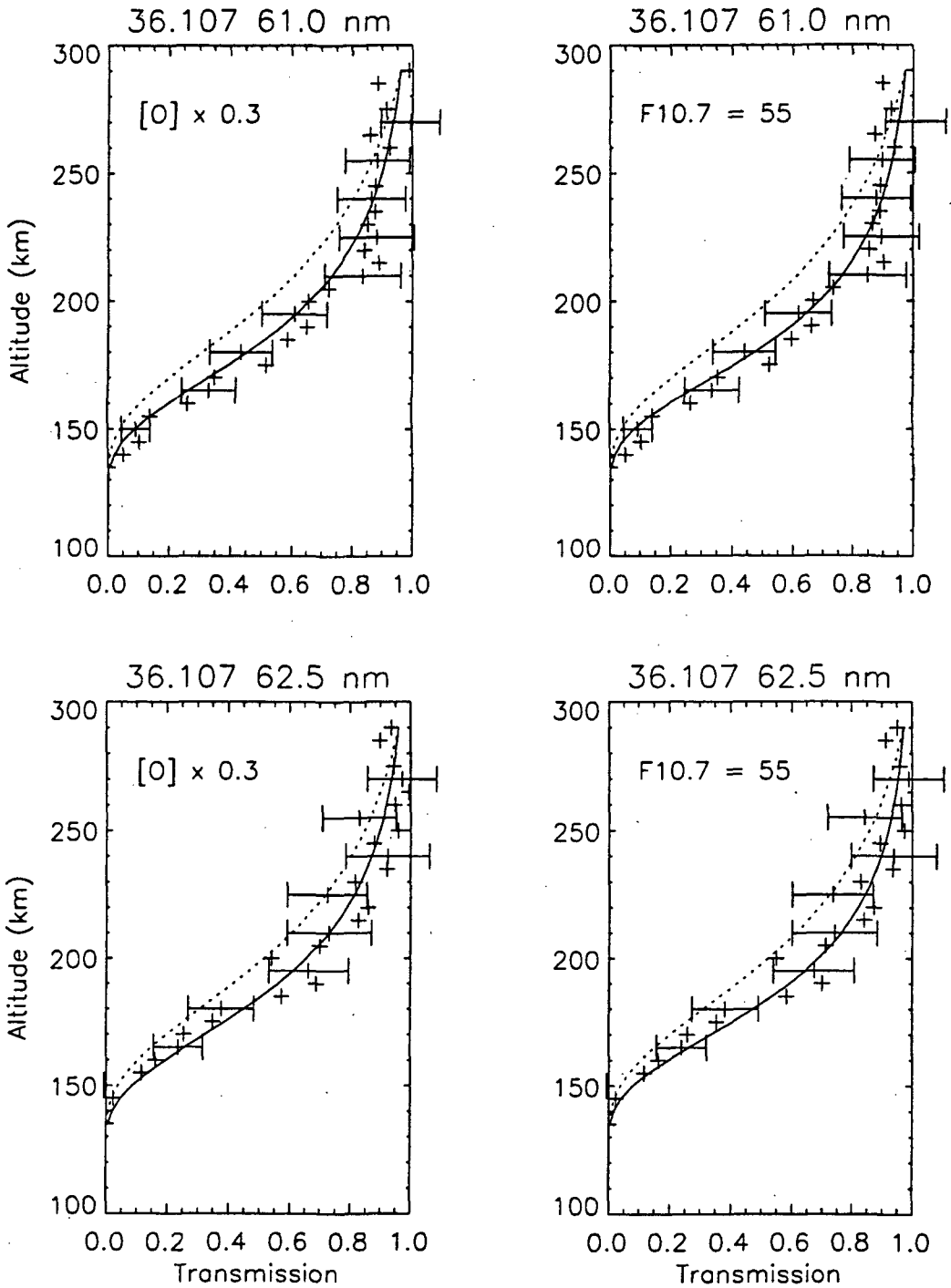


Figure 5-10 Flight 36.107 atmospheric transmission for solar emission lines. Dotted line represents MSIS prediction. In the left panels, solid lines are model predictions obtained by scaling MSIS O; in the right panels, solid lines are model predictions obtained by reducing MSIS F10.7 and, therefore, temperature. Crosses are measurements.

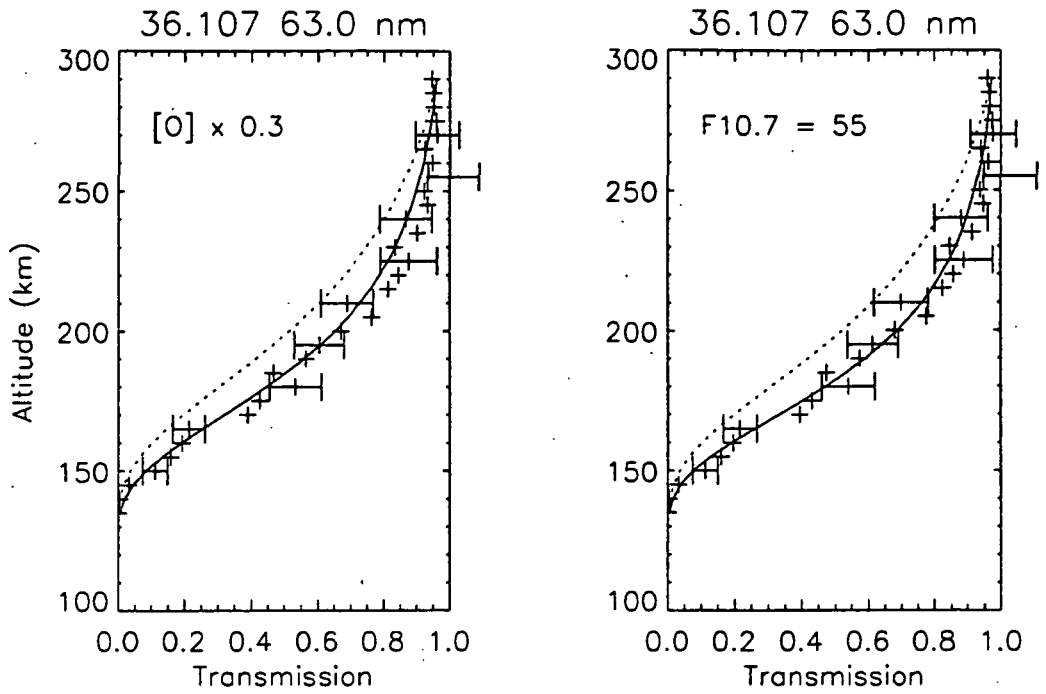


Figure 5-11 Flight 36.107 atmospheric transmission for solar emission lines. Dotted line represents MSIS prediction. In the left panels, solid lines are model predictions obtained by scaling MSIS O; in the right, solid lines are model predictions obtained by reducing MSIS F10.7 and, therefore, temperature. Crosses are measurements.

understood than the O density variability, it is reasonable that the MSIS model correctly predicts temperature, but overestimates O densities. Therefore, it is concluded that the model atmospheres containing the O scalings are the more proper results and these results will be used in the airglow calculations in Chapter VI.

Uncertainties in the inferred neutral densities are estimated by comparison of measured and calculated attenuation profiles with O scaling factors slightly larger and smaller than the values stated in Table 5-2. It is found that similar fits to those shown in Figures 5-3 through 5-11 are found for O densities of ±20% relative to those of Table 5-2. Therefore, a 20% uncertainty is attributed to the derived model atmosphere profiles. A $\chi^2$ analysis of the 36.124 results supports this conclusion.

**Table 5-2 MSIS Parameter Modifications Derived from EGS Data**

| | 36.098 | 36.107 | 36.124 |
|---|---|---|---|
| [O] Scaling Factor | 0.5 | 0.3 | 0.5 |
| $T_\infty$ (MSIS prediction) | 1137 K | 982 K | 868 K |
| F10.7 (adjusted) | 125 | 55 | 55 |
| $T_\infty$ (adjusted F10.7) | 1001 K | 709 K | 727 K |

### 5.2.4 Analysis of Solar X-ray Photometer Data

A package of six x-ray photometers was flown on each rocket flight. Although the x-ray photometers functioned properly each time, the voltage to frequency converters were saturated for 36.098, yielding no useable data. This was the result of large currents from long wavelength photons leaking to the active area of the photodiode. An improved mask design removed this problem for the later rocket flights. For these flights, each of the photometers listed in Table 4-1 obtained useful data.

Figure 5-12 shows an x-ray photometer flight profile for the Al/Sc/C coated photodiode flown on 36.124. Prior to 120 seconds, the rocket is not pointed precisely toward the sun and the data appears noisy as the sun moves in and out of the field of view. Once the rocket is pointed, the signal increases as the payload moves up in the atmosphere. At apogee, the door containing the $MgF_2$ windows is closed. This results in a low point in the data because during this period only the visible light background reaches the detector. The door is then reopened and data is taken during the down leg of the flight. As the rocket travels lower in the atmosphere, the signal decreases due to atmospheric absorption.

The analysis of the photometer data begins with the measurements made at apogee. After subtracting the visible light background signal and dividing by the aperture size, the soft x-ray radiation is converted to units of amperes per $cm^2$. Because the solar irradiance and the sensitivity of the photodiode are not constant over the instrumental passband, the conversion from current to irradiance units is not straightforward. The approach adopted here for this conversion is to scale a model spectrum so that the spectrum convolved with the photometer's wavelength dependent sensitivity yields the measured soft x-ray current. The SERF 1 model spectrum (Hinteregger *et al.*, 1981) appropriate to the conditions of the rocket flight is used for the initial spectrum. To select the wavelength regions into which the spectrum will be divided, the photometer sensitivity is convolved with the model solar spectrum as shown in Figures 5-13 and 5-14. The results of such a convolution are given in units of amperes per $cm^2$ for each wavelength interval. Dividing the result by the total current gives the fraction of current per wavelength interval. Figures 5-13 and 5-14 show these values expressed in percentages.

Analysis of Figures 5-13 and 5-14 shows that among the three photometers, the most obvious wavelength intervals are 2 - 6 nm, 6 - 17 nm, and 17 - 30 nm. A

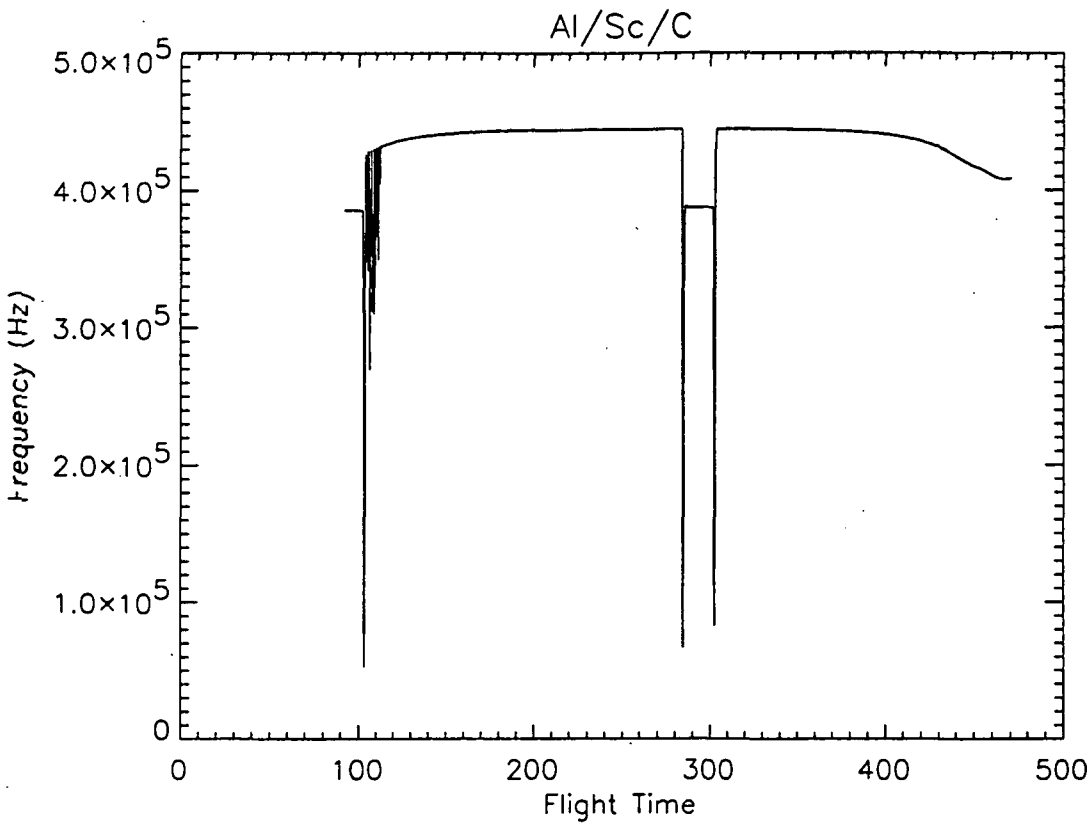


Figure 5-12 Typical flight profile for a solar x-ray photometer; the Al/Sc/C coated photodiode flown on 36.124 is shown. The period of lower count rate at apogee is the result of closing the door and placing a $MgF_2$ window in front of the photometer.

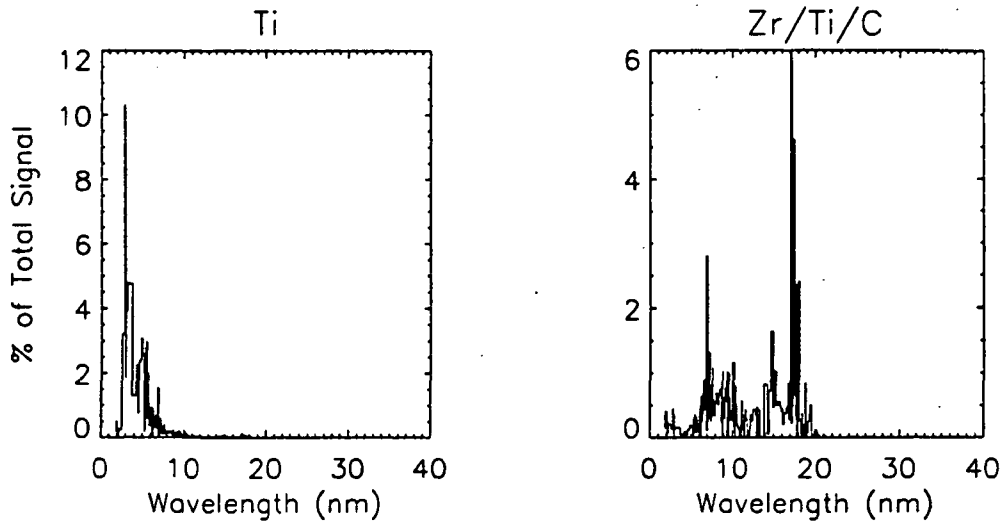


Figure 5-13 Convolution of 36.124 x-ray photometer sensitivities with reference solar spectrum.

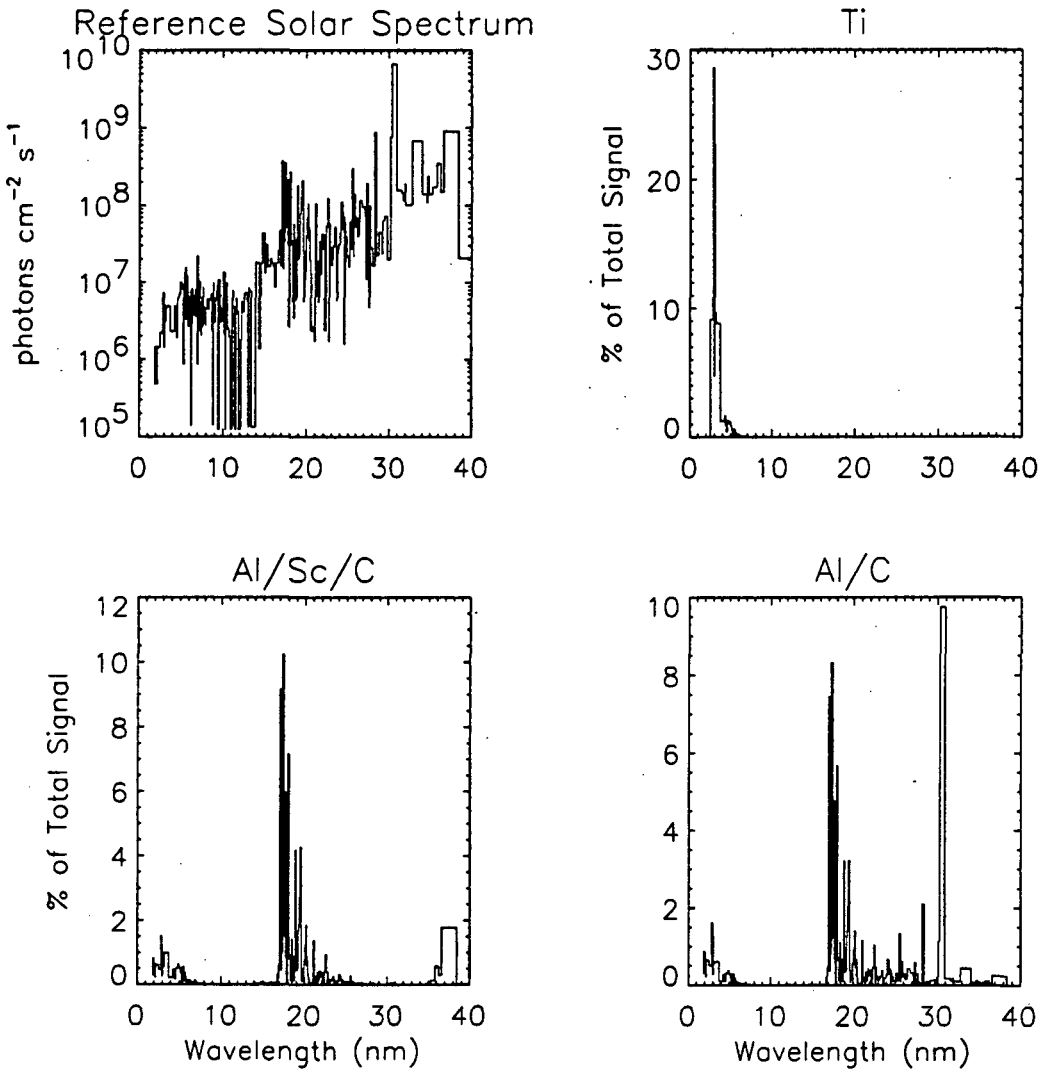


Figure 5-14 Convolution of 36.107 x-ray photometer sensitivities with reference solar spectrum. The reference solar spectrum is shown for comparison

contribution above 30 nm is from the He II 30.4 nm emission in the Al/C coated photometer data. Because this emission was measured with the EGS, that value is used in this analysis. See Appendix C for the results of the measurements.

The current $C_i$ from photodiode $i$ can be expressed in terms of solar irradiance scaling factors. The equations are of the form:

$$C_i = \sum_j A_j \left\{ \sum_\lambda \zeta_{ij}(\lambda) F_j(\lambda) \right\}, \qquad 5\text{-}3$$

where $\zeta_{ij}$ the sensitivity of diode $i$ in the spectral region $j$, $F_j$ is the solar irradiance in spectral region $j$, and $A_j$ is the scaling factor for spectral region $j$. Both $F_j$ and $\zeta_{ij}$ have the SERF 1 model resolution of approximately 0.1 nm. The goal is to solve these linear equations for the $A_j$'s. One method is to use a Ti coated photometer to solve for the 2 - 6 nm scaling factor and then use this result to calculate a 2 - 6 nm current in the other photodiodes. This current can be subtracted from the data and then a scaling factor for the 6 - 17 nm irradiance can be found with the Zr coated photometer. The process is repeated with the longer wavelength bin and the Al coated photometers. A more rigorous method of least squares fitting is also used. The similarity in results indicate that either technique is acceptable. The results for the scaling factors are shown in Table 5-3. Appendix C tabulates the results and corresponding uncertainties obtained with the back substitution method in the approximately 1 nm bins described in Chapter III.

Uncertainty in the soft x-ray measurements comes from several sources. Calibration uncertainties are included and were described in Chapter IV. Because calibrations are made at the center of the photodiode, there is an uncertainty in assuming uniform sensitivity across the active area. Although this can only be quantified by a detailed mapping of the active area, an estimate of the two sigma uncertainty is 20%. This value is arrived at by analysis of 36.107 flight data from the Al/C and Al/Sc/C photodiodes, which are sensitive in nearly the same wavelength regions. A two sigma

**Table 5-3 Scale Factors and Solar Irradiances from SXP Data**

| $\lambda_{min}$ (nm) | $\lambda_{max}$ (nm) | 36.107 Scale Factors | | 36.124 Scale Factors | |
|---|---|---|---|---|---|
| 1.8 | 6.0 | 1.35 | | 2.24 | |
| 6.0 | 17.0 | - | | 2.26 | |
| 17.0 | 30.0 | 2.06 | | 1.57 | |
| | | 36.107 Irradiance† | | 36.124 Irradiance† | |
| | | Measured | Predicted | Measured | Predicted |
| 2 | 10 | 0.75 | 0.93 | 1.15 | 0.72 |
| 5 | 57.5 | 37.2 | 29.6 | 25.9 | 23.2 |

† Irradiances are summed from $\lambda_{min}$ to $\lambda_{max}$ and are in units of photons $cm^{-2}$ $s^{-1}$ and are in units of $10^9$ photons $cm^{-2}$ $s^{-1}$. Predictions are from fit to values found in Feng *et al.* (1989, see Section 5.2.4).

uncertainty of 20% accounts for differences in absolute irradiances derived from these two photodiodes. This uncertainty also includes the application of model sensitivities to wavelength regions where no calibrations are made. An uncertainty is also introduced by currents being comparable in magnitude to noise fluctuation in the data. For example, in the Al/Sc/C photodiode, the 29-30 nm solar irradiance produces a signal which is nearly at the limit of the photometer's ability to measure current; therefore, the irradiance in this bin has a relatively large uncertainty. To quantify this uncertainty, the current produced in each wavelength bin is compared to the statistical noise of 100 Hz in the flight data. The ratio of the measurement limit, expressed in amperes, to the current produced in the irradiance bin can be converted to percentage and is the measurement uncertainty. Multiplying by two gives the two sigma measurement uncertainty which is combined with the uncertainties described above to give the values in Appendix C.

A validation of the photometer data can be made by examining the profile of the data as the rocket descends in altitude. An atmospheric transmission can be calculated for soft x-rays using the same technique described in Section 5.2.3. Using the derived solar irradiance, the modeled transmission, and the measured photometer sensitivities, a current at each altitude is calculated. The measured current can be scaled to match the model at apogee; the result yields a comparison of modeled and measured soft x-ray transmission. The atmospheric attenuation describes the shape of the current profile, as opposed to the magnitude of the profile. However, the comparison is useful because if the wavelength intervals used in the analysis are too large or too small, then the variation within that interval may not be truly represented by the analysis. Also, there would be a discrepancy between the measured and predicted profiles because the absorption cross sections are rapidly varying below 30 nm. Agreement in the shape of the profile is a demonstration that the proper background signal was removed from the data. The profiles for the Al/Sc/C coated photometer flown on both 36.107 and 36.124

are shown in Figure 5-15. The agreement is good, providing more confidence in the conclusions.

Table 5-3 lists the derived scaling factors for model solar irradiances. For both 36.107 and 36.124, scaling factors of approximately two were required to reproduce the x-ray photometer data. The corresponding integrated irradiances from 2 to 10 nm and from 5 to 57.5 nm are also listed in Table 5-3 for comparisons. For 36.107, at wavelengths where the x-ray photometers were not sensitive, the SERF I model is used with no scaling factors. Feng *et al.* (1989) tabulate several solar soft x-ray irradiance measurements and show an irradiance range of 0.5 x $10^9$ to 1.5 x $10^9$ photons $cm^{-2}$ $s^{-1}$ in the wavelength region of 2 to 10 nm for F10.7 values of 70 to 125. For the same levels of solar activity, Feng *et al.* show a range of 15 x $10^9$ to 40 x $10^9$ photons $cm^{-2}$ $s^{-1}$ for the wavelength region 5 to 57.5 nm. A linear fit can be performed to the measurements tabulated in Feng *et al.* to give the following results:

$$I_{2-10} = 0.22 + 0.0059xF10.7, \qquad 5\text{-}4a$$

$$I_{5-57.5} = 7.42 + 0.18xF10.7, \qquad 5\text{-}4b$$

where $I_{2-10}$ and $I_{5-57.5}$ are the integrated solar irradiances from 2 to 10 nm and 5 to 57.5 nm respectively. Table 5-3 also lists the results of using Equations 5-4a and 5-4b to predict the irradiances for flights 36.107 and 36.124. The predicted and measured irradiances are in very good agreement with differences of approximately 20% and as large as 40%. Given the scatter in the measurements tabulated by Feng *et al.*, the comparison is quite good. This comparison demonstrates that the measurements reported here are in good agreement with other measurements.

### 5.2.5 Reduction of FUV Airglow Measurements

The FUV airglow instrument obtained data during each of the three rocket flights. Profiles of LBH band and oxygen line emissions were measured from 120 km to apogee altitude; see Table 5-1. Unfortunately, for 36.098 and 36.107, the detector

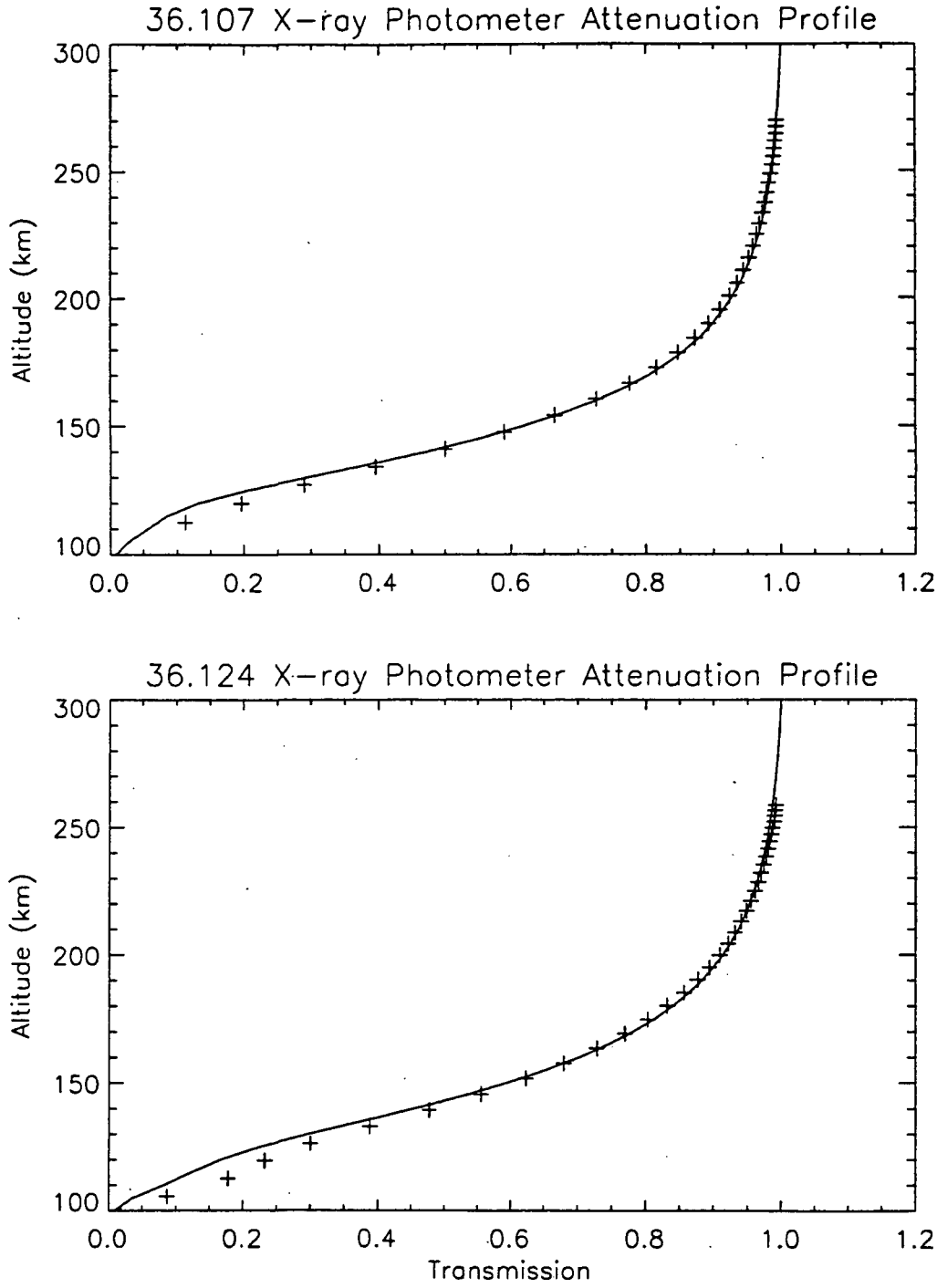


Figure 5-15 Attenuation profiles of the Al/Sc/C coated photodiode flown on 36.107 and 36.124. Crosses are data points. Solid line is prediction using MSIS atmosphere with scaled O and solar irradiance using the derived scaling factors.

suffered from significant background counts. The background counts were due to electromagnetic interference (EMI) from signals in cable bundles which travel through the airglow section of the payload from the solar section. For 36.124, the wires between the detector and the charge amplifiers were shortened and the EMI was removed.

Figure 5-16 shows a raw FUV airglow spectrum for 36.124. The LBH bands and oxygen lines are labeled. The pixel to pixel variation in the data is due to a combination of flat field response of the detector and counting statistics. The brightest LBH features in the spectrum are the (4,0) and (2,0) bands. The (2,0) band is not blended with other emissions. The (4,0) band at 132.5 nm is partially blended with the scattered light from the very bright OI 130.4 nm emission. The effects of scattered light from gratings have been studied in detail by Woods *et al.* (1994). Figure 5-17 shows a raw spectrum for 36.098 and 36.107. Although the effect of the EMI is obvious, the airglow features are clearly resolved.

To obtain profiles of count rate versus altitude, the counts from each pixel contributing to a given emission are summed into 5 km altitude bins. For the (4,0) band of LBH, contributions from the scattered light wings of the OI 130.4 nm line are subtracted off. This subtraction is accomplished by using the shape of the 130.4 nm line measured at apogee, and scaling it according to the integrated count rates at lower altitudes. At apogee, emission from the LBH bands is negligible compared to the OI counts in the same pixel locations. Therefore, at apogee, the counts in the pixels which contain the LBH feature at lower altitudes are assumed to contain only counts from the OI feature. The sum of the counts in these pixels at higher altitudes is then scaled by the ratio of the OI 130.4 nm brightness at each altitude to the brightness at apogee. The resulting profile is then subtracted from each of the LBH (4,0) sums to yield an altitude profile of count rate for the LBH (4,0) band emission.

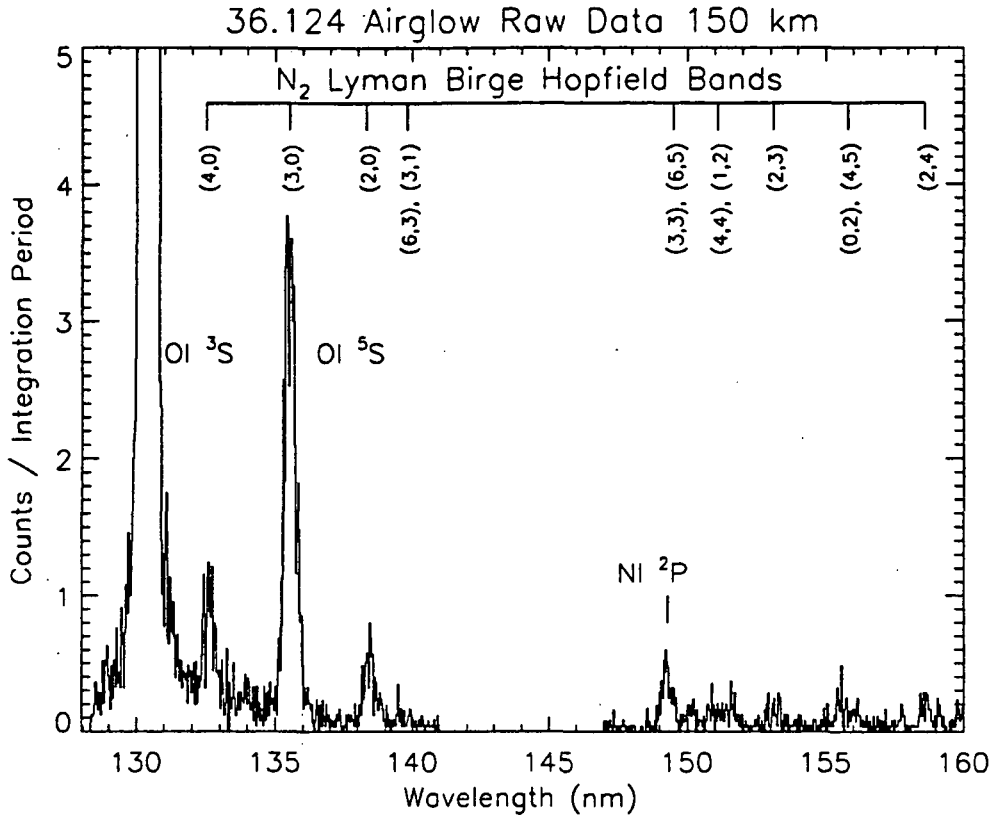


Figure 5-16 Raw 36.124 FUV airglow spectrum at 150 km. Emissions of OI, NI, and $N_2$ are labeled. Data between 142 and 147 nm are not shown due to a defect in the CODACON detector.

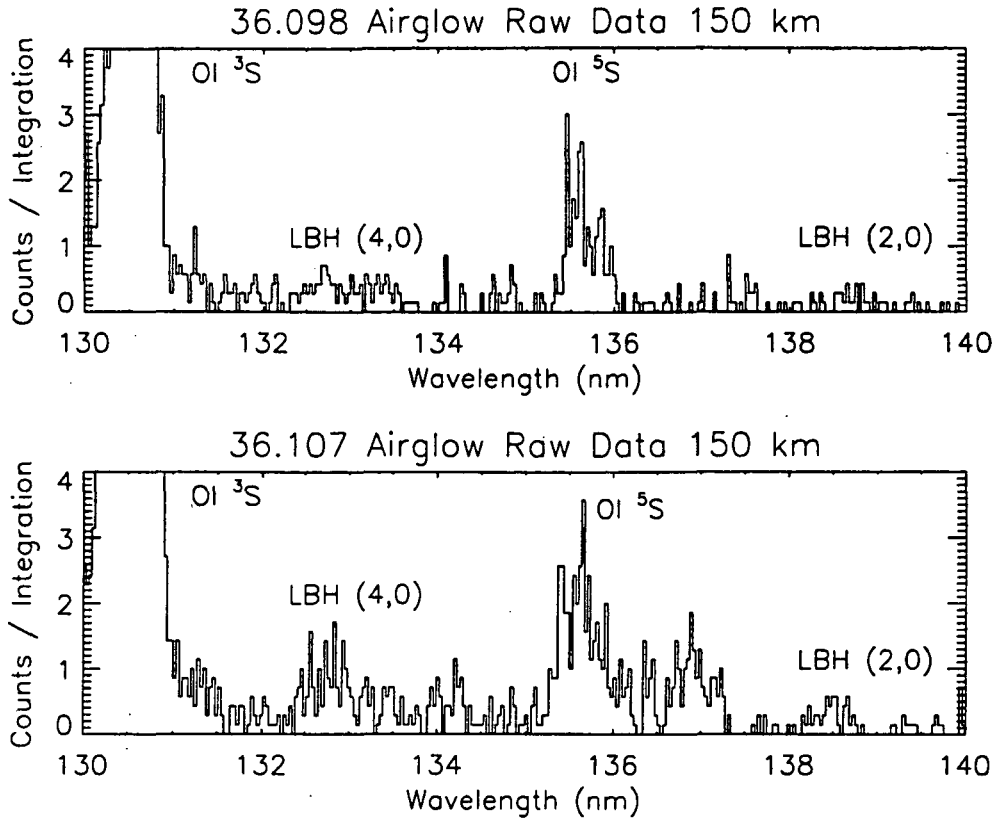


Figure 5-17 Raw 36.098 and 36.107 FUV airglow spectrum at 150 km. Data at longer wavelengths is not shown due to contamination by background signals. Some background signal is evident in the figure.

For the 36.098 and 36.107 flights, the above procedure is also followed. In these cases however, the goal is not only to subtract the OI 130.4 nm background from the 132.5 nm signal, but also to subtract the background noise counts across the detector. The OI emissions are bright enough at all altitudes so that contamination is small. The OI background is estimated by finding the background in the surrounding pixels and assuming it to be the same over pixels containing the OI emissions. For the LBH bands, the apogee signal is assumed to be entirely due to contamination. By summing the counts across the brightest contamination feature at each altitude and scaling the apogee spectrum according to this profile, a background spectrum is obtained for each altitude. By subtracting these spectra from the raw spectra at each altitude, the measured spectra due to airglow is obtained. The pixels containing the emissions can then be summed at each altitude to obtain profiles of count rate versus altitude.

An effect of the high background counts in 36.098 and 36.107 was to create secondary images of the emissions. The measured spectra contained a feature at a wavelength where no airglow is present. This feature tracked the bright OI 130.4 emission exactly. This behavior of the old style gray-code CODACON detector is expected for count rates larger than approximately 10 KHz. The newer style, uniform-code CODACON detector, as used on the EGS, does not exhibit this behavior except at extremely large count rates above approximately 50 KHz. The fraction of counts in secondary images is assumed to be the same for all emissions; therefore, the correction for the 130.4 nm emission was applied to the other emissions. This correction resulted in an approximately 10% increase in brightness. No secondary images appear in the 36.124 data.

Once altitude profiles are obtained, the conversion to brightness units is performed. Recall that for the EGS, the irradiance was derived by dividing the

measured spectrum by the calibration curve. The calibration for the EGS was obtained by using a continuum source. For the airglow instrument, the calibration was obtained at individual wavelengths using a Pt lamp. The units for this calibration are counts second$^{-1}$ Rayleigh$^{-1}$. To obtain the brightness of a feature at an altitude, the count rate at the altitude is divided by the calibration at the wavelength of the feature. Because both the calibration and data reduction procedures require integration over the pixels containing a feature, the flat field response of the detector can be ignored.

Figures 5-18 through 5-20 show the altitude profiles of the OI lines and two LBH bands for each of the rocket flights. Table 5-4 lists the peak brightnesses for each of these emissions. The LBH emissions are similar at high altitudes, as predicted by Franck-Condon theory. At low altitudes, the 138.3 nm emission is significantly weaker than the 132.5 nm emission due to absorption by $O_2$ being more significant at 138.3 nm than at 132.5 nm. The cross section for pure absorption by $O_2$ is shown in Figure 3-11. The LBH (3,0) band underlies the OI 135.6 nm emission accounting for approximately 15% of the intensity at 150 km. The FUV airglow spectrograph does not contain sufficient spectral resolution to resolve the two emissions; therefore, when comparing this data to theory, the model results for the LBH (3,0) band and the OI 135.6 nm emission will have to summed.

The $CaF_2$ lens used in the airglow telescope was calibrated at a room temperature of approximately 25° C (see Chapter IV). Although $CaF_2$ transmission is known to vary with temperature, flight temperature monitors in the telescope did not shown any significant deviation from 25° C. Therefore, the room temperature calibration is assumed to be valid throughout the flight.

The TV camera was co-aligned with the airglow instrument for each of the three flights and was used for real time attitude verification. Corrections were made at apogee to ensure limb viewing of the airglow spectrograph. Based on the uncertainty in

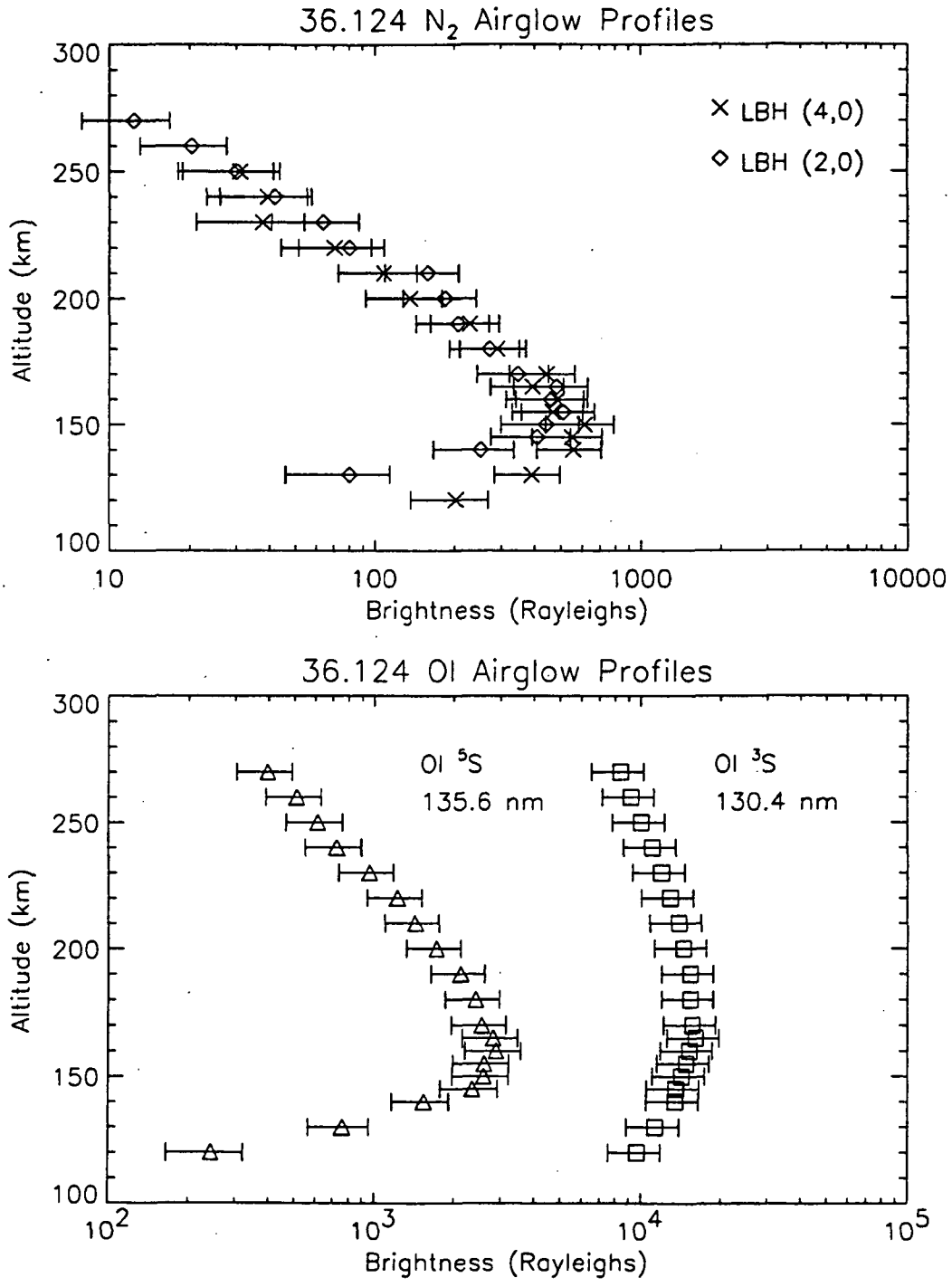


Figure 5-18 Altitude profiles of $N_2$ and OI FUV airglow emissions for 36.124.

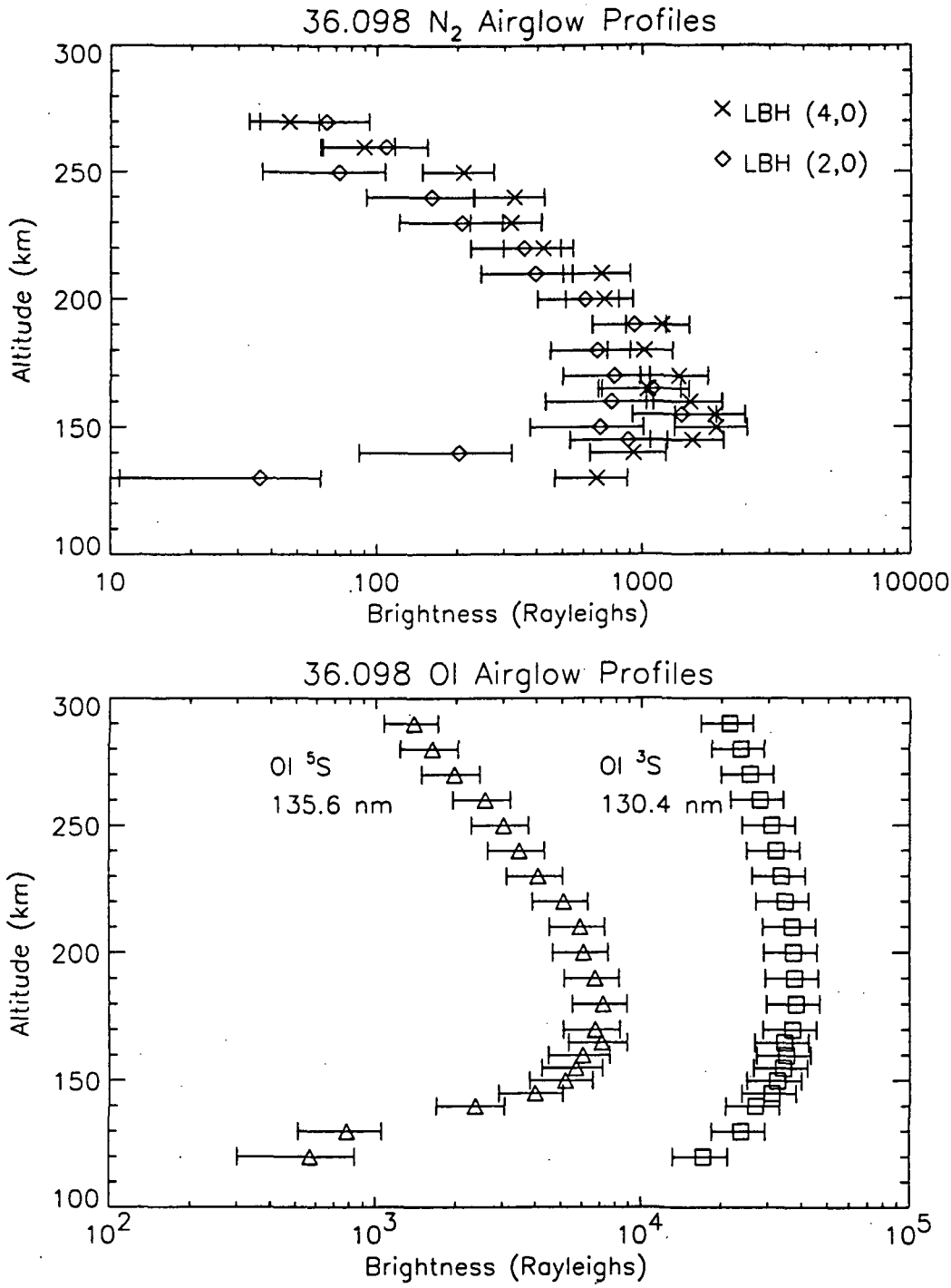


Figure 5-19 Altitude profiles of $N_2$ and OI FUV airglow emissions for 36.098.

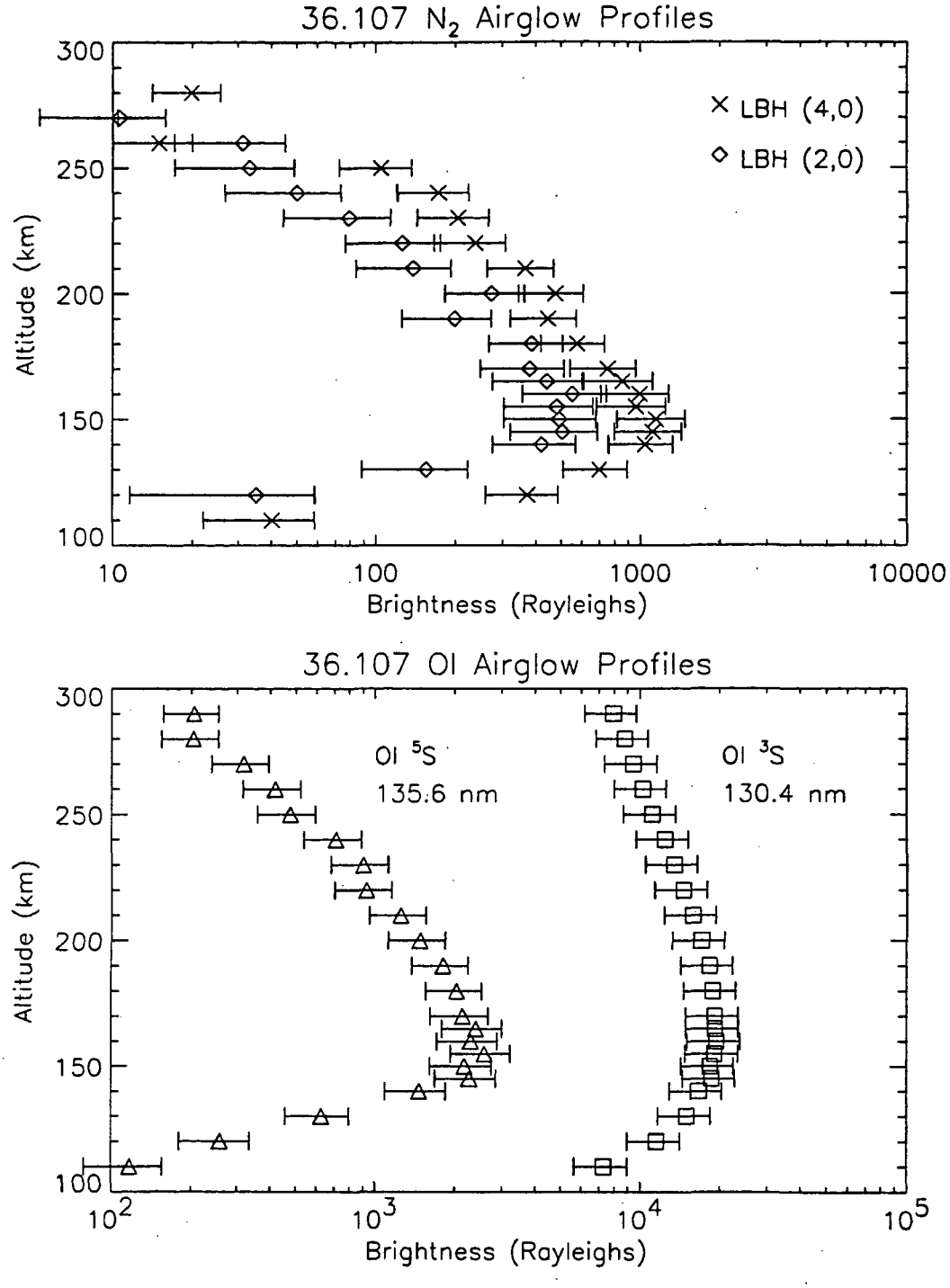


Figure 5-20 Altitude profiles of $N_2$ and OI FUV airglow emissions for 36.107.

measuring the angles on the TV screen, the uncertainty in this method is approximately 0.25°. For all calculations in Chapter VI, it is assumed that the airglow instrument is limb viewing (90° observation zenith angle).

**Table 5-4 Peak Brightnesses for Airglow Emissions†**

| | 36.098 | 36.107 | 36.124 |
|---|---|---|---|
| $N_2$ LBH (4,0) 132.5 nm | 2.0 | 1.1 | 0.62 |
| $N_2$ LBH (2,0) 138.3 nm | 1.4 | 0.49 | 0.51 |
| OI $^5S$ 135.6 nm | 7.2 | 2.7 | 2.9 |
| OI $^3S$ 130.4 nm | 38.2 | 19.3 | 16.1 |

† All brightnesses are in units of kilorayleighs. See Section 4.3.3.1 for uncertainties.

## 5.3 Summary

The goal of this chapter was to convert the rocket measurements into physical units. The solar instruments provided solar irradiance as well as atmospheric structure information. For each flight, the MSIS model atmosphere overestimated the amount of EUV attenuation. Further analysis indicated that only the MSIS O density was overestimated. For both 36.107 and 36.124, a factor of approximately two scaling of SERF 1 model solar irradiances was required to account for the x-ray photometer data. These results were in excellent agreement with other measurements (Feng *et al.*, 1989, Ogawa *et al.*, 1990). Appendix C lists the solar irradiance results; Table 5-2 describes the atmospheric structure results. Although some of the FUV airglow data was contaminated, backgrounds were subtracted and airglow profiles are shown in Figures 5-18 through 5-20. In Chapter VI, airglow model predictions based on the measured solar irradiance and inferred atmospheric densities will be compared to these profiles.

# Chapter VI

# Comparison of Airglow Measurements to Models

## 6.1 Introduction

The goal of this dissertation is to study the response of the upper atmosphere to variations in solar irradiance. In Chapter III, models were described which predict airglow brightnesses. These models require solar irradiance and atmospheric densities as input parameters. In Chapter V, measurements of solar irradiance, the neutral atmosphere, and the Earth's FUV airglow were described. In the following sections the model results are compared to the airglow data.

## 6.2 Application of Numerical Models

The */glow* photoelectron model was described in Chapter III. This model uses solar irradiance to calculate photoelectron spectra at altitudes between 100 and 1000 km. The solar irradiance for each rocket flight was determined in Chapter V and is tabulated in approximately 1 nm bins in Appendix C. This irradiance binning scheme is used in the */glow* model. The atmospheric profiles inferred in Chapter V are assumed. From the calculated photoelectron spectra and the electron impact excitation cross sections of Chapter II, volume excitation rates are calculated using Equation 3-12.

For LBH, the volume excitation rate at each altitude is multiplied by a synthetic spectrum appropriate for the temperature at that altitude. The synthetic spectrum is in 0.1 nm bins. Each wavelength bin is integrated along the line of sight of the airglow instrument according to the optically thin radiative transfer algorithm described in Chapter III, yielding a model spectrum. By summing the spectrum over individual emission features at each altitude, brightness profiles are obtained.

Initial volume excitation rates of the OI emissions are input into the optically thick radiative transfer algorithm described in Chapter III. The resultant final excitation

rates are then integrated along the line of sight of the airglow instrument using Equation 3-20. For the OI 130.4 nm emission, both the resonant scattering of sunlight and photoelectron impact excitation sources are considered. The solar 130.4 nm irradiances implemented in the model were measured by the SOLSTICE instrument aboard the UARS satellite are used. These irradiances are listed in Table 5-1 and are provided by Dr. T. N. Woods (private communication, 1995). Pure absorption by $O_2$ is taken into account for each emission as described in Chapter III.

The LBH (3,0) underlies the OI 135.6 nm emission; typical contributions are on the order of 15%. The spectral resolution of the FUV airglow instrument is not sufficient to resolve the two features; therefore, the modeled LBH (3,0) brightness is added to the modeled OI 135.6 nm brightness for each comparison.

For both the optically thin and optically thick emissions, the excitation rate integrations along the line of sight of the instrument are carried out over 0.25° increments above and below the limb. In Chapter 4, it was shown that the telescope on the airglow instrument yielded different field of view responses for different wavelengths. The integration is scaled at each wavelength according to the appropriate field of view profiles displayed in Figure 4-11. Summing the scaled results at each altitude yields brightness profiles which can be compared to the measurements.

## 6.3 Comparison of Model Results to Airglow Data

In this section, comparisons are made between the model described above and the FUV airglow measurements. For each rocket flight, the LBH (4,0) and (2,0) bands and the OI 135.6 and 130.4 nm lines are studied. These are the brightest emissions in the measured spectra and are best suited for studying the effects of solar irradiance on the upper atmosphere. In comparing the model results and data, the uncertainties in all measurements must be considered. From Chapter V, the airglow data has an uncertainty of approximately 25% and the inferred atmospheric densities have an uncertainty of approximately 20%. From Appendix C, the uncertainties in the solar

irradiance vary with wavelength; a representative uncertainty for the solar soft x-ray irradiance is 25%. These uncertainties are two sigma values. Assuming the uncertainty in the model calculations is due only to uncertainty in solar soft x-ray irradiance and neutral atmosphere, the root mean square uncertainty in model and measurement comparisons is approximately 40%.

### 6.3.1 Analysis of 36.124 Data

The data set from 36.124 is superior to the data sets of the previous flights. The airglow instrument suffered no significant background counts and the solar instruments measured the solar irradiance from 2 to 120 nm with no gaps. The completeness of this data set implies that the comparison between the airglow measurement and the model should be the most accurate.

Figure 6-1 compares the 36.124 model results with the 36.124 airglow data described in Chapter V. The upper panel displays the results for the two LBH emissions; for both features, agreement is excellent at all altitudes. The model reproduces the data curves in magnitude and shape, placing the peak brightness at the correct altitude. The agreement is equally good for both emissions. Because the LBH (2,0) band is significantly absorbed by $O_2$, and the LBH (4,0) band is not, this agreement provides confidence that the $O_2$ density, as well as the absorption by $O_2$, are correct in the model.

The lower panel of Figure 6-1 compares the measurement and the model calculation of the OI emissions. Excellent agreement is again obtained. This is particularly true for the $^3S$ emission at 130.4 nm. For the $^5S$ emission at 135.6 nm, the model accurately reproduced the peak brightness. However, the altitude of the peak from the model is slightly higher (less than 5 km) than from the data. Also, the data have a slightly steeper slope at higher altitudes. These small differences may indicate that the true O density is slightly different than the uniformly scaled O density inferred in Chapter V.

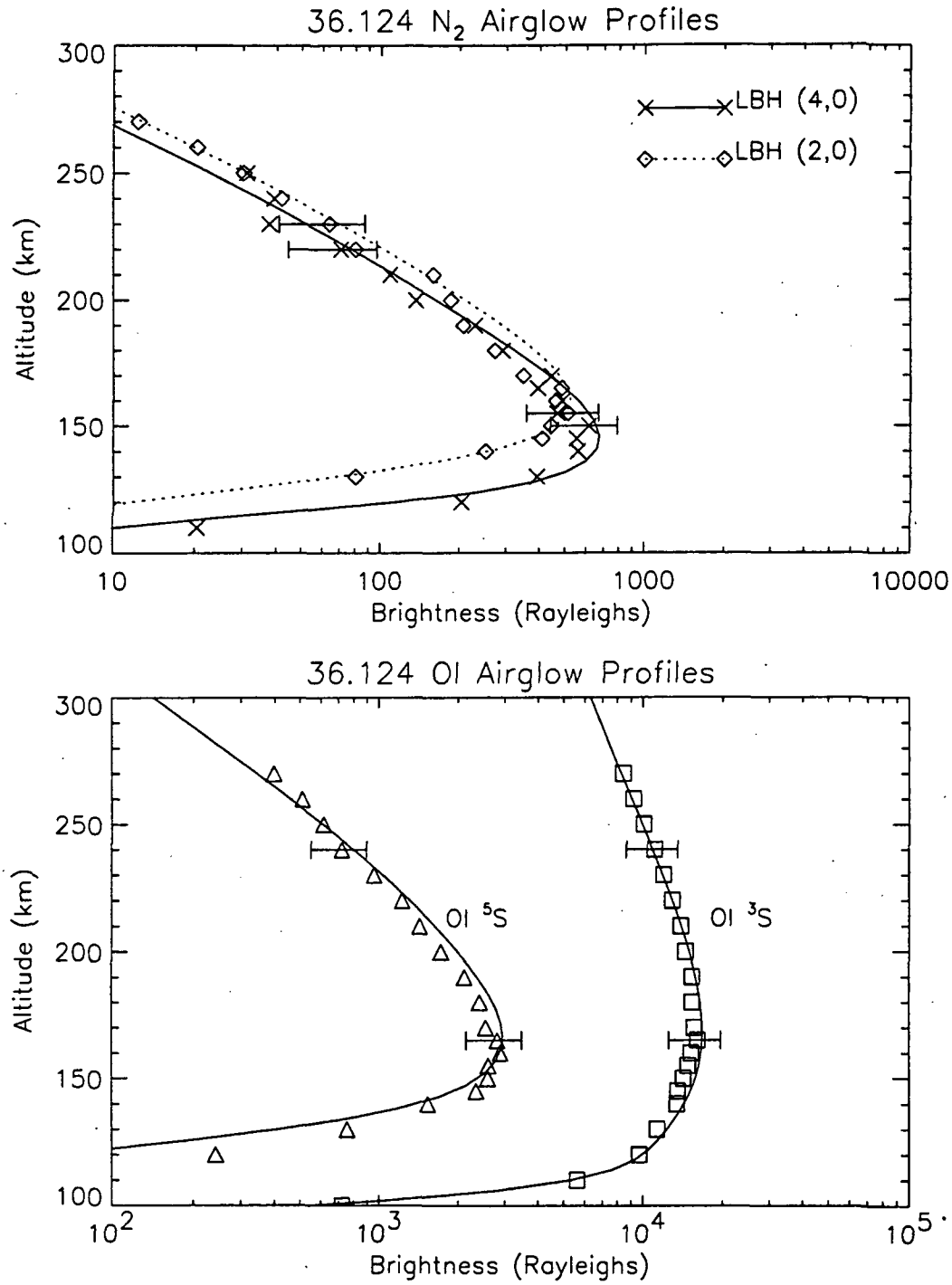


Figure 6-1 Comparison of modeled and measured airglow for 36.124.

### 6.3.2 Analysis of 36.098 Data

For the 36.098 rocket flight, the solar x-ray photometers did not provide useful data. Thus, modeling must begin without measurements of the solar irradiance below 30 nm. For this wavelength region, the SERF 1 model solar irradiance appropriate to the day of the launch is used. The model atmosphere inferred in Chapter V is assumed.

Figure 6-2 compares the measurements and model calculations of the FUV airglow. Although there is scatter in the LBH data, the model clearly underestimates the magnitude of the emissions. This discrepancy is true for the OI data as well.

In Chapter V, it was shown that the x-ray photometer measurements required approximate factor of two scalings of the SERF 1 model solar irradiances to explain the data. This scaling is true for wavelengths below 30 nm and for both 36.107 and 36.124. Because the solar irradiance below 30 nm was not measured on 36.098, a logical step would be to perform the airglow calculation with the model solar irradiance below 30 nm scaled by a factor of two. Figure 6-3 shows the results of 36.098 airglow measurements and model calculations using this approach. As in Figure 6-2, measured solar irradiance is used above 30 nm. The comparison between model and measurement is much improved. Although the magnitude of the peak brightness of the LBH bands is still underestimated by the model, the agreement is much closer than in Figure 6-2. The correlation between the model and the data for the OI 135.6 nm emission is also quite good. Although there is disagreement at the higher altitudes, the peak brightness in the measurements is well reproduced by the model.

Unfortunately, the agreement between the model and the measurement is still poor for the OI 130.4 nm emission. Although the shapes of the profiles are very similar, the peak brightness in the model calculation is only 0.65 times the measured peak brightness. Considering the success in reproducing the measurements for the other emissions, the discrepancy in the 130.4 nm profiles is unusual. The LBH comparisons show that the scaled model solar irradiance is valid, and the OI 135.6 nm

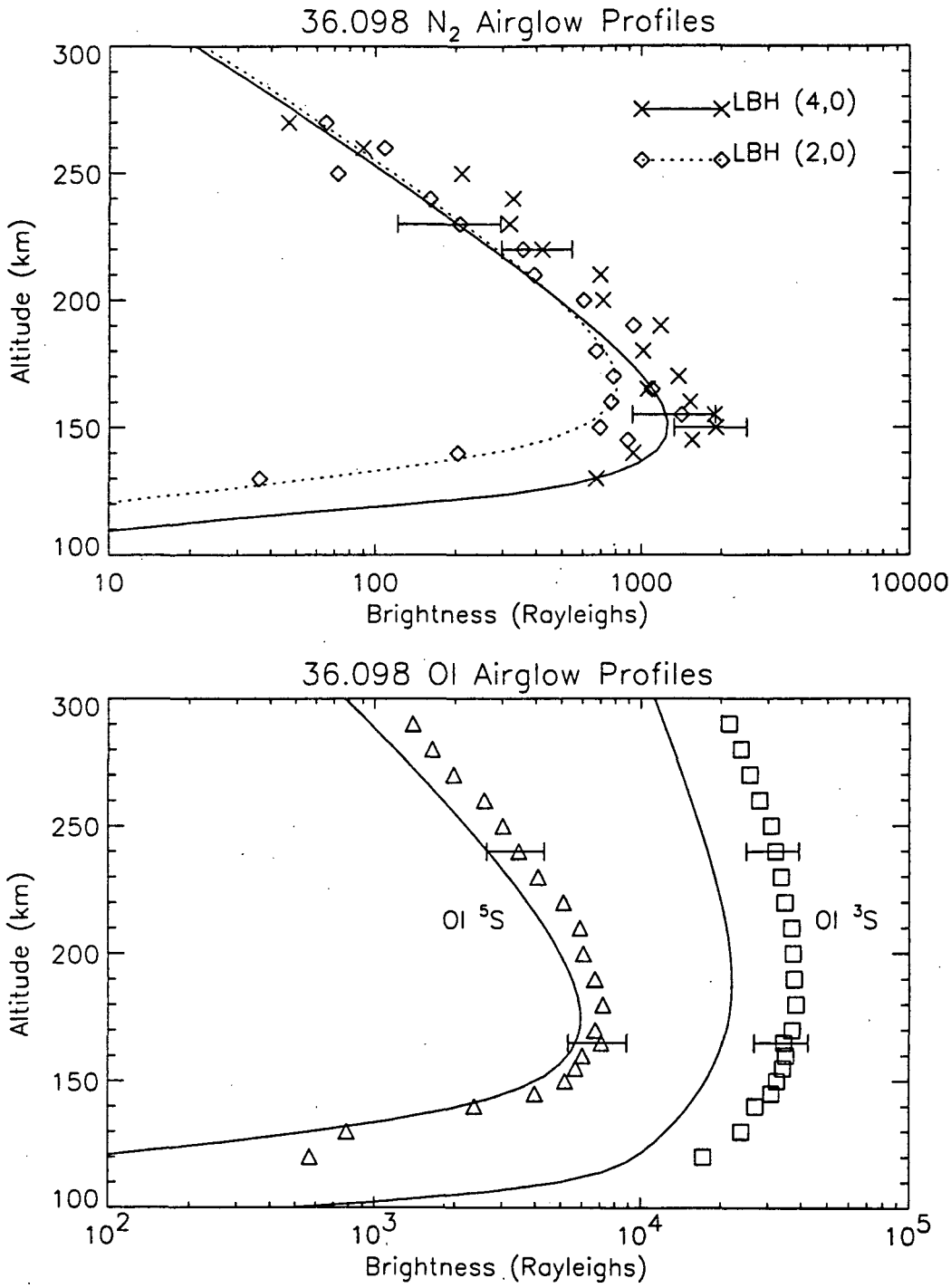


Figure 6-2 Comparison of modeled and measured airglow for 36.098. Because no solar irradiance measurements were made below 30 nm, the SERF 1 model solar irradiance appropriate to the conditions of the rocket launch is used.

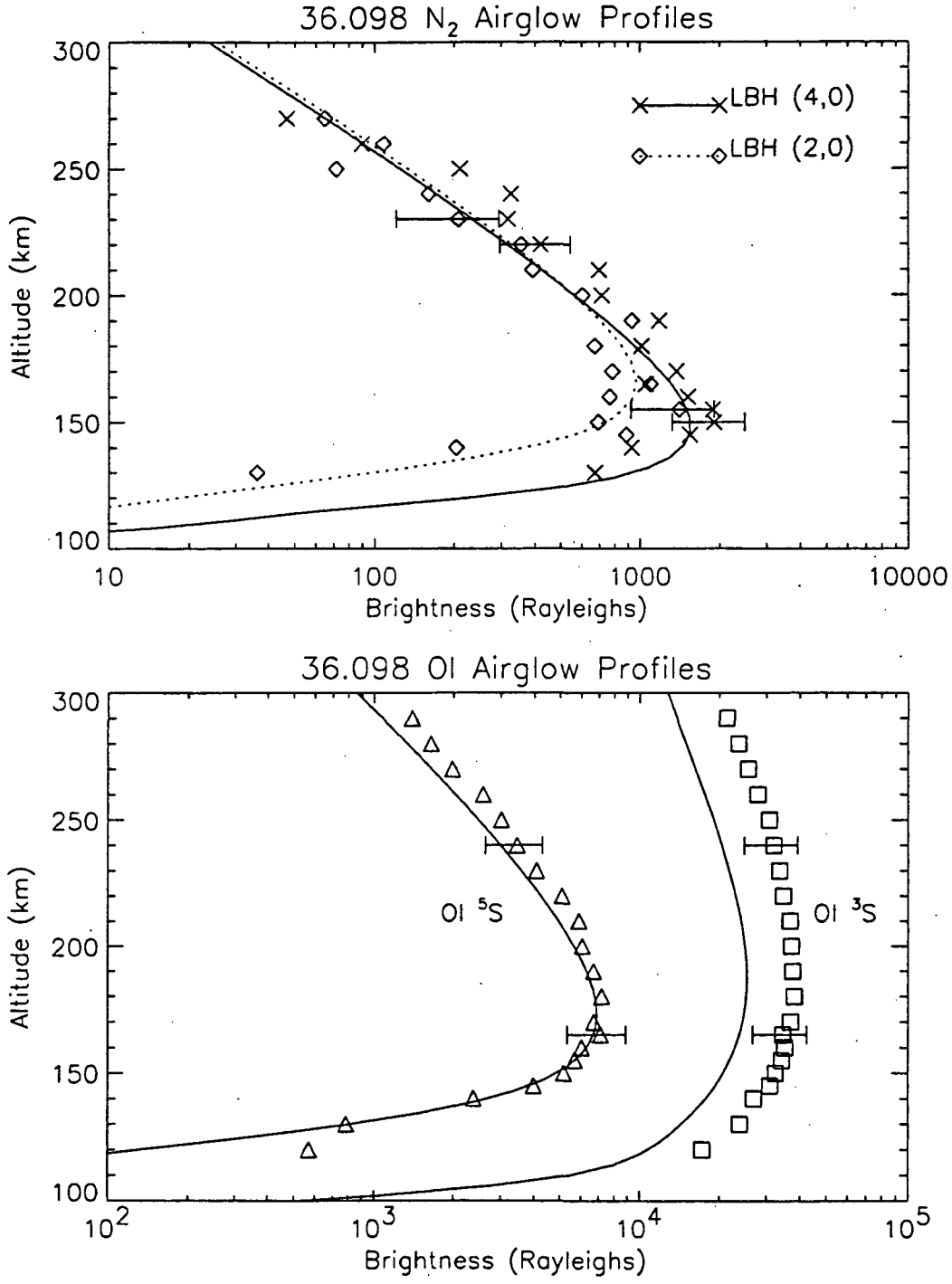


Figure 6-3 Comparison of modeled and measured airglow for 36.098. Here, the SERF 1 model solar irradiance below 30 nm has been scaled by a factor of two.

comparisons show that the inferred O density is appropriate. The success in the previous comparisons also indicates that it is unlikely that the discrepancy is an instrumental effect. This theory is reinforced by the fact that the sensitivity of the airglow instrument was unchanged between the three rocket flights. One possible explanation lies in the transmission of the $CaF_2$ filter in the airglow instrument telescope. $CaF_2$ transmission is known to be a function of temperature; however, the temperature differences inside the telescope on the three rocket flights differed by less than 5° C. Such temperature changes affect transmission on the order of 1% at 130.4 nm (Samson, 1967) and are therefore negligible. Also, the effect of a warm $CaF_2$ filter would be to reduce transmission and lower the measured count rate leading to an underestimate of the brightness. In the case of these measurements, the brightnesses are too large reinforcing the conclusion that the discrepancy is not an instrumental effect.

The disagreement between the modeled OI 130.4 nm profiles and the data is near the edge of the combined measurement uncertainties; however, the success in modeling the other emissions, in particular the OI 135.6 nm emission, suggests the airglow models are correct. The lack of an instrumental solution to the discrepancy then suggests that an excitation source in the modeling is being underestimated.

### 6.3.3 Analysis of 36.107 Data

The 36.107 data set contains solar irradiance measurements from 2 through 120 nm, excluding 6 through 17 nm. Although the airglow instrument detector suffered contamination, the LBH and OI emission brightnesses were successfully extracted from the data.

Using the same procedures described above, model calculations of airglow brightnesses were performed for the 36.107 flight. Figure 6-4 compares the model results with the measurements. The LBH (4,0) band is well reproduced by the model. Above 200 km, scatter in the data weakens the comparison; however, the shape and magnitude of the peak emission layer are in excellent agreement. In contrast, the LBH

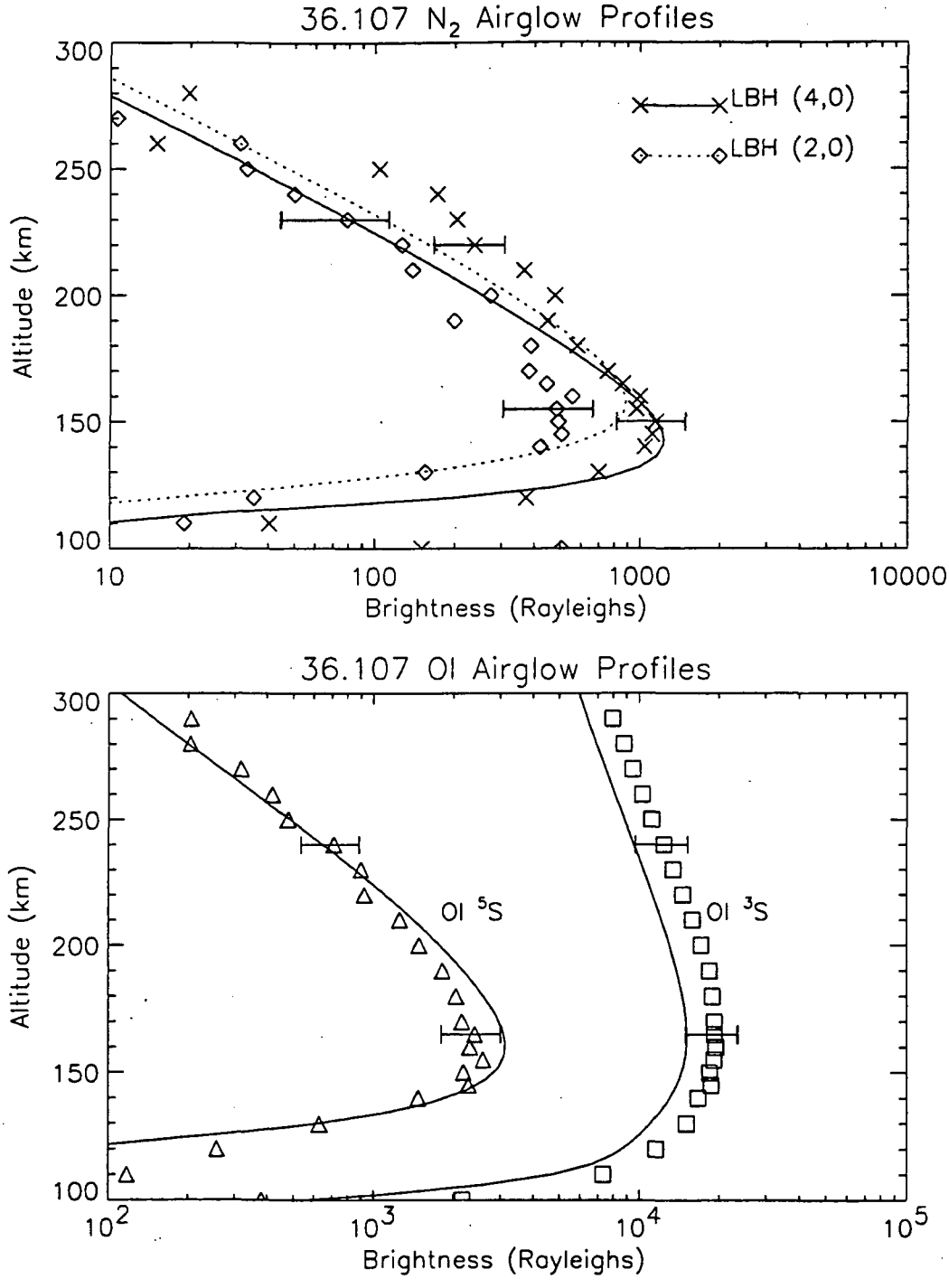


Figure 6-4 Comparison of modeled and measured airglow for 36.107.

(2,0) band is not well reproduced by the model. Above 170 km, the model and data agree; near the peak emission layer, however, the magnitude of the measurements are only about 0.6 times the model results.

The magnitudes of the OI 135.6 nm model and the measurements are in reasonable agreement, but the model is slightly brighter and falls off more rapidly with altitude. These disagreements are small and may indicate that the uniform scaling of the MSIS O profile in Chapter V is not entirely adequate. As in the 36.098 case, the OI 130.4 nm emission is underestimated by the model. The shape of the measured profiles is well reproduced by the model; however, the magnitude of the calculated brightness is 75% of the measured brightness. Although the discrepancy is within the uncertainties of the measurements, the same arguments as for the 36.098 discrepancies apply; the success in modeling the other airglow emissions implies that larger excitation rates to the $^3S$ state are needed in the model.

The discrepancy between the calculated and measured LBH (2,0) brightnesses may be the result of a larger $O_2$ density in the atmosphere than is used in the model. The LBH (2,0) band is significantly absorbed by $O_2$, whereas molecular absorption of the LBH (4,0) band is negligible. The EUV attenuation measurements described in Chapter V did not yield any information concerning $O_2$ densities. To test the above hypothesis, model calculations were performed with the MSIS $O_2$ density scaled by a factor of two. Scaling the $O_2$ density is not expected to alter the solar attenuation results of Chapter V because $O_2$ was shown to be a negligible absorber at the wavelengths considered. The results of airglow model calculations with the scaled $O_2$ atmosphere are shown in Figure 6-5.

With the $O_2$ scaling, the comparisons between calculated and measured LBH (4,0) and OI 130.4 nm brightnesses are unchanged. For the OI 135.6 nm emission, agreement is improved near the peak. Below the peak, however, the comparison is somewhat degraded, with the model underestimating the brightness. For the LBH (2,0)

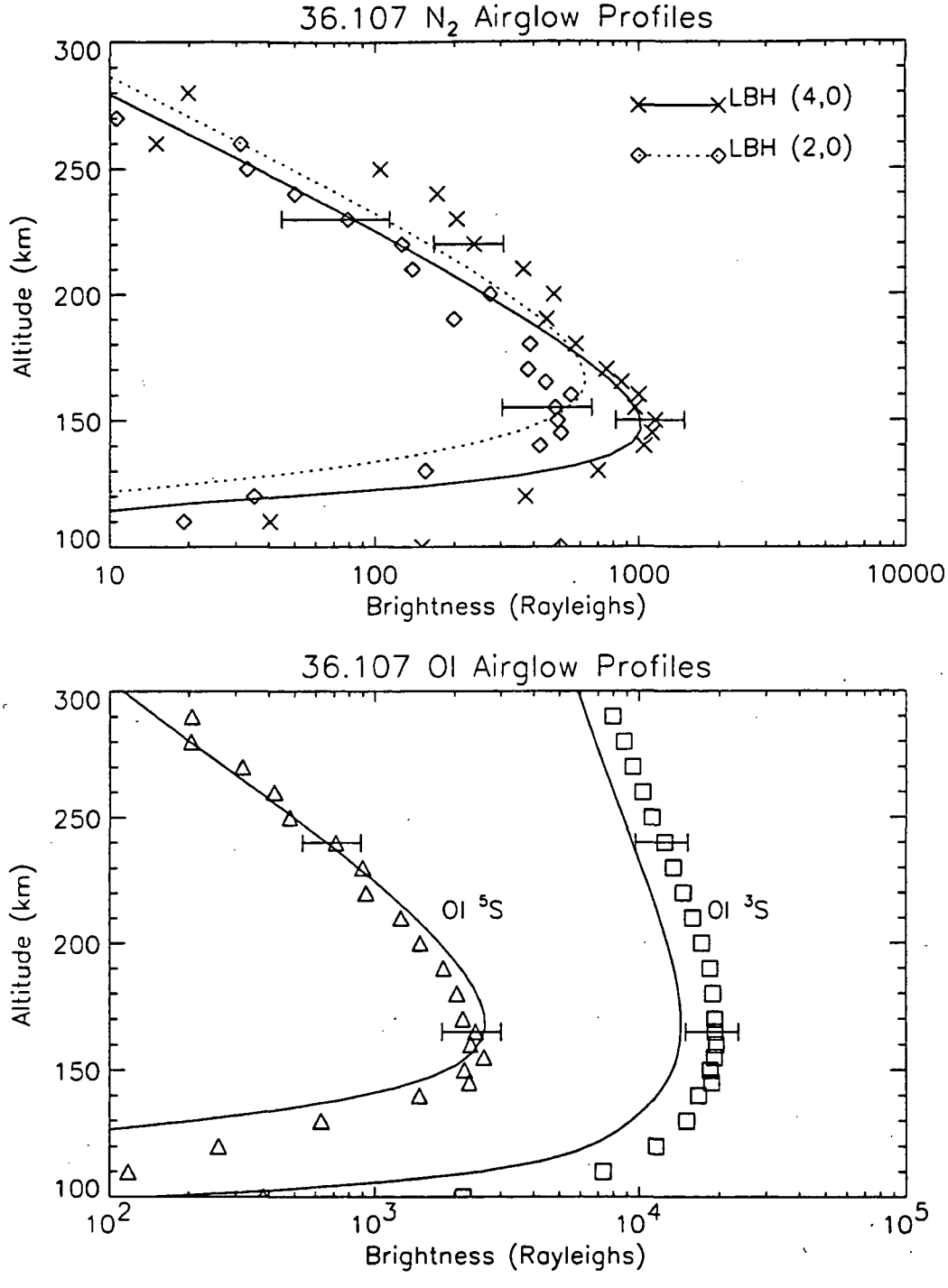


Figure 6-5 Comparison of modeled and measured airglow for 36.107. Here, the MSIS $O_2$ density has been scaled by a factor of two.

band, the magnitude of the peak is in much better agreement between model and measurement. The altitude of peak brightness is slightly higher in the model than in the data, and the model underestimates the brightness below the peak.

While agreement between the data and the scaled $O_2$ model is not perfect, it is reasonable to conclude that the disagreements between model and measurement for the 36.107 case are due to uncertainty in the neutral atmosphere. The results stated in the previous sections concerning the ability to properly model LBH and OI 135.6 nm emissions are unaffected. However, for the OI 130.4 nm emission, larger excitation rates are needed to explain the 36.098 and 36.107 measurements.

### 6.3.4 Discussion of Comparison Results

The LBH (4,0) band emissions are well reproduced by the airglow model for all three rocket flights. The LBH (2,0) band is also well reproduced by the model for 36.098 and 36.124. For 36.107, however, a discrepancy exists between the model prediction and the measurement. As stated above, this discrepancy is probably due to an underestimate of the $O_2$ density by MSIS. This is a reasonable conclusion given the large overestimate, greater than a factor of three, of the O density by MSIS. For the other rocket flights the overestimate was a factor of two. The improvement in the model and data comparison after scaling the MSIS $O_2$ density by a factor of two demonstrates the utility of the LBH (2,0) bands as an indicator of $O_2$ density. The conclusion from these comparisons is that the LBH band emission in the atmosphere is well understood and can be accurately reproduced by model calculations, under the assumptions discussed in Chapter III.

The magnitude of the OI 135.6 nm emission for each rocket flight is also well reproduced by the model calculations. In general, the results of the model and data comparisons provide confidence that the OI 135.6 nm emission is understood and can be used as a monitor of atomic oxygen in the upper atmosphere. The modeled brightness profiles decreased slightly more rapidly than the data profiles. This

difference in slope may be an indication that there is a small additional source of excitation at the higher altitudes. At night, the OI 135.6 nm emission is excited by radiative recombination of $O^+$. This source of excitation is typically ignored in the daytime, but it may have some importance at high altitudes and may explain the differences in shape between the modeled and measured profiles.

While the modeled OI 130.4 nm emission accurately reproduced the measurement for the 36.124 rocket flight, the model underestimated the brightnesses for the 36.098 and 36.107 flights. The disagreement is larger with increasing solar activity. The 36.098 rocket flight was at time of higher solar activity than 36.107, which was in turn at a higher level of solar activity than 36.124. In Chapter II, radiative entrapment of resonant transitions was described as a source of $^3S$ excitation. Some of the contributing states were analyzed by Cotton *et al.* (1993b). Perhaps states not analyzed by Cotton *et al.* are important at higher solar activity. This suggestion is not an obvious conclusion, as other researchers have obtained agreement between models and measurement of the OI 130.4 nm emission at high and low solar activity (see Chapter II and the review by Meier, 1991). These researchers did not, however, have simultaneous measurements of the solar irradiance and O density and thus their scaling of these input parameters into their models may have been incorrect. Based upon the work described here, it is concluded that the OI 130.4 nm emission in the upper atmosphere is not fully understood. Further work on the spectroscopy and radiative transfer of this emission is required.

## 6.4 Production of Airglow Emissions by Solar Irradiance

The previous sections concluded that the LBH band emissions are well understood in the atmosphere. The utility of LBH band measurements lies in their response to variability in the solar irradiance. It is useful then to examine which wavelengths of solar irradiance lead to LBH excitation. To perform this study, the airglow model is again applied to the 36.124 data. For this application, calculations are

performed individually for each wavelength bin in the solar irradiance. This mode of calculation allows viewing of LBH excitation as a function of altitude and of solar irradiance wavelength.

Figure 6-6 is a surface plot showing the results of such a calculation. The importance of the solar HeII 30.4 nm emission to the emission rate is apparent. Most of the LBH excitation is due to solar irradiance between 17 and 31 nm. Figure 6-6 shows the trend of shorter wavelength irradiance penetrating deeper into the atmosphere. Below 130 km, most of the LBH excitation is due to solar irradiances below 10 nm.

Figure 6-7 plots the LBH excitation at one altitude as a function of solar irradiance. The upper panel of Figure 6-7 shows that the largest contributor to the excitation rate at 200 km is the solar HeII 30.4 nm emission. At 150 km, the 30.4 nm emission is still the largest contributor, but the importance of the irradiance below 30 nm is increased. At 150 km, approximately one half of the LBH excitation is due to solar irradiance above 30 nm. Figure 6-7 also shows the LBH excitation at 110 km; at this altitude essentially all excitation is due to solar irradiance below 10 nm. This result is significant in that it demonstrates that the energetics of the lower thermosphere are controlled by solar soft x-rays below 10 nm as suggested by Barth *et al.* (1988) and Siskind *et al.* (1990).

Given that the LBH bands can be used as monitors of solar energy deposition, it is useful to examine the variability of LBH band brightness with solar activity. Figure 6-8 shows this variability. The upper panel of Figure 6-8 graphs the LBH (4,0) band peak brightness as a function of integrated solar irradiance. The crosses on this plot represent the integrated solar irradiance as measured for each of the rocket flights. The solid line is the best linear fit and the fit coefficients are shown in the upper left corner. For 36.098, the irradiances below 30 nm are scaled by a factor of two as suggested above. The middle panel of Figure 6-8 shows variation of the LBH (4,0) band brightness versus solar HeII 30.4 nm irradiance. The lower panel of Figure 6-8 plots

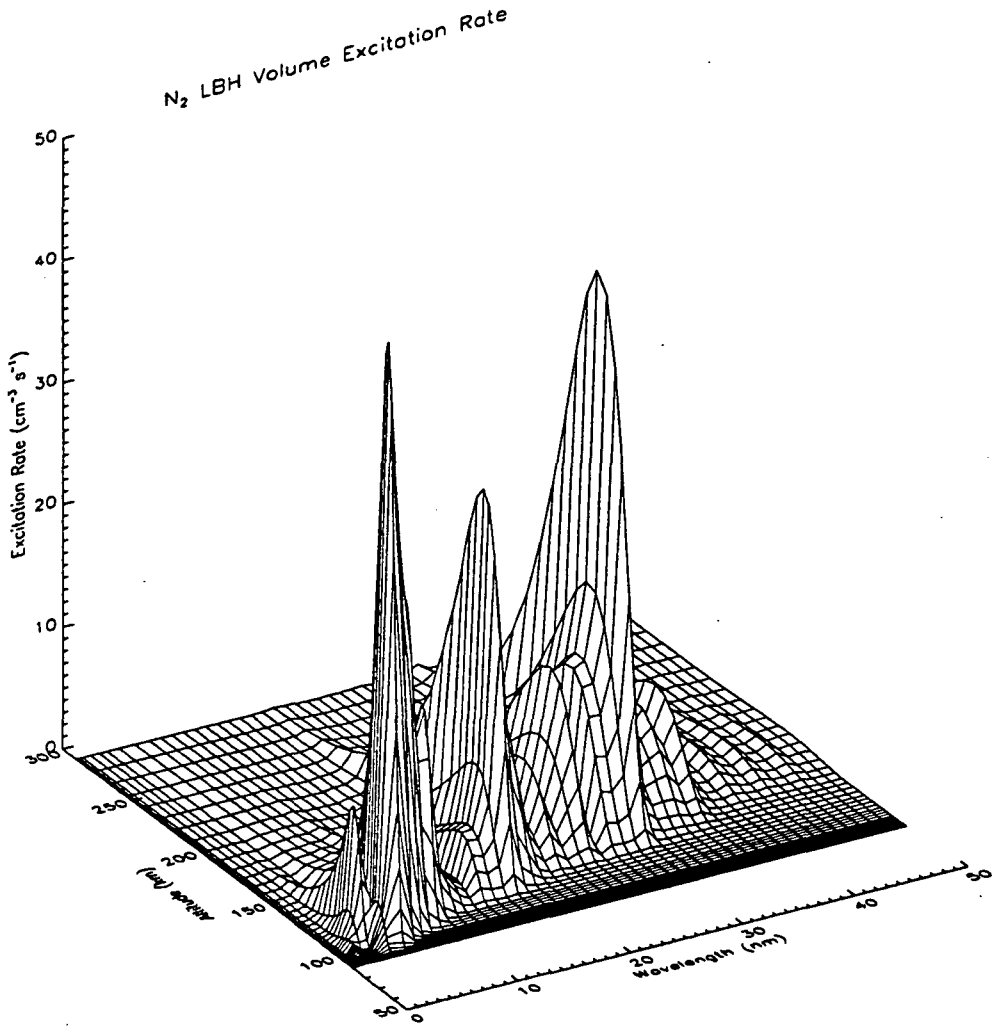


Figure 6-6 LBH volume excitation rate as a function of solar irradiance wavelength and of altitude.

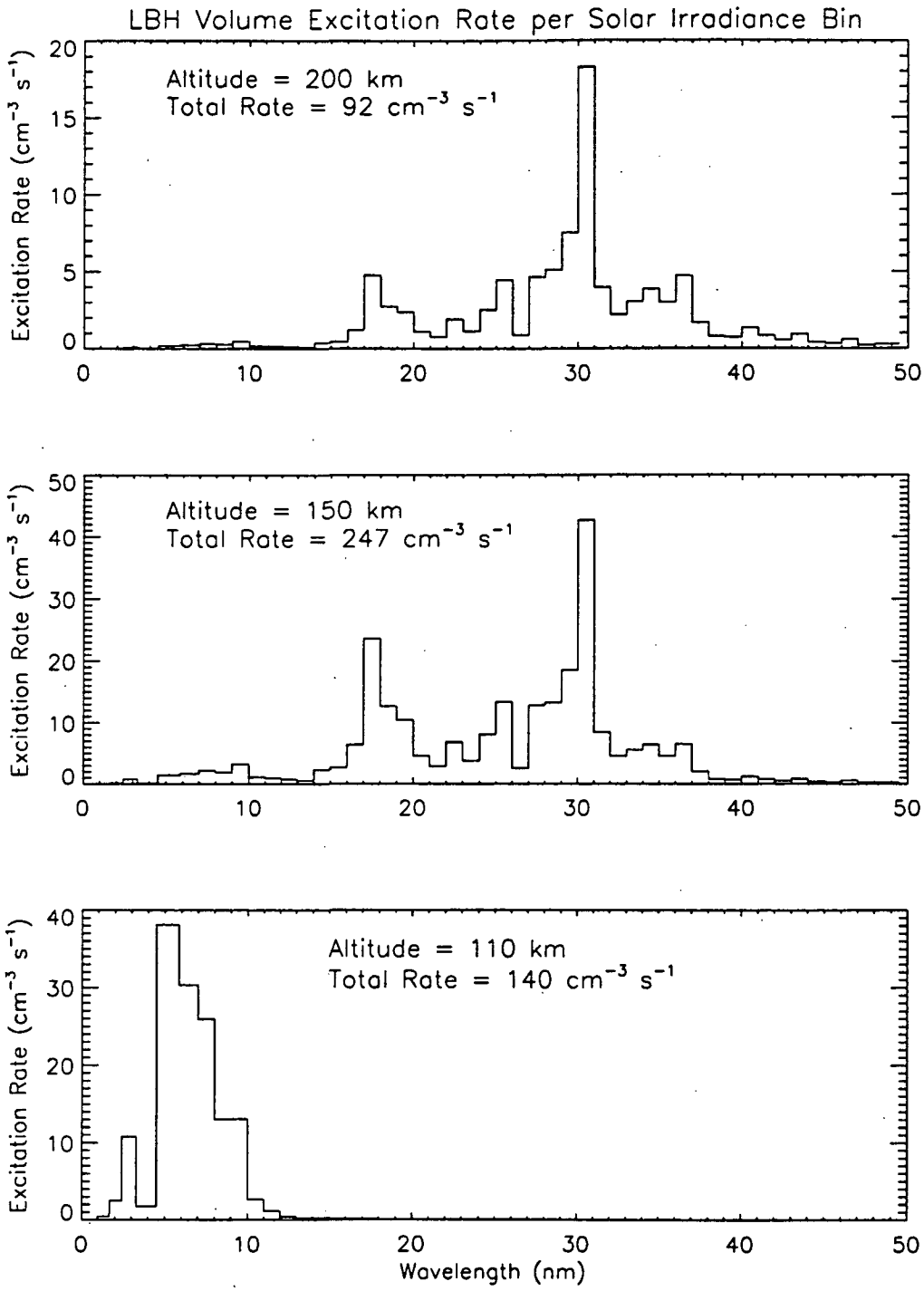


Figure 6-7 LBH volume excitation rate as a function of solar irradiance wavelength, shown for 110, 150, and 200 km.

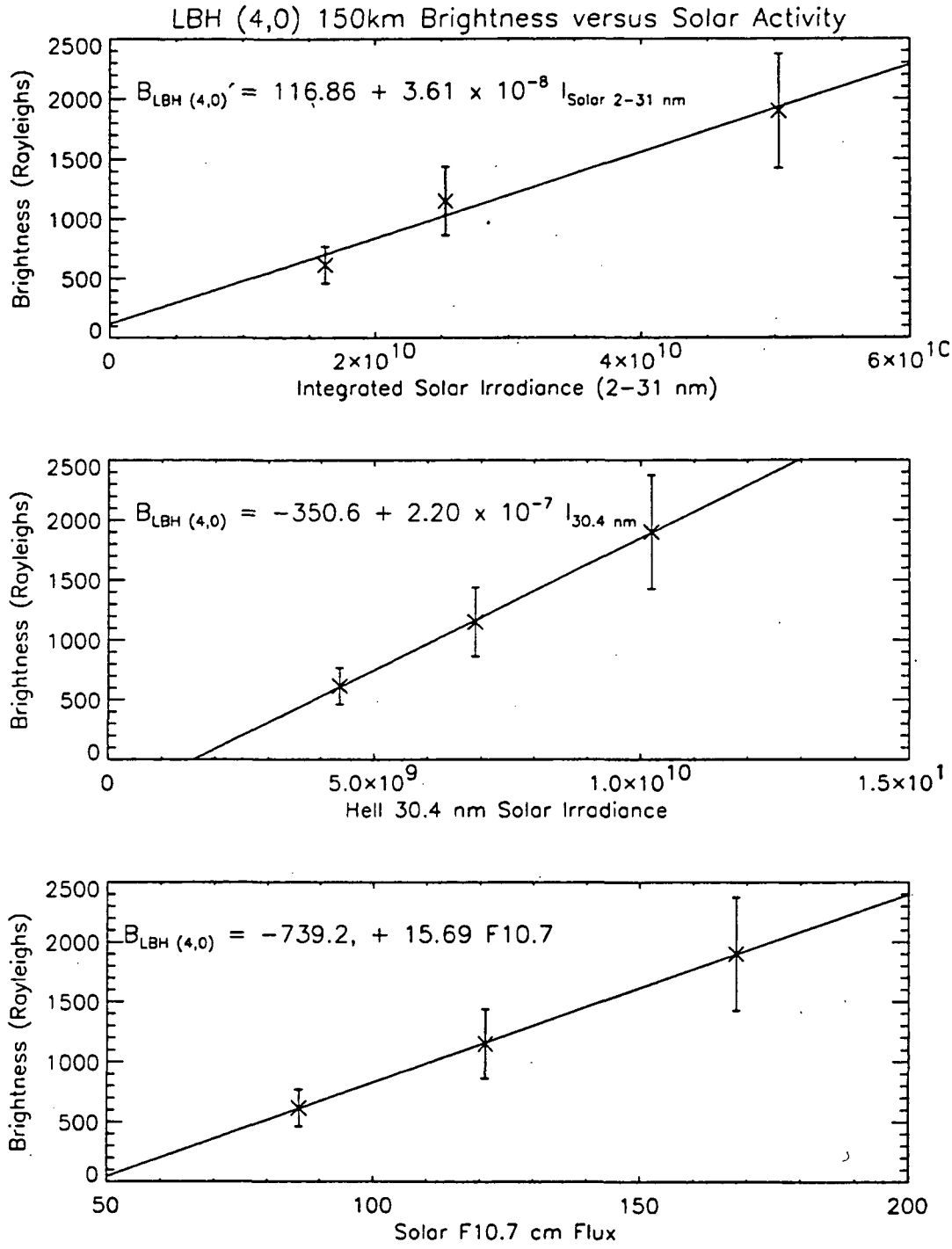


Figure 6-8 Measured variability of the LBH (4,0) 150 km limb viewing brightness with solar activity. The linear relationship is demonstrated for integrated solar soft x-ray integrated irradiance, solar 30.4 nm irradiance, and for solar F10.7 cm flux.

the LBH (4,0) band peak brightness versus solar F10.7 cm flux, which is a proxy for solar soft x-ray irradiance. Figure 6-8 shows a linear relationship between LBH band brightness and solar activity. This result further demonstrates the utility of LBH band measurements as inferences of solar energy deposition.

Figure 6-9 compares the variability of the LBH (4,0) band at 110 km to solar variability. In this case, the (4,0) band brightness is plotted versus integrated solar soft x-ray irradiance, solar integrated 2 - 10 nm irradiance, and solar f10.7 values. Again, the best fit lines are shown with fit coefficients displayed in the upper left corner. At 110 km the LBH band excitation rate responds primarily to solar 2 - 10 nm irradiance; thus, a measurement of 110 km LBH band brightness can be used to infer solar energy deposition at this altitude. This result is significant because 110 km is the altitude at which nitric oxide has a peak density. Nitric oxide has been shown to be highly variable in the lower thermosphere, responding to variations in solar soft x-ray irradiance (Barth *et al.*, 1988; Siskind *et al.*, 1990). The ability to remotely sense energy deposition into this altitude region will be a great asset to studies of nitric oxide variability.

## 6.5 Summary

This chapter used the measured solar irradiance and the inferred neutral densities of Chapter V to calculate model airglow profiles for each of the three rocket flights. The calculated airglow profiles were compared to those measured by the FUV airglow instrument. Several conclusions were reached by these comparisons. The LBH band system excitation is well understood in the Earth's atmosphere and a linear relationship exists between solar irradiance and LBH brightness. This relationship can be applied to infer solar irradiance from LBH airglow measurements. The magnitude of the OI 135.6 nm emission is also understood, but a minor additional source of excitation at high altitudes may be required to explain the data above 200 km. Radiative recombination of $O^+$ was suggested as this additional source of excitation. Although the

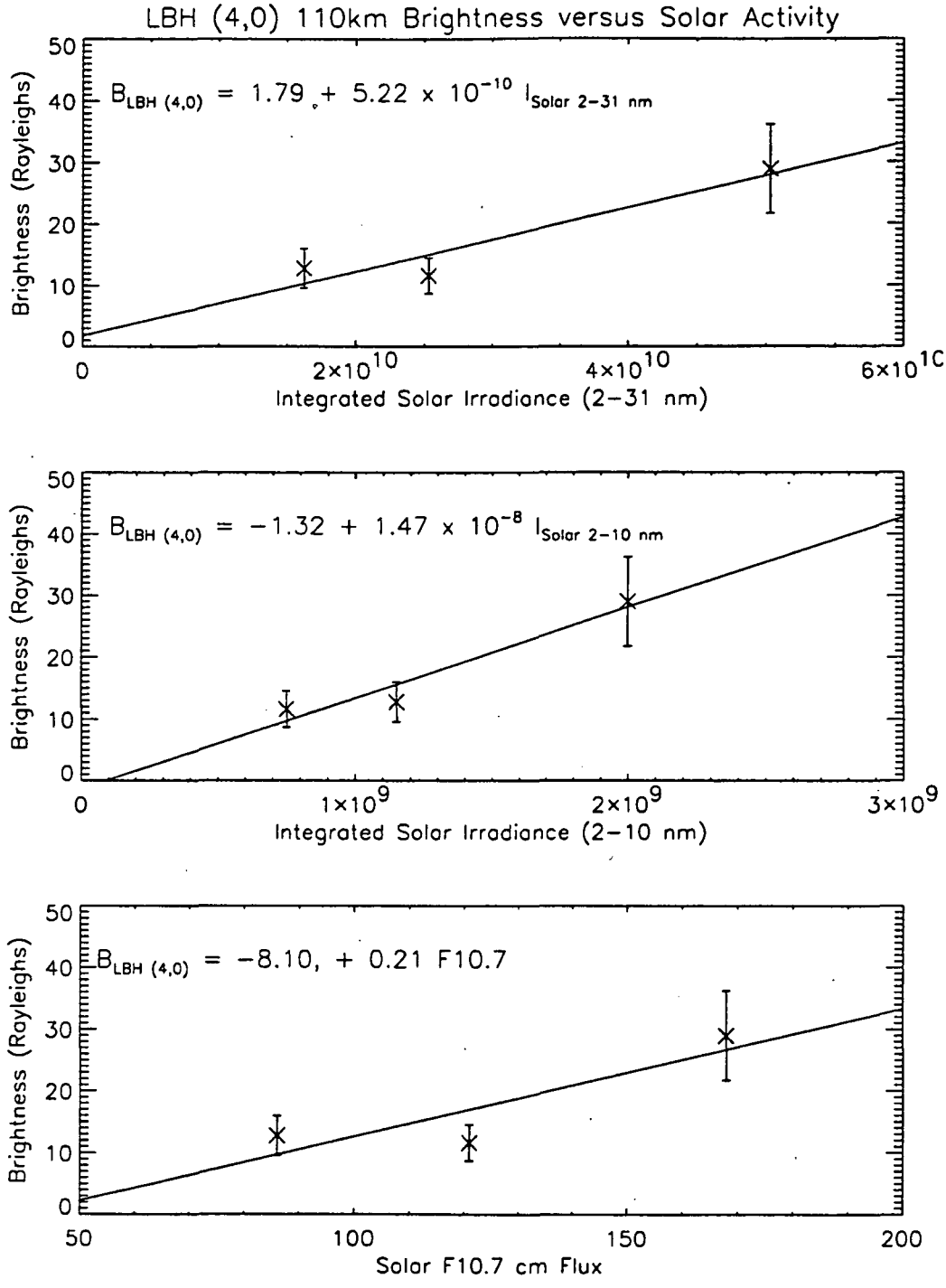


Figure 6-9 Calculated variability of the LBH (4,0) 110 km limb viewing brightness with solar activity. The best fit linear relationship is demonstrated for integrated solar soft x-ray integrated irradiance, integrated solar 2-10 nm irradiance, and for solar F10.7 cm flux.

C-3.

model and data comparisons for the OI 130.4 nm emission were quite successful for the 36.124 rocket flight, the model underestimated the measured brightness for the 36.098 and 36.107 cases. Enhanced cascade contributions from radiatively entrapped transitions was suggested as a possible source of excitation. Further work into the spectroscopy and radiative transfer of the $^3S$ state is required to understand the OI 130.4 nm emission.

# Chapter VII

## Effect of Solar Soft X-rays on Nitric Oxide Production

### 7.1 Introduction

The response of the upper atmosphere to variations in solar irradiance has been examined in terms of thermospheric airglow brightness. In addition to the excitation of FUV airglow emissions, the photoelectrons created by solar soft x-rays are also involved in ionization and dissociation processes. These processes can lead to enhanced production of Nitric Oxide (NO) densities in the lower thermosphere and are described in this chapter. The NOx 1-D photochemical model is updated to incorporate the */glow* photoelectron calculation. The new NOx 1-D is compared to the old version and it is shown that the new model is more efficient at producing NO.

### 7.2 NOx 1-D Photochemical Model

The presence of nitric oxide in the thermosphere is the result of a very complex system of chemical and physical processes. The NOx 1-D photochemical model calculates NO profiles for given geophysical conditions. The term 1-D indicates that the model is one dimensional: vertical transport of atmospheric constituents is accounted for, but horizontal transport and time dependence are neglected. The model is described in detail by Cleary (1986), Siskind (1988), Eparvier (1991), and Barth (1992). In this section the model is described with emphasis on the effect of solar irradiance and photoelectrons. Except as noted, all chemical reaction rates currently used in this work are those listed by Barth *et al.* (1995).

#### 7.2.1 Model Formalism

A schematic representation of the processes which produce or remove nitric oxide from the thermosphere is presented in Figure 7-1. At the top of the figure are the

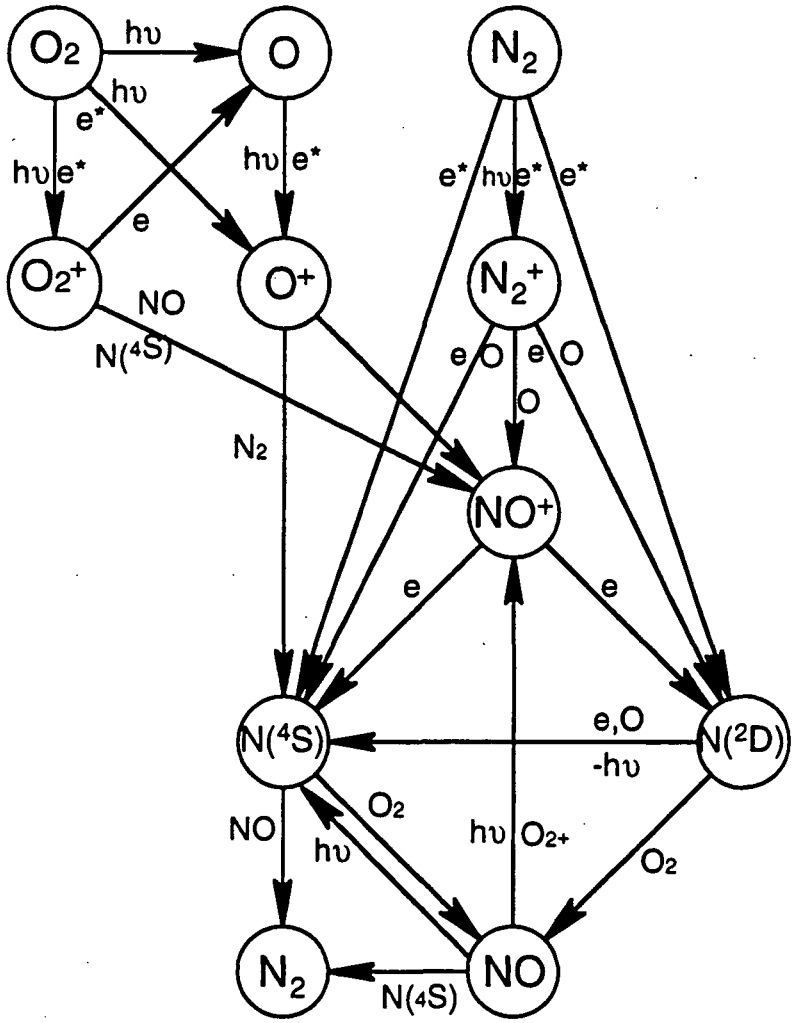


Figure 7-1 A schematic representation of thermospheric NO chemistry.

major species of the thermosphere: $O_2$, O, and $N_2$. These are ionized by solar photons (hυ) to produce ions ($O_2^+$, $O^+$, and $N_2^+$) and energetic electrons (e*). This process, as calculated by */glow*, was described in Sections 2.1. From Figure 7-1 it can be seen that the production of nitric oxide occurs as molecular oxygen reacts with atomic nitrogen in the reaction:

$$N(^2D,^4S) + O_2 \rightarrow NO + O. \qquad 7\text{-}1$$

Here N($^2$D) and N($^4$S) are nitrogen atoms in different electronic states. N($^4$S) is atomic nitrogen in the ground state and N($^2$D) is atomic nitrogen in an excited state. The extra energy of the N($^2$D) atom makes the reaction 7-1 proceed in a very rapid manner compared to the rate with N($^4$S). An important aspect to understanding nitric oxide is to understand the production of N($^2$D).

Figure 7-1 shows that there are several methods for producing N($^2$D). One of the methods is dissociative recombination of $NO^+$,

$$NO^+ + e \rightarrow N(^2D,^4S) + O, \qquad 7\text{-}2$$

or similarly there is dissociative recombination of $N_2$,

$$N_2^+ + e \rightarrow 2N(^2D,^4S). \qquad 7\text{-}3$$

Note that both of the above reactions occur with ambient electrons as opposed to the energetic photoelectrons. Solar irradiance is important here as it provides the original ionization which produced the ions leading to the presence of $NO^+$. The other mechanisms for producing N($^2$D) involve photoelectrons more directly. The first of these mechanisms is the dissociation of $N_2$ by photoelectrons,

$$N_2 + e^* \rightarrow 2N(^2D,^4S) + e. \qquad 7\text{-}4$$

This process requires approximately 10 eV of electron energy to accomplish. Another way photoelectrons lead to N($^2$D) is through the following reactions (see Figure 7-1):

$$N_2 + e^* \rightarrow N_2^+ + e, \text{ and} \qquad 7\text{-}5$$

$$N_2^+ + O \rightarrow NO^+ + N(^2D). \qquad 7\text{-}6$$

Having established the method by which photoelectrons lead to nitric oxide production, the importance of solar irradiance, especially the soft x-rays which produce most of the photoelectrons, is now clear. In the next section the cross sections for the above processes are evaluated in detail. The formalism of the NOx 1-D model is now described.

To solve for the density of an atmospheric constituent, the one dimensional mass continuity equation is solved neglecting horizontal transport:

$$\frac{\partial n_s}{\partial t} = P_s - L_s n_s - \frac{\partial \Phi_s}{\partial z}, \qquad 7\text{-}7$$

where $n_s$ is the number density of species $s$, $P_s$ is the production rate of species $s$ ($cm^{-3}$ $s^{-1}$), $L_s$ is the loss rate of species $s$ ($s^{-1}$), and $\Phi_s$ is the vertical flux of the species $s$ ($cm^{-2}$ $s^{-1}$). The production and loss rates are due to the processes listed above and to the processes depicted in Figure 7-1. The complete list of chemical reactions and reaction rates is described in detail by Barth *et al.* (1995). The detailed description of the solution of Equation 7-7 can be found in Cleary (1986), Siskind (1988), and Eparvier (1991). Briefly, Equation 7-7 is discretized and solved using the Crank-Nicholson finite difference technique (Von Rosenberg, 1969) for both NO and $N(^4S)$ as diffusion is important for these constituents. For $N_2^+$, $N^+$, $O_2^+$, $O^+$, $O^+(2D)$ , $NO^+$, and $N(^2D)$, chemical processes occur much more quickly than diffusive processes; therefore, the last term in Equation 7-7 can be ignored, simplifying the solution.

### 7.2.2 The PEGFAC Photoelectron Model.

Previous to this work, the photoelectron calculation used in the NOx 1-D model was PEGFAC (PhotoElectron G FACtor). This model is described in detail by Strickland and Meier (1982). PEGFAC is fundamentally different from */glow* in that it

is a "local" photoelectron calculation. The local approximation is the assumption that energetic electrons created in a given altitude bin deposit all their energy into that bin. This approximation neglects all electron transport and ignores elastic scattering. This assumption is valid up to altitudes of 300 km (Strickland and Meier, 1982).

Examining Equations 3-1 and 3-2 shows that ignoring elastic scattering in the local approximation sets $T_1$ equal to zero and removes the first term of $T_2$. This assumption leads to a much simpler form of Equation 3-8. Since all altitude derivatives of the photoelectron flux go to zero, the photoelectron equation can now be written in terms of production and loss in an analogous way to Equation 7-7:

$$\frac{\partial \phi}{\partial t} = P - L\phi, \qquad 7\text{-}8$$

where now $P$ and $L$ are production and loss rates for photoelectrons, and $\phi$ is the flux of photoelectrons. Assuming steady state leads to:

$$\phi = \frac{P}{L}. \qquad 7\text{-}9$$

The above result leads to a much simpler numerical solution than the one used in */glow*. Although, the above discussion describes the formalism of the local calculation, in practice PEGFAC uses a matrix method solution.

Aside from transport processes, the other major difference between PEGFAC and */glow* is that PEGFAC ignores Auger processes. This assumption combined with the fact that the energy grid extends only to 400 eV means that solar irradiance of wavelengths less than 3.1 nm is ignored. The assumed photoabsorption and photoionization cross sections and branching probabilities are taken from the compilation of Conway (1988).

In the PEGFAC model, the solar irradiance longer than 5 nm is binned according to the scheme of Torr *et al.* (1979). The effects of binning schemes on

photoelectron calculations were described in 3.5. The Torr *et al.* scheme contains 5 nm continuum bins from 5 to 105 nm and several bins which contain only isolated lines. PEGFAC, as it is incorporated into NOx 1-D, treats continuum bins and line bins separately. The numerical method employed does not allow for production of photoelectrons from photons of energy less than the average photon energy in the lowest wavelength bin. Since the lowest bin covers from 5 to 10 nm, which is a factor of 2 in energy, all photons of wavelength less than 7.5 nm do not contribute. This method has the effect of neglecting 2/3 of the energy contained in the 5 to 10 nm bin and has consequences which will be demonstrated in the following section. It should be stressed that this feature is present in the PEGFAC model as incorporated in NOx 1-D and is not true of PEGFAC as used in other applications.

As discussed in Chapter I, large solar soft x-ray fluxes have been suggested as an explanation for large abundances of nitric oxide. Given that there have previously been no simultaneous measurements of NO and the solar soft x-ray irradiance, the soft x-ray irradiance is considered a parameter in the NO calculation and is implemented by using a scaling factor parameter. The scaling factor is applied to the solar minimum soft x-ray irradiance from the SC#21REFW reference spectrum (Hinteregger *et al.*, 1981) only from 1.8 to 5.0 nm.

### 7.2.3 $N_2$ Photoelectron Dissociation Cross Section

Previously, the total cross section for dissociation of $N_2$ was taken from Zipf and McLaughlin (1978). They obtained their cross section by summing the contributions to dissociation and predissociation from all the important excited states and from dissociative ionization. They also measured the branching ratio for predissociation for many of the excited states. The method involved the use of accurate cross sections for excitation of the states; these cross sections were based upon generalized oscillator strengths from Lassettre (1974). By measuring the cross section

for emission from a given state, they could obtain the predissociation cross section from the difference between the excitation and emission cross sections.

Since the work of Zipf and McLaughlin, Zipf and Erdman (1985) and Ajello *et al.* (1989) have shown that the emission cross section standard to which they compared was in error and that their emission cross section measurements need to be scaled by a factor of 0.36. Lowering the magnitude of the measured cross sections has the effect of increasing the predissociation branching ratio which would then increase the cross section for dissociation. It turns out, however, that the states which contribute the most dissociation have branching ratios very near unity. Here, branching ratio is defined as the fraction of excitation leading to predissociation. The emission cross section is a very small fraction of the excitation cross section, so although the modification to the cross section is large, the effect on the branching ratio is very small. Thus the Zipf and McLaughlin total cross section does not require modification. Zipf and McLaughlin compared their results to other measurements made much earlier and using different and more complicated techniques. The values compared very well, providing more confidence in their results. The Zipf and McLaughlin total cross section is used in each of the following calculations and is plotted in Figure 7-2. For comparison the cross section for ionization of $N_2$ by photoelectron impact is also shown. Note that dissociative ionization is included in the total cross section for dissociation.

### 7.2.4 Comparison of NOx 1-D with */glow* and PEGFAC

For this work, NOx 1-D model is updated to incorporate */glow* for the photoelectron calculation. Figures 7-3 through 7-5 compare the results of NOx 1-D using PEGFAC with the new version of the model using */glow*. The comparisons are made by examining photoelectron impact ionization and dissociation of $N_2$, and production of NO. The model runs are made for the solar maximum and solar minimum using the parameters listed in Table 3-1. For solar minimum the x-ray scaling factor

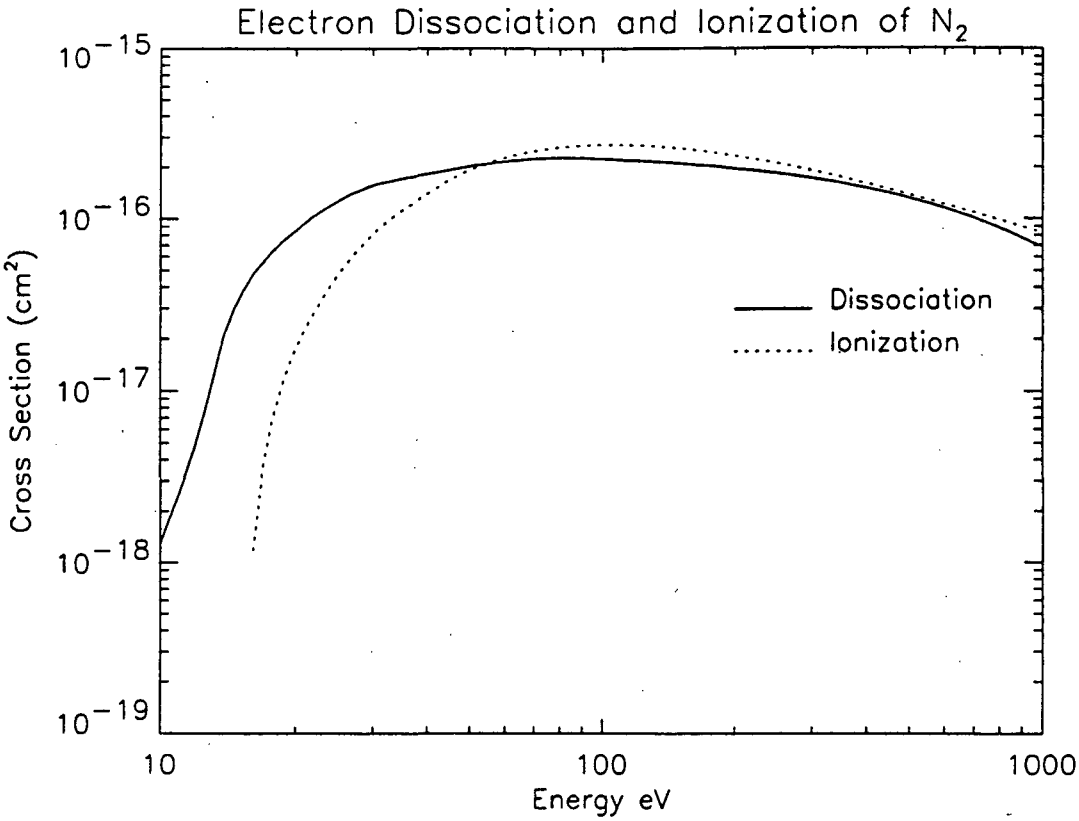


Figure 7-2 Total cross sections for ionization and dissociation of $N_2$ by photoelectron impact.

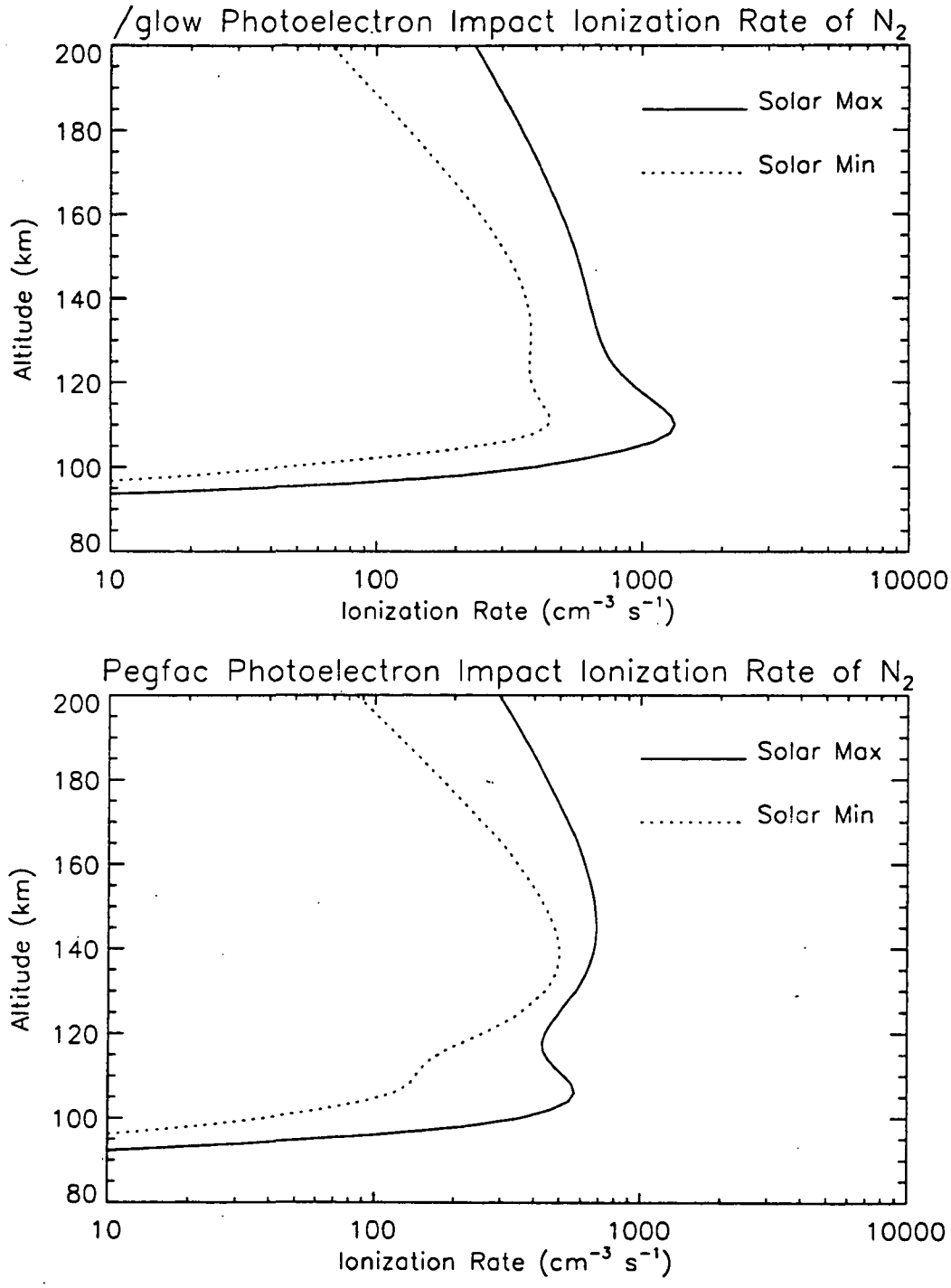


Figure 7-3 Calculations of photoelectron impact ionization of $N_2$ from the */glow* and PEGFAC models. See Table 3-1 for geophysical conditions.

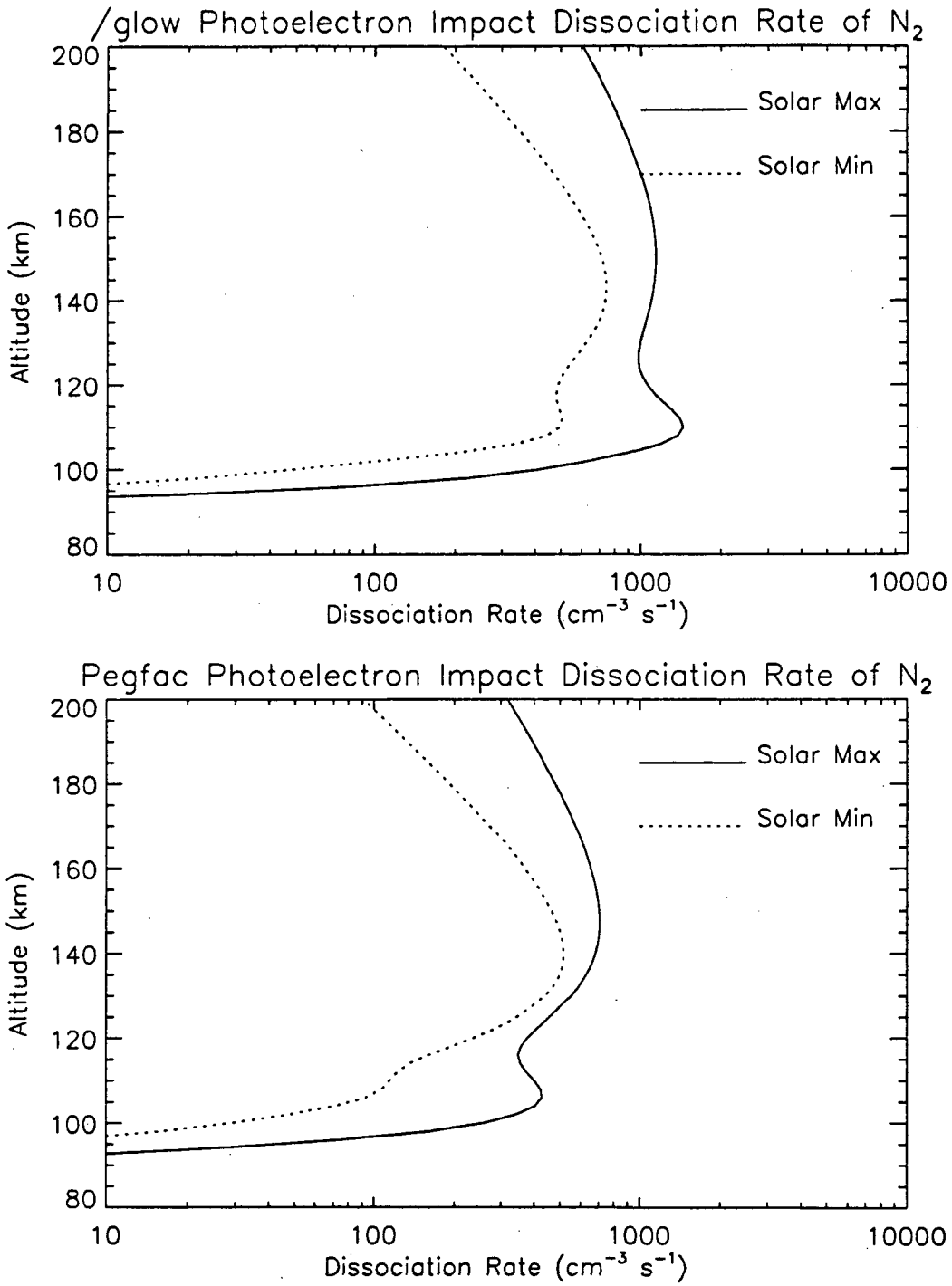


Figure 7-4 Calculations of photoelectron impact dissociation of $N_2$ from the */glow* and PEGFAC models. See Table 3-1 for geophysical conditions.

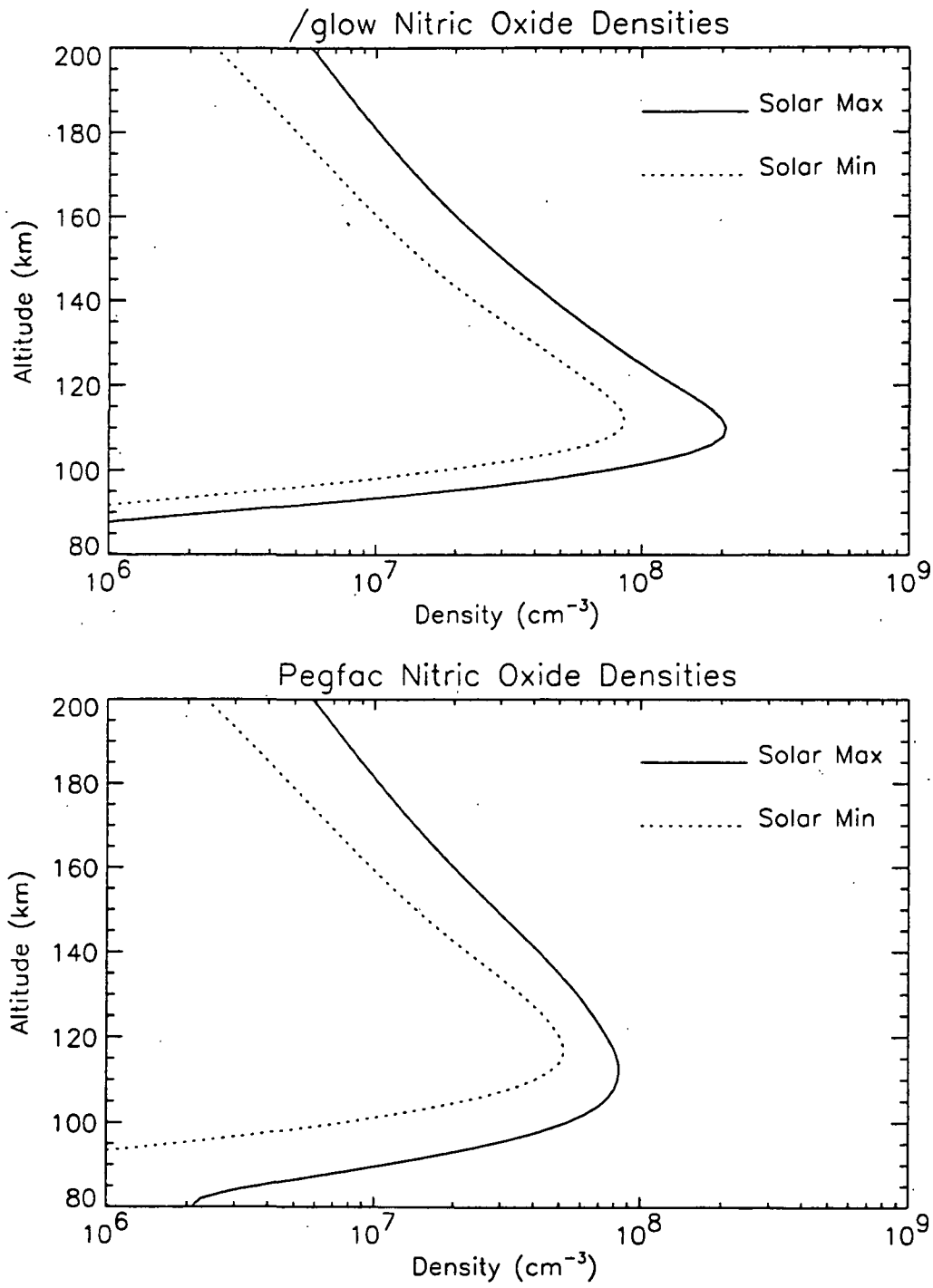


Figure 7-5 Predictions of NO density by the NOx 1-D model using */glow* and PEGFAC. See Table 3-1 for geophysical conditions.

used is 1, at solar maximum a value of 10 is used; these values correspond to irradiances of 0.015 and 0.150 ergs $cm^{-2}$ $s^{-1}$ respectively. Apart from different models assumed for the photoelectron calculation, there are no differences in the NOx 1-D models used in the following comparisons. Siskind *et al.* (1990) compare electron impact ionization of $N_2$ for different levels of solar activity using PEGFAC. While they used large x-ray scaling factors in attempting to reproduce their rocket data, the calculations with unity x-ray scaling factor are comparable to those in this work at altitudes where the soft x-rays are the dominant energy source. Care must be exercised in such comparisons as the geophysical conditions for the two sets of calculations are different. Since the work of Siskind *et al.*, the NOx 1-D photochemistry has been updated (Barth *et al.*, 1995); therefore, direct comparisons of NO densities cannot be made.

Figure 7-3 shows rates of photoelectron impact ionization of $N_2$. At solar maximum, */glow* produces more ionization at all altitudes, and at solar minimum, PEGFAC produces more ionization above 120 km. The enhanced production by */glow* is due to the processes described above, the Auger processes, and the contribution from 5 to 10 nm. The solar minimum comparison is interesting because it is not expected that PEGFAC should produce more energy than */glow*. The reason for the discrepancy is that PEGFAC uses solar irradiance values taken from Torr *et al.* (1979). These irradiances were an early version of those that formed the SC21REFW reference spectrum and the Hinteregger irradiance model. Torr & Torr (1985) and Hinteregger *et al.* (1981) later revised these results and presented an approximately 20% reduction in solar irradiance. The */glow* model incorporates the later results. Thus the disagreement between the two models is understood as differences in solar irradiances and from the lack of high energy processes in PEGFAC.

Figure 7-4 shows that throughout the solar cycle, */glow* produces more photoelectron impact dissociation of $N_2$ than PEGFAC. The discrepancy is approximately a factor of 2 to 3. The larger production by */glow* is expected from the discussion above, however it is noted that the ratio is larger for dissociation of $N_2$ than for ionization of $N_2$. The explanation comes from consideration of the shape of the photoelectron spectrum. The cross section for dissociation of $N_2$ by photoelectrons peaks at a high energy (100 eV), and the cross section is significant at high energies. The */glow* model produces more energy at the lower altitudes because of its inclusion of higher energy processes thus resulting in a photoelectron spectrum which has more integrated energy and contains more high energy photoelectrons. Therefore, a process such as dissociation by electron impact which favors high electron energies is enhanced by */glow* relative to PEGFAC.

The results of the above discussion on the production of nitric oxide are shown in Figure 7-5. The */glow* model leads to more nitric oxide by a factor of 2 at solar minimum and a factor 3 at solar maximum. Note that at high altitudes during solar minimum the two models are in good agreement. This is due to the diminished role of the soft x-rays at high altitudes and at solar minimum.

The increased production of NO from the inclusion of the */glow* model into the NOx 1-D calculation shows that solar soft x-rays are more efficient at producing NO than previously understood. Siskind *et al.* (1990), using the previous version of NOx 1-D, suggested solar soft x-ray variability of over 50 to explain their sounding rocket measurement of NO densities. The above results show that this value should be reduced by at least a factor of 3. This reduction would result in solar soft x-ray variability in better agreement with that described in Chapter V. Siskind *et al.* (1995) have reexamined the solar soft x-ray effect on NO using NOx 1-D with an improved photochemistry and an improved photoelectron calculation including Auger processes

(Strickland *et al.*, manuscript in preparation, 1995). They concur that solar soft x-rays are more efficient at producing NO than previously thought; however direct comparison is difficult due to differences in the photochemical models.

## 7.3 Summary

In this chapter, the mechanisms leading to the production of NO were discussed. A one dimensional photochemical model for calculating NO density, given solar soft x-ray irradiances, was described. Previously, this model incorporated the PEGFAC photoelectron calculation; in this work, the model was updated to include the */glow* photoelectron calculation. Comparisons between the two models showed that, over the solar cycle, the new model produced more NO by factors of 2 to 3. The differences were attributed to the inclusion of Auger processes and to a more accurate numerical method. Previous suggestions of large solar soft x-ray irradiance variability based on NO measurements and modeling should be reexamined.

# Chapter VIII

# Conclusions

## 8.1 Summary

The goal of this dissertation was to study the response of the upper atmosphere to variations in the solar soft x-ray irradiance. Of particular importance was to address the question of whether the magnitude of the solar soft x-ray irradiance could be inferred from measurements of the terrestrial FUV airglow. While these issues have been previously examined, this dissertation represents the first analysis of simultaneous measurements of solar irradiance, the neutral atmosphere, and the thermospheric FUV airglow.

The brightest features in the FUV airglow are the OI 130.4 and 135.6 nm emissions and the $N_2$ Lyman Birge Hopfield (LBH) bands. Although the OI 130.4 nm emission is also excited by resonant scattering of sunlight, each of these emissions is primarily excited by impact with photoelectrons. In Chapter II a review of past cross section measurements and their application to airglow modeling was presented; in particular, the origins of the cross sections used in this dissertation were described.

To calculate photoelectron excitation, the */glow* model of Solomon *et al.* (1988) was used. Following a two stream formalism, the */glow* model includes electron transport. An optically thin radiative transfer algorithm was employed to integrate the LBH excitation rates through the atmosphere, yielding LBH band brightnesses. For the optically thick OI emissions, the Feautrier solution to the radiative transfer equation of Gladstone (1982, 1988) was applied. It was shown that care must be exercised in binning the solar irradiance; for any calculation where photoionization is important, the CIII emission at 97.7 nm must considered separately.

The solar and terrestrial emissions were measured with the identical rocket payload flown three times. Each of the three flights occurred at different levels of solar activity. An EUV grating spectrograph measured the solar irradiance from 30 to 120 nm. X-ray photometers measured the solar soft x-ray irradiance from 2 to 30 nm. Both of these instruments were calibrated using synchrotron radiation sources at NIST. Calibrations of the x-ray photometers were extended to short wavelengths using models of thin film transmission and photodiode sensitivity. An FUV spectrograph measured the terrestrial airglow from 130 to 160 nm. The sensitivity of this instrument was obtained with laboratory light sources and photomultiplier tubes referenced to NIST calibrated photodiodes.

In addition to measurements of the solar irradiance and the airglow brightness, the data sets from the rocket flights allowed inference of neutral atmospheric densities. Because the rockets observed the sun continually as they moved through the atmosphere, the attenuation of the EUV irradiance was measured. Using known absorption cross sections, density profiles of atomic oxygen were inferred. The profiles were approximately a factor of two lower than predictions by the MSIS model atmosphere for the conditions of the rocket launches.

For each rocket flight, model airglow calculations were made using the measured solar irradiance and the inferred neutral atmosphere. The profiles obtained from these calculations were then compared to the airglow measurements. The results of these comparisons form the basis for assessing both the current understanding of airglow production and whether FUV airglow can be used as a remote sensing tool. The LBH (4,0) and (2,0) bands and the OI $^3S$ and $^5S$ at 130.4 and 135.6 nm respectively were analyzed.

The most significant conclusion in this dissertation is that the airglow models correctly reproduced the measured LBH profiles for each rocket flight. Because the flights occurred during different levels of solar activity, the assumption that the LBH

brightnesses can be used to infer the magnitude of the photoelectron flux and thus the solar irradiance is validated. The LBH bands were found to respond predominantly to solar irradiance of wavelengths near and below 30.4 nm. At low altitudes, the solar irradiance responsible for LBH emissions occurs at wavelengths less than 10 nm.

The OI $^5S$ emission at 135.6 nm was also well reproduced by the airglow models. The model profiles decrease slightly faster with altitude than do the measurements. A suggestion was made that radiative recombination of $O^+$ may make a small contribution to the OI 135.6 nm brightness at higher altitudes. This contribution is negligible at the altitude of the peak of the OI 135.6 nm emission and therefore does not inhibit the use of this emission as a remote sensor of atomic oxygen.

While the airglow models correctly reproduced the measured profiles of OI $^3S$ at 130.4 nm for the final rocket experiment, the comparison was very poor for the first two measurements. For flights 36.098 and 36.107, the airglow models underestimated the observed brightness. It is unlikely that the discrepancy is an instrumental effect because the airglow instrument calibration procedures are identical for each wavelength and each flight. The conclusions drawn were that the OI $^3S$ emission is not fully understood and additional excitation is required to explain the observations. A possible mechanism, which may explain the discrepancy, is that branch contributions from radiative entrapment of higher transitions increase with solar activity. Further research into the spectroscopy and radiative transfer of the OI $^3S$ emission is warranted.

In addition to excitation of airglow emissions, solar soft x-rays lead to enhanced production of nitric oxide. Previous analyses showed that large variability in solar soft x-rays could account for the large variability in NO densities through electron impact ionization and dissociation of $N_2$. These studies used the NOx 1-D photochemical model, incorporating the PEGFAC local photoelectron calculation. In the present analysis, the NOx 1-D model was updated to include the */glow* model for photoelectron calculations. Comparisons between the old and new versions of the NOx 1-D model

demonstrated the effect of solar soft x-rays on NO production. The new version, with */glow*, was found to be more efficient at producing NO. The differences between the models were attributed to numerical methods and to the inclusion of Auger processes in the photoelectron calculation.

## 8.2 Future Research

This dissertation concluded that it is indeed appropriate to use the LBH bands as monitors of solar energy deposition; this approach should be applied in future airglow measurements such as the NASA TIMED mission which contains an FUV airglow instrument (A. B. Christensen, P.I.) and by the RAIDS experiment (R. P. McCoy, P.I.). A continuation of this research would be to study the response of the LBH airglow to auroral energy deposition.

The OI $^5$S emission at 135.6 nm is also well understood. Above 200 km, radiative recombination of $O^+$ may play a small role in the excitation of this emission. The importance of this contribution at altitudes above the peak emission layer should be assessed for a complete understanding of the $^5$S excitation mechanisms.

The airglow models used in the present analyses did not reproduce the OI $^3$S emission at 130.4 nm for two of the three rocket flights. It was suggested that branch contributions from radiative entrapment of higher transitions are larger than previously believed. Further work into the spectroscopy and radiative transfer of this emission is needed.

To fully understand the importance of solar soft x-rays in the production of NO, simultaneous measurements of solar irradiance and NO densities are required. An ongoing program using sounding rockets obtains such data (C. A. Barth, P.I.). The Student Nitric Oxide Explorer (SNOE, C. A. Barth, P.I.) will make simultaneous NO and solar soft x-ray irradiance measurements using the x-ray photometers described in this dissertation. SNOE will also measure FUV LBH and OI emissions to determine auroral energy deposition.

## Bibliography


Ajello, J. M., Emission Cross Sections of $N_2$ in the Vacuum Ultraviolet by Electron Impact, *J. Chem. Phys.*, **53**, 1156, 1970.

Ajello, J. M. and D. E. Shemansky, A Reexamination of Important $N_2$ Cross Sections by Electron Impact with Application to the Dayglow: The Lyman-Birge-Hopfield bands System and NI (119.99 nm), *J. Geophys. Res.*, **90**, 9845, 1985.

Ajello, J. M., G. K. James, B. O. Franklin, and D. E. Shemansky, Medium Resolution Studies of Extreme Ultraviolet Emission from N2 by Electron Impact: Vibrational Perterbations and Cross Sections of the $c_4' \Sigma^+_u$ and $b' \Sigma^+_u$ states, *Phys Rev A.*, **40**, 3524, 1989.

Avakyan, S. V., M. N. Vlasov, and I. A. Krinberg, Comparisons of the Fluxes and Spectra of Auger Electrons and Photoelectrons in the Earth's Ionosphere and Plasmasphere, *Geomagnetism and Aeronomy*, **17**, 54, 1977.

Ayres, T. R., A Physically Realistic Approximate Form for the Redistribution Function $R_{II\text{-}A}$, *Ap., J.*, **294**, 153, 1985.

Bailey, S. M. and T. N. Woods, Calibration of Multiple Diffraction Orders at SURF-II, *Proceedings of the Ninth Workshop on the Vacuum Ultraviolet Calibration of Space Instruments*, 47, 1993.

Barth, C. A., Ultraviolet Spectroscopy of the Planets, *Jet Propulsion Laboratory Technical Report No. 32-822*, 1965.

Barth, C. A., Ultraviolet Spectroscopy of the Planets, from *The Middle Ultraviolet: Its Science and Technology*, A. E. S. Green editor, John Wiley and Sons, New York, 1966.

Barth, C. A. and S. Schaffner, Ogo 4 Spectrometer Measurements of the Tropical Ultraviolet Airglow, *J. Geophys. Res.*, **75**, 4299, 1970.

Barth, C. A., W. K. Tobiska, D. E. Siskind, and D. D. Cleary, Solar-Terrestrial Coupling: Low Latitude Thermospheric Nitric Oxide, *Geophys. Res. Lett.*, **15**, 92, 1988.

Barth, C. A., Nitric Oxide in the Lower Thermosphere, *Planet. Space Sci.*, **40**, 315, 1992.

Barth, C. A., C. B. Farmer, D. E. Siskind, and J. P. Perich, ATMOS Observations of Nitric Oxide in the Mesosphere and Lower Thermosphere, To Be Submitted to *J. Geophys. Res.*, 1995.

Belitza, D., International Reference Ionosphere: Recent Developments, *Radio Sci.*, **21**, 343, 1986.

Benesch, W., J. T. Vanderslice, S. G.Tilford, and P. G. Wilkinson, Franck-Condon Factors for Observed Transitions in $N_2$ above 6 eV, *Astrophys. J.*, **143**, 236, 1966.

Berkowitz, J., *Photoabsorption, Photoionization, and Photoelectron Spectroscopy*, Academic Press, New York, 1979.

Bowers, C. W., *Spectroscopy of the Far and Extreme Ultraviolet Dayglow*, Ph. D. Thesis, Johns Hopkins Univ., Baltimore Md., 1985.

Bowers, C. W., P. D. Feldman, P. D. Tennyson, and M. Kane, Observations of the OI Ultraviolet Intercombination Emissions in the Terrestrial Dayglow, *J. Geophys. Res.*, **92**, 239, 1987.

Borst, W. L., Excitation of Several Important Metastable States of $N_2$ by Electron Impact, *Phys. Rev. A.*, **5**, 648, 1972.

Brinkmann, R. T. and S. Trajmar, Electron Impact Excitation of $N_2^*$, *Ann. Geophys.*, **26**, 201, 1970.

Brunger, M. J. and P. J. O. Teubner, Differential Cross Sections for Electron-Impact Excitation of the Electronic States of $N_2$, *Phys. Rev. A.*, **41**, 1413, 1990.

Buansanto, M. J., S. C. Solomon, and W. K. Tobiska, Comparison of Measured and Modeled Solar EUV Flux and its Effect on the E-F1 Region of the Ionosphere, *J. Geophys. Res.*, **97**, 10513, 1992.

Budzien, S. A., P. D. Feldman, and R. R. Conway, Observations of the ultraviolet airglow by the Ultraviolet Limb Imaging Experiment on STS-39, *J. Geophys. Res.*, **99**, 23275, 1994.

Burnett, T. and S. P. Rountree, Differential and Total Cross Sections for Electron-Impact Ionization of Atomic Oxygen, *Phys. Rev. A.*, **20**, 1468, 1979.

Canfield, L. R., New Far UV Detector Calibration Facility at the National Bureau of Standards, *Applied Optics*, **26**, 3831, 1987.

Canfield, L. R., J. Kerner, and R. Korde, Stability and Quantum Efficiency Performance of Silicon Photodiode Detectors in the Far Ultraviolet, *Applied Optics*, **28**, 3940, 1989.

Cartwright, D. C., S. Trajmar, A. Chutjian, and W. Williams, Electron Impact Excitation of the Electronic States of $N_2$, II, Integral Cross Sections at Incident Energies from 10 to 50 eV, *Phys. Rev. A.*, **16**, 1041, 1977.

Cartwright, D. C., Vibrational Populations of the Excited States of $N_2$ Under Auroral Conditions, *J. Geophys. Res.*, **83**, 517, 1978.

Christensen, A. B., R. W. Eastes, P. D. Feldman, and E. P. Gentieu, High Resolution Dayglow OI (1304Å) and OI (989Å) Rocket Observations, *J. Geophys. Res.*, **87**, 6317, 1982.

Cicerone, R. J. and S. A. Bowhill, Photoelectron Fluxes in the Ionosphere Computed by a Monte Carlo Method, *J. Geophys. Res.*, **76**, 8299, 1971.

Cicerone, R. J., W. E. Swartz, R. S. Stolarski, A. F. Nagy, and J. S. Nisbet, Thermalization and Transport of Photoelectrons: A Comparison of Theoretical Approaches, *J. Geophys. Res.*, **78**, 6709, 1973.

Cleary, D. D., *Analysis of Nitric Oxide Fluorescence Bands from High Latitude Rocket Observations of the Thermospheric Dayglow*, Ph.D. Thesis, University of Colorado, 1986.

Condon, E. U. and G. H. Shortley, *The Theory of Atomic Spectra*, Cambridge University Press, Cambridge (1963).

Conway, R. R., Self-Absorption of the $N_2$ Lyman-Birge-Hopfield Bands in the Far Ultravioled Dayglow, *J. Geophys. Res.*, **87**, 859, 1982.

Conway, R. R., Photoabsorption and Photoionization Cross Sections of O, $O_2$ and $N_2$ for Photoelectron Production Calculations: A Compilation of Recent Laboratory Measurements, *NRL Memo. Rpt. 6155*, 1988.

Conway, R. R., R. R. Meier, and R. E. Huffman, Abundance of Atomic Oxygen in the Lower Thermosphere from Satellite Observations of the OI 1641Å Dayglow, *Planet. Space Sci.*, **36**, 963, 1988.

Cotton, D. M., S. Chakrabarti, and G. R. Gladstone, Preliminary Results from the Berkeley EUV Airglow Rocket Spectrometer: OI and $N_2$ FUV/EUV Dayglow in the Thermosphere and Lower Exosphere, *J. Geophys. Res.*, **98**, 21627, 1993a.

Cotton, D. M., S. Chakrabarti, and G. R. Gladstone, Optically Thick Cascade to the OI 3s $^3$S State in the Earth's Thermosphere, *J. Geophys. Res.*, **98**, 21643, 1993b.

Cotton, D. M., G. R. Gladstone, and S. Chakrabarti, Sounding Rocket Observation of a Hot Atomic Oxygen Geocorona, *J. Geophys. Res.*, **98**, 21651, 1993c.

Dalgarno, A., M. B. McElroy, and R. J. Moffeitt, Electron Temperatures in the Ionosphere, *Planet. Space Sci.*, **11**, 463, 1963.

Dalgarno, A., M. B. McElroy, and A. I. F. Stewart, Electron Impact Excitation of the Dayglow, *J. Atmos. Sci.*, **26**, 753, 1969.

Doering, J. P. and E. E. Gulcicek, Absolute Differential and Integral Electron Excitation Cross Sections for Atomic Oxygen 8. The $^3P$ - $^5S^0$ Transition (1356Å) from 13.9 to 30 eV, *J. Geophys. Res.*, **94**, 2733, 1989.

Dunford, H. B., Elements of Diatomic Molecular Spectra, Addison-Wesley, Reading, Massachussettes, 1968.

Eastes, R. W., P. D. Feldman, E. P. Gentieu, and A. B. Christensen, The Ultraviolet Dayglow at Solar Maximum, 1, Far UV Spectroscopy at 3.5Å Resolution, *J. Geophys. Res.*, **90**, 6594, 1985.

Eastes, R. W. and W. E. Sharp, Rocket-Borne Spectrographic Measurements in the Ultraviolet Aurora: The Lyman-Birge-Hopfield Bands, *J. Geophys. Res.*, **92**, 10095, 1987.

Eparvier, F. G., Nitric Oxide in the Lower Thermosphere, PhD Thesis, University of Colorado, 1991.

Erdman, P. W. and E. C. Zipf, Electron Impact Excitation of the OI 7990Å Multiplet, *J. Geophys. Res.*, **88**, 7245, 1983.

Fastie, W. G., H. M. Crosswhite, and T. P. Markham, Far Ultra-Violet Spectra with a Rocket Ebert Spectrophotometer, *Ann. Geophys.*, **17**, 109, 1961.

Fastie, W. G., H. M. Crosswhite, and D. F. Heath, Rocket Spectrophotometer Airglow Measurements in the Far Ultraviolet, *J. Geophys. Res.*, **69**, 4129, 1964.

Feng, W. H. S. Ogawa, and D. L. Judge, The Absolute Solar Soft X Ray Flux in the 20 - 100Å Region, *J. Geophys. Res.*, **94**, 9125, 1989.

Fennelly, J. A. and D. G. Torr, Photoionization and Photoabsorption Cross Sections of O, N2, O2 and N for Aeronomic Calculations, *At. Data and Nuc. Data Tables*, **51**, 321, 1992.

Finn, T. G. and J. P. Doering, Measurement of the 13 to 100 eV Electron Impact Excitation Cross Sectionfor the $X^1\Sigma_g^+$ - $a^1\Pi_g$ Transition in $N_2$,*J. Chem. Phys.*, **64**, 4490, 1976.

Freund, R. S., Radiative Lifetime of $N_2$ ($a\ ^1\pi_g$) and the Formation of Metastable $N_2$ ($a'\ ^1\Sigma_u^-$), *J. Chem. Phys.*, **56**, 4344, 1972.

Furst, M. L. and R. M. Graves, Spectrometer Calibrations at SURF II, *Proceedings of the Ninth Workshop on the Vacuum Ultraviolet Calibration of Space Instruments*, 41, 1993.

Gentieu, E. P., P. D. Feldman, and R. R. Meier, Spectroscopy of the Extreme Ultraviolet Dayglow at 6.5Å Resolution: Atomic and Ionic Emisions Between 530 and 1240Å., *Geophys. Res. Lett.*, **8**, 325, 1979.

Gibson, S. T., H. P. F. Gies, A. J. Blake, D. G. McCoy, and P. J. Rodgers, Temperature Dependence in the Schumann-Runge Photoabsorption Continuum of Oxygen, *J. Quant. Spectrosc. Radiat. Transfer*, **30**., 385, 1983.

Gladstone, G. R., Radiative Transfer with Partial Frequency Redistribution in Inhomogeneous Atmospheres: Application to the Jovian Aurora, **27**, 545, *J. Quant. Spectrosc. Radiat. Transfer*, 1982.

Gladstone, G. R., UV Resonance Line Dayglow Emissions on Earth and Jupiter, *J. Geophys. Res.*, **93**, 14, 623, 1988.

Gladstone, G. R., Solar OI 1304-Å Triplet Line Profiles, *J. Geophys. Res*, **97**, 19519, 1992.

Green, A. E. S. and C. A. Barth, Calculations of the Photoelectron Excitation of the Dayglow, *J. Geophys. Res.*, **72**, 3975, 1967.

Green, A. E. S. and T. Sawada, Ionization Cross Sections and Secondary Electron Distributions, *J. Atmos. Terres. Phys.*, **34**, 1719, 1972.

Green, A. E. S. and R. S. Stolarski, Analytic Models of Electron Impact Excitation Cross Sections, *J. Atmos. Terres. Phys.*, **34**, 1703, 1972.

Gulcicek, E. E. and J. P. Doering, Absolute Differential and Integral Electron Excitation Cross Sections for Atomic Oxygen 5. Revised Values for the P - $^3S^\circ$ (1304Å) and $^3P$ - $^3D^\circ$ (989Å) Transition Below 30 eV, *J. Geophys. Res.*, **93**, 5879, 1988.

Gulcicek, E. E., J. P. Doering, and S. O. Vaughan, Absolute Differential and Integral Cross Sections for Atomic Oxygen 6. The $^3P$ - $^3P$ and $^3P$ - $^5P$ Transitions from 13.87 to 100 eV, *J. Geophys. Res.*, **93**, 5885, 1988.

Hanson, W. B. and F. S. Johnson, Electron Temperatures in the Ionosphere, *Mem. Soc. Roy. Sci. Liege*, **5**, 390, 1961.

Handke, PhD Thesis, University of Berlin, 1898.

Hedin, A. E., MSIS-86 Thermospheric Model, *J. Geophys. Res.*, **92**, 4649, 1987.

Henke, B. L, P. Lee, T. J. Tanaka, R. L. Shimabukuro, and B. K. Fujikawa, Low-Energy X-ray Interaction Coefficients: Photoabsorption, Scattering and Reflection, *At. Data Nuc. Data Tables*, **27**, 1, 1982.

Henke, B. L., J. C. Davis, E. M. Gullikson, and R. C. Perera, A Preliminary Report on X ray Photoabsorption Coefficients and Atomic Scattering Factors for 92 Elements in the 10-10,000 eV Region, *Lawrence Berkeley Laboratory Report LBL-26259*, 1988.

Herzberg, G., *Molecular Spectra and Molecular Structure I., Spectra of Diatomic Molecules*, reprint of 2nd ed. with corrections, Krieger, Malabar, Florida, 1989

Hinteregger, H. E., L. A. Hall, and G. Schmidtke, Solar XUV Radiation and Neutral Particle Distribution in the July 1963 Thermosphere, *Space Res.*, **5** 1175, 1965.

Hinteregger, H. E., K. Fukui, and G. R. Gilson, Observational, Reference and Model Data on Solar EUV, From Measurementson AE-E, *Geophys. Res. Lett.*, **8**, 1147, 1981.

Huber, K. P. and G. Herzberg, *Molecular Spectra and Molecular Structure IV, Constants of Diatomic Molecules*, Van Nostrad Reinhold, New York, New York, 1979.

Hummer, D. G., Non-Coherent Scattering, I, The Redistribution Functions with Doppler Broadening, *Monthly Notices Roy. Astron. Soc.*, **125**, 21, 1962.

Hummer, D. G., Non-Coherent Scattering, VI, Solutions of the Transfer Problem with a Frequency Dependent Source Function, *Monthly Notices Roy. Astron. Soc.*, **145**, 95, 1969.

Jackman, C. H., R. H. Garvey, and A. E. S. Green, Electron Impact on Atmospheric Gases, I, Updated Cross Sections, *J. Geophys. Res.*, **82**, 5081, 1977.

Julienne, P. S. and J. Davis, Cascade and Radiation Trapping Effects on Atmospheric Atomic Oxygen Emission Excited by Electron Impact, *J. Geophys. Res.*, **81**, 1397, 1976.

Kirby, K., E. R. Constantinides, S. Babeu, M. Oppenheimer, and G. A. Victor, Photoionization and photoabsorption cross sections of He, O, $N_2$ and $O_2$ for aeronomic calculations, *At. Data and Nucl. Data Tables*, **23**, 63, 1979.

Korde, R. and J. Geist, Quantum Efficiency Stability of Silicon Photodiodes, *Applied Optics*, **26**, 5284, 1987.

Korde, R., L. R. Canfield, and B. Wallis, Stable High Quantum Efficiency Silicon Photodiodes for Vacuum-UV Applications, *SPIE*, 932, 153, 1988.

Korde, R. and L. R. Canfield, Silicon Photodiodes with Stable Near Theoretical Quantum Efficiency in the Soft X-ray Region, *SPIE*, 1140, 126, 1989.

Kovacs, I., *Rotational Structure in the Spectra of Diatomic Molecules*, Elsevier, New York, 1969.

Kreplin, R. W., The Solar Cycle Variation of Soft X-Ray Emission, *Ann. Geophys.*, **26**, 567, 1970.

Kreplin, R. W. and D. M. Horan, Variability of X-Ray and EUV Solar Radiation in Solar Cycles 20 and 21, *Proceedings of the Workshop on the Solar Electromagnetic Radiation Study for Solar Cycle 22*, R. F. Donnelly editor, 405, 1992.

Lassettre, E. N., Inelastic electron scattering. In *Methods of Experimental Physics*, ed. D. Williams, Academic Press, 1974.

Lean, J. L., and A. J. Blake, The Effect of Temperature on Thermospheric Molecular Oxygen Absorption in the Schumann-Runge Continuum, *J. Geophys. Res.*, **86**, 211, 1981.

Lean, J., Solar Ultraviolet Variations: A Review, *J. Geophys. Res.*, **92**, 839, 1987.

Lean, J., A Comparison of the Sun's Extreme Ultraviolet Irradiance Variations, *J. Geophys. Res.*, **95**, 11933, 1990.

Link, R., *Dayside Magnetospheric Cleft Auroral Processes*, Ph.D. Thesis, York University, Toronto, Canada, 1982.

Link, R., S. Chakrabarti, G. R. Gladstone, and J. C. McConnel, An Analysis of Satellite Observations of the OI EUV Dayglow, *J. Geophys. Res.*, **93**, 2693, 1988a.

Link, R., G. R. Gladstone, S. Chakrabarti, and J. C. McConnel, A Reanalysis of Rocket Measurements of the Ultraviolet Dayglow, *J. Geophys. Res.*, **93** 14631, 1988b.

Link, R., Feautrier Solution of the Electron Transport Equation, *J. Geophys. Res.*, **97**, 159, 1992.

Loftus, A. and P. H. Krupenie, The Spectrum of Molecular Nitrogen, *J. Phys. Chem. Ref. Data*, **6**, 113, 1977.

Malitson, I. H., *Applied Optics*, **2**, 1103, 1963.

Mason, N. J. and W. R. Newell, Electron Impact Total Excitation Cross Section of the $a^1\Pi_g$ State of $N_2$, *J. Phys. B: At. Mol Phys.*, **20**, 3913, 1987.

Manson, J. E., The Solar Extreme Ultraviolet Between 30 and 205Å on November 9, 1971, Compared with Previous Measurements in this Spectral Region, *J. Geophys. Res.*, **81**, 1629, 1976.

McClintock, W. E., C. A. Barth, R. E. Steele, G. M. Lawrence, and J. G. Timothy, Rocket-borne instrument with a high-resolution microchannel plate detector for planetary UV spectroscopy, *Appl. Opt.*, **21**, 3071, 1982.

McCoy, R. P., K. F. Dymond, G. G. Fritz, S. E. Thonnard, R. R. Meier, and P. A. Regeon, Far- and Extreme-Ultraviolet Limb Imaging Spectrograph for DMSP Satellites, *SPIE, Instrumentation for Planetary and Remote Sensing*, **1745**, 310, 1992.

Meier, R. R., D. J. Strickland, P. D. Feldman, and E. P. Gentieu, The Ultraviolet Dayglow 1. Far UV Emissions of N and $N_2$, *J. Geophys. Res.*, **85**, 2177, 1980.

Meier, R. R., R. R. Conway, P. D. Feldman, D. J. Strickland, and E. P. Gentieu, Analysis of Nitorgen and Oxygen Far Ultraviolet Auroral Emissions, *J. Geophys. Res.*, **87**, 2444, 1982.

Meier, R. R. and D. E. Anderson Jr., Determination of the Atmospheric Composition and Temperature from U. V. Airglow, *Planet. Space Sci.*, **31**, 967, 1983.

Meier, R. R., R. R. Conway, D. E. Anderson, Jr., P. D. Feldman, R. W. Eastes, E. P. Gentieu, and A. B. Christensen, The Ultraviolet Dayglow at Solar Maximum 3. Photoelectron-Excited Emissions of $N_2$ and O, *J. Geophys. Res.*, **90**, 6608, 1985.

Meier, R. R., D. E. Anderson, L. J. Paxton, R. P. McCoy, and S. Chakrabarti, The OI $3d\ ^3D^0 - 2p^4\ ^3P$ Transition at 1026 Å in the Day Airglow, *J. Geophys. Res.*, **92**, 8767, 1987.

Meier, R. R., Remote Sensing of the Upper Atmosphere, *Space Science Reviews*, **58**, 1, 1991.

Mihalas, D., *Stellar Atmospheres*, W. H. Freeman and Co., San Francisco, 1978.

Morrison, M. D. and R. R. Meier, The OI 989 and 1173Å Multiplets in the Dayglow, *Planet. Space Sci.*, **36**, 987, 1988.

Morrison, M. D., C. W. Bowers, P. D. Feldman, and R. R. Meier, The EUV Dayglow at High Spectral Resolution, *J. Geophys. Res.*, **95**, 4113, 1990.

Mount, G. H. and G. J. Rottman, Solar Absolute Spectral Irradiance 118-300 nm: July 25, 1983, *J. Geophys. Res.*, **90**, 13031, 1985.

Nagy, A. F. and P. M. Banks, Photoelectron Fluxes in the Ionosphere, *J. Geophys. Res.*, **75**, 6260, 1970.

Ogawa, H. S., L. R. Canfield, D. McCullin, and D. L. Judge, Sounding Rocket Measurement of the Absolute Solar EUV Flux Utilizing a Silicon Photodiode, *J. Geophys. Res.*, **95**, 4291, 1990.

Oran, E. S. and D. J. Strickland, Photoelectron Flux in the Earth's Ionosphere, *Planet. Space Sci.*, **26**, 1161, 1978.

Paxton, L. J., C. I. Meng, G. H. Fountain, B. S. Ogorzalek, E. H. Darlington, S. A. Gary, J. O. Goldsten, D. Y. Kusnierkiewicz, S. C. Lee, L. A. Linstrom, J. J. Maynard, K. Peacock, D. F. Persons, and B. E. Smith, Special Sensor Ultraviolet Spectrographic Imager: An Instrument Description, *SPIE, Instrumentation for Planetary and Remote Sensing*, **1745**, 2, 1992.

Pilling, M. J., A. M. Bass, and W. Braun, A Cruve of Growth Determination of the f-Value for the Fourth Positive System of CO and the Lyman-Birge-Hopfield System of $N_2$, *J. Quant. Spectrosc. Radiat. Transfer*, **11**, 1593, 1971.

Powell, F. R., P. W. Vedder, J. F. Lindblom, and S. F. Powell, Thin Film Filter Performance for Extreme Ultraviolet and X-ray Applications, *SPIE*, **26**, 614, 1990.

Prinz, D. K. and R. R. Meier, OGO-4 Observations of the Lyman-Birge-Hopfield Emission in the Day Airglow, *J. Geophys. Res.*, **76**, 6146, 1971.

Richards, P. G. and D. G. Torr, An Investigation of the Consistency of the Ionospheric Measurements the Photoelectron Flux and Solar EUV Flux, *J. Geophys. Res.*, **89**, 5625, 1984.

Richards, P. G. and D. G. Torr, The Altitude Variation of the Ionospheric Photoelectron Flux, A Comparison of Theory and Measurement, *J. Geophys. Res.*, **90**, 2877, 1985.

Richards, P. G. and D. G. Torr, Theoretical Modeling of the Dependence of the $N_2$ Second Positive 3371Å Auroral Emission on Characteristic Energy, *J. Geophys. Res.*, **95**, 10337, 1990.

Rottman, G. J., Solar Cycle Variation of Ultraviolet, 120-200 nm, Irradiance Measured by the Solar Mesosphere Explorer, 1982 through 1985, *Eos*, **66**, 1009, 1985.

Rountree, S. P. and R. J. W. Henry, Electron-Impact Excitation Cross Sections for Atomic Oxygen: $^3P$ - $^3S$, *Phys. Rev. A*, **6**, 2106, 1972.

Rountree, S. P., Electron-Impact Excitation of Atomic Oxygen: $^3P$ - 3s $^5S^0$ and $^3P$ - 3s $^3S^0$, *J. Phys. B: Atom. Molec. Phys.*, **10**, 2719, 1977.

Samson, J. A. R., *Techniques of Vacuum Ultraviolet Spectroscopy*, Wiley, New York, 1967.

Shemansky, D. E., Transition Probabilities and Collision Broadening Cross Section of the $N_2$ Lyman-Birge-Hopfield System, *J. Chem. Phys.*, **51**, 5487, 1969.

Siskind, D. E., *The Response of Thermospheric Nitric Oxide to an Auroral Storm*, Ph. D. Thesis, University of Colorado, 1988.

Siskind, D. E., C. A. Barth, and D. D. Cleary, The Possible Effect of Solar Soft X Rays on Thermospheric Nitric Oxide, *J. Geophys. Res.*, **95**, 4311, 1990.

Siskind, D. E., D. J. Strickland, R. R. Meier, T. Majeed, and F. G. Eparvier, On the Relationship between the Solar Soft X-ray Flux and Thermospheric Nitric Oxide: An update with an Improved Photochemical Model, *J. Geophys. Res* , Accepted, 1995.

Solomon, S. C., P. B. Hays and V. J. Abreu, The Auroral 6300Å Emission: Observations and Modeling, *J. Geophys. Res.*, **93**, 9867, 1988.

Solomon, S. C. and V. J. Abreu, The 630 nm Dayglow, *J. Geophys. Res.*, **94**, 6817, 1989.

Solomon, S. C., Auroral Electron Transport Using the Monte Carlo Method, *Geophys. Res. Letters*, **20**, 185, 1993.

Stamnes, K., On the Two Stream Approach to Electron Transport and Thermalization, *J. Geophys. Res.*, **86**, 2405, 1981a.

Stamnes, K., Electron Transport and Energy Degradation: On the Numerical Solution to the Two-Stream Equations, *Sci. Rep. UAG R-286*, Geophys. Inst., Univ. of Alaska, Fairbanks, 1981b.

Stewart, A. I. F., Photoionization Coefficients and Photoelectron Impact Excitation Efficiencies in the Daytime Ionosphere, *J. Geophys. Res.*, **75**, 6333, 1970.

Stone, E. J. and E. C. Zipf, Electron Impact Excitation on the $^3S^0$ and $^5S^0$ States of Atomic Oxygen, *J. Chem. Phys.*, **60**, 4237, 1974.

Strickland, D. J., D. L. Book, T. P. Coffey, and J. A. Fedder, Transport Equation Techniques for the Deposition of Auroral Electrons, *J. Geophys. Res.*, **81**, 2755, 1976.

Strickland, D. J. and R. R. Meier, A Photoelectron Model for the Rapid Calculation of Atmospheric Excitation Rates, *NRL Memorandum Report 5004*, 1982.

Strickland, D. J. and D. E. Anderson, Jr, Radiation Transport Effects on the 1356Å Limb Intensity Profile in the Dayglow, *J. Geophys. Res.*, **88**, 9260, 1983.

Takacs, P. Z. and P. D. Feldman, Far Ultraviolet Atomic and Molecular Nitrogen Emissions in the Dayglow, *J. Geophys. Res.*, **82**, 5011, 1977.

Tatum, J. B., The Interpretation of Intensities Diatomic Molecular Spectra, *Astrophys. J. Supp. Ser.* , **14**, 21, 1967.

Tayal, S. S. and R. J. W. Henry, Electron-Impact Excitation of Atomic Oxygen, *Phys. Rev. A.*, **38**, 5945, 1988.

Timothy, A. F. and J. G. Timothy, Long-Term Intensity Variations in the Solar Helium II Lyman Alpha Line, *J. Geophys. Res.*, **75**, 6950, 1970.

Thorne, A. P., *Spectrophysics*, 2nd. ed., Chapman and Hall, London, 1988.

Tobiska, W. K. and C. A. Barth, A Solar EUV Flux Model, *J. Geophys. Res.*, **95**, 8243, 1990.

Tobiska, W. K., Revised Solar Extreme Ultraviolet Flux Model, *J. Atmos. Terr. Phys.*, **53**, 1005, 1991.

Torr, M. R., D. G. Torr, R. A. Ong, and H. E. Hinteregger, Ionization Frequencies for Major Thermospheric Constituents as a Function of Solar Cycle 21, *Geophys. Res. Lett.*, **6**, 771, 1979.

Torr, M. R. and D. G. Torr, Ionization Frequencies for Solar Cycle 21: Revised, *J. Geophys. Res.*, **90**, 6675, 1985.

Torr, M. R., D. G. Torr, T. Chang, P. Richards, and G. Germany, $N_2$ Lyman Birge Hofield Dayglow from ATLAS 1, *J. Geophys. Res.*, **99**, 21397, 1994.

Trajmar, S., D. F. Register and A. Chutjian, Electron Scattering by Molecules II, Experimental Methods and Data, *Phys. Reports*, **97**, 219, 1983.

Vallance Jones, A., *Aurora*, D. Reidel co., Holland, 1974.

van der Burgt, P. J. M., W. B. Westerveid, and J. S. Risley, Photoemission Cross Sections for Atomic Transitions in the Extreme Ultraviolet Due to Electron Collisions with Atoms and Molecules, *J. Phys. Chem. Ref. Data*, **18**, 1757, 1989.

Vaughn, S. O. and J. P. Doering, Absolute Experimental Differential and Integral Electron Excitation Cross Sections for Atomic Oxygen 3. The ($^3P$ - $^3D^o$) Transition (989Å) From 20 to 200 eV With Improved Values for the ($^3P$ - $^3S^o$) Transition (1304Å), *J. Geophys. Res.*, **92**, 7749, 1987

Von Rosenberg, D. U., *Methods for Numerical Solution of Partial Differential Equations*, American Elsevier, New York, New York, 1969.

Wang, J., D. G. McCoy, A. J. Blake, and L. Torup, Effects of the Close Approach of Potential Curves in Photoabsorption by Diatomic Molecules-II. Temperature Dependence of the $O_2$ Cross Section in the Region 130-160 nm, *J. Quant. Spectrosc. Radiat. Transfer*, **38**, 19, 1987.

Winningham, J. D., D. T. Decker, J. U. Kozyra, J. R. Jasperse, and A. F. Nagy, Energetic (> 60 eV) Atmospheric Photoelectrons, *J. Geophys. Res.*, **94**, 15225, 1989.

Woods, T. N. and G. J. Rottman, Solar EUV Irradiance Derived From a Sounding Rocket Experiment on November 10, 1988, *J. Geophys. Res.*, **95**, 6227, 1990.

Woods, T. N., R. T. Wrigley III, G. J. Rottman, and R. E. Haring, Scattered Light Properties of Diffraction Gratings, *Applied Optics*, **33**, 4273, 1994.

Woods, T. N., G. J. Rottman, S. M. Bailey and S. C. Solomon, Far Ultraviolet and Extreme Ultraviolet Instrumentation for Measuring the Solar Spectral Irradiance and the Terrestrial Airglow, *Optical Engineering*, **33**, 438, 1994.

Zetner, P. W. and S. Trajmar, in *Abstracts of the Fifteenth International Conference on the Physics of Electronic and Atomic Collisions*, Brighton, 1987, edited by J. Geddes, H. B. Gilbody, A. E. Kingston and C. J. Latimer (Queen's University, Belfast), 301, 1987.

Zipf, E. C. and R. W. McLaughlin, On the Dissociation of Nitrogen by Electron Impact and by EUV Photo-Absorption, *Planet. Space Sci.*, **26**, 449, 1978.

Zipf, E. C. and P. W. Erdman, Electron Impact Excitation of Atomic Oxygen: Revised Cross Sections, *J. Geophys. Res.*, **90**, 11087, 1985.

Zombeck, M. V., *Handbook of Space Astronomy and Astrophysics*, Cambridge University Press, Cambridge, 1990.

# Appendix A

## Analytic Models of Electron Impact Cross Sections

In the */glow* model, analytic representations are used for all inelastic cross sections. This appendix describes the forms for the analytic expressions. These representations allow cross sections to be expressed by a unique set of parameters. Tables are provided which contain the parameters for each of the cross sections used in the */glow* model. Elastic scattering cross sections and elastic and inelastic backscatter probabilities are tabulated. The sources for all material presented are described by Solomon *et. al.* (1988).

Jackman *et al.* (1977) provide the following expression for the differential cross section $S$ for ionization by electron impact:

$$S(E,T) = \frac{A(E)\Gamma^2(E)}{\left[T - T_0(E)\right]^2 + \Gamma^2(E)}, \qquad \text{A-1}$$

where $E$ is the energy of the primary electron before the collision and $T$ is the energy of the secondary electron produced by the collision. The following forms give $A$, $\Gamma$, and $T_0$:

$$A(E) = \left(\frac{K}{E} + K_B\right)\ln\left(\frac{E}{J} + J_B + \frac{J_C}{E}\right), \qquad \text{A-2}$$

$$\Gamma(E) = \frac{\Gamma_S E}{E + \Gamma_B}, \qquad \text{A-3}$$

$$T_0(E) = T_S - \frac{T_A}{E + T_B}. \qquad \text{A-4}$$

In Equations A-2 through A-4, $K$, $K_B$, $J$, $J_B$, $J_C$, $\Gamma_S$, $\Gamma_B$, $T_S$, $T_A$, and $T_B$ are adjustable parameters that are different for different ionization cross sections. To obtain the integral cross section for ionization, the differential cross section $S$ must be integrated

PRECEDING PAGE BLANK NOT FILMED

PAGE 232 INTENTIONALLY BLANK

over secondary electron energies. This integration has been performed by Green and Sawada (1972) to achieve the following result:

$$\sigma_i(E) = \int_0^{T_M} S(E,T)dT = A\left[\tan^{-1}\left(\frac{T_M - T_0}{\Gamma}\right) + \tan^{-1}\left(\frac{T_0}{\Gamma}\right)\right]. \qquad \text{A-5}$$

Here, $T_M$ is the maximum energy possible for the secondary electron, assuming that the primary electron is the more energetic one after the collision. This maximum energy can be written:

$$T_M = \frac{1}{2}(E - I), \qquad \text{A-6}$$

where $I$ is the energy of ionization.

Table A-1 tabulates the values of the above parameters for the ionized states of O, $O_2$, and $N_2$ used by */glow*. For all cases, the values of $K_B$, $J_B$, and $J_C$ are zero and therefore are not listed.

Analytic expressions of cross sections for excitation by electron impact have been developed by Green and Stolarski (1972). The following form is used:

$$\sigma_E(E) = \frac{q_0 A}{W^2}\varepsilon^{-\Omega}\Phi_I(\varepsilon), \qquad \text{A-7}$$

where,

$$q_0 = 4\pi a_0^2 R^2. \qquad \text{A-8}$$

In these equations, $a_0$ is the Bohr radius and $R$ is the Rydberg energy; therefore, $q_0$ has the value 6.514 x $10^{-14}$ $eV^2$ $cm^2$. The symbol $W$ denotes the threshold excitation energy, $\varepsilon = E/W$, and A and $\Omega$ are adjustable parameters. The function $\Phi$ is referred to as the low energy modifier and it describes the behavior of the cross section near the threshold energy. Green and Stolarski provided several forms for $\Phi$. The form used by */glow* is written:

$$\Phi = \left[1 - \varepsilon^{-\gamma}\right]^{\nu}, \qquad \text{A-8}$$

where $\gamma$ and $\nu$ are fitting parameters.

Table A-2 lists the values of $W$, $A$, $\Omega$, $\nu$, and $\gamma$ for the excited states of O, $O_2$, and $N_2$ used by */glow*. Tables A-3 through A-5 tabulate the values of the elastic scattering cross sections and the elastic and inelastic backscatter probabilities used by */glow*. The data are not expressed analytically, instead the values are tabulated as a function of electron energy. When used by */glow*, they are interpolated onto the */glow* energy grid. The sources of the data are described by Solomon *et al.* (1988).

**Table A-1 Ionization Cross Section Parameters**

| Ion State | I | K | J | $T_S$ | $T_A$ | $T_B$ | $\Gamma_S$ | $\Gamma_B$ |
|---|---|---|---|---|---|---|---|---|
| O | | | | | | | | |
| $^4S$ | 13.6 | 1.13 | 1.81 | 6.41 | 3450.0 | 162.0 | 13.0 | -00.815 |
| $^2D$ | 16.9 | 1.25 | 1.79 | 6.41 | 3450.0 | 162.0 | 13.0 | -00.815 |
| $^2P$ | 18.5 | 0.67 | 1.78 | 6.41 | 3450.0 | 162.0 | 13.0 | -00.815 |
| $O_2$ | | | | | | | | |
| $X\ ^2\pi_g$ | 12.1 | 0.47 | 3.76 | 1.86 | 1000.0 | 024.2 | 18.5 | 12.100 |
| $a\ ^4\pi_u$ | 16.1 | 1.13 | 3.76 | 1.86 | 1000.0 | 032.2 | 18.5 | 16.100 |
| $A\ ^2\pi_u$ | 16.9 | 1.13 | 3.76 | 1.86 | 1000.0 | 033.8 | 18.5 | 16.900 |
| $b\ ^4\Sigma_g^-$ | 18.2 | 1.01 | 3.76 | 1.86 | 1000.0 | 036.4 | 18.5 | 18.200 |
| $B\ ^2\Sigma_g^-$ | 20.0 | 0.65 | 3.76 | 1.86 | 1000.0 | 040.6 | 18.5 | 20.300 |
| $c\ ^4\Sigma_u$- $^2\pi$ (III) | 23.0 | 0.95 | 3.76 | 1.86 | 1000.0 | 046.0 | 18.5 | 23.000 |
| 37 eV state | 37.0 | 0.59 | 3.76 | 1.86 | 1000.0 | 074.0 | 18.5 | 37.000 |
| $N_2$ | | | | | | | | |
| $X\ ^2\Sigma_g^+$ | 15.6 | 2.42 | 1.74 | 4.71 | 1000.0 | 031.2 | 13.8 | 15.580 |
| $A\ ^2\Sigma_u$ | 16.7 | 1.06 | 1.74 | 4.71 | 1000.0 | 033.5 | 13.8 | 16.730 |
| $B\ ^2\Sigma_u^+$ | 18.8 | 0.55 | 1.74 | 4.71 | 1000.0 | 037.5 | 13.8 | 18.750 |
| $D\ ^2\pi_g$ | 22.0 | 0.37 | 1.74 | 4.71 | 1000.0 | 044.0 | 13.8 | 22.000 |
| $C\ ^2\Sigma_u^+$ | 23.6 | 0.37 | 1.74 | 4.71 | 1000.0 | 047.2 | 13.8 | 23.600 |
| 40 ev state | 40.0 | 0.53 | 1.74 | 4.71 | 1000.0 | 080.0 | 13.8 | 40.000 |

**Table A-2 Excitation Cross Section Parameters**

| Excited State | W | A | Ω | ν | γ |
|---|---|---|---|---|---|
| O | | | | | |
| $^1D$ | 1.96 | 0.010 | 1.00 | 2.00 | 1.00 |
| $^1S$ | 4.17 | 0.004 | 1.00 | 1.04 | 0.50 |
| 3s $^5S$ | 9.29 | 0.179 | 3.00 | 2.53 | 1.02 |
| 3s $^3S$ | 9.53 | 0.356 | 0.75 | 0.54 | 0.01 |
| 3p $^5P$ | 10.76 | 0.065 | 3.00 | 2.43 | 4.19 |
| 3p $^3P$ | 10.97 | 0.024 | 0.85 | 2.87 | 4.88 |
| 3d $^3D$ | 12.07 | 0.029 | 0.75 | 0.93 | 0.66 |
| 3s' $^3D$ | 12.54 | 0.122 | 0.75 | 0.72 | 0.17 |
| $O_2$ | | | | | |
| a | 0.98 | 0.080 | 2.00 | 6.18 | 0.53 |
| b | 1.64 | 0.021 | 2.00 | 4.14 | 0.51 |
| A +A' + c | 4.50 | 0.022 | 1.15 | 1.00 | 0.98 |
| B | 8.44 | 0.340 | 0.75 | 1.05 | 0.99 |
| 9.9 ev state | 9.90 | 0.066 | 0.75 | 1.60 | 1.86 |
| Σ Rydberg† | 13.50 | 1.110 | 0.75 | 3.00 | 1.00 |
| Σ Vibrational ‡ | 0.25 | 3.480 | 7.00 | 10.87 | 1.00 |
| $N_2$ | | | | | |
| A + B + W | 6.17 | 2.770 | 3.00 | 4.53 | 1.42 |
| B' | 8.16 | 0.114 | 3.00 | 4.78 | 3.54 |
| C | 11.03 | 0.179 | 3.00 | 4.32 | 12.70 |
| a + a' + w | 8.40 | 0.100 | 1.00 | 4.05 | 5.20 |
| b | 12.85 | 0.876 | 0.75 | 1.47 | 0.86 |
| b' | 14.00 | 0.601 | 0.75 | 1.27 | 0.45 |
| Σ Rydberg† | 13.75 | 1.890 | 0.75 | 3.00 | 1.00 |
| Σ Vibrational‡ | 1.85 | 1.350 | 8.00 | 1.58 | 1.00 |

†Denotes the sum of the Rydberg states.

‡Denotes the sum of the vibrational states.

**Table A-3 Elastic Cross Sections and Backscatter Probabilities for O**

| Energy (eV) | Elastic Cross Section (cm2) | Elastic Backscatter Probability | Inelastic Backscatter Probability |
|---|---|---|---|
| 1 | 5.00E-16 | 0.50000 | 0.60000 |
| 2 | 6.00E-16 | 0.49500 | 0.60000 |
| 4 | 7.50E-16 | 0.46800 | 0.60000 |
| 6 | 7.60E-16 | 0.43600 | 0.60000 |
| 8 | 7.70E-16 | 0.42000 | 0.60000 |
| 10 | 7.80E-16 | 0.40500 | 0.60000 |
| 12 | 7.50E-16 | 0.37000 | 0.55000 |
| 14 | 7.20E-16 | 0.36000 | 0.46000 |
| 16 | 6.90E-16 | 0.34000 | 0.40000 |
| 18 | 6.70E-16 | 0.33000 | 0.36000 |
| 20 | 6.50E-16 | 0.32000 | 0.32000 |
| 30 | 5.60E-16 | 0.27000 | 0.22000 |
| 40 | 4.60E-16 | 0.24000 | 0.15000 |
| 50 | 4.00E-16 | 0.22000 | 0.10000 |
| 60 | 3.50E-16 | 0.20000 | 0.08200 |
| 70 | 3.20E-16 | 0.18000 | 0.07000 |
| 80 | 2.90E-16 | 0.17000 | 0.06100 |
| 90 | 2.70E-16 | 0.16000 | 0.05400 |
| 100 | 2.50E-16 | 0.15000 | 0.05000 |
| 150 | 1.90E-16 | 0.13000 | 0.04400 |
| 200 | 1.50E-16 | 0.11500 | 0.03800 |
| 300 | 1.20E-16 | 0.09000 | 0.02800 |
| 500 | 8.00E-17 | 0.06800 | 0.02000 |
| 1000 | 5.00E-17 | 0.04600 | 0.01050 |
| 2000 | 3.02E-17 | 0.02400 | 0.00600 |
| 3000 | 1.99E-17 | 0.01660 | 0.00400 |
| 5000 | 1.20E-17 | 0.01000 | 0.00250 |
| 10000 | 6.08E-18 | 0.00510 | 0.00130 |
| 20000 | 3.06E-18 | 0.00255 | 0.00060 |
| 40000 | 1.55E-18 | 0.00125 | 0.00030 |
| 50000 | 1.24E-18 | 0.00100 | 0.00025 |

**Table A-4 Elastic Cross Sections and Backscatter Probabilities for $O_2$**

| Energy (eV) | Elastic Cross Section (cm2) | Elastic Backscatter Probability | Inelastic Backscatter Probability |
|---|---|---|---|
| 1 | 5.50E-16 | 0.50000 | 0.50000 |
| 2 | 6.90E-16 | 0.50000 | 0.50000 |
| 3 | 7.50E-16 | 0.49000 | 0.50000 |
| 5 | 8.50E-16 | 0.44500 | 0.50000 |
| 7 | 9.60E-16 | 0.42700 | 0.48000 |
| 10 | 1.00E-15 | 0.40500 | 0.44000 |
| 15 | 1.00E-15 | 0.36800 | 0.36000 |
| 20 | 9.00E-16 | 0.34300 | 0.28000 |
| 30 | 8.30E-16 | 0.31600 | 0.20000 |
| 40 | 7.70E-16 | 0.28900 | 0.14000 |
| 50 | 6.90E-16 | 0.25800 | 0.10000 |
| 70 | 5.70E-16 | 0.22000 | 0.07000 |
| 100 | 4.40E-16 | 0.18400 | 0.05000 |
| 150 | 3.30E-16 | 0.16400 | 0.04600 |
| 200 | 2.70E-16 | 0.13300 | 0.04300 |
| 300 | 2.10E-16 | 0.11000 | 0.03700 |
| 400 | 1.80E-16 | 0.10000 | 0.03200 |
| 500 | 1.60E-16 | 0.09200 | 0.02800 |
| 600 | 1.40E-16 | 0.08500 | 0.02400 |
| 700 | 1.30E-16 | 0.08000 | 0.02100 |
| 1000 | 1.10E-16 | 0.06800 | 0.01600 |
| 2000 | 7.00E-17 | 0.03700 | 0.00900 |
| 3000 | 5.00E-17 | 0.02600 | 0.00620 |
| 5000 | 3.00E-17 | 0.01600 | 0.00400 |
| 10000 | 1.53E-17 | 0.00800 | 0.00200 |
| 20000 | 7.72E-18 | 0.00400 | 0.00100 |
| 40000 | 3.90E-18 | 0.00200 | 0.00050 |
| 50000 | 3.13E-18 | 0.00160 | 0.00040 |

**Table A-5 Elastic Cross Sections and Backscatter Probabilities for $N_2$**

| Energy (eV) | Elastic Cross Section (cm2) | Elastic Backscatter Probability | Inelastic Backscatter Probability |
|---|---|---|---|
| 1 | 9.00E-16 | 0.50000 | 0.50000 |
| 2 | 2.27E-15 | 0.50000 | 0.50000 |
| 2.5 | 2.52E-15 | 0.50000 | 0.50000 |
| 3 | 1.93E-15 | 0.49000 | 0.50000 |
| 4 | 1.32E-15 | 0.46800 | 0.50000 |
| 5 | 1.15E-15 | 0.44500 | 0.50000 |
| 6 | 1.16E-15 | 0.43600 | 0.50000 |
| 8 | 1.17E-15 | 0.42000 | 0.50000 |
| 10 | 1.18E-15 | 0.40500 | 0.50000 |
| 15 | 1.14E-15 | 0.36800 | 0.50000 |
| 20 | 1.13E-15 | 0.34300 | 0.44000 |
| 30 | 9.50E-16 | 0.31600 | 0.30000 |
| 40 | 8.60E-16 | 0.28900 | 0.20000 |
| 50 | 7.30E-16 | 0.25800 | 0.13000 |
| 70 | 5.90E-16 | 0.22000 | 0.09000 |
| 100 | 4.70E-16 | 0.18400 | 0.06000 |
| 200 | 3.30E-16 | 0.14000 | 0.05000 |
| 300 | 2.50E-16 | 0.11000 | 0.04200 |
| 500 | 1.60E-16 | 0.08400 | 0.03200 |
| 700 | 1.30E-16 | 0.07400 | 0.02500 |
| 1000 | 1.10E-16 | 0.06300 | 0.02000 |
| 2000 | 6.35E-17 | 0.03400 | 0.01100 |
| 3000 | 4.18E-17 | 0.02400 | 0.00800 |
| 5000 | 2.54E-17 | 0.01500 | 0.00500 |
| 10000 | 1.28E-17 | 0.00740 | 0.00250 |
| 20000 | 6.44E-18 | 0.00370 | 0.00120 |
| 40000 | 3.27E-18 | 0.00180 | 0.00060 |
| 50000 | 2.62E-18 | 0.00140 | 0.00050 |

## Appendix B

## Solar Irradiance and Cross Sections in */glow* Bins

Appendix B lists the photoabsorption and photoionization cross sections in the wavelength bins used for the model calculations. The cross sections are listed in Tables B-1 through B-3 for each of the major thermospheric constituents. Also listed are branching ratios for photoionization to excited states and dissociative photoionization.

The cross sections are taken from the high resolution tabulation of Fennelly and Torr (1992). The branching ratios are taken from Conway (1988). All of the states in the Conway compilation are accounted for, but here, all of the dissociating states are summed. The tabulated values are the result of weighted averages over the wavelength interval. The irradiance in each interval is weighted according to the SC#21REFW reference solar spectrum (Hinteregger *et al.*, 1981). The SC#21REFW solar irradiance in each bin is also listed. From 0.05 to 0.8 nm, the solar irradiance values are solar minimum estimates based on GOES satellite photometric measurements. The GOES 0.1 to 0.8 nm measurements are available daily from the Space Environment Laboratory. The estimates are obtained by assuming the irradiance does not vary over the wavelength range of the GOES channel. From 0.8 to 1.8 nm, the solar irradiance values are taken from Manson (1976).

The compilations of Conway (1988) and Fennelly and Torr (1992) do not extend below 1.8 nm. Thus, below this value the branching ratios are assumed to be constant with wavelength and the cross sections are logarithmic extrapolations from the longer wavelength data.

## Table B-1 Binned Solar Irradiance and Cross Sections for O

| Wavelengths Bins (nm) | | Solar Irrad. (ph $cm^{-2}$ $s^{-1}$) | Ionized State Branching Ratios | | | | | Total Cross Sections ($cm^2$) | |
|---|---|---|---|---|---|---|---|---|---|
| λ min | λ max | | $^4S$ | $^2D$ | $^2P$ | $^4P$ | $^2P$ | Ionization | Absorption |
| 0.05 | 0.10 | 1.00E+01 | 0.29 | 0.33 | 0.21 | 0.10 | 0.07 | 2.00E-23 | 2.00E-23 |
| 0.10 | 0.20 | 1.00E+02 | 0.29 | 0.33 | 0.21 | 0.10 | 0.07 | 2.00E-22 | 2.00E-22 |
| 0.20 | 0.40 | 2.00E+02 | 0.29 | 0.33 | 0.21 | 0.10 | 0.07 | 2.00E-21 | 2.00E-21 |
| 0.40 | 0.80 | 1.00E+04 | 0.29 | 0.33 | 0.21 | 0.10 | 0.07 | 1.20E-20 | 1.20E-20 |
| 0.80 | 1.80 | 2.00E+06 | 0.29 | 0.33 | 0.21 | 0.10 | 0.07 | 7.00E-19 | 7.00E-19 |
| 1.80 | 2.30 | 9.00E+05 | 0.29 | 0.33 | 0.21 | 0.10 | 0.07 | 1.84E-20 | 1.84E-20 |
| 2.30 | 3.20 | 6.70E+06 | 0.30 | 0.32 | 0.21 | 0.10 | 0.07 | 6.90E-20 | 6.90E-20 |
| 3.20 | 4.40 | 3.80E+06 | 0.30 | 0.32 | 0.21 | 0.10 | 0.08 | 1.37E-19 | 1.37E-19 |
| 4.40 | 6.00 | 8.56E+07 | 0.30 | 0.32 | 0.21 | 0.10 | 0.08 | 2.43E-19 | 2.43E-19 |
| 6.00 | 7.00 | 7.65E+07 | 0.30 | 0.32 | 0.21 | 0.10 | 0.08 | 4.26E-19 | 4.26E-19 |
| 7.00 | 8.00 | 7.93E+07 | 0.30 | 0.32 | 0.21 | 0.10 | 0.08 | 6.41E-19 | 6.41E-19 |
| 8.00 | 9.00 | 6.57E+07 | 0.30 | 0.32 | 0.21 | 0.10 | 0.08 | 9.04E-19 | 9.04E-19 |
| 9.00 | 10.00 | 9.40E+07 | 0.30 | 0.32 | 0.21 | 0.10 | 0.08 | 1.12E-18 | 1.12E-18 |
| 10.00 | 11.00 | 3.09E+07 | 0.30 | 0.32 | 0.21 | 0.10 | 0.08 | 1.34E-18 | 1.34E-18 |
| 11.00 | 12.00 | 2.13E+07 | 0.30 | 0.32 | 0.21 | 0.10 | 0.08 | 1.61E-18 | 1.61E-18 |
| 12.00 | 13.00 | 1.59E+07 | 0.30 | 0.32 | 0.21 | 0.10 | 0.08 | 1.91E-18 | 1.91E-18 |
| 13.00 | 14.00 | 1.06E+07 | 0.30 | 0.32 | 0.21 | 0.10 | 0.08 | 2.08E-18 | 2.08E-18 |
| 14.00 | 15.00 | 5.59E+07 | 0.29 | 0.32 | 0.21 | 0.10 | 0.08 | 2.23E-18 | 2.23E-18 |
| 15.00 | 16.00 | 6.10E+07 | 0.28 | 0.33 | 0.21 | 0.10 | 0.08 | 2.33E-18 | 2.33E-18 |
| 16.00 | 17.00 | 1.32E+08 | 0.28 | 0.33 | 0.22 | 0.10 | 0.08 | 3.02E-18 | 3.02E-18 |
| 17.00 | 18.00 | 8.46E+08 | 0.27 | 0.33 | 0.22 | 0.10 | 0.08 | 3.45E-18 | 3.45E-18 |
| 18.00 | 19.00 | 4.46E+08 | 0.27 | 0.34 | 0.22 | 0.10 | 0.08 | 3.88E-18 | 3.88E-18 |
| 19.00 | 20.00 | 3.57E+08 | 0.27 | 0.34 | 0.22 | 0.10 | 0.08 | 4.20E-18 | 4.20E-18 |

| | | | | | | | | | |
|---|---|---|---|---|---|---|---|---|---|
| 20.00 | 21.00 | 1.42E+08 | 0.26 | 0.34 | 0.22 | 0.10 | 0.08 | 4.50E-18 | 4.50E-18 |
| 21.00 | 22.00 | 9.24E+07 | 0.26 | 0.34 | 0.22 | 0.10 | 0.07 | 4.87E-18 | 4.87E-18 |
| 22.00 | 23.00 | 2.39E+08 | 0.26 | 0.35 | 0.22 | 0.10 | 0.07 | 5.17E-18 | 5.17E-18 |
| 23.00 | 24.00 | 1.32E+08 | 0.26 | 0.35 | 0.23 | 0.10 | 0.07 | 5.43E-18 | 5.43E-18 |
| 24.00 | 25.00 | 3.18E+08 | 0.25 | 0.35 | 0.23 | 0.10 | 0.07 | 5.67E-18 | 5.67E-18 |
| 25.00 | 26.00 | 5.50E+08 | 0.25 | 0.36 | 0.23 | 0.10 | 0.07 | 6.06E-18 | 6.06E-18 |
| 26.00 | 27.00 | 1.05E+08 | 0.25 | 0.36 | 0.23 | 0.10 | 0.06 | 6.26E-18 | 6.26E-18 |
| 27.00 | 28.00 | 2.73E+08 | 0.25 | 0.36 | 0.23 | 0.10 | 0.06 | 6.67E-18 | 6.67E-18 |
| 28.00 | 29.00 | 1.37E+08 | 0.25 | 0.37 | 0.23 | 0.10 | 0.05 | 7.10E-18 | 7.10E-18 |
| 29.00 | 30.00 | 1.48E+08 | 0.25 | 0.37 | 0.24 | 0.09 | 0.05 | 7.46E-18 | 7.46E-18 |
| 30.00 | 31.00 | 6.24E+09 | 0.25 | 0.37 | 0.24 | 0.09 | 0.04 | 7.70E-18 | 7.70E-18 |
| 31.00 | 32.00 | 4.10E+08 | 0.26 | 0.39 | 0.25 | 0.10 | 0.00 | 8.15E-18 | 8.15E-18 |
| 32.00 | 33.00 | 4.70E+06 | 0.26 | 0.39 | 0.25 | 0.10 | 0.00 | 8.27E-18 | 8.27E-18 |
| 33.00 | 34.00 | 3.40E+07 | 0.26 | 0.40 | 0.25 | 0.09 | 0.00 | 8.77E-18 | 8.77E-18 |
| 34.00 | 35.00 | 4.18E+08 | 0.26 | 0.40 | 0.25 | 0.09 | 0.00 | 9.15E-18 | 9.15E-18 |
| 35.00 | 36.00 | 1.03E+08 | 0.26 | 0.40 | 0.25 | 0.09 | 0.00 | 9.44E-18 | 9.44E-18 |
| 36.00 | 37.00 | 8.33E+08 | 0.26 | 0.40 | 0.25 | 0.08 | 0.00 | 9.82E-18 | 9.82E-18 |
| 37.00 | 38.00 | 0.00E+00 | 0.26 | 0.41 | 0.25 | 0.08 | 0.00 | 1.05E-17 | 1.05E-17 |
| 38.00 | 39.00 | 0.00E+00 | 0.26 | 0.41 | 0.25 | 0.08 | 0.00 | 1.11E-17 | 1.11E-17 |
| 39.00 | 40.00 | 1.56E+07 | 0.26 | 0.41 | 0.25 | 0.07 | 0.00 | 1.18E-17 | 1.18E-17 |
| 40.00 | 41.00 | 1.79E+08 | 0.26 | 0.41 | 0.25 | 0.07 | 0.00 | 1.16E-17 | 1.16E-17 |
| 41.00 | 42.00 | 8.80E+06 | 0.26 | 0.41 | 0.26 | 0.07 | 0.00 | 1.12E-17 | 1.12E-17 |
| 42.00 | 43.00 | 0.00E+00 | 0.27 | 0.42 | 0.26 | 0.05 | 0.00 | 1.14E-17 | 1.14E-17 |
| 43.00 | 44.00 | 2.05E+08 | 0.27 | 0.43 | 0.27 | 0.03 | 0.00 | 1.14E-17 | 1.14E-17 |
| 44.00 | 45.00 | 0.00E+00 | 0.28 | 0.44 | 0.27 | 0.01 | 0.00 | 1.17E-17 | 1.17E-17 |
| 45.00 | 46.00 | 9.10E+06 | 0.28 | 0.45 | 0.27 | 0.00 | 0.00 | 1.20E-17 | 1.20E-17 |
| 46.00 | 47.00 | 2.00E+08 | 0.28 | 0.45 | 0.27 | 0.00 | 0.00 | 1.19E-17 | 1.19E-17 |
| 47.00 | 48.00 | 3.24E+07 | 0.28 | 0.45 | 0.27 | 0.00 | 0.00 | 1.20E-17 | 1.20E-17 |
| 48.00 | 49.00 | 6.50E+07 | 0.28 | 0.45 | 0.27 | 0.00 | 0.00 | 1.28E-17 | 1.28E-17 |

| | | | | | | | | | |
|---|---|---|---|---|---|---|---|---|---|
| 49.00 | 50.00 | 1.69E+08 | 0.28 | 0.45 | 0.27 | 0.00 | 0.00 | 1.20E-17 | 1.20E-17 |
| 50.00 | 51.00 | 1.43E+08 | 0.28 | 0.45 | 0.27 | 0.00 | 0.00 | 1.18E-17 | 1.18E-17 |
| 51.00 | 52.00 | 3.35E+07 | 0.28 | 0.45 | 0.27 | 0.00 | 0.00 | 1.20E-17 | 1.20E-17 |
| 52.00 | 53.00 | 1.11E+08 | 0.28 | 0.45 | 0.27 | 0.00 | 0.00 | 1.20E-17 | 1.20E-17 |
| 53.00 | 54.00 | 1.86E+08 | 0.29 | 0.45 | 0.26 | 0.00 | 0.00 | 1.22E-17 | 1.22E-17 |
| 54.00 | 55.00 | 2.32E+07 | 0.29 | 0.45 | 0.26 | 0.00 | 0.00 | 1.24E-17 | 1.24E-17 |
| 55.00 | 56.00 | 8.84E+08 | 0.29 | 0.45 | 0.26 | 0.00 | 0.00 | 1.26E-17 | 1.26E-17 |
| 56.00 | 57.00 | 1.34E+08 | 0.29 | 0.45 | 0.26 | 0.00 | 0.00 | 1.28E-17 | 1.28E-17 |
| 57.00 | 58.00 | 6.89E+07 | 0.29 | 0.45 | 0.26 | 0.00 | 0.00 | 1.29E-17 | 1.29E-17 |
| 58.00 | 59.00 | 1.59E+09 | 0.29 | 0.45 | 0.25 | 0.00 | 0.00 | 1.31E-17 | 1.31E-17 |
| 59.00 | 60.00 | 2.09E+08 | 0.30 | 0.45 | 0.25 | 0.00 | 0.00 | 1.33E-17 | 1.33E-17 |
| 60.00 | 61.00 | 4.50E+08 | 0.30 | 0.45 | 0.25 | 0.00 | 0.00 | 1.34E-17 | 1.34E-17 |
| 61.00 | 62.00 | 1.67E+07 | 0.30 | 0.45 | 0.25 | 0.00 | 0.00 | 1.34E-17 | 1.34E-17 |
| 62.00 | 63.00 | 1.60E+09 | 0.31 | 0.45 | 0.24 | 0.00 | 0.00 | 1.34E-17 | 1.34E-17 |
| 63.00 | 64.00 | 2.49E+07 | 0.31 | 0.45 | 0.24 | 0.00 | 0.00 | 1.33E-17 | 1.33E-17 |
| 64.00 | 65.00 | 3.30E+07 | 0.31 | 0.45 | 0.24 | 0.00 | 0.00 | 1.32E-17 | 1.32E-17 |
| 65.00 | 66.00 | 2.18E+07 | 0.31 | 0.45 | 0.24 | 0.00 | 0.00 | 1.29E-17 | 1.29E-17 |
| 66.00 | 67.00 | 6.20E+06 | 0.32 | 0.45 | 0.23 | 0.00 | 0.00 | 1.24E-17 | 1.24E-17 |
| 67.00 | 68.00 | 1.06E+07 | 0.42 | 0.58 | 0.00 | 0.00 | 0.00 | 1.10E-17 | 1.10E-17 |
| 68.00 | 69.00 | 1.39E+08 | 0.42 | 0.58 | 0.00 | 0.00 | 0.00 | 2.24E-17 | 2.24E-17 |
| 69.00 | 70.00 | 4.35E+07 | 0.43 | 0.57 | 0.00 | 0.00 | 0.00 | 9.24E-18 | 9.24E-18 |
| 70.00 | 71.00 | 4.02E+08 | 0.43 | 0.57 | 0.00 | 0.00 | 0.00 | 1.14E-17 | 1.14E-17 |
| 71.00 | 72.00 | 8.01E+07 | 0.44 | 0.56 | 0.00 | 0.00 | 0.00 | 9.00E-18 | 9.00E-18 |
| 72.00 | 73.00 | 1.86E+07 | 0.44 | 0.56 | 0.00 | 0.00 | 0.00 | 1.59E-17 | 1.59E-17 |
| 73.00 | 74.00 | 2.42E+07 | 0.90 | 0.10 | 0.00 | 0.00 | 0.00 | 1.09E-17 | 1.09E-17 |
| 74.00 | 75.00 | 3.06E+07 | 1.00 | 0.00 | 0.00 | 0.00 | 0.00 | 1.29E-17 | 1.29E-17 |
| 75.00 | 76.00 | 1.42E+08 | 1.00 | 0.00 | 0.00 | 0.00 | 0.00 | 9.93E-18 | 9.93E-18 |
| 76.00 | 77.00 | 3.97E+08 | 1.00 | 0.00 | 0.00 | 0.00 | 0.00 | 4.02E-18 | 4.02E-18 |
| 77.00 | 78.00 | 3.08E+08 | 1.00 | 0.00 | 0.00 | 0.00 | 0.00 | 3.87E-18 | 3.87E-18 |

| | | | | | | | | | |
|---|---|---|---|---|---|---|---|---|---|
| 78.00 | 79.00 | 6.39E+08 | 1.00 | 0.00 | 0.00 | 0.00 | 0.00 | 3.72E-18 | 3.72E-18 |
| 79.00 | 80.00 | 5.86E+08 | 1.00 | 0.00 | 0.00 | 0.00 | 0.00 | 4.37E-18 | 4.37E-18 |
| 80.00 | 81.00 | 1.40E+08 | 1.00 | 0.00 | 0.00 | 0.00 | 0.00 | 3.55E-18 | 3.55E-18 |
| 81.00 | 82.00 | 1.80E+08 | 1.00 | 0.00 | 0.00 | 0.00 | 0.00 | 5.89E-18 | 5.89E-18 |
| 82.00 | 83.00 | 2.32E+08 | 1.00 | 0.00 | 0.00 | 0.00 | 0.00 | 2.93E-18 | 2.93E-18 |
| 83.00 | 84.00 | 9.64E+08 | 1.00 | 0.00 | 0.00 | 0.00 | 0.00 | 3.30E-18 | 3.30E-18 |
| 84.00 | 85.00 | 3.83E+08 | 1.00 | 0.00 | 0.00 | 0.00 | 0.00 | 3.25E-18 | 3.25E-18 |
| 85.00 | 86.00 | 4.93E+08 | 1.00 | 0.00 | 0.00 | 0.00 | 0.00 | 3.13E-18 | 3.13E-18 |
| 86.00 | 87.00 | 6.32E+08 | 1.00 | 0.00 | 0.00 | 0.00 | 0.00 | 3.10E-18 | 3.10E-18 |
| 87.00 | 88.00 | 8.13E+08 | 1.00 | 0.00 | 0.00 | 0.00 | 0.00 | 1.12E-17 | 1.12E-17 |
| 88.00 | 89.00 | 1.04E+09 | 1.00 | 0.00 | 0.00 | 0.00 | 0.00 | 3.44E-18 | 3.44E-18 |
| 89.00 | 90.00 | 1.34E+09 | 1.00 | 0.00 | 0.00 | 0.00 | 0.00 | 2.76E-18 | 2.76E-18 |
| 90.00 | 91.00 | 1.84E+09 | 1.00 | 0.00 | 0.00 | 0.00 | 0.00 | 2.75E-18 | 2.75E-18 |
| 91.00 | 92.00 | 1.22E+09 | 1.00 | 0.00 | 0.00 | 0.00 | 0.00 | 2.91E-19 | 2.91E-19 |

**Table B-2 Binned Solar Irradiance and Cross Sections for $O_2$**

| Wavelengths Bins (nm) | | Solar Irrad. (ph $cm^{-2}$ $s^{-1}$) | Ionized State Branching Ratios | | | | Total Cross Sections ($cm^2$) | |
|---|---|---|---|---|---|---|---|---|
| λ min | λ max | | $X\ ^2\pi_g$ | $a^4\pi_u+A^2\pi_u$ | $b\ ^4\Sigma_g^-$ | Diss | Ionization | Absorption |
| 0.05 | 0.10 | 1.00E+01 | 0.00 | 0.00 | 0.00 | 1.00 | 4.00E-23 | 4.00E-23 |
| 0.10 | 0.20 | 1.00E+02 | 0.00 | 0.00 | 0.00 | 1.00 | 4.00E-22 | 4.00E-22 |
| 0.20 | 0.40 | 2.00E+02 | 0.00 | 0.00 | 0.00 | 1.00 | 4.00E-21 | 4.00E-21 |
| 0.40 | 0.80 | 1.00E+04 | 0.00 | 0.00 | 0.00 | 1.00 | 2.40E-20 | 2.40E-20 |
| 0.80 | 1.80 | 2.00E+06 | 0.00 | 0.00 | 0.00 | 1.00 | 1.40E-19 | 1.40E-19 |
| 1.80 | 2.30 | 9.00E+05 | 0.00 | 0.00 | 0.00 | 1.00 | 3.57E-20 | 3.57E-20 |
| 2.30 | 3.20 | 6.70E+06 | 0.01 | 0.01 | 0.01 | 0.97 | 1.37E-19 | 1.37E-19 |
| 3.20 | 4.40 | 3.80E+06 | 0.02 | 0.02 | 0.02 | 0.95 | 2.69E-19 | 2.69E-19 |
| 4.40 | 6.00 | 8.56E+07 | 0.03 | 0.03 | 0.02 | 0.91 | 5.16E-19 | 5.16E-19 |
| 6.00 | 7.00 | 7.65E+07 | 0.05 | 0.04 | 0.03 | 0.88 | 8.13E-19 | 8.13E-19 |
| 7.00 | 8.00 | 7.93E+07 | 0.06 | 0.06 | 0.04 | 0.84 | 1.14E-18 | 1.14E-18 |
| 8.00 | 9.00 | 6.57E+07 | 0.08 | 0.07 | 0.05 | 0.80 | 1.58E-18 | 1.58E-18 |
| 9.00 | 10.00 | 9.40E+07 | 0.09 | 0.08 | 0.06 | 0.77 | 2.01E-18 | 2.01E-18 |
| 10.00 | 11.00 | 3.09E+07 | 0.11 | 0.10 | 0.07 | 0.73 | 2.44E-18 | 2.44E-18 |
| 11.00 | 12.00 | 2.13E+07 | 0.13 | 0.11 | 0.08 | 0.68 | 2.96E-18 | 2.96E-18 |
| 12.00 | 13.00 | 1.59E+07 | 0.15 | 0.13 | 0.09 | 0.62 | 3.64E-18 | 3.64E-18 |
| 13.00 | 14.00 | 1.06E+07 | 0.16 | 0.14 | 0.10 | 0.59 | 4.04E-18 | 4.04E-18 |
| 14.00 | 15.00 | 5.59E+07 | 0.19 | 0.17 | 0.12 | 0.53 | 5.05E-18 | 5.05E-18 |
| 15.00 | 16.00 | 6.10E+07 | 0.20 | 0.17 | 0.12 | 0.51 | 5.73E-18 | 5.73E-18 |
| 16.00 | 17.00 | 1.32E+08 | 0.20 | 0.18 | 0.13 | 0.48 | 6.53E-18 | 6.53E-18 |
| 17.00 | 18.00 | 8.46E+08 | 0.21 | 0.19 | 0.13 | 0.46 | 6.95E-18 | 6.95E-18 |
| 18.00 | 19.00 | 4.46E+08 | 0.23 | 0.20 | 0.13 | 0.44 | 7.65E-18 | 7.65E-18 |
| 19.00 | 20.00 | 3.57E+08 | 0.25 | 0.19 | 0.13 | 0.43 | 8.40E-18 | 8.40E-18 |
| 20.00 | 21.00 | 1.42E+08 | 0.25 | 0.20 | 0.13 | 0.42 | 9.04E-18 | 9.04E-18 |

| | | | | | | | | |
|---|---|---|---|---|---|---|---|---|
| 21.00 | 22.00 | 9.24E+07 | 0.25 | 0.20 | 0.13 | 0.41 | 9.92E-18 | 9.92E-18 |
| 22.00 | 23.00 | 2.39E+08 | 0.26 | 0.21 | 0.14 | 0.40 | 1.07E-17 | 1.07E-17 |
| 23.00 | 24.00 | 1.32E+08 | 0.25 | 0.22 | 0.14 | 0.39 | 1.15E-17 | 1.15E-17 |
| 24.00 | 25.00 | 3.18E+08 | 0.27 | 0.21 | 0.14 | 0.38 | 1.22E-17 | 1.22E-17 |
| 25.00 | 26.00 | 5.50E+08 | 0.28 | 0.22 | 0.14 | 0.37 | 1.34E-17 | 1.34E-17 |
| 26.00 | 27.00 | 1.05E+08 | 0.28 | 0.21 | 0.13 | 0.37 | 1.40E-17 | 1.40E-17 |
| 27.00 | 28.00 | 2.73E+08 | 0.29 | 0.20 | 0.13 | 0.38 | 1.51E-17 | 1.51E-17 |
| 28.00 | 29.00 | 1.37E+08 | 0.29 | 0.21 | 0.13 | 0.37 | 1.58E-17 | 1.58E-17 |
| 29.00 | 30.00 | 1.48E+08 | 0.30 | 0.21 | 0.12 | 0.37 | 1.64E-17 | 1.64E-17 |
| 30.00 | 31.00 | 6.24E+09 | 0.31 | 0.21 | 0.13 | 0.35 | 1.68E-17 | 1.68E-17 |
| 31.00 | 32.00 | 4.10E+08 | 0.32 | 0.22 | 0.13 | 0.33 | 1.71E-17 | 1.71E-17 |
| 32.00 | 33.00 | 4.70E+06 | 0.33 | 0.22 | 0.13 | 0.32 | 1.72E-17 | 1.72E-17 |
| 33.00 | 34.00 | 3.40E+07 | 0.35 | 0.23 | 0.13 | 0.29 | 1.74E-17 | 1.74E-17 |
| 34.00 | 35.00 | 4.18E+08 | 0.36 | 0.23 | 0.13 | 0.28 | 1.77E-17 | 1.77E-17 |
| 35.00 | 36.00 | 1.03E+08 | 0.37 | 0.23 | 0.13 | 0.27 | 1.79E-17 | 1.79E-17 |
| 36.00 | 37.00 | 8.33E+08 | 0.38 | 0.24 | 0.13 | 0.25 | 1.83E-17 | 1.83E-17 |
| 37.00 | 38.00 | 0.00E+00 | 0.40 | 0.23 | 0.13 | 0.25 | 1.87E-17 | 1.87E-17 |
| 38.00 | 39.00 | 0.00E+00 | 0.41 | 0.22 | 0.12 | 0.25 | 1.92E-17 | 1.92E-17 |
| 39.00 | 40.00 | 1.56E+07 | 0.42 | 0.22 | 0.12 | 0.24 | 1.96E-17 | 1.96E-17 |
| 40.00 | 41.00 | 1.79E+08 | 0.42 | 0.22 | 0.12 | 0.24 | 1.97E-17 | 1.97E-17 |
| 41.00 | 42.00 | 8.80E+06 | 0.42 | 0.23 | 0.12 | 0.24 | 2.02E-17 | 2.02E-17 |
| 42.00 | 43.00 | 0.00E+00 | 0.41 | 0.24 | 0.12 | 0.23 | 2.05E-17 | 2.05E-17 |
| 43.00 | 44.00 | 2.05E+08 | 0.39 | 0.25 | 0.13 | 0.23 | 2.08E-17 | 2.08E-17 |
| 44.00 | 45.00 | 0.00E+00 | 0.40 | 0.25 | 0.13 | 0.23 | 2.12E-17 | 2.12E-17 |
| 45.00 | 46.00 | 9.10E+06 | 0.40 | 0.25 | 0.12 | 0.23 | 2.16E-17 | 2.16E-17 |
| 46.00 | 47.00 | 2.00E+08 | 0.39 | 0.25 | 0.13 | 0.23 | 2.19E-17 | 2.19E-17 |
| 47.00 | 48.00 | 3.24E+07 | 0.38 | 0.26 | 0.13 | 0.23 | 2.23E-17 | 2.23E-17 |
| 48.00 | 49.00 | 6.50E+07 | 0.37 | 0.27 | 0.13 | 0.23 | 2.28E-17 | 2.28E-17 |
| 49.00 | 50.00 | 1.69E+08 | 0.36 | 0.28 | 0.13 | 0.23 | 2.34E-17 | 2.34E-17 |

| | | | | | | | | |
|---|---|---|---|---|---|---|---|---|
| 50.00 | 51.00 | 1.43E+08 | 0.35 | 0.29 | 0.13 | 0.23 | 2.38E-17 | 2.38E-17 |
| 51.00 | 52.00 | 3.35E+07 | 0.34 | 0.30 | 0.14 | 0.23 | 2.43E-17 | 2.43E-17 |
| 52.00 | 53.00 | 1.11E+08 | 0.34 | 0.31 | 0.14 | 0.21 | 2.47E-17 | 2.47E-17 |
| 53.00 | 54.00 | 1.86E+08 | 0.34 | 0.32 | 0.16 | 0.19 | 2.53E-17 | 2.53E-17 |
| 54.00 | 55.00 | 2.32E+07 | 0.34 | 0.31 | 0.18 | 0.17 | 2.53E-17 | 2.53E-17 |
| 55.00 | 56.00 | 8.84E+08 | 0.32 | 0.28 | 0.23 | 0.17 | 2.60E-17 | 2.60E-17 |
| 56.00 | 57.00 | 1.34E+08 | 0.31 | 0.26 | 0.26 | 0.17 | 2.60E-17 | 2.60E-17 |
| 57.00 | 58.00 | 6.89E+07 | 0.30 | 0.27 | 0.26 | 0.17 | 2.57E-17 | 2.57E-17 |
| 58.00 | 59.00 | 1.59E+09 | 0.28 | 0.29 | 0.26 | 0.17 | 2.27E-17 | 2.27E-17 |
| 59.00 | 60.00 | 2.09E+08 | 0.23 | 0.30 | 0.35 | 0.11 | 2.78E-17 | 2.78E-17 |
| 60.00 | 61.00 | 4.50E+08 | 0.25 | 0.37 | 0.30 | 0.07 | 2.64E-17 | 2.81E-17 |
| 61.00 | 62.00 | 1.67E+07 | 0.27 | 0.39 | 0.29 | 0.05 | 2.57E-17 | 2.64E-17 |
| 62.00 | 63.00 | 1.60E+09 | 0.30 | 0.35 | 0.31 | 0.03 | 3.07E-17 | 3.17E-17 |
| 63.00 | 64.00 | 2.49E+07 | 0.32 | 0.32 | 0.32 | 0.04 | 2.60E-17 | 2.62E-17 |
| 64.00 | 65.00 | 3.30E+07 | 0.33 | 0.31 | 0.32 | 0.04 | 2.50E-17 | 2.56E-17 |
| 65.00 | 66.00 | 2.18E+07 | 0.30 | 0.33 | 0.33 | 0.04 | 2.62E-17 | 2.71E-17 |
| 66.00 | 67.00 | 6.20E+06 | 0.27 | 0.38 | 0.35 | 0.00 | 2.54E-17 | 2.57E-17 |
| 67.00 | 68.00 | 1.06E+07 | 0.35 | 0.40 | 0.25 | 0.00 | 2.04E-17 | 2.09E-17 |
| 68.00 | 69.00 | 1.39E+08 | 0.53 | 0.47 | 0.00 | 0.00 | 2.04E-17 | 2.06E-17 |
| 69.00 | 70.00 | 4.35E+07 | 0.59 | 0.41 | 0.00 | 0.00 | 1.96E-17 | 2.13E-17 |
| 70.00 | 71.00 | 4.02E+08 | 0.66 | 0.34 | 0.00 | 0.00 | 2.39E-17 | 2.76E-17 |
| 71.00 | 72.00 | 8.01E+07 | 0.56 | 0.44 | 0.00 | 0.00 | 2.46E-17 | 2.96E-17 |
| 72.00 | 73.00 | 1.86E+07 | 0.59 | 0.41 | 0.00 | 0.00 | 2.57E-17 | 3.02E-17 |
| 73.00 | 74.00 | 2.42E+07 | 0.57 | 0.43 | 0.00 | 0.00 | 2.99E-17 | 3.34E-17 |
| 74.00 | 75.00 | 3.06E+07 | 0.64 | 0.36 | 0.00 | 0.00 | 1.51E-17 | 2.01E-17 |
| 75.00 | 76.00 | 1.42E+08 | 0.79 | 0.21 | 0.00 | 0.00 | 1.25E-17 | 1.99E-17 |
| 76.00 | 77.00 | 3.97E+08 | 0.91 | 0.09 | 0.00 | 0.00 | 1.10E-17 | 2.03E-17 |
| 77.00 | 78.00 | 3.08E+08 | 1.00 | 0.00 | 0.00 | 0.00 | 9.37E-18 | 1.96E-17 |
| 78.00 | 79.00 | 6.39E+08 | 1.00 | 0.00 | 0.00 | 0.00 | 1.03E-17 | 2.38E-17 |

| | | | | | | | | |
|---|---|---|---|---|---|---|---|---|
| 79.00 | 80.00 | 5.86E+08 | 1.00 | 0.00 | 0.00 | 0.00 | 9.93E-18 | 2.74E-17 |
| 80.00 | 81.00 | 1.40E+08 | 1.00 | 0.00 | 0.00 | 0.00 | 1.19E-17 | 3.37E-17 |
| 81.00 | 82.00 | 1.80E+08 | 1.00 | 0.00 | 0.00 | 0.00 | 1.46E-17 | 3.29E-17 |
| 82.00 | 83.00 | 2.32E+08 | 1.00 | 0.00 | 0.00 | 0.00 | 7.79E-18 | 2.06E-17 |
| 83.00 | 84.00 | 9.64E+08 | 1.00 | 0.00 | 0.00 | 0.00 | 4.81E-18 | 1.26E-17 |
| 84.00 | 85.00 | 3.83E+08 | 1.00 | 0.00 | 0.00 | 0.00 | 4.32E-18 | 1.21E-17 |
| 85.00 | 86.00 | 4.93E+08 | 1.00 | 0.00 | 0.00 | 0.00 | 3.82E-18 | 8.99E-18 |
| 86.00 | 87.00 | 6.32E+08 | 1.00 | 0.00 | 0.00 | 0.00 | 4.56E-18 | 7.54E-18 |
| 87.00 | 88.00 | 8.13E+08 | 1.00 | 0.00 | 0.00 | 0.00 | 5.91E-18 | 9.20E-18 |
| 88.00 | 89.00 | 1.04E+09 | 1.00 | 0.00 | 0.00 | 0.00 | 6.62E-18 | 9.82E-18 |
| 89.00 | 90.00 | 1.34E+09 | 1.00 | 0.00 | 0.00 | 0.00 | 5.40E-18 | 7.55E-18 |
| 90.00 | 91.00 | 1.84E+09 | 1.00 | 0.00 | 0.00 | 0.00 | 6.54E-18 | 9.66E-18 |
| 91.00 | 92.00 | 1.22E+09 | 1.00 | 0.00 | 0.00 | 0.00 | 8.23E-18 | 1.19E-17 |
| 92.00 | 93.00 | 3.90E+08 | 1.00 | 0.00 | 0.00 | 0.00 | 5.32E-18 | 6.71E-18 |
| 93.00 | 94.00 | 4.54E+08 | 1.00 | 0.00 | 0.00 | 0.00 | 1.97E-17 | 2.45E-17 |
| 94.00 | 95.00 | 4.58E+08 | 1.00 | 0.00 | 0.00 | 0.00 | 1.05E-17 | 1.36E-17 |
| 95.00 | 96.00 | 5.13E+07 | 1.00 | 0.00 | 0.00 | 0.00 | 2.13E-17 | 2.73E-17 |
| 96.00 | 97.00 | 6.14E+07 | 1.00 | 0.00 | 0.00 | 0.00 | 1.87E-17 | 2.35E-17 |
| 97.00 | 98.00 | 6.85E+09 | 1.00 | 0.00 | 0.00 | 0.00 | 1.61E-17 | 2.04E-17 |
| 98.00 | 99.00 | 2.80E+08 | 1.00 | 0.00 | 0.00 | 0.00 | 5.03E-18 | 6.24E-18 |
| 99.00 | 100.00 | 4.88E+08 | 1.00 | 0.00 | 0.00 | 0.00 | 9.68E-18 | 1.36E-17 |
| 100.00 | 101.00 | 1.26E+08 | 1.00 | 0.00 | 0.00 | 0.00 | 2.76E-18 | 3.25E-18 |
| 101.00 | 102.00 | 2.36E+08 | 1.00 | 0.00 | 0.00 | 0.00 | 1.03E-18 | 1.32E-18 |
| 102.00 | 103.00 | 4.56E+09 | 1.00 | 0.00 | 0.00 | 0.00 | 9.83E-19 | 1.62E-18 |

## Table B-3 Binned Solar Irradiance and Cross Sections for $N_2$

| Wavelength Bins (nm) | | Solar Irrad. ($ph\ cm^{-2}\ s^{-1}$) | Ionized State Branching Ratios | | | | | | Total Cross Sections ($cm^2$) | |
|---|---|---|---|---|---|---|---|---|---|---|
| λ min | λ max | | $X\ ^2\Sigma_g^+$ | $A\ ^2\pi_u$ | $B\ ^2\Sigma_u^+$ | $C\ ^2\Sigma_u^+$ | $F\ ^2\Sigma_g^+$ | Diss | Ionization | Absorption |
| 0.05 | 0.10 | 1.00E+01 | 0.01 | 0.01 | 0.00 | 0.00 | 0.00 | 0.97 | 3.00E-23 | 3.00E-23 |
| 0.10 | 0.20 | 1.00E+02 | 0.01 | 0.01 | 0.00 | 0.00 | 0.00 | 0.97 | 3.00E-22 | 3.00E-22 |
| 0.20 | 0.40 | 2.00E+02 | 0.01 | 0.01 | 0.00 | 0.00 | 0.00 | 0.97 | 3.00E-21 | 3.00E-21 |
| 0.40 | 0.80 | 1.00E+04 | 0.01 | 0.01 | 0.00 | 0.00 | 0.00 | 0.97 | 1.50E-20 | 1.50E-20 |
| 0.80 | 1.80 | 2.00E+06 | 0.01 | 0.01 | 0.00 | 0.00 | 0.00 | 0.97 | 9.00E-20 | 9.00E-20 |
| 1.80 | 2.30 | 9.00E+05 | 0.01 | 0.01 | 0.00 | 0.00 | 0.00 | 0.97 | 7.08E-19 | 7.08E-19 |
| 2.30 | 3.20 | 6.70E+06 | 0.01 | 0.02 | 0.00 | 0.00 | 0.00 | 0.96 | 9.78E-19 | 9.78E-19 |
| 3.20 | 4.40 | 3.80E+06 | 0.22 | 0.30 | 0.09 | 0.02 | 0.06 | 0.31 | 1.46E-19 | 1.46E-19 |
| 4.40 | 6.00 | 8.56E+07 | 0.23 | 0.31 | 0.09 | 0.02 | 0.06 | 0.29 | 2.77E-19 | 2.77E-19 |
| 6.00 | 7.00 | 7.65E+07 | 0.23 | 0.32 | 0.09 | 0.02 | 0.06 | 0.28 | 4.34E-19 | 4.34E-19 |
| 7.00 | 8.00 | 7.93E+07 | 0.23 | 0.32 | 0.09 | 0.01 | 0.06 | 0.27 | 6.14E-19 | 6.14E-19 |
| 8.00 | 9.00 | 6.57E+07 | 0.24 | 0.32 | 0.09 | 0.01 | 0.06 | 0.27 | 8.60E-19 | 8.60E-19 |
| 9.00 | 10.00 | 9.40E+07 | 0.24 | 0.33 | 0.09 | 0.01 | 0.06 | 0.27 | 1.13E-18 | 1.13E-18 |
| 10.00 | 11.00 | 3.09E+07 | 0.24 | 0.33 | 0.09 | 0.01 | 0.06 | 0.27 | 1.40E-18 | 1.40E-18 |
| 11.00 | 12.00 | 2.13E+07 | 0.24 | 0.33 | 0.10 | 0.01 | 0.06 | 0.26 | 1.73E-18 | 1.73E-18 |
| 12.00 | 13.00 | 1.59E+07 | 0.25 | 0.34 | 0.10 | 0.01 | 0.05 | 0.24 | 2.18E-18 | 2.18E-18 |
| 13.00 | 14.00 | 1.06E+07 | 0.25 | 0.34 | 0.10 | 0.01 | 0.05 | 0.24 | 2.42E-18 | 2.42E-18 |
| 14.00 | 15.00 | 5.59E+07 | 0.26 | 0.35 | 0.10 | 0.01 | 0.05 | 0.23 | 3.03E-18 | 3.03E-18 |
| 15.00 | 16.00 | 6.10E+07 | 0.25 | 0.35 | 0.10 | 0.01 | 0.05 | 0.24 | 3.50E-18 | 3.50E-18 |
| 16.00 | 17.00 | 1.32E+08 | 0.25 | 0.34 | 0.10 | 0.01 | 0.05 | 0.24 | 4.10E-18 | 4.10E-18 |
| 17.00 | 18.00 | 8.46E+08 | 0.25 | 0.34 | 0.10 | 0.01 | 0.05 | 0.24 | 4.46E-18 | 4.46E-18 |
| 18.00 | 19.00 | 4.46E+08 | 0.25 | 0.34 | 0.10 | 0.01 | 0.05 | 0.25 | 5.08E-18 | 5.08E-18 |
| 19.00 | 20.00 | 3.57E+08 | 0.24 | 0.33 | 0.10 | 0.01 | 0.06 | 0.26 | 5.73E-18 | 5.73E-18 |
| 20.00 | 21.00 | 1.42E+08 | 0.24 | 0.33 | 0.10 | 0.01 | 0.06 | 0.26 | 6.40E-18 | 6.40E-18 |

| | | | | | | | | | | |
|---|---|---|---|---|---|---|---|---|---|---|
| 21.00 | 22.00 | 9.24E+07 | 0.24 | 0.33 | 0.10 | 0.01 | 0.06 | 0.27 | 7.39E-18 | 7.39E-18 |
| 22.00 | 23.00 | 2.39E+08 | 0.23 | 0.32 | 0.09 | 0.01 | 0.06 | 0.28 | 8.32E-18 | 8.32E-18 |
| 23.00 | 24.00 | 1.32E+08 | 0.23 | 0.32 | 0.09 | 0.01 | 0.06 | 0.29 | 9.09E-18 | 9.09E-18 |
| 24.00 | 25.00 | 3.18E+08 | 0.23 | 0.32 | 0.09 | 0.01 | 0.06 | 0.28 | 9.71E-18 | 9.71E-18 |
| 25.00 | 26.00 | 5.50E+08 | 0.24 | 0.35 | 0.09 | 0.01 | 0.05 | 0.26 | 1.02E-17 | 1.02E-17 |
| 26.00 | 27.00 | 1.05E+08 | 0.24 | 0.37 | 0.09 | 0.01 | 0.05 | 0.23 | 1.04E-17 | 1.04E-17 |
| 27.00 | 28.00 | 2.73E+08 | 0.24 | 0.41 | 0.08 | 0.02 | 0.06 | 0.19 | 1.06E-17 | 1.06E-17 |
| 28.00 | 29.00 | 1.37E+08 | 0.24 | 0.42 | 0.09 | 0.02 | 0.07 | 0.16 | 1.09E-17 | 1.09E-17 |
| 29.00 | 30.00 | 1.48E+08 | 0.24 | 0.42 | 0.10 | 0.02 | 0.08 | 0.13 | 1.12E-17 | 1.12E-17 |
| 30.00 | 31.00 | 6.24E+09 | 0.24 | 0.43 | 0.11 | 0.02 | 0.10 | 0.09 | 1.17E-17 | 1.17E-17 |
| 31.00 | 32.00 | 4.10E+08 | 0.25 | 0.43 | 0.12 | 0.03 | 0.11 | 0.06 | 1.25E-17 | 1.25E-17 |
| 32.00 | 33.00 | 4.70E+06 | 0.25 | 0.44 | 0.12 | 0.03 | 0.11 | 0.06 | 1.28E-17 | 1.28E-17 |
| 33.00 | 34.00 | 3.40E+07 | 0.26 | 0.46 | 0.12 | 0.03 | 0.11 | 0.03 | 1.40E-17 | 1.40E-17 |
| 34.00 | 35.00 | 4.18E+08 | 0.28 | 0.47 | 0.11 | 0.03 | 0.09 | 0.02 | 1.50E-17 | 1.50E-17 |
| 35.00 | 36.00 | 1.03E+08 | 0.30 | 0.47 | 0.11 | 0.03 | 0.08 | 0.01 | 1.58E-17 | 1.58E-17 |
| 36.00 | 37.00 | 8.33E+08 | 0.33 | 0.47 | 0.10 | 0.03 | 0.06 | 0.01 | 1.69E-17 | 1.69E-17 |
| 37.00 | 38.00 | 0.00E+00 | 0.36 | 0.46 | 0.10 | 0.03 | 0.05 | 0.00 | 1.79E-17 | 1.79E-17 |
| 38.00 | 39.00 | 0.00E+00 | 0.39 | 0.45 | 0.09 | 0.03 | 0.03 | 0.00 | 1.90E-17 | 1.90E-17 |
| 39.00 | 40.00 | 1.56E+07 | 0.42 | 0.43 | 0.09 | 0.03 | 0.02 | 0.00 | 2.01E-17 | 2.01E-17 |
| 40.00 | 41.00 | 1.79E+08 | 0.42 | 0.44 | 0.09 | 0.03 | 0.02 | 0.00 | 2.03E-17 | 2.03E-17 |
| 41.00 | 42.00 | 8.80E+06 | 0.42 | 0.45 | 0.09 | 0.03 | 0.01 | 0.00 | 2.16E-17 | 2.16E-17 |
| 42.00 | 43.00 | 0.00E+00 | 0.43 | 0.44 | 0.09 | 0.03 | 0.01 | 0.00 | 2.22E-17 | 2.22E-17 |
| 43.00 | 44.00 | 2.05E+08 | 0.43 | 0.44 | 0.09 | 0.04 | 0.00 | 0.00 | 2.28E-17 | 2.28E-17 |
| 44.00 | 45.00 | 0.00E+00 | 0.43 | 0.44 | 0.08 | 0.04 | 0.00 | 0.00 | 2.30E-17 | 2.30E-17 |
| 45.00 | 46.00 | 9.10E+06 | 0.43 | 0.45 | 0.08 | 0.04 | 0.00 | 0.00 | 2.31E-17 | 2.31E-17 |
| 46.00 | 47.00 | 2.00E+08 | 0.42 | 0.46 | 0.07 | 0.05 | 0.00 | 0.00 | 2.32E-17 | 2.32E-17 |
| 47.00 | 48.00 | 3.24E+07 | 0.41 | 0.46 | 0.07 | 0.05 | 0.00 | 0.00 | 2.34E-17 | 2.34E-17 |
| 48.00 | 49.00 | 6.50E+07 | 0.41 | 0.47 | 0.08 | 0.04 | 0.00 | 0.00 | 2.35E-17 | 2.35E-17 |
| 49.00 | 50.00 | 1.69E+08 | 0.41 | 0.49 | 0.08 | 0.02 | 0.00 | 0.00 | 2.35E-17 | 2.35E-17 |
| 50.00 | 51.00 | 1.43E+08 | 0.40 | 0.51 | 0.08 | 0.01 | 0.00 | 0.00 | 2.36E-17 | 2.36E-17 |

| | | | | | | | | | | |
|---|---|---|---|---|---|---|---|---|---|---|
| 51.00 | 52.00 | 3.35E+07 | 0.40 | 0.52 | 0.08 | 0.00 | 0.00 | 0.00 | 2.43E-17 | 2.43E-17 |
| 52.00 | 53.00 | 1.11E+08 | 0.39 | 0.52 | 0.09 | 0.00 | 0.00 | 0.00 | 2.48E-17 | 2.48E-17 |
| 53.00 | 54.00 | 1.86E+08 | 0.38 | 0.52 | 0.10 | 0.00 | 0.00 | 0.00 | 2.52E-17 | 2.52E-17 |
| 54.00 | 55.00 | 2.32E+07 | 0.37 | 0.53 | 0.10 | 0.00 | 0.00 | 0.00 | 2.51E-17 | 2.51E-17 |
| 55.00 | 56.00 | 8.84E+08 | 0.35 | 0.54 | 0.11 | 0.00 | 0.00 | 0.00 | 2.41E-17 | 2.41E-17 |
| 56.00 | 57.00 | 1.34E+08 | 0.35 | 0.55 | 0.10 | 0.00 | 0.00 | 0.00 | 2.29E-17 | 2.29E-17 |
| 57.00 | 58.00 | 6.89E+07 | 0.35 | 0.56 | 0.09 | 0.00 | 0.00 | 0.00 | 2.25E-17 | 2.25E-17 |
| 58.00 | 59.00 | 1.59E+09 | 0.36 | 0.54 | 0.09 | 0.00 | 0.00 | 0.00 | 2.24E-17 | 2.24E-17 |
| 59.00 | 60.00 | 2.09E+08 | 0.32 | 0.58 | 0.10 | 0.00 | 0.00 | 0.00 | 2.26E-17 | 2.26E-17 |
| 60.00 | 61.00 | 4.50E+08 | 0.30 | 0.59 | 0.12 | 0.00 | 0.00 | 0.00 | 2.28E-17 | 2.28E-17 |
| 61.00 | 62.00 | 1.67E+07 | 0.30 | 0.58 | 0.12 | 0.00 | 0.00 | 0.00 | 2.30E-17 | 2.30E-17 |
| 62.00 | 63.00 | 1.60E+09 | 0.31 | 0.58 | 0.11 | 0.00 | 0.00 | 0.00 | 2.34E-17 | 2.34E-17 |
| 63.00 | 64.00 | 2.49E+07 | 0.32 | 0.57 | 0.11 | 0.00 | 0.00 | 0.00 | 2.36E-17 | 2.36E-17 |
| 64.00 | 65.00 | 3.30E+07 | 0.31 | 0.58 | 0.11 | 0.00 | 0.00 | 0.00 | 2.37E-17 | 2.37E-17 |
| 65.00 | 66.00 | 2.18E+07 | 0.30 | 0.59 | 0.11 | 0.00 | 0.00 | 0.00 | 2.40E-17 | 2.40E-17 |
| 66.00 | 67.00 | 6.20E+06 | 0.33 | 0.64 | 0.03 | 0.00 | 0.00 | 0.00 | 2.34E-17 | 2.57E-17 |
| 67.00 | 68.00 | 1.06E+07 | 0.31 | 0.69 | 0.00 | 0.00 | 0.00 | 0.00 | 3.33E-17 | 3.43E-17 |
| 68.00 | 69.00 | 1.39E+08 | 0.32 | 0.68 | 0.00 | 0.00 | 0.00 | 0.00 | 3.07E-17 | 3.23E-17 |
| 69.00 | 70.00 | 4.35E+07 | 0.36 | 0.64 | 0.00 | 0.00 | 0.00 | 0.00 | 2.78E-17 | 3.33E-17 |
| 70.00 | 71.00 | 4.02E+08 | 0.37 | 0.63 | 0.00 | 0.00 | 0.00 | 0.00 | 2.54E-17 | 2.65E-17 |
| 71.00 | 72.00 | 8.01E+07 | 0.39 | 0.61 | 0.00 | 0.00 | 0.00 | 0.00 | 1.68E-17 | 2.37E-17 |
| 72.00 | 73.00 | 1.86E+07 | 0.57 | 0.43 | 0.00 | 0.00 | 0.00 | 0.00 | 1.79E-17 | 3.19E-17 |
| 73.00 | 74.00 | 2.42E+07 | 0.67 | 0.33 | 0.00 | 0.00 | 0.00 | 0.00 | 1.24E-17 | 2.28E-17 |
| 74.00 | 75.00 | 3.06E+07 | 0.75 | 0.25 | 0.00 | 0.00 | 0.00 | 0.00 | 8.32E-18 | 2.33E-17 |
| 75.00 | 76.00 | 1.42E+08 | 0.95 | 0.05 | 0.00 | 0.00 | 0.00 | 0.00 | 1.32E-17 | 2.57E-17 |
| 76.00 | 77.00 | 3.97E+08 | 1.00 | 0.00 | 0.00 | 0.00 | 0.00 | 0.00 | 4.18E-17 | 7.76E-17 |
| 77.00 | 78.00 | 3.08E+08 | 1.00 | 0.00 | 0.00 | 0.00 | 0.00 | 0.00 | 1.03E-17 | 1.94E-17 |
| 78.00 | 79.00 | 6.39E+08 | 1.00 | 0.00 | 0.00 | 0.00 | 0.00 | 0.00 | 9.61E-18 | 2.22E-17 |
| 79.00 | 80.00 | 5.86E+08 | 1.00 | 0.00 | 0.00 | 0.00 | 0.00 | 0.00 | 1.06E-17 | 2.35E-17 |

# Appendix C

## Results of Solar Irradiance Measurements

In Chapter V, the data from the solar instruments was discussed. The irradiance derived from these measurements is tabulated in Tables C-1 through C-3. These tables report the results from both the solar x-ray photometers and the EUV grating spectrograph. The irradiances are combined into individual tables for each rocket flight. For those wavelengths where there were no measurements, the SERF 1 model solar irradiance (Hinteregger *et al.*, 1981) is substituted as discussed in Chapter VI. Uncertainties for each measurement are also tabulated; all reported uncertainties are two sigma values. Where model solar irradiance is used, no uncertainties are quoted.

**Table C-1 Solar Irradiance for October 27, 1992 (Rocket Flight 36.098)**

| Wavelength Bins (nm) | | Solar Irradiance (ph $cm^{-2}$ $s^{-1}$) | Uncertainty (%) |
|---|---|---|---|
| $\lambda_{min}$ | $\lambda_{max}$ | | |
| 0.05 | 0.1 | 1.00E+01 | |
| 0.1 | 0.2 | 1.00E+02 | |
| 0.2 | 0.4 | 2.00E+02 | |
| 0.4 | 0.8 | 1.00E+04 | |
| 0.8 | 1.8 | 2.00E+06 | |
| 1.8 | 2.3 | 1.20E+07 | |
| 2.3 | 3.2 | 4.09E+07 | |
| 3.2 | 4.4 | 2.48E+07 | |
| 4.4 | 6 | 2.29E+08 | |
| 6 | 7 | 1.98E+08 | |
| 7 | 8 | 1.89E+08 | |
| 8 | 9 | 1.38E+08 | |
| 9 | 10 | 1.79E+08 | |
| 10 | 11 | 5.50E+07 | |
| 11 | 12 | 4.20E+07 | |
| 12 | 13 | 3.06E+07 | |
| 13 | 14 | 2.08E+07 | |
| 14 | 15 | 1.12E+08 | |
| 15 | 16 | 1.91E+08 | |
| 16 | 17 | 2.51E+08 | |
| 17 | 18 | 1.46E+09 | |
| 18 | 19 | 1.03E+09 | |
| 19 | 20 | 1.13E+09 | |
| 20 | 21 | 6.49E+08 | |
| 21 | 22 | 5.02E+08 | |
| 22 | 23 | 6.09E+08 | |
| 23 | 24 | 3.22E+08 | |
| 24 | 25 | 8.07E+08 | |
| 25 | 26 | 1.52E+09 | |
| 26 | 27 | 5.27E+08 | |
| 27 | 28 | 1.01E+09 | |
| 28 | 29 | 2.22E+09 | |
| 29 | 30 | 6.52E+09 | 68.7 |
| 30 | 31 | 1.02E+10 | 66.2 |

| | | | |
|---|---|---|---|
| 31 | 32 | 1.99E+09 | 58.1 |
| 32 | 33 | 6.42E+08 | 36.8 |
| 33 | 34 | 1.13E+09 | 21.2 |
| 34 | 35 | 1.71E+09 | 15.8 |
| 35 | 36 | 1.58E+09 | 14.4 |
| 36 | 37 | 1.37E+09 | 14.0 |
| 37 | 38 | 4.20E+08 | 16.3 |
| 38 | 39 | 2.10E+08 | 19.0 |
| 39 | 40 | 2.10E+08 | 17.9 |
| 40 | 41 | 1.69E+08 | 18.7 |
| 41 | 42 | 3.25E+08 | 13.3 |
| 42 | 43 | 1.99E+08 | 16.8 |
| 43 | 44 | 2.74E+08 | 13.5 |
| 44 | 45 | 2.21E+08 | 14.0 |
| 45 | 46 | 1.60E+08 | 15.9 |
| 46 | 47 | 4.48E+08 | 10.5 |
| 47 | 48 | 2.61E+08 | 12.0 |
| 48 | 49 | 4.08E+08 | 10.0 |
| 49 | 50 | 8.47E+08 | 7.7 |
| 50 | 51 | 6.71E+08 | 7.7 |
| 51 | 52 | 3.59E+08 | 8.8 |
| 52 | 53 | 2.92E+08 | 9.3 |
| 53 | 54 | 2.81E+08 | 9.3 |
| 54 | 55 | 2.48E+08 | 9.7 |
| 55 | 56 | 6.73E+08 | 6.7 |
| 56 | 57 | 2.49E+08 | 9.2 |
| 57 | 58 | 3.72E+08 | 8.1 |
| 58 | 59 | 1.44E+09 | 5.6 |
| 59 | 60 | 3.25E+08 | 8.3 |
| 60 | 61 | 1.06E+09 | 6.3 |
| 61 | 62 | 3.09E+08 | 9.0 |
| 62 | 63 | 1.66E+09 | 6.0 |
| 63 | 64 | 3.69E+08 | 8.6 |
| 64 | 65 | 1.59E+08 | 12.2 |
| 65 | 66 | 1.35E+08 | 12.7 |
| 66 | 67 | 1.64E+08 | 11.8 |
| 67 | 68 | 1.88E+08 | 11.7 |
| 68 | 69 | 2.71E+08 | 10.1 |
| 69 | 70 | 2.18E+08 | 11.5 |
| 70 | 71 | 4.40E+08 | 8.4 |
| 71 | 72 | 2.55E+08 | 10.5 |
| 72 | 73 | 1.98E+08 | 11.6 |
| 73 | 74 | 2.15E+08 | 11.1 |
| 74 | 75 | 2.97E+08 | 10.6 |
| 75 | 76 | 4.32E+08 | 9.5 |
| 76 | 77 | 1.01E+09 | 7.6 |
| 77 | 78 | 7.06E+08 | 8.2 |
| 78 | 79 | 1.33E+09 | 6.9 |
| 79 | 80 | 5.38E+08 | 8.2 |

| | | | |
|---|---|---|---|
| 80 | 81 | 6.63E+08 | 7.9 |
| 81 | 82 | 7.61E+08 | 8.0 |
| 82 | 83 | 1.06E+09 | 7.9 |
| 83 | 84 | 1.81E+09 | 7.4 |
| 84 | 85 | 1.24E+09 | 7.9 |
| 85 | 86 | 1.55E+09 | 7.4 |
| 86 | 87 | 1.57E+09 | 7.4 |
| 87 | 88 | 1.92E+09 | 7.5 |
| 88 | 89 | 2.27E+09 | 8.0 |
| 89 | 90 | 3.02E+09 | 8.6 |
| 90 | 91 | 3.45E+09 | 9.1 |
| 91 | 92 | 2.25E+09 | 9.0 |
| 92 | 93 | 1.02E+09 | 10.1 |
| 93 | 94 | 8.69E+08 | 10.4 |
| 94 | 95 | 1.02E+09 | 10.6 |
| 95 | 96 | 4.14E+08 | 13.8 |
| 96 | 97 | 9.46E+08 | 13.6 |
| 97 | 98 | 1.02E+10 | 11.8 |
| 98 | 99 | 6.95E+08 | 14.5 |
| 99 | 100 | 7.55E+08 | 14.8 |
| 100 | 101 | 1.72E+08 | 19.6 |
| 101 | 102 | 3.78E+08 | 19.6 |
| 102 | 103 | 8.13E+09 | 17.4 |

**Table C-2 Solar Irradiance for October 4, 1993 (Rocket Flight 36.107)**

| Wavelength Bins (nm) | | Solar Irradiance (ph $cm^{-2}$ $s^{-1}$) | Uncertainty (%) |
|---|---|---|---|
| $\lambda_{min}$ | $\lambda_{max}$ | | |
| 0.05 | 0.1 | 1.00E+01 | |
| 0.1 | 0.2 | 1.00E+02 | |
| 0.2 | 0.4 | 2.00E+02 | |
| 0.4 | 0.8 | 1.00E+04 | |
| 0.8 | 1.8 | 2.00E+06 | |
| 1.8 | 2.3 | 7.07E+06 | |
| 2.3 | 3.2 | 2.74E+07 | 21.7 |
| 3.2 | 4.4 | 1.62E+07 | 57.0 |
| 4.4 | 6 | 2.02E+08 | 53.8 |
| 6 | 7 | 1.32E+08 | |
| 7 | 8 | 1.34E+08 | |
| 8 | 9 | 9.70E+07 | |
| 9 | 10 | 1.37E+08 | |
| 10 | 11 | 4.34E+07 | |
| 11 | 12 | 3.36E+07 | |
| 12 | 13 | 2.46E+07 | |
| 13 | 14 | 1.67E+07 | |
| 14 | 15 | 8.00E+07 | |
| 15 | 16 | 1.14E+08 | |
| 16 | 17 | 1.95E+08 | |
| 17 | 18 | 2.27E+09 | 21.6 |
| 18 | 19 | 1.39E+09 | 21.6 |
| 19 | 20 | 1.36E+09 | 21.7 |
| 20 | 21 | 7.13E+08 | 22.0 |
| 21 | 22 | 5.21E+08 | 23.6 |
| 22 | 23 | 8.22E+08 | 22.7 |
| 23 | 24 | 4.53E+08 | 27.8 |
| 24 | 25 | 1.08E+09 | 23.1 |
| 25 | 26 | 1.96E+09 | 22.2 |
| 26 | 27 | 5.57E+08 | 34.2 |
| 27 | 28 | 1.26E+09 | 35.2 |
| 28 | 29 | 1.83E+09 | 29.2 |
| 29 | 30 | 2.94E+09 | 20.2 |
| 30 | 31 | 6.89E+09 | 14.9 |
| 31 | 32 | 2.06E+09 | 20.3 |
| 32 | 33 | 9.49E+08 | 21.7 |
| 33 | 34 | 8.42E+08 | 17.7 |
| 34 | 35 | 8.11E+08 | 16.0 |
| 35 | 36 | 8.10E+08 | 13.8 |
| 36 | 37 | 8.30E+08 | 11.8 |
| 37 | 38 | 3.86E+08 | 14.0 |
| 38 | 39 | 2.14E+08 | 16.0 |
| 39 | 40 | 1.41E+08 | 19.1 |

| | | | |
|---|---|---|---|
| 40 | 41 | 1.93E+08 | 15.4 |
| 41 | 42 | 2.35E+08 | 13.7 |
| 42 | 43 | 2.01E+08 | 14.9 |
| 43 | 44 | 2.44E+08 | 13.2 |
| 44 | 45 | 1.70E+08 | 14.2 |
| 45 | 46 | 1.52E+08 | 14.7 |
| 46 | 47 | 4.09E+08 | 9.9 |
| 47 | 48 | 2.00E+08 | 12.1 |
| 48 | 49 | 3.14E+08 | 10.1 |
| 49 | 50 | 5.06E+08 | 8.2 |
| 50 | 51 | 5.97E+08 | 7.3 |
| 51 | 52 | 2.23E+08 | 9.7 |
| 52 | 53 | 2.68E+08 | 8.7 |
| 53 | 54 | 2.54E+08 | 8.9 |
| 54 | 55 | 1.98E+08 | 9.6 |
| 55 | 56 | 6.80E+08 | 6.2 |
| 56 | 57 | 2.30E+08 | 8.5 |
| 57 | 58 | 2.87E+08 | 8.0 |
| 58 | 59 | 1.31E+09 | 5.2 |
| 59 | 60 | 2.91E+08 | 7.8 |
| 60 | 61 | 7.66E+08 | 6.2 |
| 61 | 62 | 3.35E+08 | 8.0 |
| 62 | 63 | 1.37E+09 | 5.6 |
| 63 | 64 | 5.98E+08 | 6.7 |
| 64 | 65 | 1.71E+08 | 11.0 |
| 65 | 66 | 1.07E+08 | 12.9 |
| 66 | 67 | 1.41E+08 | 11.6 |
| 67 | 68 | 1.35E+08 | 12.4 |
| 68 | 69 | 2.56E+08 | 9.4 |
| 69 | 70 | 1.90E+08 | 11.1 |
| 70 | 71 | 4.54E+08 | 7.8 |
| 71 | 72 | 2.39E+08 | 9.9 |
| 72 | 73 | 1.79E+08 | 11.1 |
| 73 | 74 | 1.89E+08 | 10.8 |
| 74 | 75 | 2.66E+08 | 10.3 |
| 75 | 76 | 4.11E+08 | 9.1 |
| 76 | 77 | 9.04E+08 | 7.4 |
| 77 | 78 | 5.73E+08 | 8.1 |
| 78 | 79 | 1.24E+09 | 6.7 |
| 79 | 80 | 5.49E+08 | 7.7 |
| 80 | 81 | 5.18E+08 | 8.0 |
| 81 | 82 | 6.33E+08 | 7.9 |
| 82 | 83 | 8.63E+08 | 7.9 |
| 83 | 84 | 1.70E+09 | 7.2 |
| 84 | 85 | 1.05E+09 | 7.8 |
| 85 | 86 | 1.35E+09 | 7.4 |
| 86 | 87 | 1.31E+09 | 7.4 |
| 87 | 88 | 1.59E+09 | 7.5 |
| 88 | 89 | 1.95E+09 | 8.1 |

| | | | |
|---|---|---|---|
| 89 | 90 | 2.58E+09 | 8.8 |
| 90 | 91 | 3.06E+09 | 9.1 |
| 91 | 92 | 2.14E+09 | 8.9 |
| 92 | 93 | 9.83E+08 | 10.1 |
| 93 | 94 | 7.74E+08 | 10.3 |
| 94 | 95 | 7.16E+08 | 11.0 |
| 95 | 96 | 4.89E+08 | 12.6 |
| 96 | 97 | 7.14E+08 | 13.7 |
| 97 | 98 | 8.78E+09 | 12.1 |
| 98 | 99 | 6.29E+08 | 14.6 |
| 99 | 100 | 7.88E+08 | 15.6 |
| 100 | 101 | 3.66E+08 | 17.3 |
| 101 | 102 | 3.49E+08 | 19.4 |
| 102 | 103 | 5.52E+09 | 17.8 |

**Table C-3 Solar Irradiance for November 3, 1994 (Flight 36.124)**

| Wavelength Bins (nm) | | Solar Irradiance (ph $cm^{-2}$ $s^{-1}$) | Uncertainty (%) |
|---|---|---|---|
| $\lambda_{min}$ | $\lambda_{max}$ | | |
| 0.05 | 0.1 | 1.00E+01 | |
| 0.1 | 0.2 | 1.00E+02 | |
| 0.2 | 0.4 | 2.00E+02 | |
| 0.4 | 0.8 | 1.00E+04 | |
| 0.8 | 1.8 | 2.00E+06 | |
| 1.8 | 2.3 | 7.07E+06 | |
| 2.3 | 3.2 | 2.03E+07 | 23.2 |
| 3.2 | 4.4 | 1.13E+07 | 48.6 |
| 4.4 | 6 | 2.40E+08 | 20.8 |
| 6 | 7 | 2.20E+08 | 20.7 |
| 7 | 8 | 2.37E+08 | 20.3 |
| 8 | 9 | 1.69E+08 | 20.8 |
| 9 | 10 | 2.59E+08 | 20.5 |
| 10 | 11 | 8.44E+07 | 25.2 |
| 11 | 12 | 6.67E+07 | 30.1 |
| 12 | 13 | 4.91E+07 | 41.0 |
| 13 | 14 | 3.31E+07 | 61.2 |
| 14 | 15 | 1.42E+08 | 27.3 |
| 15 | 16 | 1.62E+08 | 29.8 |
| 16 | 17 | 3.78E+08 | 25.1 |
| 17 | 18 | 1.42E+09 | 20.1 |
| 18 | 19 | 7.61E+08 | 20.2 |
| 19 | 20 | 6.34E+08 | 20.5 |
| 20 | 21 | 2.86E+08 | 23.1 |
| 21 | 22 | 1.84E+08 | 33.4 |
| 22 | 23 | 4.51E+08 | 26.0 |
| 23 | 24 | 2.61E+08 | 50.2 |
| 24 | 25 | 5.87E+08 | 43.3 |
| 25 | 26 | 1.01E+09 | 66.7 |
| 26 | 27 | 2.05E+08 | 96.6 |
| 27 | 28 | 1.08E+09 | 33.7 |
| 28 | 29 | 1.18E+09 | 28.2 |
| 29 | 30 | 1.76E+09 | 17.9 |
| 30 | 31 | 4.35E+09 | 11.7 |
| 31 | 32 | 9.13E+08 | 17.7 |
| 32 | 33 | 5.04E+08 | 21.3 |
| 33 | 34 | 6.52E+08 | 17.9 |
| 34 | 35 | 7.83E+08 | 14.9 |
| 35 | 36 | 5.88E+08 | 14.1 |
| 36 | 37 | 8.98E+08 | 10.7 |
| 37 | 38 | 3.13E+08 | 15.4 |
| 38 | 39 | 1.48E+08 | 19.2 |
| 39 | 40 | 1.40E+08 | 18.8 |

| | | | |
|---|---|---|---|
| 40 | 41 | 2.74E+08 | 13.5 |
| 41 | 42 | 1.87E+08 | 16.2 |
| 42 | 43 | 1.38E+08 | 17.8 |
| 43 | 44 | 2.76E+08 | 12.8 |
| 44 | 45 | 1.52E+08 | 16.0 |
| 45 | 46 | 1.55E+08 | 14.9 |
| 46 | 47 | 3.95E+08 | 10.0 |
| 47 | 48 | 1.97E+08 | 13.0 |
| 48 | 49 | 3.38E+08 | 10.6 |
| 49 | 50 | 5.63E+08 | 8.1 |
| 50 | 51 | 4.67E+08 | 8.2 |
| 51 | 52 | 2.15E+08 | 10.6 |
| 52 | 53 | 2.16E+08 | 9.6 |
| 53 | 54 | 2.58E+08 | 8.8 |
| 54 | 55 | 1.79E+08 | 10.4 |
| 55 | 56 | 6.99E+08 | 6.5 |
| 56 | 57 | 2.33E+08 | 9.3 |
| 57 | 58 | 2.23E+08 | 9.2 |
| 58 | 59 | 9.88E+08 | 5.6 |
| 59 | 60 | 3.06E+08 | 8.1 |
| 60 | 61 | 7.05E+08 | 6.3 |
| 61 | 62 | 3.37E+08 | 8.3 |
| 62 | 63 | 1.33E+09 | 5.7 |
| 63 | 64 | 2.66E+08 | 9.5 |
| 64 | 65 | 1.29E+08 | 12.7 |
| 65 | 66 | 1.02E+08 | 13.7 |
| 66 | 67 | 1.25E+08 | 13.6 |
| 67 | 68 | 1.06E+08 | 14.0 |
| 68 | 69 | 2.55E+08 | 9.8 |
| 69 | 70 | 1.99E+08 | 11.5 |
| 70 | 71 | 4.45E+08 | 8.0 |
| 71 | 72 | 2.21E+08 | 10.3 |
| 72 | 73 | 1.72E+08 | 11.7 |
| 73 | 74 | 2.14E+08 | 11.0 |
| 74 | 75 | 2.49E+08 | 10.0 |
| 75 | 76 | 3.25E+08 | 9.3 |
| 76 | 77 | 9.75E+08 | 7.0 |
| 77 | 78 | 5.82E+08 | 7.7 |
| 78 | 79 | 1.07E+09 | 6.4 |
| 79 | 80 | 5.12E+08 | 8.0 |
| 80 | 81 | 5.87E+08 | 7.7 |
| 81 | 82 | 5.72E+08 | 7.7 |
| 82 | 83 | 8.08E+08 | 7.6 |
| 83 | 84 | 1.59E+09 | 6.3 |
| 84 | 85 | 1.13E+09 | 7.2 |
| 85 | 86 | 1.16E+09 | 6.9 |
| 86 | 87 | 1.24E+09 | 6.7 |
| 87 | 88 | 1.65E+09 | 6.7 |
| 88 | 89 | 1.72E+09 | 6.6 |

| | | | |
|---|---|---|---|
| 89 | 90 | 2.09E+09 | 6.7 |
| 90 | 91 | 2.53E+09 | 6.9 |
| 91 | 92 | 2.13E+09 | 7.2 |
| 92 | 93 | 7.69E+08 | 8.5 |
| 93 | 94 | 7.48E+08 | 8.8 |
| 94 | 95 | 6.81E+08 | 8.7 |
| 95 | 96 | 2.72E+08 | 12.9 |
| 96 | 97 | 2.75E+08 | 13.4 |
| 97 | 98 | 4.33E+09 | 7.5 |
| 98 | 99 | 5.80E+08 | 10.9 |
| 99 | 100 | 9.88E+08 | 9.9 |
| 100 | 101 | 4.12E+08 | 12.1 |
| 101 | 102 | 5.05E+08 | 12.2 |
| 102 | 103 | 3.58E+09 | 8.6 |